BEILSTEIN JOURNAL OF NANOTECHNOLOGY

Nanomaterial-based cancer theranostics

Edited by Vladimir Sivakov

Imprint

Beilstein Journal of Nanotechnology
www.bjnano.org
ISSN 2190-4286
Email: journals-support@beilstein-institut.de

The *Beilstein Journal of Nanotechnology* is published by the Beilstein-Institut zur Förderung der Chemischen Wissenschaften.

Beilstein-Institut zur Förderung der Chemischen Wissenschaften
Trakehner Straße 7–9
60487 Frankfurt am Main
Germany
www.beilstein-institut.de

BEILSTEIN JOURNAL OF NANOTECHNOLOGY

Surface-enhanced Raman spectroscopy of cell lysates mixed with silver nanoparticles for tumor classification

Mohamed Hassoun[1,2], Iwan W.Schie[1], Tatiana Tolstik[1,3], Sarmiza E. Stanca[1], Christoph Krafft[*1] and Juergen Popp[1,2]

Full Research Paper

Open Access

Address:
[1]Leibniz Institute of Photonic Technology, Albert Einstein Str. 9, 07745 Jena, Germany, [2]Institute of Physical Chemistry & Abbe Center of Photonics, Friedrich Schiller University Jena, Helmholtzweg 4, 07743 Jena, Germany and [3]Department of Internal Medicine IV, Division of Gastroenterology, Hepatology and Infectious Diseases, Jena University Hospital, Erlanger Allee 101, 07745 Jena, Germany

Email:
Christoph Krafft[*] - christoph.krafft@leibniz-ipht.de

* Corresponding author

Keywords:
cell lysate; silver nanoparticles; surface-enhanced Raman spectroscopy (SERS); tumor-cell differentiation

Beilstein J. Nanotechnol. **2017,** *8,* 1183–1190.
doi:10.3762/bjnano.8.120

Received: 24 November 2016
Accepted: 08 May 2017
Published: 01 June 2017

This article is part of the Thematic Series "Nanomaterial-based cancer theranostics".

Guest Editor: V. Sivakov

Abstract

The throughput of spontaneous Raman spectroscopy for cell identification applications is limited to the range of one cell per second because of the relatively low sensitivity. Surface-enhanced Raman scattering (SERS) is a widespread way to amplify the intensity of Raman signals by several orders of magnitude and, consequently, to improve the sensitivity and throughput. SERS protocols using immuno-functionalized nanoparticles turned out to be challenging for cell identification because they require complex preparation procedures. Here, a new SERS strategy is presented for cell classification using non-functionalized silver nanoparticles and potassium chloride to induce aggregation. To demonstrate the principle, cell lysates were prepared by ultrasonication that disrupts the cell membrane and enables interaction of released cellular biomolecules to nanoparticles. This approach was applied to distinguish four cell lines – Capan-1, HepG2, Sk-Hep1 and MCF-7 – using SERS at 785 nm excitation. Six independent batches were prepared per cell line to check the reproducibility. Principal component analysis was applied for data reduction and assessment of spectral variations that were assigned to proteins, nucleotides and carbohydrates. Four principal components were selected as input for classification models based on support vector machines. Leave-three-batches-out cross validation recognized four cell lines with sensitivities, specificities and accuracies above 96%. We conclude that this reproducible and specific SERS approach offers prospects for cell identification using easily preparable silver nanoparticles.

Introduction

Cytopathology is the histopathologic inspection of cells. Dyes, such as hematoxylin for cell nuclei or eosin for cytoplasm, are commonly used to stain cells with subsequent microscopic assessment by pathologists. Complementary tools are immunocytochemistry, which uses fluorescence-labeled antibodies against cellular antigens, and flow cytometry, which combines

several detection channels based on light scattering, absorption and fluorescence with microfluidic flow systems.

Raman spectroscopy has been proposed as promising technique for cell characterization and cell identification because of its high chemical specificity under label-free and non-destructive conditions [1,2]. Raman spectroscopy is based on inelastic light scattering from molecular bonds. It probes the molecular vibrations of all cellular biomolecules, such as nucleic acids, proteins, lipids and carbohydrates and provides chemical fingerprint spectra of cells. The throughput of spontaneous Raman spectroscopy for cell classification is limited to the range of one cell per second by the inherently low efficiency of the inelastic scattering process of photons and the resultant low signal intensity. Compared to modern flow cytometers with a throughput of thousands cells per second, this severely restricts the applicability of Raman spectroscopy in this field. This limitation can be overcome by signal-enhancement approaches including surface-enhanced Raman scattering (SERS), resonance Raman scattering, coherent anti-Stokes Raman scattering and stimulated Raman scattering [3]. For the analysis of liquids, SERS is the most frequently applied approach and has been used for analyte detection in the submicromolar range [4,5]. SERS fingerprint spectra of molecules are generated when incident light excites localized surface plasmons on nanometer-sized metallic structures. A strong electromagnetic field is then created near the metallic surface and enhances the Raman scattering of nearby molecules. The plasmonic properties of SERS-active nanoparticles depend on the preparation conditions, the type of metal, the size and the shape of these nanoparticles [6-10], and their aggregation state [11,12]. Increasing the size of nanoparticle aggregates shifts the excitation wavelength to the near-IR region and therefore longer excitation wavelengths can be used for SERS measurements.

SERS was also suggested for cell identification [13,14]. While the signal intensity is similar to that of fluorescence emission, SERS nanoparticles do not suffer from photobleaching and offer a high multiplex capability due to narrow band widths. Enhancement of Raman signal of cells can be realized by (1) various techniques of nanoparticles delivery into cells, such as spontaneous uptake, microinjection, electroporation [15-20] or (2) binding of antibody-functionalized nanoparticles to specific antigens [21-23]. The disadvantages of approach (1) include the poor reproducibility due to nonspecific binding of nanoparticles, the long time needed for nanoparticles uptake by cells, and the heterogeneity of nanoparticles inside cells. Approach (2) is complicated because of complex protocols for nanoparticle preparation with Raman reporters, protective shells and antibodies. Furthermore, approach (2) cannot be considered to be label-free anymore. In the context of microbial identification, bacterial cells were lysed by sonication, and the bacterial lysate were mixed with nanoparticles to allow interaction between nanoparticles and bacterial biomolecules [24]. This gave very reproducible SERS spectra.

The current study transfers this SERS approach to distinguish four human cancer cell lines. These cell lines are two liver cancer cell lines (HepG2 isolated from liver tissue of a male patient with well differentiated hepatocellular carcinoma and SK-Hep1 received from ascetic fluid of a patient with adenocarcinoma of the liver), one breast cancer cell line (MCF-7 obtained from a female patient) and one human pancreatic ductal adenocarcinoma cell line (Capan-1). A protocol was developed to disrupt the cell walls by sonication and to allow for the interaction of silver nanoparticles with the released cellular biomolecules. The measured SERS spectra from six different batches were subjected to a support vector machine (SVM) to train classification models. The sensitivities, specificities and accuracies of the SVM model were calculated by cross-validation schemes. This proof-of-principle demonstrates that non-functionalized, easy-to-prepare silver nanoparticles give reproducible SERS spectra that can be used for the identification of human cancer cells.

Results and Discussion

The absorption band of silver (Ag) nanoparticles corresponds to the maximum of the plasmon resonance which is near 415 nm (Figure 1a). Shifting the plasmon resonance of our nanoparticles to the near-IR spectral region was achieved by aggregation using potassium chloride (KCl). When nanoparticles aggregate, they become electronically coupled, which results in a change of the surface plasmon resonance compared to individual particles. Figure 1b shows the effect of adding KCl to Ag nanoparticles on the optical absorption characteristics. The aggregated nanoparticles have a broad absorption band that allowed for SERS measurements with an excitation laser at 785 nm.

The size and shape of Ag nanoparticles were also analyzed by electron microscopy. Transmission electron microscopy (TEM) images and scanning electron microscopy (SEM) images of silver nanoparticles are compared in Figure 2a and b. The average size of the Ag nanoparticles was determined to be around 50 nm with a high degree of polydispersity in size ranging from 10 to 100 nm. The Ag nanoparticles do not tend to aggregate to a single specific shape after adding KCl. Instead, they form different shapes from spheres to rods. The cells, before and after sonication, were mixed with Ag nanoparticles and SEM images were recorded to better understand the diffusion of nanoparticles inside the cells. Nanoparticles represented by light spots are shown on the surface of a cell wall in Figure 2c and during interaction with cellular biomolecules in Figure 2d.

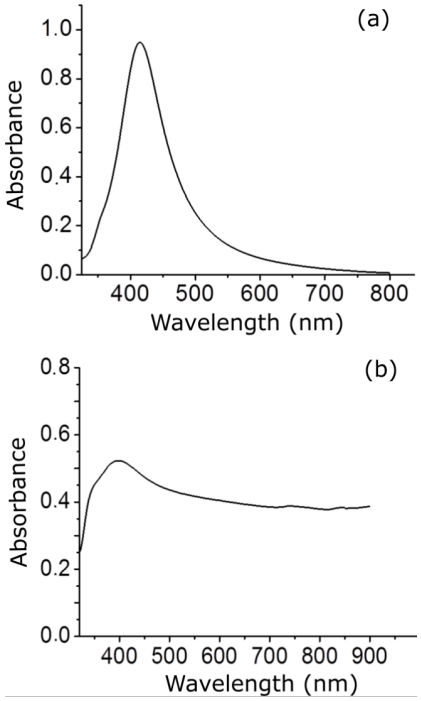

Figure 1: UV–vis absorption spectra of (a) silver nanoparticles with an absorption band at 415 nm and (b) solution of silver nanoparticles and potassium chloride. The absorption band of aggregated nanoparticles was shifted to near infrared region.

Cellular biomolecules including nucleic acids, proteins, carbohydrates and lipids are released after disruption of the cell membranes and can interact with nanoparticles. The spectral bands obtained from SERS measurements can then be assigned to biomolecules of cell nucleus and the cytoplasm. The raw spectra were baseline-subtracted and normalized. Figure 3 shows the processed mean SERS spectra and the standard deviation for each of the four cell lines Capan-1, HepG2, MCF-7 and Sk-Hep1. The band at 660 cm^{-1} is assigned to carboxylate [25]. Spectral contributions of adenine from nucleic acids and metabolites appear at 723 and 1339 cm^{-1} and can be assigned to adenine ring-breathing modes [18,26,27]. Protein vibrations contribute to the band at 900 cm^{-1}. The bands at 800 and 960 cm^{-1} can be assigned to CN stretching vibrations. Carbohydrates are represented by bands in the spectral region of 1000–1100 cm^{-1}. The bands at 1289 cm^{-1} and 1660 cm^{-1} can be assigned to the amide III and amide I vibrational modes of peptide bonds in proteins, respectively [18,26,28]. The band at 1450 cm^{-1} arises from CH_2 deformation vibrations of all biomolecules. The bands at 2923 and 2952 cm^{-1} can be assigned to CH_2 and CH_3 stretching vibrations of all biomolecules [24,26,28]. The reproducibility of these spectra was tested by measuring the SERS spectra from six batches of the four cell lines. The small standard deviation values proved the high reproducibility.

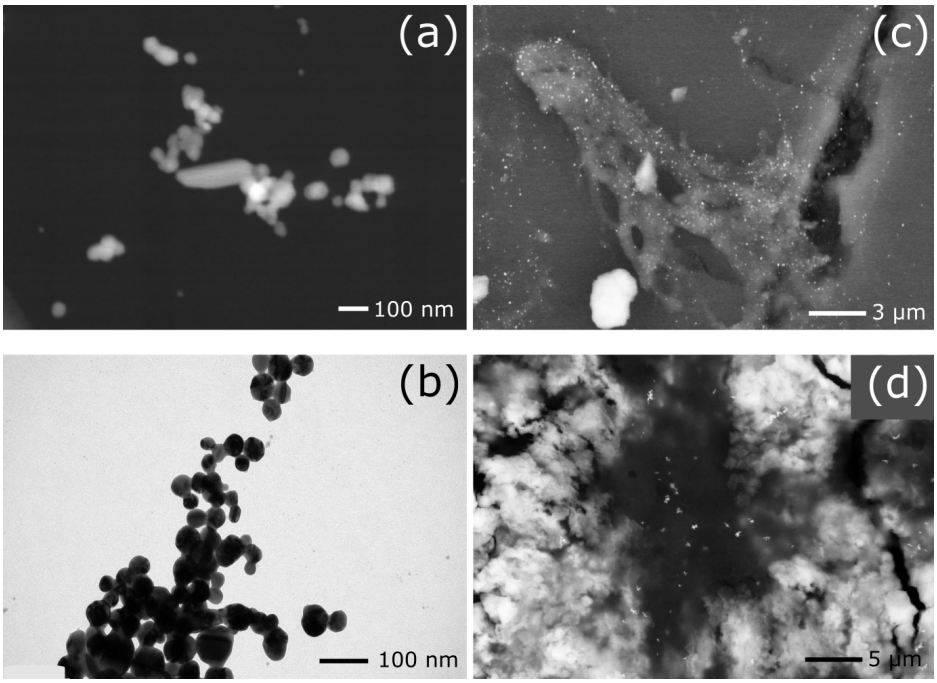

Figure 2: (a) Scanning electron microscopy (SEM) image of silver nanoparticles. The nanoparticles have a high degree of polydispersity in size ranging from 10 to 100 nm with an average size close to 50 nm. (b) Transmission electron microscopy image of silver nanoparticles showing their predominantly spherical shape and polydispersity in size. (c) SEM image of intact cells mixed with nanoparticles showing the distribution of nanoparticles on the surface of the cell. (d) SEM image of cell lysate mixed with nanoparticles showing released cellular biomolecules with nanoparticles after disruption of cell membrane.

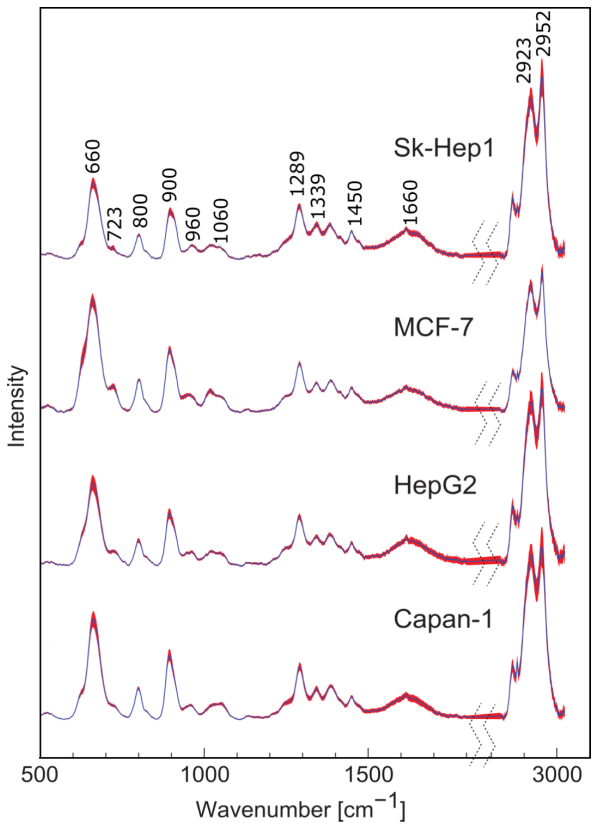

Figure 3: Preprocessed mean SERS spectra and standard deviations of the different cell lines. Labeled bands are assigned to cellular biomolecules including nucleic acids, proteins and carbohydrates. The low standard deviation values (represented by the red shadow) emphasize the high reproducibility of the technique.

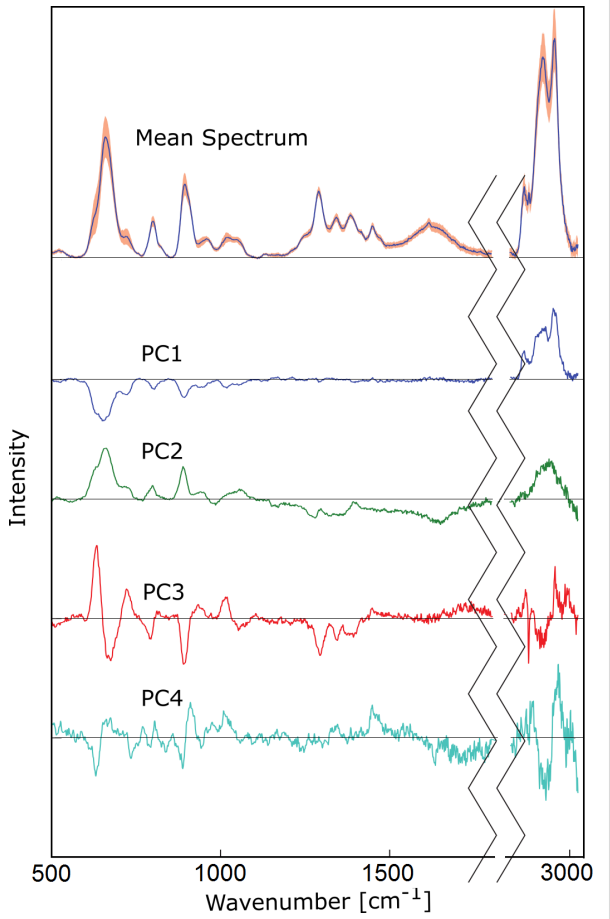

Figure 4: First four principal components used for the support vector machine model. These loadings represent 89% of data variance between MCF-7, Capan-1, SK-Hep1 and HepG2 cell lines.

It is evident from Figure 3 that the SERS spectra of the individual cell lines are highly similar and the cell lines cannot easily be distinguished by univariate analysis of single bands or band ratios. Therefore, multivariate classification was applied for differentiation of the cell lines. Prior to multivariate classification the data size was reduced by principal component analysis (PCA). Figure 4 shows the first four principal components (PCs) that described 89% of the variances of the data set required for cell line differentiation. PC1 loadings showed negative bands in the fingerprint range from 600 to 1200 cm^{-1} and positive signals from 2800 to 3000 cm^{-1}. The most pronounced spectral features were (i) positive bands near 660, 900 and 2900 cm^{-1} in PC2 loadings, (ii) a derivative-like feature at 660 cm^{-1} and negative bands near 723 and 1339 cm^{-1} in PC3 loadings, and (iii) negative band near 660 and derivative-like feature near 900 cm^{-1} in PC4 loadings. In general, we did not notice a significant difference in the amide content inside the four cell lines. The main differences were assigned to vibrations of nucleic acids, $CH_{2/3}$ from the whole cell contents and the carboxylate moieties.

The score values of the first four PCs are plotted in Figure 5. Based on four PCs the main variations between the four cell lines were explained, and cells could be differentiated. Negative PC1 scores separated the spectra of the MCF-7 cell line from the spectra of the other cell lines having positive PC1 score values. PC2, PC3 and PC4 distinguished Capan-1, SK-Hep1 and Hep-G2.

The first four PCs were used as input for classification based on support vector machines (SVM). The SVM model was trained with three batches of cell lines and then tested with three different batches of the same cell lines. This allowed for 20 different batch permutations for validation and gave a reliable unbiased classification model. The test was run 20 times and the sensitivity, specificity and accuracy of the SVM model in each run were calculated. Table 1 shows the number of spectra that were classified correctly for each cell line in the 20 tests. Of 939 trial tests of Capan-1 spectra, the SVM model was able to identify the spectra correctly as Capan-1 cells 906 times with

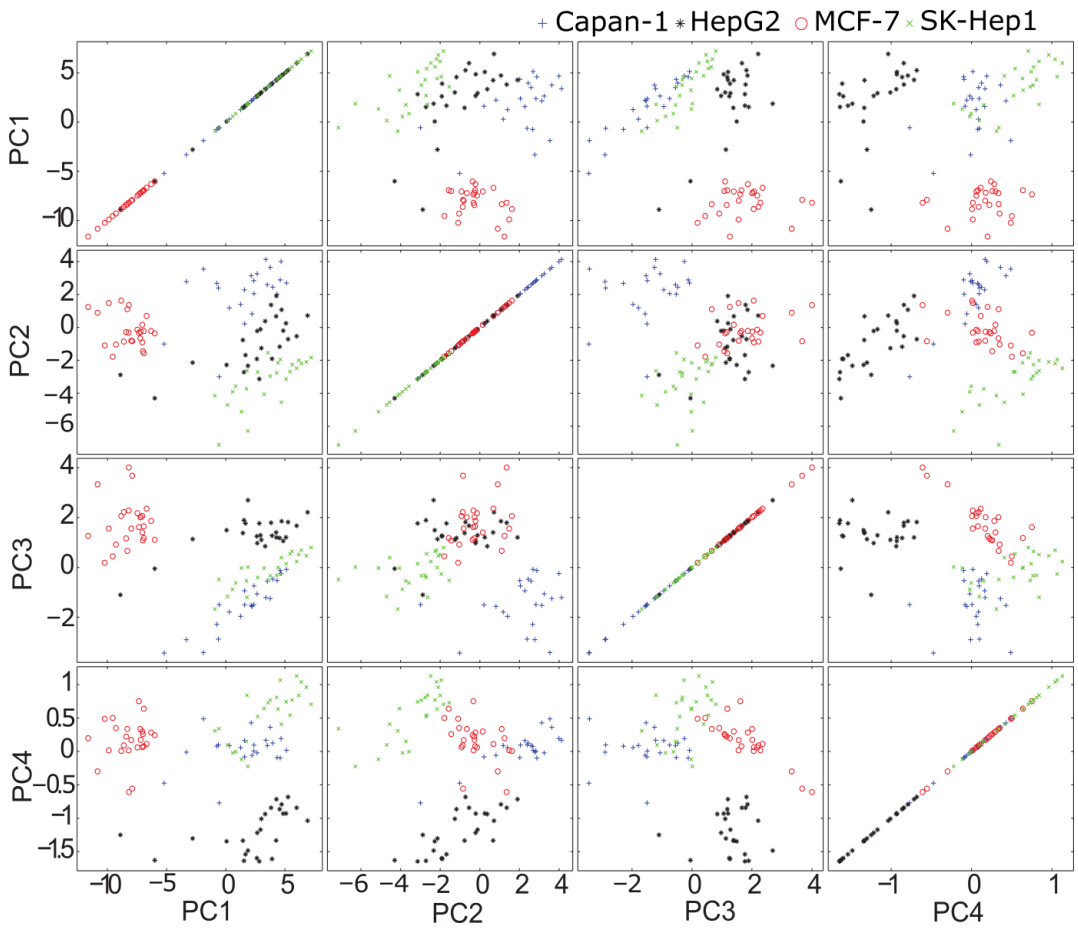

Figure 5: Score values of first four principal components of different cell lines. The four cell lines, MCF-7 (red circle), Capan-1 (blue plus sign), SK-Hep1 (green cross) and HepG2 (black star) are distinguished based on the first four PCs.

Table 1: Results of the identification of different cell lines. The support vector machine model (SVM) model was trained with spectra taken from three different batches of each cell line and tested with data taken from the remaining three batches. The SVM model was run for 20 different permutations.

sample cell line	identified by SVM as			
	Capan-1	HepG2	MCF-7	SK-Hep1
Capan-1	906	6	3	24
HepG2	74	898	33	0
MCF-7	0	0	932	0
SK-Hep1	22	0	0	980

96.7% accuracy. In case of Hep-G2 cells the model was able to correctly identify the spectra 898 times out of 1005 trials with 97.1% accuracy. The MCF-7 cell line was identified correctly in all 932 test trials with a very high accuracy of 99.1%. The identification of Sk-Hep1 cell line was true in 980 times out of 1002 trials with 98.8% accuracy.

Table 2 summarizes the mean values of the sensitivity, specificity and accuracy plus the deviation of each value. The highest mean sensitivity value of 100% was obtained in the case of MCF-7 cell line as the PC1 includes most of information about

Table 2: Mean sensitivity, specificity and accuracy values of support vector machine model for each cell line (in percentage).

	cell line			
	Capan-1	HepG2	MCF-7	SK-Hep1
mean sensitivity %	96.5 ± 4.4	89.4 ± 10.5	100	97.8 ± 2.9
mean specificity %	96.7 ± 3.7	99.8 ± 0.5	98.8 ± 1.7	99.2 ± 1.2
accuracy %	96.7	97.1	99.1	98.8

variations between MCF-7 cells versus Capan-1, HepG2 and SK-Hep1 cells. The lowest sensitivity value was obtained in the case of HepG2 cell line with 89.4%. The maximum and minimum mean specificity values are 99.8% in case of HepG2 and 96.7% in case of Capan-1. These results confirm the ability to detect the molecular variations between the different tumor cell lines based on the SERS spectra of cell lysates mixed with nanoparticles and SVM-based classification.

Conclusion

Four different human tumor cell lines, Capan-1, HepG2, Sk-Hep1 and MCF-7, were lysed using ultrasonication and then mixed with aggregated silver nanoparticles. The reproducibility of SERS spectra was demonstrated by preparing six batches and measuring them under the same conditions. The values of standard deviation, calculated for different batches, were small. PCA was performed to reduce the size of the data and assess variations between the four cell lines. Four PCs were used as input to a SVM model to classify these cell lines. Leave-three-batches-out cross validation was performed to test the stability of the SVM model. The SVM model was able to identify the different cell lines from each other with very high accuracy, sensitivity and specificity. The accuracy values were 96.7%, 97.1%, 99.1% and 98.8% for identification of Capan-1, HepG2, MCF-7 and Sk-Hep1, respectively. These values agree with classification results based on Raman spectra [29]. Compared to Raman spectra of intact cells, the SERS spectra of cell lysates contain fewer bands whose intensities are enhanced. More importantly, the variations in SERS spectra between different cells are also enhanced that contribute to accurate and stable classification.

The presented approach is a rapid, easy, efficient, highly reliable and specific strategy to identify and classify different human cancer cell lines without need for complex sample preparation procedures. To reduce the sample volume and measurement time towards few milliseconds, and automate mixing of solvents and acquisition of SERS spectra, this approach will be transferred to a droplet-based microfluidic lab-on-chip device [24]. After delivery of non-functionalized nanoparticles into cells [20], the SERS approach can also increase the throughput of tumor cell recognition in microfluidic chips at continuous flow [30]. With exposure times in the millisecond range, SERS assessment of millions of cells comes within reach in the future. A possible scenario for screening of millions of blood cells and enumeration of rare circulating tumor cells in blood of cancer patients is a combination of all approaches mentioned above: generation of droplets with single cells in a microfluidic chip, addition of cell lysis buffer, nanoparticles and activation salt, mixing of all solvents and collection of SERS spectra for classification.

Experimental

Nanoparticle preparation

Silver nitrate (ACS reagent, ≥99%), sodium hydroxide, hydroxylamine hydrochloride (reagent plus, 99%) and potassium chloride were purchased from Sigma–Aldrich. Distilled water was used for all preparations. The silver nanoparticle colloids were synthesized according to the protocol described by Leopold and Lendl [31]. Briefly, 1 mM silver nitrate was added to a solution of 1.5 mM hydroxylamine hydrochloride and 3 mM sodium hydroxide. The whole mixture was stirred during the addition of the silver nitrate. As a sign of a successful preparation the color of the solution changed from grey to yellow. The silver colloids were then preserved in the refrigerator at 4 °C. 1 M of KCl was prepared in distilled water. The preparation procedure can be performed quickly and at room temperature.

Nanoparticle characterization

Transmission electron microscopy (TEM): 5 µL of the particle dispersion were deposited on a carbon-coated 400 mesh copper grid. After 1 min of adsorption the excess liquid was blotted off with filter paper. Dried samples were then examined by a JEM 1400 (JEOL, Tokyo, Japan) transmission electron microscope.

Scanning electron microscopy (SEM): Measurements were performed by a field emission microscope JSM-6300F (JEOL, Tokyo, Japan). The energy of the exciting electrons was 5 keV. Beside the detector for secondary electrons (SEI) the system is equipped with different detector types (semiconductor and YAG) for backscattered electrons.

Spectrophotometry: The UV–vis spectra of silver nanoparticles and KCl-aggregated silver nanoparticles were measured in the spectral range of 200–800 nm with a Jasco V-670 diode UV–vis spectrophotometer (Hachioji, Tokyo, Japan) using plastic cuvettes (Brand GmbH Wertheim Germany) of 1 cm light path.

Cell cultivation

Liver cancer cell lines (HepG2 and SK-Hep1) were cultivated in RPMI 1640 liquid medium with 20 mM HEPES, stable glutamine (FG 1235, Biochrom AG, Germany), 10% fetal bovine serum (10099-133, Life Technologies, Germany) together with 100 units/mL of penicillin and 100 µg/mL of streptomycin (15140, Gibco®, Life Technologies GmbH, Germany). Cultivation of MCF-7 breast cancer cells was performed in RPMI 1640 with 2.0 g/L $NaHCO_3$ (F 1215, Biochrom AG, Germany) and 40 mg/L folic acid (F7876, Sigma–Aldrich, Germany) with the same amount of fetal bovine serum, penicillin and streptomycin as described above for liver cells. The pancreatic cancer cell

line Capan-1 was cultured in IMDM medium (12440-053, Life Technologies, Germany) complemented with 20% fetal bovine serum (10099-133, Life Technologies, Germany), 100 units/mL of penicillin and 100 µg/mL of streptomycin (15140, Gibco®, Life Technologies GmbH, Germany). The cells were maintained in an incubator at 37 °C, 90% humidity and 5% carbon dioxide in air. 75 cm^2 cell culture flasks (658170; Greiner Bio-One GmbH, Germany) were used for cultivation of the cell lines. Every two or three days the medium was changed until approximately 100% confluence was reached. Cells were detached from the substrate by a 0.05% of trypsin–EDTA solution (L2143; Biochrom AG, Germany) and fast frozen at −20 °C. The final number of cells in each flask was around 10^7 cells/mL, which was confirmed by cell counting, using Neubauer Chamber (0.0025 mm^2; Marienfied, Germany). In order to prove the reproducibility of our experiments six batches of each of the four cell lines were prepared. The optical density of different cell lines were measured using Eppendorf Biophotometer plus. The optical density of 0.25 was correlated to an averaged cell number of 10^7 cells/mL.

Cell sonication

Cells were sonicated using an ultrasonic probe system (Brandelin SONOPULS HD 2070) with a maximum output power of 70 W. This sonication technique helps disrupting the cell membranes and allows for an interaction of released cell components with the silver nanoparticles. The probe was inserted inside an Eppendorf tube containing 1 mL of the cells in PBS solution. The sonication was applied in 3 cycles of 15 s each and 5 s break in between with a power set to 20%. The cell lysate was then transferred to a new tube and stored until further processing in a freezer.

Raman spectroscopy and SERS measurements

SERS measurements were performed on a commercial Raman microscopy system (Holoprobe, Kaiser Optical system, USA). This system consists of a multi-mode diode laser with 785 nm excitation wavelength (Invictus NIR laser), an *f*/1.8 spectrograph with a holographic transmission grating (Kaiser Optical system, USA), and a Peltier-cooled back-illuminated deep-depletion CCD detector (iDus420, Andor, Ireland). The microscope was coupled to the Raman system with fibers of 65 µm core diameter. A 10×/0.25 objective lens (Leica, Germany) was used for all SERS measurements. The laser wavelength was calibrated using cyclohexane. The system was intensity calibrated using a white light source. The laser power was fixed at 50 mW with an acquisition time of 5 s. Each batch was lysed and divided into eight to ten samples. 100 µL of the silver nanoparticles were mixed with 100 µL KCl as aggregating agent, and then 100 µL of cell lysate were added to the mixture with a final ratio of 1:1:1. 200 µL solution was filled in vials that were cut from 0.2 mL 96-well thin wall thermal cycler plates, and the laser beam was focused on the surface of the mixture. One spectrum was collected from each sample. The experiments were repeated using six batches for each cell line and the reproducibility was tested by calculating the standard deviation from the mean spectra.

Data analysis

The intensity-corrected SERS spectra were exported to Matlab (The Mathworks, USA) and pre-processed before the evaluation of the spectral classification models. The imported spectra were corrected for the dark current and the constant voltage bias by subtracting a smoothed dark spectrum. The resulting spectra were corrected for the polynomial background arising from residual excitation light using the penalized least squares-based Whittaker smoother algorithm outlined by Eilers [32]. The background corrected data was cropped to a low-wavenumber region between 500 and 1800 cm^{-1} and a high-wavenumber region between 2828 and 3028 cm^{-1}. Both regions were combined and area-normalized relative to the spectral wavenumber region. Spectral classification was performed by support vector machines (SVM) with a linear kernel, using the libSVM Matlab library by Chang [33]. The classification was performed batch-wise; three batches were used to build a model and the remaining three batches were used for testing. With six total batches 20 different batch permutations were used for model building and for model testing. Before performing the SVM-based classification the dimensionality of the data set was reduced by principal component analysis (PCA) for the three batches, where on average the first four principal components (PCs) describe 89% of the data variance. The classification was performed on the score values of the first four PCs. After training the SVM model with the score values of the training batches the spectra of the test batches were projected onto the four loading vectors created by the training batches, and the resulting score values were used as the test set. The confusion matrices established after testing each batch permutation were summed up.

Acknowledgements

The Ph.D. work of M. Hassoun is supported by a grant from the German Academic Exchange Service (DAAD). The authors thank Franka Jahn for TEM images and Dr. Jan Dellith for SEM images.

References

1. Chan, J. W. *J. Biophotonics* **2013,** *6,* 36–48. doi:10.1002/jbio.201200143
2. Galler, K.; Bräutigam, K.; Große, C.; Popp, J.; Neugebauer, U. *Analyst* **2014,** *139,* 1237–1273. doi:10.1039/c3an01939j

3. Krafft, C.; Dietzek, B.; Schmitt, M.; Popp, J. *J. Biomed. Opt.* **2012,** *17,* 040801. doi:10.1117/1.JBO.17.4.040801
4. Cialla, D.; Pollok, S.; Steinbrücker, C.; Weber, K.; Popp, J. *Nanophotonics* **2014,** *3,* 383–411. doi:10.1515/nanoph-2013-0024
5. Harper, M. M.; McKeating, K. S.; Faulds, K. *Phys. Chem. Chem. Phys.* **2013,** *15,* 5312–5328. doi:10.1039/c2cp43859c
6. Fleger, Y.; Rosenbluh, M. *Int. J. Opt.* **2009,** *2009,* 475941. doi:10.1155/2009/475941
7. Li, X.; Lenhart, J. J. *Environ. Sci. Technol.* **2012,** *46,* 5378–5386. doi:10.1021/es204531y
8. Tian, F.; Bonnier, F.; Casey, A.; Shanahan, A. E.; Byrne, H. J. *Anal. Methods* **2014,** *6,* 9116–9123. doi:10.1039/C4AY02112F
9. Hering, K. K.; Möller, R.; Fritzsche, W.; Popp, J. *ChemPhysChem* **2008,** *9,* 867–872. doi:10.1002/cphc.200700591
10. Yang, J.; Zhen, L.; Ren, F.; Campbell, J.; Rorrer, G. L.; Wang, A. X. *J. Biophotonics* **2015,** *8,* 659–667. doi:10.1002/jbio.201400070
11. Yaffe, N. R.; Ingram, A.; Graham, D.; Blanch, E. W. *J. Raman Spectrosc.* **2010,** *41,* 618–623. doi:10.1002/jrs.2495
12. Abdali, S.; Johannessen, C.; Nygaard, J.; Nørbygaard, T. *J. Phys.: Condens. Matter* **2007,** *19,* 285205. doi:10.1088/0953-8984/19/28/285205
13. Palonpon, A. F.; Ando, J.; Yamakoshi, H.; Dodo, K.; Sodeoka, M.; Kawata, S.; Fujita, K. *Nat. Protoc.* **2013,** *8,* 677–692. doi:10.1038/nprot.2013.030
14. Nolan, J. P.; Duggan, E.; Liu, E.; Condello, D.; Dave, I.; Stoner, S. A. *Methods* **2012,** *57,* 272–279. doi:10.1016/j.ymeth.2012.03.024
15. Huefner, A.; Septiadi, D.; Wilts, B. D.; Patel, I. I.; Kuan, W.-L.; Fragniere, A.; Barker, R. A.; Mahajan, S. *Methods* **2014,** *68,* 354–363. doi:10.1016/j.ymeth.2014.02.006
16. Kneipp, J.; Kneipp, H.; McLaughlin, M.; Brown, D.; Kneipp, K. *Nano Lett.* **2006,** *6,* 2225–2231. doi:10.1021/nl061517x
17. Kneipp, J.; Kneipp, H.; Rajadurai, A.; Redmond, R. W.; Kneipp, K. *J. Raman Spectrosc.* **2009,** *40,* 1–5. doi:10.1002/jrs.2060
18. Kneipp, K.; Haka, A. S.; Kneipp, H.; Badizadegan, K.; Yoshizawa, N.; Boone, C.; Shafer-Peltier, K. E.; Motz, J. T.; Dasari, R. R.; Feld, M. S. *Appl. Spectrosc.* **2002,** *56,* 150–154. doi:10.1366/0003702021954557
19. Lee, S.; Kim, S.; Choo, J.; Shin, S. Y.; Lee, Y. H.; Choi, H. Y.; Ha, S.; Kang, K.; Oh, C. H. *Anal. Chem.* **2007,** *79,* 916–922. doi:10.1021/ac061246a
20. Lin, J.; Chen, R.; Feng, S.; Li, Y.; Huang, Z.; Xie, S.; Yu, Y.; Cheng, M.; Zeng, H. *Biosens. Bioelectron.* **2009,** *25,* 388–394. doi:10.1016/j.bios.2009.07.027
21. Freitag, I.; Matthäus, C.; Csaki, A.; Clement, J. H.; Cialla-May, D.; Weber, K.; Krafft, C.; Popp, J. *J. Biomed. Opt.* **2015,** *20,* 055002. doi:10.1117/1.JBO.20.5.055002
22. Nima, Z. A.; Mahmood, M.; Xu, Y.; Mustafa, T.; Watanabe, F.; Nedosekin, D. A.; Juratli, M. A.; Fahmi, T.; Galanzha, E. I.; Nolan, J. P.; Basnakian, A. G.; Zharov, V. P.; Biris, A. S. *Sci. Rep.* **2014,** *4,* 4752. doi:10.1038/srep04752
23. Pallaoro, A.; Hoonejani, M. R.; Braun, G. B.; Meinhart, C. D.; Moskovits, M. *ACS Nano* **2015,** *9,* 4328–4336. doi:10.1021/acsnano.5b00750
24. Walter, A.; März, A.; Schumacher, W.; Rösch, P.; Popp, J. *Lab Chip* **2011,** *11,* 1013–1021. doi:10.1039/c0lc00536c
25. Kahraman, M.; Yazıcı, M. M.; Şahin, F.; Çulha, M. *Langmuir* **2008,** *24,* 894–901. doi:10.1021/la702240q
26. Palonpon, A. F.; Sodeoka, M.; Fujita, K. *Curr. Opin. Chem. Biol.* **2013,** *17,* 708–715. doi:10.1016/j.cbpa.2013.05.021
27. Chen, T.; Kuo, C.; Chou, Y.; Liang, N. *Langmuir* **1989,** *5,* 887–891. doi:10.1021/la00088a001
28. Neugebauer, U.; Clement, J. H.; Bocklitz, T.; Krafft, C.; Popp, J. *J. Biophotonics* **2010,** *3,* 579–587. doi:10.1002/jbio.201000020
29. Dochow, S.; Beleites, C.; Henkel, T.; Mayer, G.; Albert, J.; Clement, J.; Krafft, C.; Popp, J. *Anal. Bioanal. Chem.* **2013,** *405,* 2743–2746. doi:10.1007/s00216-013-6726-3
30. Freitag, I.; Beleites, C.; Dochow, S.; Clement, J. H.; Krafft, C.; Popp, J. *Analyst* **2016,** *141,* 5986–5989. doi:10.1039/C6AN01739H
31. Leopold, N.; Lendl, B. *J. Phys. Chem. B* **2003,** *107,* 5723–5727. doi:10.1021/jp027460u
32. Eilers, P. H. C. *Anal. Chem.* **2003,** *75,* 3631–3636. doi:10.1021/ac034173t
33. Chang, C.-C.; Lin, C.-J. *ACM Trans. Intell. Syst. Technol. (TIST)* **2011,** *2,* 27. doi:10.1145/1961189.1961199

License and Terms

BEILSTEIN JOURNAL OF NANOTECHNOLOGY

Nano-engineered skin mesenchymal stem cells: potential vehicles for tumour-targeted quantum-dot delivery

Liga Saulite*[1], Dominyka Dapkute[2,3], Karlis Pleiko[1], Ineta Popena[1], Simona Steponkiene[2], Ricardas Rotomskis[2,4] and Una Riekstina[1]

Full Research Paper

Open Access

Address:
[1]Faculty of Medicine, University of Latvia, Raina blvd. 19, LV-1586, Riga, Latvia, [2]Biomedical Physics Laboratory, National Cancer Institute, P. Baublio Street 3b, LT-08406 Vilnius, Lithuania, [3]Life Science Center, Vilnius University, Sauletekio al. 7, LT-10257, Vilnius, Lithuania and [4]Laser research center, Vilnius University, Sauletekio al. 9, corp. 3, LT-10222, Vilnius, Lithuania

Email:
Liga Saulite* - liga.saulite@lu.lv

* Corresponding author

Keywords:
endocytosis; mesenchymal stem cells; quantum dots; stem cell differentiation

Beilstein J. Nanotechnol. **2017,** *8,* 1218–1230.
doi:10.3762/bjnano.8.123

Received: 14 December 2016
Accepted: 10 May 2017
Published: 07 June 2017

This article is part of the Thematic Series "Nanomaterial-based cancer theranostics".

Guest Editor: V. Sivakov

Abstract

Nanotechnology-based drug design offers new possibilities for the use of nanoparticles in imaging and targeted therapy of tumours. Due to their tumour-homing ability, nano-engineered mesenchymal stem cells (MSCs) could be utilized as vectors to deliver diagnostic and therapeutic nanoparticles into a tumour. In the present study, uptake and functional effects of carboxyl-coated quantum dots QD655 were studied in human skin MSCs. The effect of QD on MSCs was examined using a cell viability assay, Ki67 expression analysis, and tri-lineage differentiation assay. The optimal conditions for QD uptake in MSCs were determined using flow cytometry. The QD uptake route in MSCs was examined via fluorescence imaging using endocytosis inhibitors for the micropinocytosis, phagocytosis, lipid-raft, clathrin- and caveolin-dependent endocytosis pathways. These data showed that QDs were efficiently accumulated in the cytoplasm of MSCs after incubation for 6 h. The main uptake route of QDs in skin MSCs was clathrin-mediated endocytosis. QDs were mainly localized in early endosomes after 6 h as well as in late endosomes and lysosomes after 24 h. QDs in concentrations ranging from 0.5 to 64 nM had no effect on cell viability and proliferation. The expression of MSC markers, CD73 and CD90, and hematopoietic markers, CD34 and CD45, as well as the ability to differentiate into adipocytes, chondrocytes, and osteocytes, were not altered in the presence of QDs. We observed a decrease in the QD signal from labelled MSCs over time that could partly reflect QD excretion. Altogether, these data suggest that QD-labelled MSCs could be used for targeted drug delivery studies.

Introduction

Despite remarkable advances in targeted therapies of various human malignancies, cancer is one of the leading causes of death worldwide [1]. Nanoparticles (NPs) could be linked to various drugs, thereby making them suitable for tumour imaging and targeted therapy [2]. However, the fact that NPs are quickly recognised by immune cells and cleared from the blood stream by reticuloendothelial system limits their utility as drug carriers [3]. Recent studies have shown that nano-engineered mesenchymal stem cells (MSCs) could be used as tumour-targeted therapeutic carriers, reflecting their tumour-homing capabilities [4-6].

MSCs are present in many tissues of the human body, including bone marrow, adipose tissues, skin and dental pulp. According to current understanding, MSCs are defined as adherent cells with a spindle-like morphology, expressing CD105 (SH2 or endoglin), CD73 (SH3 and SH4), CD106 (VCAM-1), CD44 (hyaluronic acid receptor), CD90 (Thy 1.1), CD29, CD146 and CD166 surface markers [7,8]. MSCs can be induced to differentiate in vitro into adipogenic, osteogenic, chondrogenic and myogenic cells. Moreover, other cell types, such as neurons, glial cells and smooth muscle cells, could be obtained from MSCs under the appropriate cell culture conditions [9,10].

Among the broad variety of investigated NPs, quantum dots (QDs) have demonstrated extensive application capabilities. High photostability and brightness, broad excitation and narrow fluorescence-emission spectra are some of the main properties required for the generation of new fluorescent nano-agents. The unique optical and electronic properties of QDs indicate their great potential in cancer diagnostics. The photoluminescence spectrum of carboxyl QD655 makes them ideal candidates for cancer theranostics as it overlaps with the optical transparency window of biological tissue [11]. Additionally, large and easily altered surfaces facilitate modifications of various NPs. These modifications increase the solubility of QDs to make QDs unnoticeable by the immune system, increase the QD half-life in the blood stream and target QDs to specific ligands or antigens [12]. Different therapeutic and recognition molecules can be attached to the surfaces of NPs and act synergistically [13,14]. QDs were also chosen for their applicability as resonant energy donors in photodynamic therapy. For example, the second-generation photosensitizer chlorin e6 has the absorption band at 654 nm and carboxyl QD655 would be excellent energy donors in such complexes. There were successful attempts to use a similar quantum dot–chlorin e6 complex in photodynamic cancer therapy [15]. Another study has shown that QDs, conjugated with antibodies against CD44, a marker of cancer stem-like cells, can be selectively engulfed by breast cancer cells [16]. Such surface modifications increase the potential of QDs for the use in targeted cancer diagnostics and therapies.

There is still doubt regarding the potential harmful effects of NPs or QDs on the differentiation capacity and self-renewal ability of adult stem cells. CdSe/ZnS QD labelling has been reported to adversely affect the osteogenesis and chondrogenesis capacities of bone marrow MSCs [17]. The impact of QD labelling on the biological properties of targeted stem cells, such as proliferation, cell cycle, and apoptosis, remains elusive. Therefore, further research on MSCs with regard to the delivery of QDs for monitoring and treating tumours is required.

Skin is the largest organ of the human body. It ensures the protection and insulation of the inner tissues [18] and also acts as a barrier against the penetration of QDs [19]. Nano-engineered skin MSCs could be used in cell-based skin cancer (SC) therapies [20,21]. MSCs loaded with anti-cancer drugs can reduce melanoma tumour growth in vivo, suggesting that these molecules are suitable vectors for therapeutic applications [22].

The aim of the present study was to analyse the accumulation, release, toxicity and functional effects of carboxyl QD655 on skin-derived MSCs to assess their potential use as vectors for the targeting of SC or other tumours.

Results

Optimal QD labelling conditions for MSCs

The concentration-dependent cytotoxicity of QDs was analysed in MSC cultures after 24 and 48 h using a colorimetric CCK-8 assay, which measures intracellular dehydrogenase activity (Figure 1). QDs did not significantly affect MSC viability after 24 or 48 h at any of the tested QD concentrations.

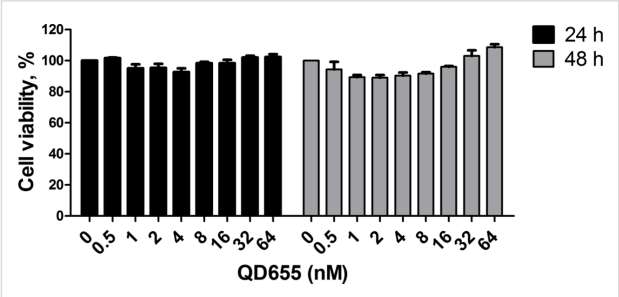

Figure 1: The concentration-dependent effect of QDs on the viability of MSCs. Viability was measured by a colorimetric assay (CCK-8) after incubation with QDs at 0.5–64 nM for 24 and 48 h.

In order to select the optimal incubation time for QD uptake in skin MSCs, cells were incubated with 16 nM QDs for time periods ranging from 15 min to 48 h (Figure 2a). The QD

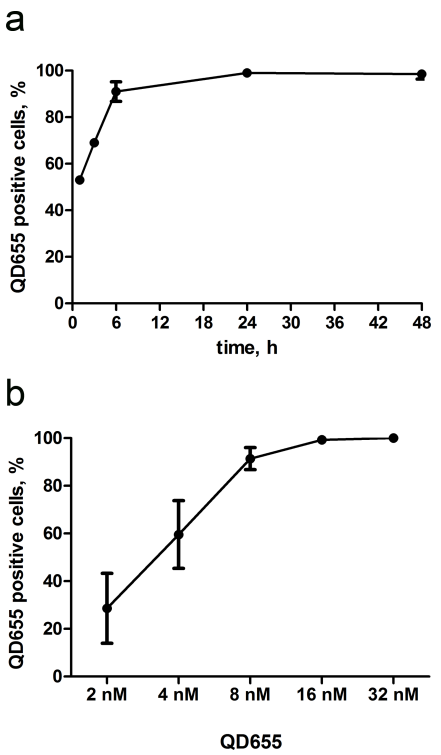

Figure 2: Evaluation of the optimal QD uptake conditions in skin MSCs. Time-dependent (a) and concentration-dependent (b) uptake dynamics in MSCs using flow cytometry analysis. The percentage of QD655-positive cells was obtained from the analysis of flow-cytometry histogram data.

uptake kinetics was calculated based on changes in fluorescence intensity. The plateau phase was reached after 24 h of incubation, consistent with observations in other cell lines [23]. The optimal incubation time for QD uptake was 6 h, after which up to 95% of the cells had incorporated QDs. Thus, a 6 h incubation time was used in all experiments, unless otherwise stated.

The optimal QD concentration for the uptake experiments was determined using serial dilutions of QDs from 2 up to 32 nM (Figure 2, b). The QD-positive cell number exponentially increased, and saturation was obtained at 16 nM, when cells were 99% QD-positive. Therefore, a 16 nM QD concentration was selected for further experiments, unless otherwise stated.

To determine whether MSCs release QDs in the environment after uptake, the supernatant was removed from cells after primary QD labelling. After rigorous rinsing, fresh complete or serum-free medium was applied to the QD-labelled cells. Next, the QD fluorescence intensity was determined in cells at 24 and 48 h after primary labelling. We observed a 30% decrease of the QD signal in cells propagated in complete medium and a 40% decrease of the QD signal under serum-free conditions after 24 h of incubation (Figure 3a). After 48 h, the number of QD-positive cells decreased even further in serum-free cultivated cells (Figure 3a). Supernatant from primarily QD-labelled MSCs was transferred to fresh MSCs for secondary labelling experiments. After 24 h, 3% of the cells in complete medium had taken up QDs, whereas under serum-free conditions, 7% of MSCs had taken up QDs in the secondary labelling experiments (Figure 3b). After 48 h QD uptake was detectable in approximately 1.5% of cells cultivated either in complete or serum-free medium (Figure 3b).

To determine the effect of cell division on the decrease of the QD signal, QD-labelled MSCs were propagated in complete and serum-free medium. Ki67 expression was clearly inhibited in cells cultivated in serum-free medium, which did not proliferate after 24 and 48 h, thereby excluding the probability of QD transfer to daughter cells (Figure 3c). Inhibition of proliferation was additionally confirmed by analysing the cell number in the respective medium (data not shown). The addition of QDs did not change the expression of Ki67 (data not shown).

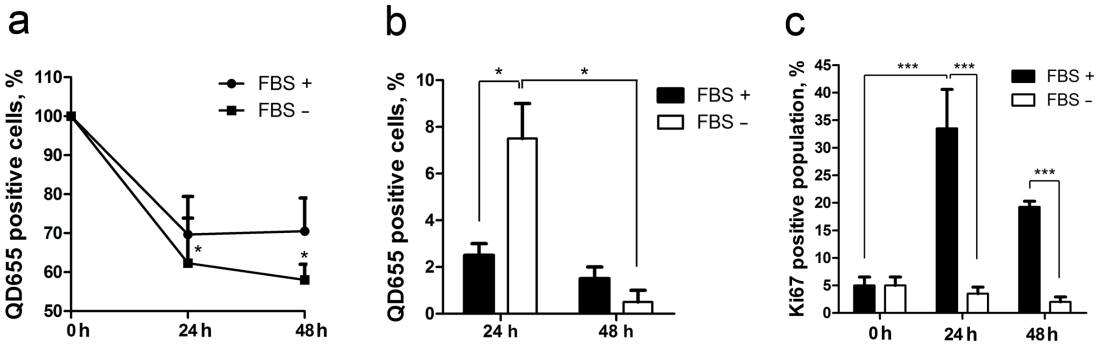

Figure 3: The release of QDs from MSCs. (a) QD loss in complete medium (FBS +) and serum-free medium (FBS −) after primary QD labelling (0 h) and 24 and 48 h after labelling. The statistical significance is shown in comparison to 0 h. (b) Secondary QD labelling of MSCs by supernatants from primarily labelled MSCs. (c) The comparison of Ki67 expression in complete and serum-free medium after labelling (0 h) and after 24 h and 48 h of cultivation; *p-value < 0.05, ***p-value < 0.001.

QD effect on immunophenotype, proliferation and differentiation of MSCs

The skin MSC population used in the present study was over 95% positive for MSC markers CD73 and CD90, whereas hematopoietic markers CD45 and CD34 were not expressed (Figure 4a). To estimate the effect of QDs on the MSC immunophenotype, expression of CD73 and CD90 was analysed after incubation with QDs for 48 h. Although CD105 is often used as a MSC marker together with CD73 and CD90, this marker was excluded from the analysis because of the fluorescence channel overlap with QDs (APC label, FL4). The data showed that QDs did not change the expression of CD73, CD90, CD34 and CD45 in MSCs (Figure 4a).

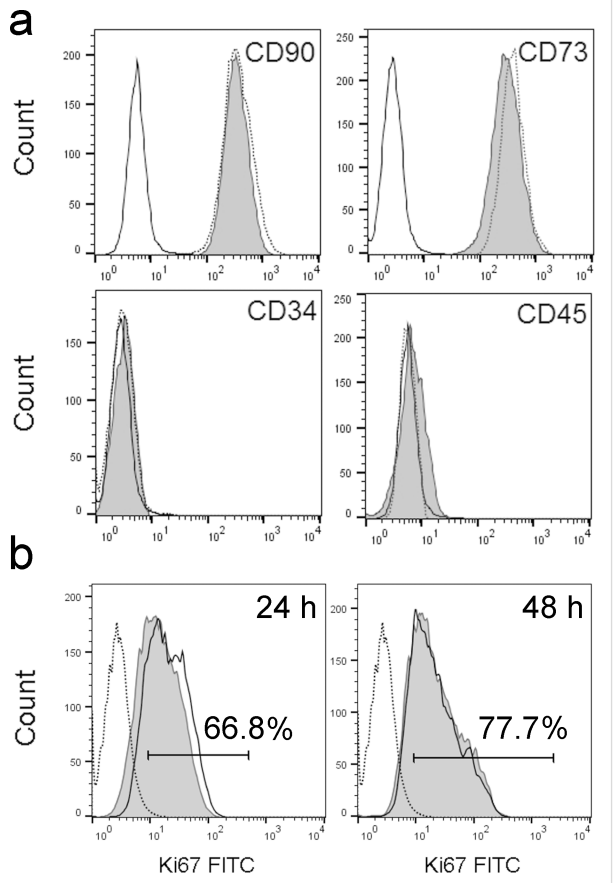

Figure 4: Representative data on the impact of QDs on immunophenotype and proliferation of MSCs. (a) Characterization of MSC markers CD90, CD73 and hematopoietic markers CD34 and CD45 in MSCs. Open histogram: unlabelled cells, dotted-line histogram: MSCs without QDs, grey histogram: QD-labelled MSCs. (b) Ki67 expression in MSCs after 24 h and 48 h of incubation with 16 nM QDs. Open histogram: unlabelled cells, dotted-line histogram: isotype control, grey histogram: QD-labelled cells.

The effect of QDs on proliferation was analysed based on Ki67 expression (Figure 4b). After incubation for 24 h, 67% of unlabelled and QD-labelled MSCs expressed the Ki67 marker. After 48 h, the Ki67-positive population increased to 78% in both cell populations. QDs did not show any effect on the proliferation of MSCs.

The differentiation of MSCs into adipocytes, chondrocytes and osteocytes was not affected by the presence of QDs (Figure 5). Quantification assays for Alcian Blue staining and Alizarin Red S staining confirmed that QDs did not influence chondrogenesis and osteogenesis of skin MSCs (Figure 6).

Analysis of the uptake pathway of QDs

MSCs were pre-treated with endocytosis inhibitors and subsequently labelled with QDs. The effect of serum proteins on the efficiency of QD uptake was analysed based on the comparison of QD uptake in complete and serum-free media (Figure 7). The effect of endocytosis inhibitors differed between complete and serum-free medium. In complete medium, a tendency of decreased QD uptake was observed using chlorpromazine (CPZ), an inhibitor of clathrin-mediated endocytosis (Figure 7a, c). In serum-free medium, QD uptake was significantly inhibited by CPZ and nystatin, an inhibitor of caveolin/lipid raft-mediated endocytosis (Figure 7b,d). In serum-free medium, the cells internalized more QDs according to the fluorescence intensity analysis (Figure 7c,d).

The intracellular localization of QDs after uptake was observed in BacMam 2.0-transfected MSCs. Excessive QD accumulation was initiated between 1 and 6 h. After 6 h, most of the QDs were localized in early endosomes (Figure 8) in both the cell periphery and perinuclear area. After 6 h, almost no QDs were localized in mature endosomes (data not shown). After 24 and 48 h, QD-containing early endosomes matured into late endosomes and lysosomes.

Discussion

Human MSCs have been widely investigated for their potential use in various therapeutic applications, due to their plasticity and migration ability. It has been proposed that MSC migration towards injury and inflammation sites could be used to deliver diagnostic and therapeutic nano-agents [24]. Studies on melanoma [25], prostate cancer [26], breast cancer [6] and lung cancer [27] have shown the ability of MSCs to home to cancer sites in vivo. In the tumour microenvironment, MSCs play a role in the formation of the tumour stroma and support cancer metastasis [28]. Lourenco et al. showed that MSC migration towards cancer cells is induced by MIF–CXCR4 chemotaxis [29]. Moreover, in close proximity of the tumour, cancer-associated fibroblast formation is induced by the release of vesicles containing miRNA from cancer cells. This leads to melanoma growth and invasion [30]. Therefore, skin-derived MSCs could serve as an appropriate model to study the stem cell (SC)

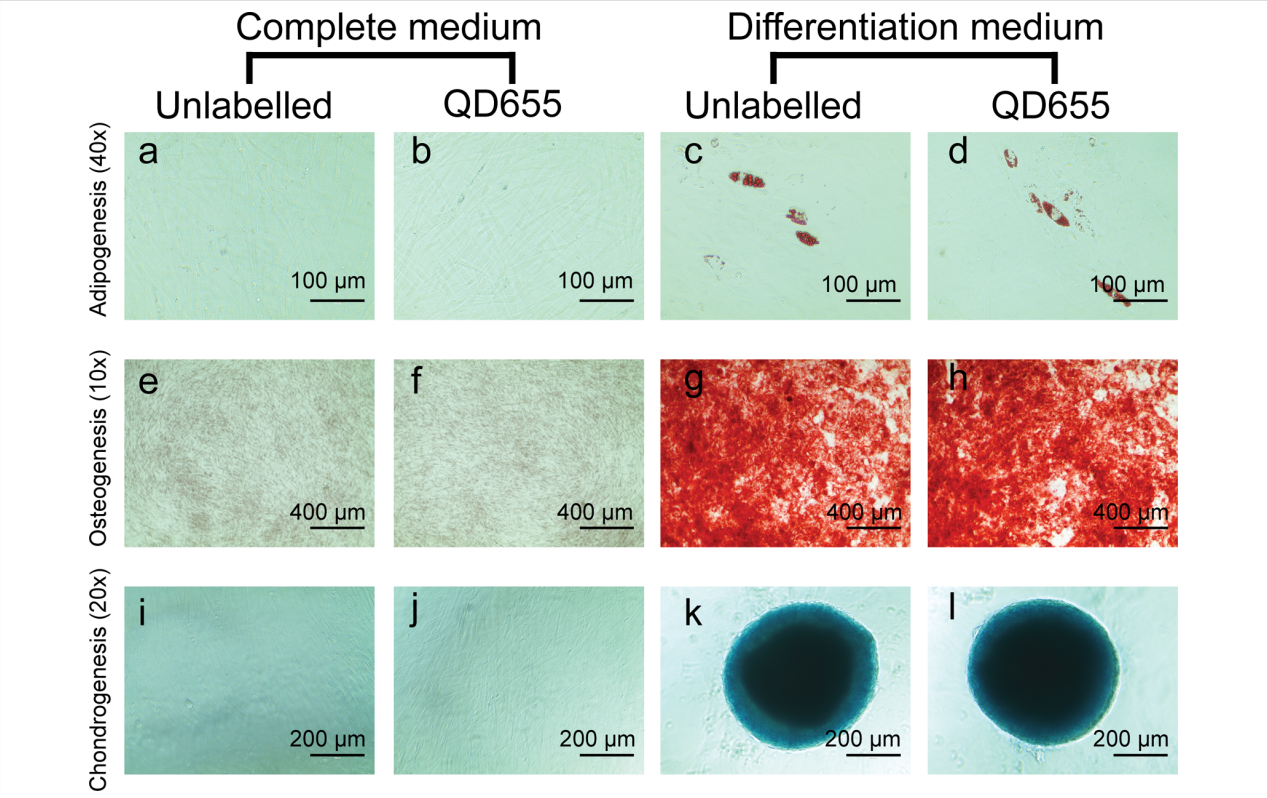

Figure 5: Differentiation of MSCs into adipocytes, chondrocytes and osteocytes. Oil Red O staining of cells in complete medium without (a) or with QD labelling (b); cells in adipogenesis medium without (c) or with QD labelling (d). Alizarin Red S staining on cells in complete medium in the absence or presence of QDs (e, f); cells in osteogenesis differentiation medium in the absence or presence of QDs (g, h). Alcian Blue staining on cells in complete medium (i, j) and chondrogenesis differentiation medium (k, l) in the absence or presence of QDs.

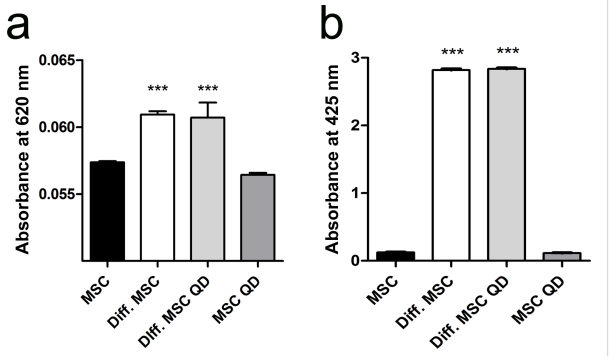

Figure 6: Quantification of osteogenesis and chondrogenesis in MSCs. Absorbance of Alizarin Red S (a) and Alcian Blue (b) extraction from MSC differentiation. Diff. MSC: differentiated MSCs, diff. MSC QD: differentiated MSCs labelled with QDs. Significance compared between differentiated and undifferentiated samples; ***p-value < 0.001.

tumour microenvironment and design SC-targeted therapeutics. In the present study, we addressed whether QD-loaded skin MSCs could serve as vectors to deliver NPs to cancer sites. To answer this question, the biological response of skin MSCs to QDs was investigated.

The results showed that QDs do not induce changes in immunophenotype, proliferation and viability of skin MSCs, indicating that QDs are biocompatible with MSCs. These results are consistent with those of studies on bone marrow mesenchymal stem cells and mouse embryonic stem cells, which show similar effects after QD labelling [31,32]. We observed variations in Ki67 expression in skin MSCs, regardless of QD addition, which might reflect the differences in donor age and passage number [33]. In the present study, we observed that QD labelling did not interfere with skin MSC differentiation into osteocytes, chondrocytes and adipocytes, and moreover, QDs did not induce spontaneous differentiation. Similarly, Shah et al. reported that carboxyl QDs do not alter the differentiation potential of human bone marrow stem cells [31]. Thus, QD-labelled MSCs are potentially safe to use in long-term tumour imaging and cell tracking experiments. Although there is a great deal of concern about the potential hazards of QDs containing heavy metals, the toxicity of QDs is a topic of controversy. The toxicity and ecotoxicity of QDs is studied at various levels of biological organization, from cell monolayers to primates and even ecosystems [34,35]. The potential toxicological effects of QDs are usually based on the release of free cadmium (Cd) [36]. However, QD shell and surface coatings

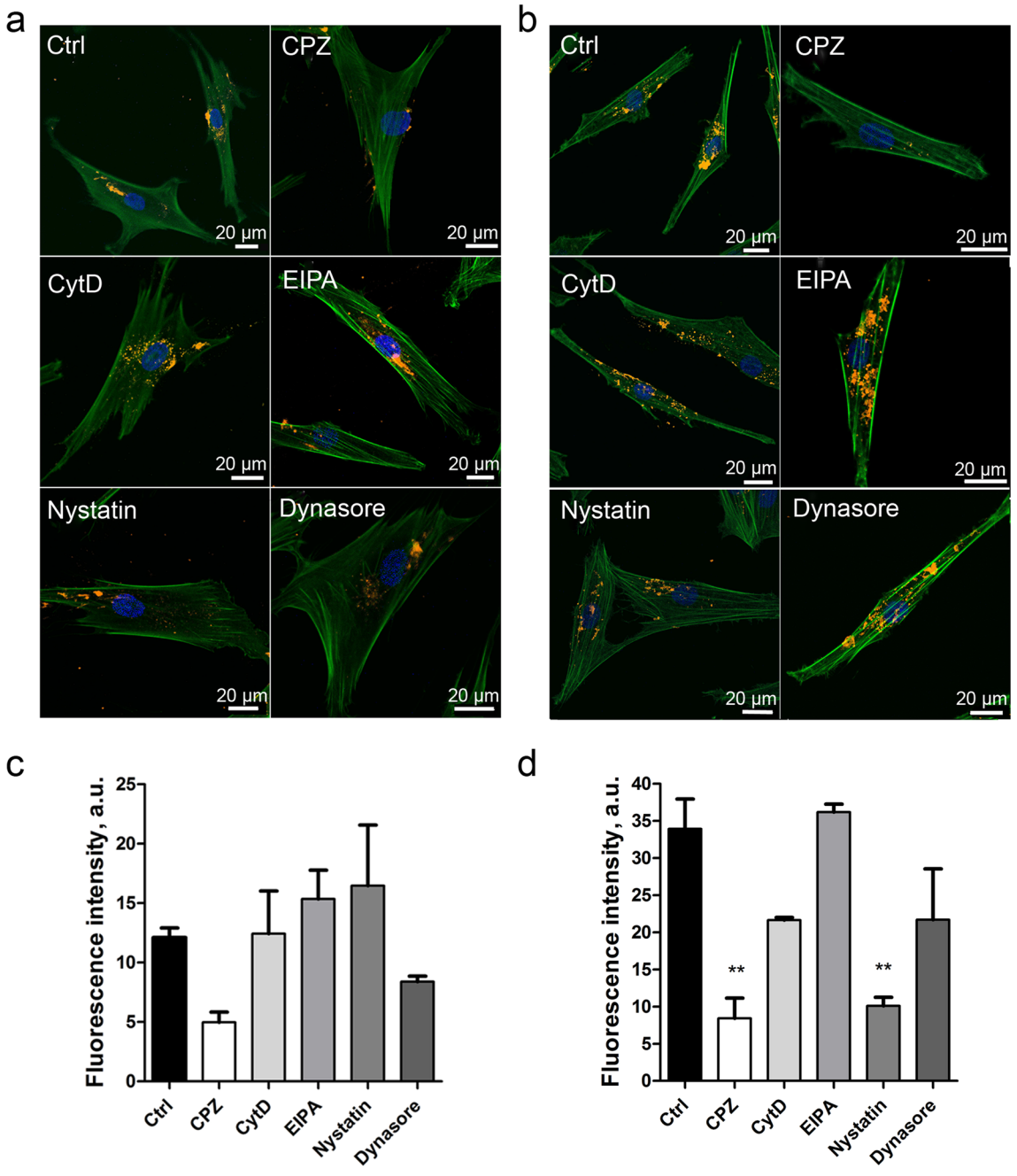

Figure 7: QD endocytic pathway in MSCs. QD uptake pathway in MSCs labelled with QDs in complete medium (a) or in serum-free medium (b). Uptake pathways were blocked using the endocytosis inhibitors CPZ, CytD, EIPA, nystatin and dynasore. Three overlaid channels represent Hoechst (blue), Phalloidin Alexa Fluor488 (green), carboxyl QD655 (yellow). Representative data are shown. QD fluorescence signal was quantified in complete (c) and in serum-free medium (d) cultivated MSCs. Statistical significance shown for the respective sample in comparison to control (Ctrl) sample; **p-value < 0.01.

protect the core, which contains toxic inorganic semiconductor materials. Unless coatings are damaged, QDs are mainly non-toxic [37]. Recently, Yaghini et al., by using non-photolytic visible wavelength excitation, have shown the formation of superoxide anion radicals by photoexcited CdSe/ZnS QDs [38]. Thus, the QDs may induce phototoxic reactions in labelled cells, which could be a desirable event in targeted tumour therapy.

The optimal uptake conditions for NPs could depend on the particle size, surface modifications, protein corona, and recipient cell line. Previous studies have suggested the incubation of

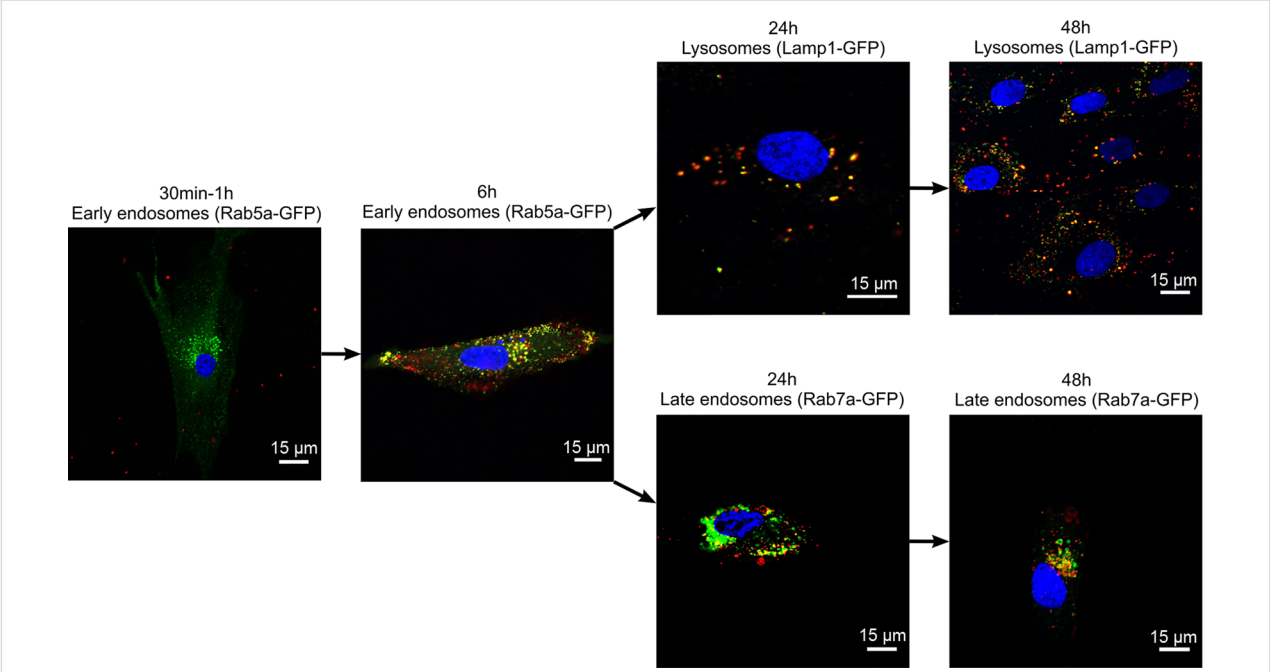

Figure 8: QD co-localization with endosomal compartments. Three overlaid channels represent the nucleus (blue), carboxyl QD655 (red) and Rab5a-GFP (early endosomes), Lamp1-GFP (lysosomes) or Rab7a-GFP (late endosomes) (green). Yellow colour demonstrates co-localization. Representative data are shown.

NIH3T3 mouse fibroblasts with 16 nM QDs for 6 h as the optimal conditions for cellular uptake experiments [39]. Given the lack of standardized NP uptake conditions in MSCs, we adjusted the protocol for QD uptake in human skin MSCs. The results showed that a 6 h incubation with 8 or 16 nM QDs is optimal for QD accumulation in more than 95% of the MSC population (Figure 2). Notably, a 1 h incubation with 5 nM and 20 nM QDs has previously been reported as sufficient for the labelling of rat bone marrow MSCs [40]. However, optimization of the NP incubation time and concentration is necessary in each individual experimental setting.

The uptake pathway of NPs varies depending on the cell and particle type. One of the factors affecting uptake is the protein corona that forms around NPs in serum-containing medium. Protein aggregates decrease gold NP uptake depending on size and cell type [41]. In the present study, we analysed the QD uptake pathways under both serum-containing and serum-free conditions. Selected inhibitors for the major uptake pathways were applied to cells prior to QD incubation. In serum-containing medium, decreased QD uptake in MSCs was observed after treatment with CPZ (Figure 7a,c). CPZ is an inhibitor of clathrin-mediated endocytosis through the anchoring of the clathrin and adaptor protein 2 (AP2) complex to endosomes, thereby preventing the assembly of coated pits at the inner plasma membrane [42]. In serum-free medium, QD uptake was decreased by CPZ and nystatin (Figure 7b,d). nystatin is an inhibitor of caveolin/lipid raft-mediated endocytosis, which disassembles caveloae and cholesterol in the membrane, but does not interfere with clathrin-mediated endocytosis [43]. Zhang et al. and Xiao et al. showed that dendritic cells and breast epithelial cells uptake carboxyl QDs via the clathrin-mediated pathway [44,45]. By contrast, experiments in HEK cells showed the uptake of carboxyl QDs through caveolin/lipid raft-mediated endocytosis; although it has been reported that caveolin-mediated endocytosis is the dominating uptake route in endothelial cells, smooth muscle cells and adipocytes [44,46]. Damalakiene et al. demonstrated that QDs possessing a protein corona are differently recognized by NIH3T3 cells and internalized by different pathways [23], consistent with the data from the present study. Interestingly, MSCs showed more effective internalization of QDs under serum-free conditions, as the protein corona interferes with QD uptake in skin MSCs. The composition of the protein corona could either enhance or decrease the cellular uptake of polystyrene-based NPs, depending on nanoparticle functionalization [47]. We have showed that NP uptake in skin MSCs is an active process and does not occur passively. For the development of cell-based tumour-targeted therapies, elucidation of the endocytic pathway is very important, because it may have an effect on the fate of QDs and/or QD-linked drugs within the cell. For example, after QD uptake by clathrin-mediated endocytosis, the QDs subsequently could be transferred to lysosomes for degradation or, depending on their surface coating, recycled to the cell surface [48]. On the contrary, QDs

taken up by caveolae-dependent endocytosis could bypass lysosomes and avoid lysosomal degradation [48]. Taken together, the accumulated experimental evidence suggests that the QD uptake pathway depends on the cell type, the formation of a protein corona and added functional groups on the NPs.

Intracellular localization of QDs in endosomes and lysosomes has been reported to be a common pathway following NP uptake through which particles are brought for lysosomal degradation [46,49]. We observed internalization of QDs in early endosomes after 6 h of incubation, followed by re-localization to late endosomes/lysosomes after 24 and 48 h of incubation (Figure 8). Cell division, excretion and degradation are the main mechanisms reported for QD signal elimination over time [50,51]. It has been implicated that the elimination rate depends on the particle size. Smaller NPs lead to faster elimination [50-52]. In the present study, we observed that the transfer of QDs to daughter cells during cell division is not the main mechanism involved in QD signal reduction in skin MSCs. Similar observations have been reported in the study of mouse embryonic stem cells, where QD loss was still detected after the inhibition of cell proliferation, suggesting that QDs might be excreted from cells [50]. Indeed, we demonstrated that MSCs could be repetitively labelled by the removal of supernatants from QD-loaded MSCs, confirming the presence of released QDs in the supernatant. After secondary labelling, the number of QD-positive MSCs was two times higher in serum-free medium compared to complete medium, likely indicating that the protein corona interferes with the QD uptake. Many types of stem cells have membrane transporters for the elimination of toxic reagents [53]. The induction of ABC transporter P-glycoprotein increases the elimination of QDs from HEK and HepG2 cells, while its inhibition demonstrated an opposite effect. The elimination rate was higher in HEK cells, because of the stem cell phenotype [54]. Expression of P-glycoprotein has also been reported in MSCs [4]. However, other data in mouse embryonic and kidney stem cells indicate that QD depletion likely occurs during cell division and that no excretion mechanisms could be observed [32]. Taken together, these data indicate that QD elimination mechanisms may be cell-type dependent. The results from skin MSCs demonstrated that the depletion of the QD signal over time could be explained by QD degradation and excretion. The fact that NPs are released from MSCs is important because of the intended use of MSCs as NP delivery vectors. We propose that cancer cell and MSC co-culture model could be used to demonstrate the applicability of QD-labelled MSCs for cancer theranostics. For example, Pietila et al. have demonstrated that direct cell–cell contact is required for QD–mortalin antibody transfer from nano-engineered MSCs to the breast cancer cell line MDA-MB-231 in vitro [55]. Alternatively, QDs or MSCs loaded with QD–drug conjugates could be used in melanoma xenograft models in vivo as was shown in a study by Studeny et al. where IFN-β-MSCs co-injected with a human melanoma cell line suppressed tumour growth in nude mice [25].

Altogether, we propose several reasons why QD-labelled skin MSCs could serve as a promising NP delivery vector. First, QD labelling would enable MSC tracking and visualization of the tumour microenvironment. Next, the cells in the tumour would take up the released QDs and then the formation of ROS could be induced through photoactivation, leading to cancer cell apoptosis. Last but not least, the secretion of sTNFR1 by skin MSCs could downregulate the pro-tumourigenic inflammatory responses [56-58].

Conclusion

Herein, we showed that carboxyl-coated QDs are biocompatible with skin MSCs. The proliferation, immunophenotype and differentiation potential of MSCs was not affected by QD accumulation in the cells. In the presence of serum, QDs were internalized in MSCs through clathrin-mediated endocytosis, whereas in the absence of serum, QD uptake occurs through the clathrin and caveolin/lipid raft-mediated endocytosis pathways. The loss of QD signal over time may possibly be explained by the excretion of QDs from MSCs, which could favour the use of MSCs as drug delivery vectors. These data validate the potential use of skin MSCs as NP delivery vectors for tumour-targeted therapies.

Experimental

Mesenchymal stem cell culture

Human skin samples were obtained from post-surgery materials with authorized approval from Research Ethics Committee, Institute of Experimental and Clinical Medicine, University of Latvia (issued 04.06.2014). Dermal MSC cultures were obtained as described elsewhere [59]. In brief, skin specimens were washed with cold phosphate-buffered saline (PBS), cut into 4–6 mm^2 pieces and incubated in 0.6 U/mL dispase (Roche, Switzerland) for 1–3 h at 37 °C to remove the epidermis. Dermis was minced manually before enzymatic digestion with 0.62 Wunsch U/mL Liberase Blendzyme 1 (Roche, Switzerland) for 30 min at 37 °C, then dissociated by vigorous pipetting and passed through a 70 μm cell strainer, followed by centrifugation at 400*g* for 5 min. The pellets were suspended in cultivation medium containing DMEM/F12 (3:1 v/v) supplemented with 10% of FBS and antibiotics (100 U/mL penicillin, 100 μg/mL streptomycin) (all from Sigma-Aldrich, USA). Cell suspensions were transferred into 25 cm^2 tissue culture flasks and grown until reaching 80% confluence in a humidified chamber at 37 °C with 5% CO_2. Cells were trypsinized with 0.25% trypsin–EDTA solution (Sigma-Aldrich,

USA). Cells at passages 2 to 5 were then frozen at −80 °C for long-term storage in a cell bank. All experiments were performed in compliance with the relevant laws and institutional guidelines. In this study five independent donor skin MSC cultures from passage 4 to passage 8 were used.

MSC surface marker analysis

Phenotyping of cell surface markers was performed by flow cytometry. The cells were stained with CD34-PE and CD45-FITC (all from BD Biosciences, USA), CD90-FITC (Dako, USA), CD73 PE (Abcam, USA) and isotype controls IgG1-FITC (Dako, USA), IgG1-PE (BD Biosciences, USA), and IgG2A-APC (BD Biosciences, USA). Flow cytometry data were acquired using a Guava EasyCyte 8HT flow cytometer and analysed using ExpressPro software (Merck Millipore, USA) comparing unlabelled, marker-labelled and isotype control populations in FL-1, FL-2 and FL-4 channels.

Quantum dots

Qdot® 655 ITK™ non-targeted carboxyl-coated quantum dots were purchased from Thermo Fisher Scientific, USA. QDs are composed of a CdSe core with a ZnS shell that are coated with amphiphilic polymers and functionalized with carboxylate. The QDs have an emission maximum at 655 nm. Xu et al. measured the hydrodynamic diameter of the nanoparticles to be 14.55 ± 4.157 nm and a zeta potential of −35.1 mV [60]. The stock solution is 8 μM in 50 mM borate, pH 9.0. Further preparations of the QD solution are described in each methodological part separately.

QD uptake dynamics using flow cytometry

To estimate the optimal QD concentration for uptake experiments, MSCs were seeded at a density of 5×10^4 cells per well in a 12-well tissue culture polystyrene plate and labelled with QDs at various concentrations in the range of 0.5 to 64 nM for 6 h in complete or serum-free medium. To determine the accumulation dynamics, 8 nM or 16 nM QDs were applied to MSCs and incubated for 0.5, 1, 3, 6, 24 and 48 h in complete medium. The cells were subsequently harvested by trypsinization, centrifuged at 250*g* for 5 min and resuspended in 200 μL of PBS. The samples were acquired on a Guava EasyCyte 8HT flow cytometer and analysed using ExpressPro software (Merck Millipore, USA) in channel FL4, comparing unlabelled and labelled cell populations.

Cell-viability assay

The impact of carboxyl-coated QD655 on the viability of MSCs was analysed using the Cell Counting Kit 8 (CCK-8) (Sigma-Aldrich, USA). A total of 5×10^3 cells per well were seeded onto 96-well plates in 100 μL of complete medium. The next day, QDs were added in serial dilutions at a twofold dilution in complete medium. The range of the tested QD concentrations ranged from 0.5–64 nM with twofold dilution. The cells were incubated with QDs for 24 and 48 h. QD untreated cells were used as a control, and the viability was defined as 100%. After incubation, 10 μL of CCK-8 reagent was added to each well and incubated for 2 h at 37 °C in 5% CO_2 at 90% humidity. The change in the medium colour corresponds to the amount of dye produced in the sample and is directly proportional to the number of viable cells. The optical density was measured using a spectrophotometer Bio-Tek *ELx808* (BioTek Instruments, USA) at a wavelength of 450 nm. The background signal of QDs from all of the tested concentrations was subtracted from the respective samples. Data were analysed in Microsoft Excel and GraphPad Prism software.

QD release assay

A total of 1×10^5 MSCs were first labelled with 16 nM QDs for 6 h in complete medium. After the primary labelling, the cell-culture supernatant was aspirated, the cells were rigorously rinsed and fresh complete or serum-free medium was added. The number of QD-positive cells was assessed using flow cytometry after 24 and 48 h. The supernatant of the primarily QD-labelled cells was collected at 24 and 48 h and subsequently applied to unlabelled cells for secondary labelling. After 24 h of incubation, the secondarily labelled cells were analysed using flow cytometry to evaluate the uptake of QD. To analyse the effect of proliferation on QD loss from the cells, QD labelled MSCs were propagated either in complete or serum-free medium and assessed for Ki67 expression (as described in method "MSC proliferation assay") and QD signal using flow cytometry.

MSC proliferation assay

The effect of QD accumulation on the proliferation of MSCs was evaluated after 24 and 48 h of incubation using the FITC Mouse Anti-Ki67 Set according to the manufacturer's instructions (BD Bioscience, USA). MSCs were seeded at a density of 5×10^4 cells per well onto 12-well plates in complete medium and allowed to adhere overnight. The medium was subsequently aspirated, and the wells were rinsed once with serum-free medium. The cells were serum-starved for 24 h to synchronize the cell cycle. Next, 16 nM of QDs in complete medium were added, and the cells were incubated for 24 or 48 h. Control wells contained cells in complete medium only. Subsequently, the cells were harvested by trypsinization, washed in PBS and centrifuged for 5 min at 250*g*. The cell pellet was fixed by suspending in 1 mL of 70% ice-cold ethanol. The samples were incubated at −20 °C for at least 2 h. The cells were subsequently washed twice with 9 mL of 1% FBS in PBS at 250*g* for 7 min. Cell pellets were resuspended in 100 μL of PBS, and 10 μL of FITC mouse anti-Ki-67 antibody and isotype control

IgG1-FITC were added to the cell suspension, mixed gently and incubated at room temperature for 30 min in the dark. After incubation, the cells were washed with 1 mL of PBS and centrifuged for 5 min at 300*g*. The pellet was suspended in 200 µL of PBS. Nonlabelled cells were used as a control to set the base line of Ki67 expression in MSCs. The isotype control was used to set the Ki67 negative population. The samples were analysed in channel FL-1 using flow cytometry.

Mesenchymal stem cell tri-lineage differentiation

MSCs were cultivated in complete medium up to 80% confluence. Differentiation into osteogenic, adipogenic and chondrogenic lineages was performed using StemPro Adipogenesis, Chondrogenesis, and Osteogenesis kits according to the manufacturer's instructions (all from ThermoFisher Scientific, USA). Briefly, for osteogenic differentiation, cells were seeded at a density of $1 \times 10^4/cm^2$ onto 24-well plates. Osteogenic differentiation medium was added; the medium was changed every three days over a period of 21 days. Spontaneous osteodifferentiation control samples were propagated in complete medium for 21 days. Adipogenic differentiation was performed after cultivating 1.82×10^4 cells in 24-well plates using adipogenic differentiation medium. The medium was changed every three days for 21 days. Spontaneous adipodifferentiation control samples were propagated in complete medium for 21 days. For the chondrogenic differentiation assay, 5 µL of a cell suspension with a density of 1.6×10^7 cells/mL in complete medium was seeded onto 96-well plates and incubated for 2 h under high-humidity conditions at 37 °C and 5% CO_2. Chondrogenic differentiation medium was added, and the medium was changed every three days for 14 days. Spontaneous chondrodifferentiation control samples were propagated in complete medium for 14 days.

Samples were incubated with 8 nM QDs in complete medium for 3 h before starting the differentiation assay. The QD concentration and incubation time were adjusted for the differentiation assay. After incubation with QDs, the medium was discarded, cells were washed with PBS and the relevant differentiation medium was added.

Evaluation of mesenchymal differentiation

Osteogenic differentiation was evaluated using Alizarin Red S staining. The cells were washed with 1 mL of PBS and fixed with 4% paraformaldehyde (PFA) at room temperature for 30 min. After fixation, the cells were washed two times with distilled water and stained with a 2% Alizarin Red S solution in water (pH adjusted to 4.2 with a 0.1% solution of NH_4OH) for 45 min at room temperature in the dark. Then, the stained cells were washed four times with 1 mL of distilled water and imaged using EVOS XL microscope (Invitrogen, USA). Samples stained with Alizarin Red S were extracted for quantitative measurements of osteogenic differentiation using 300 µL of 5% perchloric acid and gentle agitation for 10 min at room temperature. Subsequently 100 µL was transferred to a 96-well plate, and the absorbance was measured at 425 nm using an Infinite 200 PRO plate reader and i-control software (Tecan Trading AG, Switzerland).

Adipogenic differentiation was evaluated using Oil Red O staining. Cells were washed with PBS and fixed with 4% formaldehyde for 30 min at room temperature. After fixation, cells were washed with distilled water. Prior to staining, cells were incubated for 5 min at room temperature with 60% isopropanol and subsequently stained with 180 mg/L Oil Red O solution in isopropanol/water (3:2, v/v) for 15 min at room temperature. After staining, the cells were washed four to five times with distilled water and imaged.

Chondrogenic differentiation was evaluated using Alcian Blue staining. Cells were washed once with PBS and fixed with 4% PFA for 30 min at room temperature. After fixation, cells were washed with PBS and stained with a 1% Alcian Blue staining solution in 0.1 M HCl overnight at room temperature. Stained cells were washed three times with 0.1 M HCl and imaged in water.

Quantification of the Alcian Blue stain was achieved by solubilizing the stain in 50 µL of 6 M guanidine hydrochloride (Sigma-Aldrich, USA) overnight at room temperature. Absorbance was measured at 620 nm directly in a 96-well plate using an Infinite 200 PRO plate reader and i-control software.

Confocal microscopy

For confocal microscopy analysis, 1×10^4 cells per well were seeded on 8-well chamber slides (Nunc, Sigma-Aldrich, USA) in complete medium and left to adhere overnight at 37 °C, 5% CO2 and more than 90% humidity. 16 nM QDs diluted in complete medium were added, and samples were incubated from 15 min to 24 h. Control wells contained nonlabelled cells. After incubation, the medium was aspirated and each well was rinsed with 2 mL of PBS. Then, fixation with 4% PFA in PBS (w/v) for 20 min at room temperature was performed. Wells were washed three times with 0.5 mL of washing buffer containing 1% BSA (Sigma-Aldrich, USA) in PBS for 5 min each. Permeabilization and blocking was performed with 0.3% Triton X-100 (Sigma-Aldrich, USA) and 1% BSA in PBS for 45 min at room temperature. The cytoskeleton of cells was subsequently stained with methanolic Alexa Fluor488 Phalloidin (Thermo Fisher Scientific, USA) diluted 1:100 in washing buffer and incubated for 30 min at room temperature in the

dark. The samples were subsequently washed three times and counterstained with a Hoechst 33342 trihydrochloride, trihydrate (10 mg/mL) solution (Thermo Fisher Scientific, USA) diluted 1:1000 in washing buffer for 5 min at room temperature in the dark. Samples were rinsed once with PBS, mounted with ProLong Gold anti-fade mounting medium (Thermo Fisher Scientific, USA) and incubated overnight at room temperature in the dark. Samples were analysed using a Nikon eclipse Ti microscope equipped with a Nikon C2 confocal system. A Nikon S Plan Fluor ELWD 40×/0.60 objective was used. For Alexa Fluor488 Phalloidin, 488 nm was used for excitation, but for Hoechst and QD655, 405 nm lasers were used for excitation. To detect fluorescence for Hoechst - 447/60 nm, Alexa Fluor488 Phalloidin - 525/50 nm and QD655 - 561 LP band pass filters were used (Nikon, Japan). Each channel was recorded separately to avoid spectral overlap. The images were analysed using Nis-Elements C 4.13 software (Nikon, Japan).

Endocytosis inhibitor assay

To analyse the pathway of QD uptake in MSCs, five endocytosis inhibitors were selected: the clathrin pathway inhibitor chlorpromazine (CPZ), phagocytosis inhibitor cytohalasin D (CytD), macropinocytosis inhibitor ethylisopropyl amiloride (EIPA) (Cayman Chemical, USA), caveolin/lipid raft-mediated endocytosis inhibitor nystatin and caveolin-dependent endocytosis inhibitor dynasore (all from Sigma-Aldrich, USA, unless otherwise stated). The optimal inhibitor concentration was selected using the CCK-8 viability assay. Briefly, 5×10^3 cells per well were seeded on a 96-well plate in 100 µL of complete medium. The next day, endocytosis inhibitors were added in serial dilutions with a twofold dilution factor. The range of the tested inhibitor concentrations was from 1.25–160 µM. The cells were incubated with inhibitors for 24 h. After incubation, 10 µL of CCK-8 reagent was added to each well and incubated for 2 h at 37 °C in 5% CO_2 at 90% humidity. The optical density was recorded on a Bio-Tek *ELx808* instrument at 450 nm (BioTek Instruments, USA).

MSCs were seeded onto 8-well chamber slides with 2×10^4 cells per well in 0.5 mL of complete medium and incubated for 1 h with the respective inhibitors at the following concentrations: 40 µM CPZ, 2 µM CytD, 5 µM EIPA, 80 µM nystatin and 80 µM dynasore, at 37 °C, 5% CO_2 and 95% humidity. The medium was aspirated from the wells, and 16 nM QDs were added to samples in complete or serum-free medium and incubated for 6 h. The medium was aspirated and samples were rinsed with 2 mL of PBS. Control wells contained nonlabelled cells. The samples were subsequently stained with methanolic Phalloidin Alexa Fluor488 (Thermo Fisher Scientific, USA) as previously described and analysed using confocal microscopy.

Quantification of the QD fluorescent signal was achieved using Nis-Elements C 4.13 software. Single cell borders were defined according to the Phalloidin Alexa488 staining. The mean fluorescence was measured in the middle z-section of the cell in the red channel only. As a control, the background mean fluorescence from different parts of the image was measured. The QD fluorescence intensity of single cells was calculated by subtracting the background mean intensity from the single-cell mean intensity average.

Transfection assay

Analogous to the description in [61], transient transfection of MSCs was performed using Cell Light® Reagent-GFP, BacMam 2.0 (Thermo Fisher Scientific, USA) according to the manufacturer's recommendations. Briefly, MSCs were seeded at a density of 1.5×10^4 cells per well onto 12-well plates in complete growth medium. After the cells attached, BacMam 2.0 reagent was added at a concentration of 80 particles per cell (PPC). Cell Light® Early endosomes-GFP, BacMam 2.0 was used to label early endosomes (Rab5a-GFP expression), Cell Light® Late endosomes-GFP, BacMam 2.0 was used to label late endosomes (Rab7a-GFP expression), and Cell Light® Lysosomes-GFP, and BacMam 2.0 was used to label lysosomes (Lamp1-GFP expression). The cells were transfected for 72 h.

QD localization study

Transfected MSCs were trypsinized and seeded onto 8-well chambered coverslips (Nunc, Thermo Fisher Scientific, USA) at a density of 3×10^4 cells per well in medium to adhere overnight, and 16 nM of QDs diluted in complete growth medium were added, followed by incubation for 30 min and 1, 6, 24 and 48 h. After incubation, the medium was aspirated and each well was rinsed with PBS. To label nuclei, Hoechst 33342 (Sigma-Aldrich) was diluted in a complete growth medium to a concentration of 25 µg/mL and added to the wells, and the cells were immediately imaged with a laser scanning confocal microscope (Nikon Eclipse TE2000-S, C1 Plus (Nikon, Japan)) using an oil-immersion 60× NA1.4 objective (Plan Apo VC (Nikon, Japan)). A diode laser (404 nm) was used for Hoechst, an argon ion laser (488 nm) for GFP, and a helium–neon laser (543 nm) for QDs. The images were captured with the EZ-C1 v3.90 image analysis software (Nikon, Japan) and further processed using EZ-C1 Bronze v3.80 (Nikon, Japan) and ImageJ 1.48 (National Institute of Health, USA) software.

Statistical analysis

Statistical analysis was performed using GraphPad Prism Software (Graph Pad Inc., USA). The data are expressed as the representative results or the means of at least three independent experiments +/- standard error of the mean. Statistical significance was analysed using one-way ANOVA. Significance

was represented as *p-value < 0.05, **p-value < 0.01, ***p-value < 0.001.

Acknowledgements

This work was supported by Taiwan-Lithuania-Latvia mutual research collaboration fund grant (LV-LT-TW-/2016/6).

References

1. Ferlay, J.; Soerjomataram, I.; Dikshit, R.; Eser, S.; Mathers, C.; Rebelo, M.; Parkin, D. M.; Forman, D.; Bray, F. *Int. J. Cancer* **2015,** *136,* E359–E386. doi:10.1002/ijc.29210
2. Markman, J. L.; Rekechenetskiy, A.; Holler, E.; Ljubimova, J. Y. *Adv. Drug Delivery Rev.* **2013,** *65,* 1866–1879. doi:10.1016/j.addr.2013.09.019
3. Gao, Z.; Zhang, L.; Hu, J.; Sun, Y. *Nanomedicine* **2013,** *9,* 174–184. doi:10.1016/j.nano.2012.06.003
4. Sadhukha, T.; O'Brien, T. D.; Prabha, S. *J. Controlled Release* **2014,** *196,* 243–251. doi:10.1016/j.jconrel.2014.10.015
5. Usha, L.; Rao, G.; Christopherson, K., II; Xu, X. L. *PLoS One* **2013,** *8,* e67895. doi:10.1371/journal.pone.0067895
6. Kidd, S.; Spaeth, E.; Dembinski, J. L.; Dietrich, M.; Watson, K.; Klopp, A.; Battula, V. L.; Weil, M.; Andreeff, M.; Marini, F. C. *Stem Cells (Durham, NC, U. S.)* **2009,** *27,* 2614–2623. doi:10.1002/stem.187
7. Dominici, M.; Le Blanc, K.; Mueller, I.; Slaper-Cortenbach, I.; Marini, F. C.; Krause, D. S.; Deans, R. J.; Keating, A.; Prockop, D. J.; Horwitz, E. M. *Cytotherapy* **2006,** *8,* 315–317. doi:10.1080/14653240600855905
8. Maleki, M.; Ghanbarvand, F.; Reza Behvarz, M.; Ejtemaei, M.; Ghadirkhomi, E. *Int. J. Stem Cells* **2014,** *7,* 118–126. doi:10.15283/ijsc.2014.7.2.118
9. Toma, J. G.; McKenzie, I. A.; Bagli, D.; Miller, F. D. *Stem Cells (Durham, NC, U. S.)* **2005,** *23,* 727–737. doi:10.1634/stemcells.2004-0134
10. Parfejevs, V.; Gavare, M.; Cappiello, L.; Grube, M.; Muceniece, R.; Riekstina, U. *Spectroscopy (N. Y., NY, U. S.)* **2012,** *27,* 315–320. doi:10.1155/2012/286542
11. Smith, A. M.; Mancini, M. C.; Nie, S. *Nat. Nanotechnol.* **2009,** *4,* 710–711. doi:10.1038/nnano.2009.326
12. Sperling, R. A.; Parak, W. J. *Philos. Trans. R. Soc. London, Ser. A* **2010,** *368,* 1333–1383. doi:10.1098/rsta.2009.0273
13. Yong, Y.; Cheng, X.; Bao, T.; Zu, M.; Yan, L.; Yin, W.; Ge, C.; Wang, D.; Gu, Z.; Zhao, Y. *ACS Nano* **2015,** *9,* 12451–12463. doi:10.1021/acsnano.5b05825
14. Ruan, J.; Song, H.; Qian, Q.; Li, C.; Wang, K.; Bao, C.; Cui, D. *Biomaterials* **2012,** *33,* 7093–7102. doi:10.1016/j.biomaterials.2012.06.053
15. Steponkiene, S.; Valanciunaite, J.; Skripka, A.; Rotomskis, R. *J. Biomed. Nanotechnol.* **2014,** *10,* 679–686. doi:10.1166/jbn.2014.1738
16. Steponkiene, S.; Dapkute, D.; Riekstina, U.; Rotomskis, R. *J. Nanomed. Nanotechnol.* **2015,** *6,* 341. doi:10.4172/2157-7439.1000341
17. Hsieh, S.-C.; Wang, F.-F.; Lin, C.-S.; Chen, Y.-J.; Hung, S.-C.; Wang, Y.-J. *Biomaterials* **2006,** *27,* 1656–1664. doi:10.1016/j.biomaterials.2005.09.004
18. Bouwstra, J. A.; Ponec, M. *Biochim. Biophys. Acta* **2006,** *1758,* 2080–2095. doi:10.1016/j.bbamem.2006.06.021
19. Rotomskis, R. Quantum dot migration through natural barriers and distribution in the skin. In *Nanoscience in Dermatology;* Hamblin, M. R.; Avci, P.; Prow, T. W., Eds.; Elsevier: Amsterdam, Netherlands, 2016; pp 307–321. doi:10.1016/B978-0-12-802926-8.00024-0
20. Ahn, J.; Lee, H.; Seo, K.; Kang, S.; Ra, J.; Youn, H. *PLoS One* **2013,** *8,* e74897. doi:10.1371/journal.pone.0074897
21. Ramdasi, S.; Sarang, S.; Viswanathan, C. *Int. J. Hematol. Oncol. Stem Cell Res.* **2015,** *9,* 2.
22. Pessina, A.; Bonomi, A.; Coccè, V.; Invernici, G.; Navone, S.; Cavicchini, L.; Sisto, F.; Ferrari, M.; Viganò, L.; Locatelli, A.; Ciusani, E.; Cappelletti, G.; Cartelli, D.; Arnaldo, C.; Parati, E.; Marfia, G.; Pallini, R.; Falchetti, M. L.; Alessandri, G. *PLoS One* **2011,** *6,* e28321. doi:10.1371/journal.pone.0028321
23. Damalakiene, L.; Karabanovas, V.; Bagdonas, S.; Valius, M.; Rotomskis, R. *Int. J. Nanomed.* **2013,** 555–568. doi:10.2147/IJN.S39658
24. Rustad, K. C.; Gurtner, G. C. *Adv. Wound Care* **2012,** *1,* 147–152. doi:10.1089/wound.2011.0314
25. Studeny, M.; Marini, F. C.; Champlin, R. E.; Zompetta, C.; Fidler, I. J.; Andreeff, M. *Cancer Res.* **2002,** *62,* 13.
26. Brennen, W. N.; Chen, S. L.; Denmeade, S. R.; Isaacs, J. T. *Oncotarget* **2013,** *4,* 106–117.
27. Loebinger, M. R.; Kyrtatos, P. G.; Turmaine, M.; Price, A. N.; Pankhurst, Q.; Lythgoe, M. F.; Janes, S. M. *Cancer Res.* **2009,** *69,* 8862–8867. doi:10.1158/0008-5472.CAN-09-1912
28. Correa, D.; Somoza, R. A.; Lin, P.; Schiemann, W. P.; Caplan, A. I. *Int. J. Cancer* **2016,** *138,* 417–427. doi:10.1002/ijc.29709
29. Lourenco, S.; Teixeira, V. H.; Kalber, T.; Jose, R. J.; Floto, R. A.; Janes, S. M. *J. Immunol.* **2015,** *194,* 3463–3474. doi:10.4049/jimmunol.1402097
30. Dror, S.; Sander, L.; Schwartz, H.; Sheinboim, D.; Barzilai, A.; Dishon, Y.; Apcher, S.; Golan, T.; Greenberger, S.; Barshack, I.; Malcov, H.; Zilberberg, A.; Levin, L.; Nessling, M.; Friedmann, Y.; Igras, V.; Barzilay, O.; Vaknine, H.; Brenner, R.; Zinger, A.; Schroeder, A.; Gonen, P.; Khaled, M.; Erez, N.; Hoheisel, J. D.; Levy, C. *Nat. Cell Biol.* **2016,** *18,* 1006–1017. doi:10.1038/ncb3399
31. Shah, B. S.; Clark, P. A.; Moioli, E. K.; Stroscio, M. A.; Mao, J. J. *Nano Lett.* **2007,** *7,* 3071–3079. doi:10.1021/nl071547f
32. Rak-Raszewska, A.; Marcello, M.; Kenny, S.; Edgar, D.; Sée, V.; Murray, P. *PLoS One* **2012,** *7,* e32650. doi:10.1371/journal.pone.0032650
33. Candini, O.; Spano, C.; Murgia, A.; Grisendi, G.; Veronesi, E.; Piccinno, M. S.; Ferracin, M.; Negrini, M.; Giacobbi, F.; Bambi, F.; Horwitz, E. M.; Conte, P.; Paolucci, P.; Dominici, M. *Stem Cells (Durham, NC, U. S.)* **2015,** *33,* 939–950. doi:10.1002/stem.1897
34. Yong, K.-T.; Law, W.-C.; Hu, R.; Ye, L.; Liu, L.; Swihart, M. T.; Prasad, P. N. *Chem. Soc. Rev.* **2013,** *42,* 1236–1250. doi:10.1039/c2cs35392j
35. Rocha, T. L.; Mestre, N. C.; Sabóia-Morais, S. M.; Bebianno, M. J. *Environ. Int.* **2017,** *98,* 1–17. doi:10.1016/j.envint.2016.09.021
36. Chen, N.; He, Y.; Su, Y.; Li, X.; Huang, Q.; Wang, H.; Zhang, X.; Tai, R.; Fan, C. *Biomaterials* **2012,** *33,* 1238–1244. doi:10.1016/j.biomaterials.2011.10.070
37. Walling, M. A.; Novak, J. A.; Shepard, J. R. E. *Int. J. Mol. Sci.* **2009,** *10,* 441–491. doi:10.3390/ijms10020441
38. Yaghini, E.; Pirker, K. F.; Kay, C. W. M.; Seifalian, A. M.; MacRobert, A. J. *Small* **2014,** *10,* 5106–5115. doi:10.1002/smll.201401209

39. Karabanovas, V.; Zitkus, Z.; Kuciauskas, D.; Rotomskis, R.; Valius, M. *J. Biomed. Nanotechnol.* **2014,** *10,* 775–786. doi:10.1166/jbn.2014.1770
40. Muller-Borer, B. J.; Collins, M. C.; Gunst, P. R.; Cascio, W. E.; Kypson, A. P. J. *NanoBiotechnology* **2007,** 9. doi:10.1186/1477-3155-5-9
41. Cheng, X.; Tian, X.; Wu, A.; Li, J.; Tian, J.; Chong, Y.; Chai, Z.; Zhao, Y.; Chen, C.; Ge, C. *ACS Appl. Mater. Interfaces* **2015,** *7,* 20568–20575. doi:10.1021/acsami.5b04290
42. Wang, L. H.; Rothberg, K. G.; Anderson, R. G. *J. Cell Biol.* **1993,** *123,* 1107. doi:10.1083/jcb.123.5.1107
43. Zhu, X.-D.; Zhuang, Y.; Ben, J.-J.; Qian, L.-L.; Huang, H.-P.; Bai, H.; Sha, J.-H.; He, Z.-G.; Chen, Q. *J. Biol. Chem.* **2011,** *286,* 8231–8239. doi:10.1074/jbc.M110.145888
44. Xiao, Y.; Forry, S. P.; Gao, X.; Holbrook, R. D.; Telford, W. G.; Tona, A. *J. Nanobiotechnol.* **2010,** *8,* 13. doi:10.1186/1477-3155-8-13
45. Zhang, L. W.; Bäumer, W.; Monteiro-Riviere, N. A. *Nanomedicine (London, U. K.)* **2011,** *6,* 777–791. doi:10.2217/nnm.11.73
46. Zhang, L. W.; Monteiro-Riviere, N. A. *Toxicol. Sci.* **2009,** *110,* 138–155. doi:10.1093/toxsci/kfp087
47. Ritz, S.; Schöttler, S.; Kotman, N.; Baier, G.; Musyanovych, A.; Kuharev, J.; Landfester, K.; Schild, H.; Jahn, O.; Tenzer, S.; Mailänder, V. *Biomacromolecules* **2015,** *16,* 1311–1321. doi:10.1021/acs.biomac.5b00108
48. Kou, L.; Sun, J.; Zhai, Y.; He, Z. *Asian J. Pharm. Sci. (Amsterdam, Neth.)* **2013,** *8,* 1–10. doi:10.1016/j.ajps.2013.07.001
49. Huang, D.-M.; Hung, Y.; Ko, B.-S.; Hsu, S.-C.; Chen, W.-H.; Chien, C.-L.; Tsai, C.-P.; Kuo, C.-T.; Kang, J.-C.; Yang, C.-S.; Mou, C.-Y.; Chen, Y.-C. *FASEB J.* **2005,** *19,* 2014–2016. doi:10.1096/fj.05-4288fje
50. Pi, Q. M.; Zhang, W. J.; Zhou, G. D.; Liu, W.; Cao, Y. *BMC Biotechnol.* **2010,** *10,* 36. doi:10.1186/1472-6750-10-36
51. Oh, N.; Park, J. H. *Int. J. Nanomed.* **2014,** *9* (Suppl. 1), 51–63. doi:10.2147/IJN.S26592
52. Peng, L.; He, M.; Chen, B.; Wu, Q.; Zhang, Z.; Pang, D.; Zhu, Y.; Hu, B. *Biomaterials* **2013,** *34,* 9545–9558. doi:10.1016/j.biomaterials.2013.08.038
53. Sarkadi, B.; Özvegy-Laczka, C.; Német, K.; Váradi, A. *FEBS Lett.* **2004,** *567,* 116–120. doi:10.1016/j.febslet.2004.03.123
54. Al-Hajaj, N. A.; Moquin, A.; Neibert, K. D.; Soliman, G. M.; Winnik, F. M.; Maysinger, D. *ACS Nano* **2011,** *5,* 4909–4918. doi:10.1021/nn201009w
55. Pietilä, M.; Lehenkari, P.; Kuvaja, P.; Kaakinen, M.; Kaul, S. C.; Wadhwa, R.; Uemura, T. *Exp. Cell Res.* **2013,** *319,* 2770–2780. doi:10.1016/j.yexcr.2013.07.023
56. Ke, F.; Zhang, L.; Liu, Z.; Yan, S.; Xu, Z.; Bai, J.; Zhu, H.; Lou, F.; Cai, W.; Sun, Y.; Gao, Y.; Wang, H.; Wang, H. *Stem Cells Transl. Med.* **2016,** *5,* 301–313. doi:10.5966/sctm.2015-0179
57. Shi, Y.; Du, L.; Lin, L.; Wang, Y. *Nat. Rev. Drug Discovery* **2017,** *16,* 35–52. doi:10.1038/nrd.2016.193
58. Balkwill, F. *Nat. Rev. Cancer* **2009,** *9,* 361–371. doi:10.1038/nrc2628
59. Riekstina, U.; Muceniece, R.; Cakstina, I.; Muiznieks, I.; Ancans, J. *Cytotechnology* **2008,** *58,* 153. doi:10.1007/s10616-009-9183-2
60. Xu, G.; Lin, G.; Lin, S.; Wu, N.; Deng, Y.; Feng, G.; Chen, Q.; Qu, J.; Chen, D.; Chen, S.; Niu, H.; Mei, S.; Yong, K.-T.; Wang, X. *Sci. Rep.* **2016,** *6,* No. 37677. doi:10.1038/srep37677
61. Matulionyte, M.; Dapkute, D.; Budenaite, L.; Jarockyte, G.; Rotomskis, R. *Int. J. Mol. Sci.* **2017,** *18,* No. 378. doi:10.3390/ijms18020378

License and Terms

BEILSTEIN JOURNAL OF NANOTECHNOLOGY

Cationic PEGylated polycaprolactone nanoparticles carrying post-operation docetaxel for glioma treatment

Cem Varan[1] and Erem Bilensoy[*1,2]

Full Research Paper

Open Access

Address:
[1]Department of Nanotechnology and Nanomedicine, Graduate School of Science and Engineering, Hacettepe University, Ankara, 06800, Turkey and [2]Department of Pharmaceutical Technology, Faculty of Pharmacy, Hacettepe University, Ankara, 06100, Turkey

Email:
Erem Bilensoy[*] - eremino@hacettepe.edu.tr

* Corresponding author

Keywords:
bioadhesive film; cationic nanoparticle; core–shell nanoparticle; docetaxel; glioma

Beilstein J. Nanotechnol. **2017,** *8,* 1446–1456.
doi:10.3762/bjnano.8.144

Received: 30 March 2017
Accepted: 20 June 2017
Published: 12 July 2017

This article is part of the Thematic Series "Nanomaterial-based cancer theranostics".

Guest Editor: V. Sivakov

Abstract

Background: Brain tumors are the most common tumors among adolescents. Although some chemotherapeutics are known to be effective against brain tumors based on cell culture studies, the same effect is not observed in clinical trials. For this reason, the development of drug delivery systems is important to treat brain tumors and prevent tumor recurrence. The aim of this study was to develop core–shell polymeric nanoparticles with positive charge by employing a chitosan coating. Additionally, an implantable formulation for the chemotherapeutic nanoparticles was developed as a bioadhesive film to be applied at the tumor site following surgical operation for brain glioma treatment. To obtain positively charged, implantable nanoparticles, the effects of preparation technique, chitosan coating concentration and presence of surfactants were evaluated to obtain optimal nanoparticles with a diameter of less than 100 nm and a net positive surface charge to facilitate cellular internalization of drug-loaded nanoparticles. Hydroxypropyl cellulose films were prepared to incorporate these nanoparticle dispersions to complete the implantable drug delivery system.

Results: The diameter of core–shell nanoparticles were in the range of 70–270 nm, depending on the preparation technique, polymer type and coating. Moreover, the chitosan coating significantly altered the surface charge of the nanoparticles to net positive values of +30 to +50 mV. The model drug docetaxel was successfully loaded into all particles, and the drug release rate from the nanoparticles was slowed down to 48 h by dispersing the nanoparticles in a hydroxypropyl cellulose film. Cell culture studies revealed that docetaxel-loaded nanoparticles cause higher cytotoxicity compared to the free docetaxel solution in DMSO.

Conclusion: Docetaxel-loaded nanoparticles dispersed in a bioadhesive film were shown to be suitable for application of chemotherapeutics directly to the action site during surgical operation. The system was found to release chemotherapeutics for several days at the tumor site and neighboring tissue. This can be suggested to result in a more effective brain tumor treatment when compared to chemotherapeutics administered as an intravenous bolus infusion.

Introduction

A brain tumor is known as an abnormal growth of neoplastic cells within the brain or the central spinal canal. In the United States, it is estimated that 23,800 new cases and 16,700 deaths will occur in 2017 due to brain and other nervous system cancers. Brain and other nervous system cancers are the second most common tumor type from birth to the age of 19, thus having a high impact on public health and quality of life [1].

Surgical operation is the main treatment option for brain tumors; chemotherapy or radiotherapy are generally applied after surgery to remove remaining tumor cells and avoid the recurrence of the tumor [2,3]. At this stage, intravenous or orally administered chemotherapy drugs have very low efficacy due to challenges in reaching the brain and tumor area. The blood brain barrier (BBB) is the essential protection of the brain and only 1% of chemotherapeutic agents can pass this barrier without losing their pharmacological activity [4-9]. It is possible to bypass the BBB and reach the tumor site directly with implantable drug delivery systems such as Gliadel®, which is the chemotherapeutic drug carmustine-loaded wafer implant. These drug delivery systems can be implanted after surgical removal of the tumor, facilitating chemotherapy administration to prevent recurrence of the tumor at the time of tumor tissue removal by surgical operation.

Among the anticancer drugs that are used in clinics, the taxane family of drugs such as paclitaxel and docetaxel are known to be highly effective against a variety of cancer cells in vitro due to disruption of microtubule function. However, they are known to have severe solubility problems in aqueous media, therefore co-solvents or excipients are used to improve their solubility to facilitate injectable formulation development. Unfortunately, these solubilizing agents may often cause serious side effects. Thus, the necessity of a safe and effective formulation and drug delivery approach emerges for these potent anticancer drugs from the taxane family [10-13].

Successful treatment of brain cancer is dependent on the efficient and safe delivery of chemotherapeutic agents to the tumor site, while avoiding possible side effects. The development of novel drug delivery systems with reduced side effects is an important breakthrough and nanoparticles are promising in this field as they enable localized drug delivery to target sites and enhanced cellular uptake. Nanoparticle-based drug delivery systems can be prepared with synthetic and natural polymers. As an advantage, their surface properties can be modified to increase cellular penetration and prolonged drug release. Additionally, suitable nanoparticle-based drug delivery systems can bypass biological barriers or benefit from enhanced permeability and retention (EPR) effect thanks to their smaller size. They can also encapsulate hydrophobic drugs as their cargo to improve solubility at the target site. Consequently, nanoparticle-based drug delivery systems can protect drug activities in biological systems and allow targeted drug delivery [14-17].

Polycaprolactone (PCL) is a synthetic hydrophobic polymer, which is prepared by ring opening polymerization of the monomer ε-caprolactone. It is used as a polymer in preparation of nanoparticles and other drug depot and delivery systems. Moreover, PCL is reported to be nontoxic, biocompatible and biodegradable and is approved for therapeutic use in humans by the FDA. PCL can be copolymerized with other synthetic polymers such as polyethylene glycol (PEG) and polyethylene oxide (PEO) to obtain new polycaprolactone derivatives with various novel properties [18,19]. There are several studies reported on PCL as a functional excipients for the preparation of nanoparticulate drug delivery systems with favorable drug loading and release characteristics for hydrophobic anticancer molecules in particular [18-21]. However, the application of core–shell PCL nanoparticles to tumor targeting with docetaxel on a glioma model is very rare. Recently, active-targeted docetaxel-loaded PEG/PCL nanoparticles were prepared successfully for glioblastoma therapy by Gao et al. Cellular uptake and tumor spheroid uptake studies on U87 human glioma cells show that active targeted PEG/PCL nanoparticles enhanced tumor penetration [22]. Besides that, Ungaro et al. obtained docetaxel-loaded core–shell PEO/PCL nanoassemblies for passive targeting of the anticancer drug to cancer cells. Their results showed that docetaxel-loaded PEO/PCL nanoparticles were more effective on growth inhibition of breast and prostate cancer cells when compared to free docetaxel [23]. Core–shell nanoparticles are also used as non-viral vectors for the treatment of glioma. Zamora et al. prepared photochemical internalization mediated polyamine core–shell nanoparticles for tumor suppressor gene delivery. Their results showed that the prepared nanoparticles enhanced the delivery of tumor suppressor genes on U87 and U251 glioma cells [24]. Wang et al. used core–shell nanoparticles for drug and gene co-delivery. They prepared magnetic PLGA/polymeric liposome carriers to achieve sustained release of the model drug epidoxorubicin as carriers of pEGFP DNA complexes. The results demonstrated that co-delivery of drug and gene could be performed and strong inhibition effects on glioblastoma can be achieved with their system [25]. Additionally, magnetic core–shell nanoparticles have been studied for targeting and delivery of chemotherapeutic drugs for glioma treatment. Fang et al. prepared core–shell nanocapsules for co-delivery of the hydrophilic drug doxorubicin, and the hydrophobic drug curcumin. Their results showed that the synergistic cytotoxic effect on RG2 glioma cells was obtained by dual drug targeting. Besides that, the

magnetic and ligand targeting resulted in elevated cellular uptake of nanocapsules in glioma treatment [26]. Yang et al. successfully obtained targeted and traceable core–shell nanoparticles for carmustine (BCNU) delivery. These systems prolonged the half-time and also enhanced the concentration of BCNU in the brain tumor area [27]. In addition to drug delivery, core–shell nanoparticles such as magnetic nanoparticles [28], quantum dots [29], nanodiamonds [30], nanocrystals [31] and iron oxide nanoparticles [32] are studied as imaging and detection agents of glioma.

An interesting, biocompatible and simple approach is to coat the nanoparticles with cationic polymers to enhance cellular penetration and prolong retention at biological membranes. Cationic nanoparticles are able to pass through biological membranes with facilitated uptake by cells, due to their strong cellular interaction with negatively charged biological membranes. Another important advantage is that they can mask the negative charge of anionic drugs to escape the mononuclear phagocytic system (MPS). Ionic particles can be easily determined by the MPS, therefore drug-loaded particles (which have neutral or near-neutral surface charge) are more prone to escape from the MPS. Cationic nanoparticles can also condense nucleic acid (DNA, RNA) or proteins to form polyplexes for intracellular gene/drug delivery. In this context, chitosan (CS) is used as a positively charged coating polymer with optimal results. CS, which is produced commercially by deacetylation of chitin, is a linear polysaccharide. It is a biocompatible and nontoxic natural polymer [33-39] which is known to act as a penetration enhancer, mucoadhesive [40], antitumor [41] and immune-adjuvant [42], which contribute to the potential of this biopolymer for drug delivery and formulation.

Although systemic application is frequently preferred for nanomedicines, local administration is a major opportunity when on-site therapy is possible and intended for. In fact, local or implantable administration for therapeutic nanoparticles help reduce systemic side effects, bypass BBB and improve efficacy of the drug by forming a constant drug reservoir directly at target site [43-49].

The goal of this study was to evaluate and characterize implantable cationic nanoparticle-loaded film formulations as post-surgical local delivery systems for docetaxel (DOC). PCL and its derivative poly(ethylene glycol)-block-poly(ε−caprolactone) methyl ether (mePEG-PCL) were used to prepare these nanoparticles by the nanoprecipitation technique with surface modification by coating with CS. The nanoparticles were administered as a dispersion in the hydroxypropylcellulose (HpC) Klucel™ bioadhesive film. The aim was to develop an implantable, local nanomedicine capable of prolonged release at the tumor site to create a drug reservoir after surgical removal of glioma, avoiding progression and recurrence of the tumor by killing cancer cells in surrounding tissues.

Results and Discussion

Pre-formulation studies

Pre-formulation studies were evaluated to select optimal nanoparticle formulations. Particle size, polydispersity index and surface charge are known to be critical parameters that significantly affect cellular uptake, interaction with biological membranes, absorption rate, biodistribution in the body, as well as the physical stability of the nanoparticles [50]. It is known that nanoparticles can escape from systemic circulation via fenestrations, which are small openings through the endothelial barrier. The size of these fenestrations depends on the type of organ and tumor [51]. For this reason, the nanoparticle particle size is crucial for a targeted organ/tumor.

As core–shell polymeric nanoparticles can be prepared using different techniques, the optimal preparation technique was determined to obtain smaller, monodisperse nanoparticles with favorable stability. Three different preparation techniques, emulsion/solvent evaporation, double emulsion and nanoprecipitation, were used to prepare PCL or mePEG-PCL nanoparticles.

As seen in Table 1, the mean diameter of PCL nanoparticles was found to be 160–350 nm. It was clearly shown that the preparation technique significantly affects the particle size ($p < 0.05$). In addition, the polydispersity index of the PCL

Table 1: The effect of different preparation methods on physicochemical properties of blank PCL and mePEG-PCL nanoparticles ($n = 3 \pm SD$).

		Mean diameter ± SD (nm)	PDI ± SD	Zeta potential ± SD (mV)
PCL nanoparticles	nanoprecipitation	168 ± 3	0.10 ± 0.02	−17 ± 0.4
	emulsification/solvent evaporation	184 ± 3	0.29 ± 0.4	−18 ± 0.8
	double emulsion	352 ± 2	0.39 ± 0.02	−8 ± 0.1
mePEG-PCL nanoparticles	nanoprecipitation	77 ± 3	0.17 ± 0.04	−13 ± 3.2
	emulsification/solvent evaporation	146 ± 3	0.27 ± 0.004	−19 ± 1.3
	double emulsion	170 ± 2	0.19 ± 0.01	−5 ± 0.24

nanoparticles also depends on the preparation technique, directly. Studies showed that PCL nanoparticles which were prepared by emulsion-based techniques have larger diameters, especially in the case of the double emulsification technique when compared to nanoprecipitation. These results shows compare well with the literature [52-55]. According to the data in Table 1, significantly smaller nanoparticles were obtained with mePEG-PCL ($p < 0.05$). The preparation method had a similar effect on mePEG-PCL nanoparticles as well.

The double emulsion method yielded the largest particle size and polydispersity index for blank PCL and mePEG-PCL nanoparticles. The double emulsion method involves two emulsification steps. For this reason, the particle size increases in each emulsification step. In addition, double emulsion resulted in a significant difference in the zeta potential of nanoparticles ($p < 0.05$). The surface charge of blank nanoparticles prepared by double emulsification was closer to neutral charge as compared to those prepared by the nanoprecipitation or emulsification/solvent evaporation methods.

Our results clearly show that mePEG-PCL nanoparticles have significantly smaller particle size than PCL nanoparticles for all preparation techniques ($p < 0.05$). In the literature, mePEG-PCL nanoparticles prepared by nanoprecipitation have been found to be generally smaller than 120 nm [53,56-58]; however, PCL nanoparticles prepared by the same technique are between 200–300 nm [55,59]. mePEG-PCL can be solubilized in organic solvents more easily, thanks to the hydrophilic PEG chains as compared to PCL. This difference may be effective for the spontaneous formation of nanoparticles at the interface and at obtaining a smaller particle size.

Another important parameter affecting the final nanoparticle properties is reported to be the presence and concentration of the surfactant, which can influence particle size distribution and surface properties. According to the results in Table 2, the addition of surfactant did not reduce the particle size; on the contrary, the mean particle size significantly increased proportional to the concentration of PF68 for both polymer PCL and mePEG-PCL ($p < 0.05$). Although it has been shown in literature that addition of surfactant causes increased solubility of polymer in aqueous media and decreases the particle size [60], the exact opposite of this situation has been found, too [61]. In our studies, the addition of surfactant for both nanoparticle formulations may have led to the formation of an extra surfactant layer and this layer increases the particle size. Besides that, this surfactant layer probably covered the polymer surface and thus the zeta potential of the nanoparticles approached a more neutral value.

To render a positive surface charge to blank PCL or mePEG-PCL nanoparticles, chitosan was incorporated as a cationic coating polymer. The mean particle size increased with increasing CS concentration, as can be expected due to the thicker coating layer (Table 3), as has been similarly demonstrated in the literature [62-65]. CS changed the surface charge from −19 to +39 mV and further to +53 mV by increasing the concentra-

Table 2: The effect of different preparation methods on the physicochemical properties of blank PCL and mePEG-PCL nanoparticles ($n = 3 \pm$ SD).

	PF68 concentration (v/v, %)	Mean diameter ± SD (nm)	PDI ± SD	Zeta potential ± SD (mV)
PCL nanoparticles	0	150 ± 0.5	0.08 ± 1.9	−22 ± 0.009
	0.5	163 ± 0.5	0.10 ± 0.5	−20 ± 0.02
	2	194 ± 0.8	0.09 ± 0.4	−15 ± 0.006
mePEG-PCL nanoparticles	0	71 ± 0.8	0.22 ± 0.004	−22 ± 1.9
	0.5	95 ± 3.9	0.50 ± 0.03	−27 ± 2.1
	2	92 ± 1.4	0.31 ± 0.04	−20 ± 3.8

Table 3: The effect of chitosan concentration on the physicochemical properties of blank PCL and mePEG-PCL nanoparticles ($n = 3 \pm$ SD).

	Chitosan concentration (wt/v, %)	Particle size ± SD (nm)	PDI ± SD	Zeta potential ± SD (mV)
PCL nanoparticles	0	170 ± 0.1	0.07 ± 0.02	−20 ± 0.6
	0.01	196 ± 14	0.25 ± 0.03	39 ± 0.9
	0.025	218 ± 9	0.20 ± 0.02	54 ± 1.9
mePEG-PCL nanoparticles	0	71 ± 0.8	0.22 ± 0.004	−22 ± 1.9
	0.01	120 ± 2	0.39 ± 0.006	31 ± 1.8
	0.025	155 ± 1.6	0.42 ± 0.02	31 ± 1.3

tion of CS in the PCL nanoparticle formulations. In addition, the surface charge of mePEG-PCL nanoparticles significantly increased up to 31 mV, depending on the CS concentration ($p < 0.05$), directly. Chitosan-modified core–shell nanoparticles were studied for glioma therapy by Qian et al. where a PLGA nanoparticle surface was modified with CS and cellular uptake of nanoparticles was determined. They showed that cellular uptake is related to chitosan concentration and particle size. According to their results, chitosan modification increased the particle size and decreased the cellular uptake of nanoparticles [66]. Cationic core–shell nanoparticles are also quite suitable for the delivery of negatively charged gene and drug to tumor tissue. Wei et al. used cationic core–shell nanoparticles for the active targeted delivery of siRNA on an intracranial U87 glioma model. They demonstrated that active targeted and cationic core–shell nanoparticles could be effective in inhibition of tumor proliferation with higher accumulation in tumor area when they are administered intravenously [67]. Different studies also showed that nanoparticles that have a zeta potential value smaller than 30 are more stable and show reduced aggregation [68,69].

In vitro characterization of docetaxel-loaded nanoparticles

According to the results of the pre-formulation studies, the final formulation parameters were determined and nanoparticles were prepared by the nanoprecipitation technique without surfactant due to their smaller particle size and polydispersity index. In order to render the surface charge positive, 0.01% wt/v chitosan was added to the aqueous phase. This concentration was selected since nanoparticles that have zeta potential outside the range of ±30 mV are known to be prone to aggregation [54,55]. For PCL nanoparticles, the drug amount was set at 10% of the PCL weight [60,63,70]. Therefore, DOC (0.01% w/v) was added in the organic phase with the polymer in the nanoprecipitation technique for both polymers. The particle size and zeta potential of nanoparticles for PCL or mePEG-PCL nanoparticles are shown in Figure 1 and Figure 2. CS coating and drug loading causes an increase in particle size, as expected. According to our results, the drug-loaded nanoparticle diameter is generally 10 to 50 nm higher than the unloaded nanoparticles.

Physical stability of nanoparticles

The physicochemical properties of all formulations have been monitored to investigate their physical stability in aqueous medium for 30 days; the results are shown in Figure 3. The diameter of anionic and cationic PCL nanoparticles increased by 8–10 nm and mePEG-PCL nanoparticles increased by 13–23 nm during this period. However, this increase is not statistically significant. Consequently, it can be said that aqueous dispersions of drug-loaded nanoparticles are physically stable for a period of 1 month.

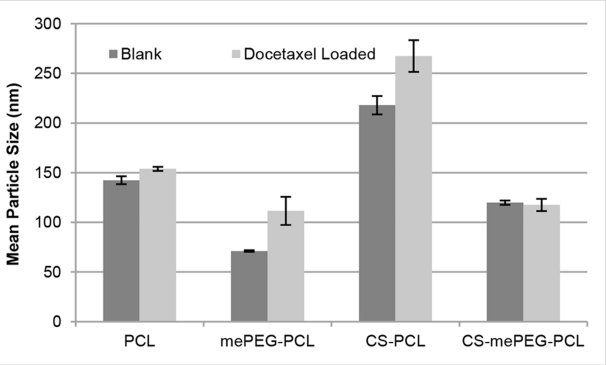

Figure 1: Particle size of blank and drug-loaded nanoparticles (n = 3, ± SD).

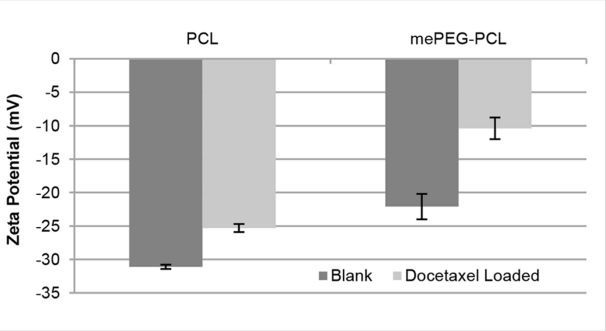

Figure 2: Zeta potential of blank and drug-loaded nanoparticles (n = 3, ± SD).

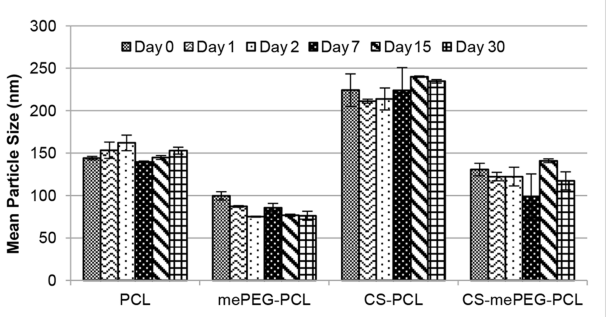

Figure 3: Mean particle diameter of nanoparticle formulations over the course of 30 days (n = 3, ± SD).

Encapsulation efficacy of drug-loaded nanoparticles

The docetaxel concentration in nanoparticle formulations was directly quantified with a validated HPLC method and expressed in terms of associated drug (%). In the literature, the encapsulation efficacy for PCL nanoparticles was found to be between 65−71% [60,70] and for mePEG-PCL nanoparticles to be 80−90% [56,58]. According to our results, the encapsulation efficacy of mePEG-PCL nanoparticles was not found to be as

high as reported in the literature. This may be caused by the differences in the molecular weight of the PCL used in mePEG-PCL.

The zeta potential of DOC solutions was measured as −14 mV and the encapsulation efficacy was significantly improved for both PCL and mePEG-PCL nanoparticles by coating with the cationic polymer CS, as shown in Figure 4. This is attributed to the strong electrostatic interaction between the anionic drug docetaxel with the cationic coating. The encapsulation efficacy of PCL and mePEG-PCL nanoparticles is not significantly different from one other ($p > 0.05$) but CS-coated mePEG-PCL nanoparticles have the largest encapsulation efficacy ($p < 0.05$). The mePEG-PCL polymer is more hydrophilic than PCL, as previously mentioned, and this property may be effective for the high encapsulation efficacy as well as smaller particle size as shown in the literature [56,58].

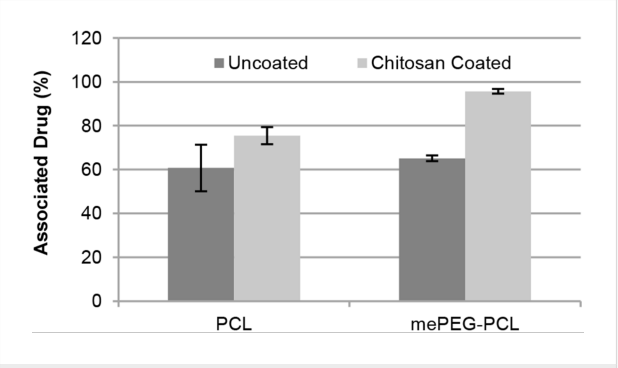

Figure 4: Docetaxel encapsulation efficiency of nanoparticle formulations (n = 3, ± SD).

In vitro release studies

The in vitro release profile of docetaxel from nanoparticle dispersion and nanoparticle-loaded HpC films was determined using the dialysis bag method in PBS pH 7.4 with HPLC. As seen in Figure 5, DOC was completely released from all nanoparticles within 1 h. The PCL nanoparticles are generally expected to give a longer release time due to slower degradation time of PCL [56,58,60] if the drug is entrapped in a nanoparticle matrix. In our study, it is suggested by the encapsulation data shown in Figure 4 that DOC is largely adsorbed onto the coating layer and therefore released rapidly by desorption of the drug from the nanoparticle surface. The slower release was achieved by loading the DOC nanoparticles into a HpC film. By examining the release profiles of DOC from nanoparticle-loaded HpC film, it can be seen that 50% DOC was released in the first 16 h and complete release of the encapsulated drug was found to occur after 48 h with a slower rate (Figure 5). The structure of the HpC film may be effective in slowing the release. The release of water-insoluble drugs from HpC films was examined by different study groups and the release profile was shown to be completed within approximately 10 h [71-73]. In another study regarding the release of paclitaxel (which is another member of taxane class, such as docetaxel, released from nanocomposite film) the initial release was observed within 7 h due to the rapid release of drugs from surface of the film [74]. Our studies proved that the DOC-encapsulated PCL-nanoparticle-loaded film formulation is quite suitable to provide a drug reservoir after surgical removal of glioma to avoid progression recurrence during the first 2 days.

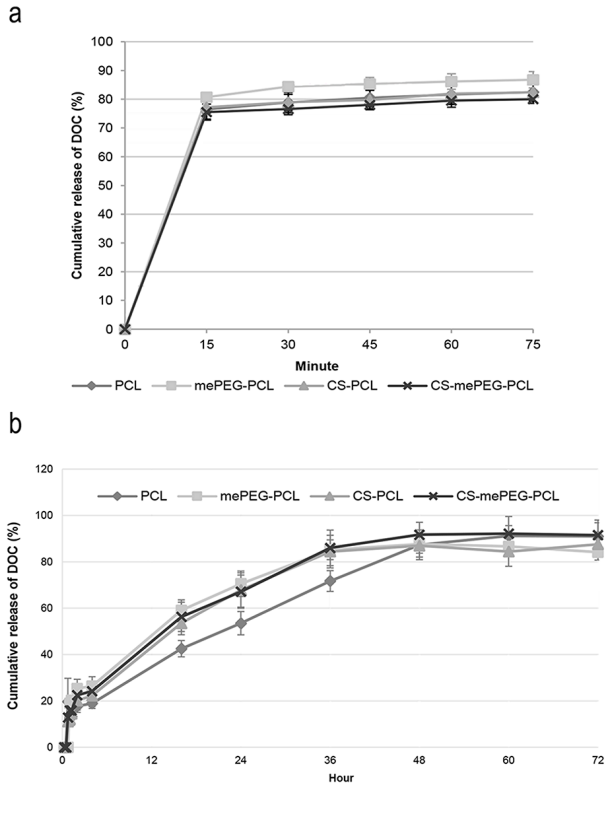

Figure 5: Cumulative release profile of DOC from nanoparticles (a) and nanoparticulate DOC from HpC films (b) (n = 3, ± SD).

Cell culture studies

Cytotoxicity assay for blank nanoparticles

Mouse fibroblast cell lines L929 (recommended by the USP for the cytotoxicity evaluation of polymeric systems) were used to determine the cytotoxicity of blank nanoparticles with MTT assay. According to MTT assay, cell viability for L929 cells is given in Figure 6 for 24 h and 48 h. When compared with the control group, the blank formulations were found to have no cytotoxic effect on L929 fibroblast cells (the differences between groups were statistically insignificant, $p > 0.05$), and it can be suggested that all formulations are safe for in vivo application, regardless of dose or time.

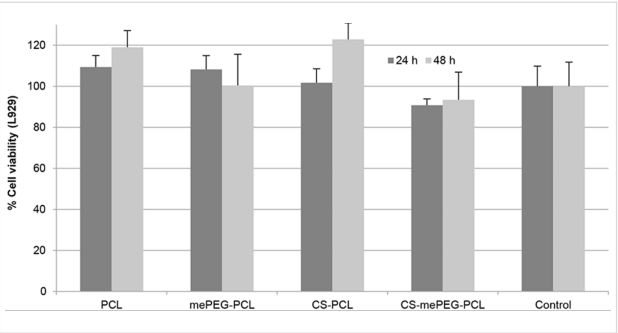

Figure 6: Cell viability of blank nanoparticles for 24 and 48 h (n = 3, ± SD).

Anticancer efficacy of docetaxel-loaded nanoparticles

The anticancer efficacy of drug-loaded nanoparticle dispersions were determined on rat glioma cell line RG2. As seen in Figure 7, anticancer efficiency is enhanced for DOC both with time-dependent and formulation-dependent mechanisms. The cell culture data showed that DOC-loaded CS-mePEG-PCL nanoparticle dispersions have a significantly higher cytotoxic effect than DOC solutions in DMSO ($p < 0.05$). Besides, blank nanoparticle formulations did not exert any toxic effect on RG2 cells. As a result, CS-coated nanoparticle formulations were found to be significantly more effective against glioma cells than nanoparticles that have negative surface charge ($p < 0.05$). Cationic nanoparticles may interact and pass the cell membrane more easily due to their opposite electrical charge with respect to the cell surface. On the other hand, it is known that chitosan also possesses intrinsic antitumor activity due to activation of the caspase-3 mechanism [41]. This may explain the synergistic mechanism of why chitosan-coated nanoparticles are more effective on cancer cells when compared with non-coated nanoparticles.

Conclusion

In this study, the anticancer drug DOC, encapsulated in anionic and cationic polymeric nanoparticles and administered in a bioadhesive film formulation, was successfully developed to apply the chemotherapeutic drug directly to the action site after surgical operation of glioma treatment. All formulations were characterized in terms of mean particle size, polydispersity index, zeta potential, drug loading capacity, drug release profile and cytotoxicity. When nanoparticle formulations are compared with each other, mePEG-PCL nanoparticles have a significantly smaller particle size. Furthermore, drug loading and anticancer efficacy in rat glioma cells were drastically increased by cationic coated with CS. Thus, mePEG-PCL and CS-coated mePEG-PCL nanoparticle formulations can be used for further studies. Moreover, the release profile was prolonged by up to 2 days due to the implantable film formulation. This result could be a solution to the premature drug release and dose dumping known to occur with the use of nanoparticles. In the light of the cell culture data, all nanoparticle formulations increased the anticancer effects of DOC in free form, while blank nanoparticles were found to be nontoxic on L929 and RG-2 cell lines. It can be said that all drug-loaded nanoparticles are biocompatible, safe and effective against glioma.

Our study emphasizes that polycaprolactone and PEGylated derivatives are suitable for the development of nanoparticles and their zeta potential can be varied with chitosan coating. When

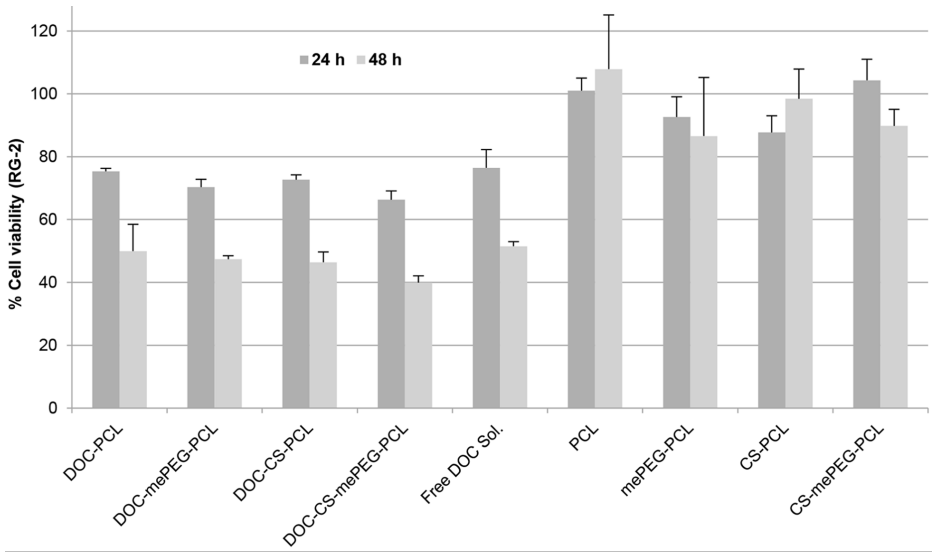

Figure 7: RG2 cell viability with blank and DOC-loaded nanoparticles for 24 and 48 h (n = 3, ± SD).

further loaded into films, these nanoparticles seem to be a potential drug delivery system for docetaxel for glioma treatment and a good candidate for further evaluation in animal studies. This film formulation can be implanted after surgical removal of a tumor and provide a drug reservoir after surgical removal of glioma during the initial days to avoid progression and recurrence by killing cancer cells in neighboring tissue.

Experimental

Materials

PCL (M_W: 80,000 Da) and mePEG-PCL (PEG:PCL M_W: 5,000:5,000 Da) were purchased from Sigma-Aldrich, USA. Chitosan (Protasan® G 113, M_W < 200 kDa, deacetylation degree 75–90%) was purchased from FMC Biopolymers, Norway. HpC (Klucel™ hydroxypropylcellulose) was purchased from Ashland, USA. The model anticancer drug, docetaxel (purity 97%), was purchased from Fluka, Switzerland. Dialysis tubing cellulose membrane (average flat width 25 mm, MWCO: 14,000 Da) and all organic solvents and chemicals were purchased from Sigma-Aldrich, Germany. Ultrapure water was obtained from a Millipore Simplicity 185 ultrapure water system, France and used without further purification.

Methods

Pre-formulation studies

Pre-formulation studies were carried out to optimize the final nanoparticle physical properties. The formulation and technological variables that are known to influence the nanoparticle properties were evaluated. Primarily, different nanoparticle preparation techniques were used to prepare the nanoparticles, which was then followed by varying formulation parameters such as surfactant concentration and coating polymer concentration, as summarized in Table 4.

Table 4: Pre-formulation parameters for nanoparticle preparation.

preparation technique	nanoprecipitation
	emulsion/solvent evaporation
	double emulsion
polymer molecular weight (Da)	mePEG-PCL (M_W: 5000:5000)
	PCL (M_W: 80,000)
surfactant (PF68) concentration (% v/v)	0
	0.5
	2
coating polymer chitosan amount (% w/v)	0
	0.01
	0.025

As different preparation techniques drastically affect the nanoparticle size and degree of drug interaction, several well-established nanoparticle preparation methods were evaluated for PCL and mePEG-PCL nanoparticles. These preparation methods can briefly be summarized as follows.

Nanoprecipitation: The polymer (PCL or MePEG-PCL) was dissolved in acetone (0.1% v/w) under moderate heating. This organic solution was added to ultrapure water (1:2 v/v) dropwise under magnetic stirring at room temperature. As a result, nanoparticles were spontaneously obtained. The organic solvent was then evaporated under vacuum at 40 °C. The formulations were filtered through a 0.45 μm pore membrane filter to eliminate polymer aggregates. Cationic-coated nanoparticles were obtained with the same technique with the minor difference that CS was dissolved in ultrapure water to form the aqueous phase during preparation.

Emulsion solvent/evaporation: The polymer (PCL or MePEG-PCL) was dissolved in dichloromethane (0.1% v/w) under magnetic stirring. This organic phase (5 mL) was added to ultrapure water (20 mL) containing PF68 (1% v/w) and polyvinyl alcohol (0.1% v/w) and emulsified by ultraturrax at 13,000 rpm. The organic solvent was evaporated under vacuum at 40 °C. The formulations were filtered through a 0.45 μm pore filter to eliminate polymer aggregates.

Double emulsion: PF68 (1% w/v) was dissolved in ultrapure water (1 mL) and the polymer (PCL or MePEG-PCL) (0.5% w/v) was dissolved in dichloromethane (5 mL) under magnetic stirring. Ultrapure water containing PF68 (1% w/v) was added to the organic solution containing polymer. This mix was emulsified by ultraturrax at 13,000 rpm. This primary emulsion was added to 20 mL ultrapure water containing PF68 (1% w/v) and polyvinyl alcohol (0.1% w/v) and emulsified by ultraturrax at 13,000 rpm. The organic solvent was evaporated under vacuum at 40 °C. The formulations were filtered through a 0.45 μm pore sized filter to eliminate polymer aggregates.

Preparation of nanoparticle-loaded film formulations

Following the selection of optimal nanoparticle formulations, docetaxel-loaded nanoparticles were loaded into film formulations to prolong the activity of the nanoparticles at the administration site. Briefly, HpC (Klucel™) was dissolved in ultrapure water (5% w/v). The lyophilized nanoparticle powder was added to this mix and stirred. This solution was slowly poured on a water-impermeable polyethylene terephthalate (PET) film and dried at room temperature for 48 h. Finally, the HpC film was removed from the surface of the PET film to obtain the final product.

Nanoparticle characterization

Particle size distribution and surface charge analysis: the mean particle diameter and polydispersity index of the nanoparticles

were determined by dynamic light scattering (DLS) technique using a Malvern NanoZS (Malvern Instruments, UK). All formulations were measured at a scattering angle of 173° at a temperature 25 °C (n = 3). The surface charge of the nanoparticles was determined by using a disposable capillary cell with the Malvern Zetasizer Nano ZS at room temperature (n = 3).

Physical stability upon storage: The physical stability of the nanoparticles was determined by repeated measurement and comparison of the particle size, polydispersity index and zeta potential data for 30 days at specific time intervals. During this time, the formulations were stored as aqueous dispersions in ultrapure water at +4 °C.

Encapsulation efficiency: DOC encapsulation of nanoparticle formulations were determined directly with validated HPLC method by using an HP Agilent 1100 instrument. The HPLC system consisted of a reverse phase Develosil ODS-UG-5 (4.6 mm/150 mm 5.6 µm) column and acetonitrile/water (50:50 v/v) as mobile phase delivered at a flow rate of 1.00 mL/min. A 50 µL injection volume was used for analysis. The DOC was quantified by a UV detector set at λ = 229.6 nm at 25 °C. Drug loading was expressed as associated drug percentage, quantifying the drug quantity bound to nanoparticles. The associated drug percentage (%) was calculated as follows:

$$\text{Associated drug (\%)} = \frac{\text{Experimental drug loading (µg)}}{\text{Initial drug quantity (µg)}} \times 100$$

In vitro docetaxel release: The in vitro release profile of DOC from nanoparticles and film formulations was determined by using the dialysis membrane technique under sink conditions in a shaking water bath at 37 °C in phosphate buffer solution (PBS) pH 7.4. Briefly, the drug-loaded nanoparticle dispersions or 1 cm^2 film were added in dialysis membrane (Cellulose Membrane MWCO: 14,000 Da, Sigma-Aldrich, Germany) and closed with stoppers. This bag was placed in PBS pH 7.4 containing 0.1% Tween 80 to provide sink conditions. Samples were taken from the PBS at specific time intervals and the released DOC amount was determined directly with validated HPLC method.

Cell culture studies

Cytotoxicity assay for blank nanoparticles and drug-loaded nanoparticles: Mouse fibroblast cells L929 were used to determine the cytotoxicity of blank nanoparticles as this is defined as a standard method for cytotoxicity determination by United States Pharmacopoeia. After the cytotoxicity testing of blank nanoparticles, rat glioma cells RG2 were used to determine the anticancer activity of docetaxel (500 nM) incorporated nanoparticles. The cell lines were cultured as a monolayer in Dulbecco's modified Eagle's medium (DMEM) supplemented with 10% fetal bovine serum (FBS), penicillin (100 units/mL) and streptomycin (100 µg/mL) and maintained at 37 °C in a humidified 5% CO_2 incubator. The cells were seeded in 96-well tissue culture and incubated for 24 and 48 h. Then, DMEM was replaced with fresh medium containing blank nanoparticle formulations and incubated for 48 h. MTT assay was applied to determine cell viability. 20 µL of MTT solution in PBS (5 mg/mL) were added in each well and incubated for 4 h. 80 µL of MTT lysis solution containing SDS (23% w/v) and DMF (45% v/v) in ultrapure water were added in plates and incubated overnight. The optical density (OD) was determined by a microplate reader (Molecular Devices, USA) at 450 nm (n = 3). The results were expressed in terms of cell viability (%) according to the equation:

$$\text{Cell Viability (\%)} = \frac{\text{Mean Absorbance of Treated Cells}}{\text{Mean Absorbance of non-Treated Cells}} \times 100.$$

Statistical analysis

All statistical analyses were performed by Student's t-test. $p < 0.05$ was considered to denote a statistically significant difference.

References

1. Siegel, R. L.; Miller, K. D.; Jemal, A. *Ca-Cancer J. Clin.* **2017,** *67,* 7–30. doi:10.3322/caac.21387
2. DeAngelis, L. M. *N. Engl. J. Med.* **2001,** *344,* 114–123. doi:10.1056/NEJM200101113440207
3. Ali-Osman, F. *Brain tumors;* Humana Press: Totowa, NJ, U.S.A., 2005. doi:10.1385/1592598439
4. Tomita, T. *J. Neuro-Oncol.* **1991,** *10,* 57–74. doi:10.1007/BF00151247
5. Pardridge, W. M. *J. Cereb. Blood Flow Metab.* **1997,** *17,* 713–731. doi:10.1097/00004647-199707000-00001
6. Groothuis, D. R. *Neuro-Oncology (Cary, NC, U. S.)* **2000,** *2,* 45–59. doi:10.1093/neuonc/2.1.45
7. Lesniak, M. S.; Langer, R.; Brem, H. *Curr. Neurol. Neurosci. Rep.* **2001,** *1,* 210–216. doi:10.1007/s11910-001-0020-z
8. Ballabh, P.; Braun, A.; Nedergaard, M. *Neurobiol. Dis.* **2004,** *16,* 1–13. doi:10.1016/j.nbd.2003.12.016
9. Pardridge, W. M. *Pharm. Res.* **2007,** *24,* 1733–1744. doi:10.1007/s11095-007-9324-2
10. Guenard, D.; Gueritte-Voegelein, F.; Potier, P. *Acc. Chem. Res.* **1993,** *26,* 160–167. doi:10.1021/ar00028a005
11. Sampath, P.; Rhines, L. D.; DiMeco, F.; Tyler, B. M.; Park, M. C.; Brem, H. *J. Neuro-Oncol.* **2006,** *80,* 9–17. doi:10.1007/s11060-006-9159-4
12. Baker, J.; Ajani, J.; Scotté, F.; Winther, D.; Martin, M.; Aapro, M. S.; von Minckwitz, G. *Eur. J. Oncol. Nurs.* **2009,** *13,* 49–59. doi:10.1016/j.ejon.2008.10.003
13. Moes, J.; Koolen, S.; Huitema, A.; Schellens, J.; Beijnen, J.; Nuijen, B. *Eur. J. Pharm. Biopharm.* **2013,** *83,* 87–94. doi:10.1016/j.ejpb.2012.09.016

14. Soppimath, K. S.; Aminabhavi, T. M.; Kulkarni, A. R.; Rudzinski, W. E. *J. Controlled Release* **2001,** *70,* 1–20. doi:10.1016/S0168-3659(00)00339-4
15. Brigger, I.; Dubernet, C.; Couvreur, P. *Adv. Drug Delivery Rev.* **2002,** *54,* 631–651. doi:10.1016/S0169-409X(02)00044-3
16. Kingsley, J. D.; Dou, H.; Morehead, J.; Rabinow, B.; Gendelman, H. E.; Destache, C. J. *J. Neuroimmune Pharmacol.* **2006,** *1,* 340–350. doi:10.1007/s11481-006-9032-4
17. Bei, D.; Meng, J.; Youan, B.-B. C. *Nanomedicine (London, U. K.)* **2010,** *5,* 1385–1399. doi:10.2217/nnm.10.117
18. Sinha, V. R.; Bansal, K.; Kaushik, R.; Kumria, R.; Trehan, A. *Int. J. Pharm.* **2004,** *278,* 1–23. doi:10.1016/j.ijpharm.2004.01.044
19. Woodruff, M. A.; Hutmacher, D. W. *Prog. Polym. Sci.* **2010,** *35,* 1217–1256. doi:10.1016/j.progpolymsci.2010.04.002
20. Gad, S. C., Ed. *Pharmaceutical manufacturing handbook: production and processes;* Wiley-Interscience: Hoboken, NJ, U.S.A., 2008.
21. Schubert, S.; Delaney, J. T., Jr.; Schubert, U. S. *Soft Matter* **2011,** *7,* 1581–1588. doi:10.1039/C0SM00862A
22. Gao, H.; Qian, J.; Yang, Z.; Pang, Z.; Xi, Z.; Cao, S.; Wang, Y.; Pan, S.; Zhang, S.; Wang, W.; Jiang, X.; Zhang, Q. *Biomaterials* **2012,** *33,* 6264–6272. doi:10.1016/j.biomaterials.2012.05.020
23. Ungaro, F.; Conte, C.; Ostacolo, L.; Maglio, G.; Barbieri, A.; Arra, C.; Misso, G.; Abbruzzese, A.; Caraglia, M.; Quaglia, F. *Nanomedicine* **2012,** *8,* 637–646. doi:10.1016/j.nano.2011.08.012
24. Zamora, G.; Wang, F.; Sun, C.-H.; Trinidad, A.; Kwon, Y. J.; Cho, S. K.; Berg, K.; Madsen, S. J.; Hirschberg, H. *J. Biomed. Opt.* **2014,** *19,* 105009. doi:10.1117/1.JBO.19.10.105009
25. Wang, H.; Su, W.; Wang, S.; Wang, X.; Liao, Z.; Kang, C.; Han, L.; Chang, J.; Wang, G.; Pu, P. *Nanoscale* **2012,** *4,* 6501–6508. doi:10.1039/c2nr31263h
26. Fang, J.-H.; Lai, Y.-H.; Chiu, T.-L.; Chen, Y.-Y.; Hu, S.-H.; Chen, S.-Y. *Adv. Healthcare Mater.* **2014,** *3,* 1250–1260. doi:10.1002/adhm.201300598
27. Yang, H.-W.; Hua, M.-Y.; Liu, H.-L.; Huang, C.-Y.; Tsai, R.-Y.; Lu, Y.-J.; Chen, J.-Y.; Tang, H.-J.; Hsien, H.-Y.; Chang, Y.-S.; Yen, T.-C.; Chen, P.-Y.; Wei, K.-C. *Biomaterials* **2011,** *32,* 6523–6532. doi:10.1016/j.biomaterials.2011.05.047
28. Yang, L.; Shao, B.; Zhang, X.; Cheng, Q.; Lin, T.; Liu, E. *J. Biomater. Appl.* **2016,** *31,* 400–410. doi:10.1177/0885328216658779
29. Durgadas, C. V.; Sreenivasan, K.; Sharma, C. P. *Biomaterials* **2012,** *33,* 6420–6429. doi:10.1016/j.biomaterials.2012.05.051
30. Slegerova, J.; Hajek, M.; Rehor, I.; Sedlak, F.; Stursa, J.; Hruby, M.; Cigler, P. *Nanoscale* **2015,** *7,* 415–420. doi:10.1039/C4NR02776K
31. Wang, G.; Ji, J.; Zhang, X.; Zhang, Y.; Wang, Q.; You, X.; Xu, X. *Sci. Rep.* **2014,** *4,* 5480. doi:10.1038/srep05480
32. Yu, F.; Zhang, L.; Huang, Y.; Sun, K.; David, A. E.; Yang, V. C. *Biomaterials* **2010,** *31,* 5842–5848. doi:10.1016/j.biomaterials.2010.03.072
33. Felt, O.; Buri, P.; Gurny, R. *Drug Dev. Ind. Pharm.* **1998,** *24,* 979–993. doi:10.3109/03639049809089942
34. Dutta, P. K.; Dutta, J.; Tripathi, V. S. *J. Sci. Ind. Res.* **2004,** *63,* 20–31.
35. Sinha, V. R.; Singla, A. K.; Wadhawan, S.; Kaushik, R.; Kumria, R.; Bansal, K.; Dhawan, S. *Int. J. Pharm.* **2004,** *274,* 1–33. doi:10.1016/j.ijpharm.2003.12.026
36. Rinaudo, M. *Prog. Polym. Sci.* **2006,** *31,* 603–632. doi:10.1016/j.progpolymsci.2006.06.001
37. Nagpal, K.; Singh, S. K.; Mishra, D. N. *Chem. Pharm. Bull.* **2010,** *58,* 1423–1430. doi:10.1248/cpb.58.1423
38. Dash, M.; Chiellini, F.; Ottenbrite, R. M.; Chiellini, E. *Prog. Polym. Sci.* **2011,** *36,* 981–1014. doi:10.1016/j.progpolymsci.2011.02.001
39. Wang, J. J.; Zeng, Z. W.; Xiao, R. Z.; Xie, T.; Zhou, G. L.; Zhan, X. R.; Wang, S. L. *Int. J. Nanomed.* **2011,** *6,* 765–774. doi:10.2147/IJN.S17296
40. Agnihotri, S. A.; Mallikarjuna, N. N.; Aminabhavi, T. M. *J. Controlled Release* **2004,** *100,* 5–28. doi:10.1016/j.jconrel.2004.08.010
41. Hasegawa, M.; Yagi, K.; Iwakawa, S.; Hirai, M. *Jpn. J. Cancer Res.* **2001,** *92,* 459–466. doi:10.1111/j.1349-7006.2001.tb01116.x
42. Seferian, P. G.; Martinez, M. L. *Vaccine* **2000,** *19,* 661–668. doi:10.1016/S0264-410X(00)00248-6
43. Fleming, A. B.; Saltzman, W. M. *Clin. Pharmacokinet.* **2002,** *41,* 403–419. doi:10.2165/00003088-200241060-00002
44. Wang, P. P.; Frazier, J.; Brem, H. *Adv. Drug Delivery Rev.* **2002,** *54,* 987–1013. doi:10.1016/S0169-409X(02)00054-6
45. Garcia-Garcia, E.; Andrieux, K.; Gil, S.; Couvreur, P. *Int. J. Pharm.* **2005,** *298,* 274–292. doi:10.1016/j.ijpharm.2005.03.031
46. Koo, Y.-E. L.; Reddy, G. R.; Bhojani, M.; Schneider, R.; Philbert, M. A.; Rehemtulla, A.; Ross, B. D.; Kopelman, R. *Adv. Drug Delivery Rev.* **2006,** *58,* 1556–1577. doi:10.1016/j.addr.2006.09.012
47. Dyke, J. P.; Sanelli, P. C.; Voss, H. U.; Serventi, J. V.; Stieg, P. E.; Schwartz, T. H.; Ballon, D.; Shungu, D. C.; Pannullo, S. C. *J. Neuro-Oncol.* **2007,** *82,* 103–110. doi:10.1007/s11060-006-9254-6
48. Neuwelt, E.; Abbott, N. J.; Abrey, L.; Banks, W. A.; Blakley, B.; Davis, T.; Engelhardt, B.; Grammas, P.; Nedergaard, M.; Nutt, J.; Pardridge, W.; Rosenberg, G. A.; Smith, Q.; Drewes, L. R. *Lancet Neurol.* **2008,** *7,* 84–96. doi:10.1016/S1474-4422(07)70326-5
49. Wolinsky, J. B.; Colson, Y. L.; Grinstaff, M. W. *J. Controlled Release* **2012,** *159,* 14–26. doi:10.1016/j.jconrel.2011.11.031
50. Duan, X.; Li, Y. *Small* **2013,** *9,* 1521–1532. doi:10.1002/smll.201201390
51. Gaumet, M.; Vargas, A.; Gurny, R.; Delie, F. *Eur. J. Pharm. Biopharm.* **2008,** *69,* 1–9. doi:10.1016/j.ejpb.2007.08.001
52. Blouza, I. L.; Charcosset, C.; Sfar, S.; Fessi, H. *Int. J. Pharm.* **2006,** *325,* 124–131. doi:10.1016/j.ijpharm.2006.06.022
53. Zheng, D.; Li, X.; Xu, H.; Lu, X.; Hu, Y.; Fan, W. *Acta Biochim. Biophys. Sin.* **2009,** *41,* 578–587. doi:10.1093/abbs/gmp045
54. Mora-Huertas, C. E.; Fessi, H.; Elaissari, A. *Int. J. Pharm.* **2010,** *385,* 113–142. doi:10.1016/j.ijpharm.2009.10.018
55. Çırpanlı, Y.; Allard, E.; Passirani, C.; Bilensoy, E.; Lemaire, L.; Çalış, S.; Benoit, J.-P. *Int. J. Pharm.* **2011,** *403,* 201–206. doi:10.1016/j.ijpharm.2010.10.015
56. Zheng, D.; Li, D.; Lu, X.; Feng, Z. *Oncol. Rep.* **2010,** *23,* 717–724. doi:10.3892/or_00000689
57. Shao, J.; Zheng, D.; Jiang, Z.; Xu, H.; Hu, Y.; Li, X.; Lu, X. *Acta Biochim. Biophys. Sin.* **2011,** *43,* 267–274. doi:10.1093/abbs/gmr011
58. Liu, Q.; Li, R.; Zhu, Z.; Qian, X.; Guan, W.; Yu, L.; Yang, M.; Jiang, X.; Liu, B. *Int. J. Pharm.* **2012,** *430,* 350–358. doi:10.1016/j.ijpharm.2012.04.008
59. Leroueil-Le Verger, M.; Fluckiger, L.; Kim, Y.-I.; Hoffman, M.; Maincent, P. *Eur. J. Pharm. Biopharm.* **1998,** *46,* 137–143. doi:10.1016/S0939-6411(98)00015-0
60. Mei, L.; Zhang, Y.; Zheng, Y.; Tian, G.; Song, C.; Yang, D.; Chen, H.; Sun, H.; Tian, Y.; Liu, K.; Li, Z.; Huang, L. *Nanoscale Res. Lett.* **2009,** *4,* 1530–1539. doi:10.1007/s11671-009-9431-6
61. Boehm, A. L. L.; Zerrouk, R.; Fessi, H. *J. Microencapsulation* **2000,** *17,* 195–205. doi:10.1080/026520400288436
62. Erdoğar, N.; Mungan, A.; Bilensoy, E. *J. Controlled Release* **2010,** *148,* E78–E79. doi:10.1016/j.jconrel.2010.07.015

63. Erdoğar, N.; Iskit, A. B.; Mungan, N. A.; Bilensoy, E. *J. Microencapsulation* **2012,** *29,* 576–582. doi:10.3109/02652048.2012.668957
64. Mazzarino, L.; Travelet, C.; Ortega-Murillo, S.; Otsuka, I.; Pignot-Paintrand, I.; Lemos-Senna, E.; Borsali, R. *J. Colloid Interface Sci.* **2012,** *370,* 58–66. doi:10.1016/j.jcis.2011.12.063
65. Bilensoy, E.; Sarisozen, C.; Esendağlı, G.; Doğan, A. L.; Aktaş, Y.; Şen, M.; Mungan, N. A. *Int. J. Pharm.* **2009,** *371,* 170–176. doi:10.1016/j.ijpharm.2008.12.015
66. Qian, L.; Zheng, J.; Wang, K.; Tang, Y.; Zhang, X.; Zhang, H.; Huang, F.; Pei, Y.; Jiang, Y. *Biomaterials* **2013,** *34,* 8968–8978. doi:10.1016/j.biomaterials.2013.07.097
67. Wei, L.; Guo, X.-Y.; Yang, T.; Yu, M.-Z.; Chen, D.-W.; Wang, J.-C. *Int. J. Pharm.* **2016,** *510,* 394–405. doi:10.1016/j.ijpharm.2016.06.127
68. Müller, R. H.; Jacobs, C.; Kayser, O. *Adv. Drug Delivery Rev.* **2001,** *47,* 3–19. doi:10.1016/S0169-409X(00)00118-6
69. Hans, M. L.; Lowman, A. M. *Curr. Opin. Solid State Mater. Sci.* **2002,** *6,* 319–327. doi:10.1016/S1359-0286(02)00117-1
70. Ma, Y.; Zheng, Y.; Zeng, X.; Jiang, L.; Chen, H.; Liu, R.; Huang, L.; Mei, L. *Int. J. Nanomed.* **2011,** *6,* 2679–2688. doi:10.2147/IJN.S25251
71. Trey, S. M.; Wicks, D. A.; Mididoddi, P. K.; Repka, M. A. *Drug Dev. Ind. Pharm.* **2007,** *33,* 727–735. doi:10.1080/03639040701199225
72. Chen, M.; Lu, J.; Deng, W.; Singh, A.; Mohammed, N. N.; Repka, M. A.; Wu, C. *AAPS PharmSciTech* **2014,** *15,* 522–529. doi:10.1208/s12249-013-0029-z
73. Repka, M. A.; Prodduturi, S.; Stodghill, S. P. *Drug Dev. Ind. Pharm.* **2003,** *29,* 757–765. doi:10.1081/DDC-120021775
74. Srinivasa Rao, S.; Rajiv, S. *Polym.-Plast. Technol. Eng.* **2014,** *53,* 1690–1696. doi:10.1080/03602559.2014.919654

License and Terms

BEILSTEIN JOURNAL OF NANOTECHNOLOGY

Development of polycationic amphiphilic cyclodextrin nanoparticles for anticancer drug delivery

Gamze Varan[1], Juan M. Benito[2], Carmen Ortiz Mellet[3] and Erem Bilensoy[*1,4]

Full Research Paper

Open Access

Address:
[1]Department of Nanotechnology and Nanomedicine, Graduate School of Science and Engineering, Hacettepe University, Ankara, 06800, Turkey, [2]Institute for Chemical Research, CSIC - University of Sevilla, Av. Américo Vespucio 49, Sevilla, 41092, Spain, [3]Department of Organic Chemistry, University of Sevilla, C/ Prof García Gonzalez 1, Sevilla, 41012, Spain and [4]Department of Pharmaceutical Technology, Faculty of Pharmacy, Hacettepe University, Ankara, 06100, Turkey

Email:
Erem Bilensoy[*] - eremino@hacettepe.edu.tr

* Corresponding author

Keywords:
amphiphilic cyclodextrin; anticancer; nanoparticle; paclitaxel; polycationic

Beilstein J. Nanotechnol. **2017,** *8,* 1457–1468.
doi:10.3762/bjnano.8.145

Received: 30 March 2017
Accepted: 14 June 2017
Published: 13 July 2017

This article is part of the Thematic Series "Nanomaterial-based cancer theranostics".

Guest Editor: V. Sivakov

Abstract

Background: Paclitaxel is a potent anticancer drug that is effective against a wide spectrum of cancers. To overcome its bioavailability problems arising from very poor aqueous solubility and tendency to recrystallize upon dilution, paclitaxel is commercially formulated with co-solvents such as Cremophor EL® that are known to cause serious side effects during chemotherapy. Amphiphilic cyclodextrins are favored oligosaccharides as drug delivery systems for anticancer drugs, having the ability to spontaneously form nanoparticles without surfactant or co-solvents. In the past few years, polycationic, amphiphilic cyclodextrins were introduced as effective agents for gene delivery in the form of nanoplexes. In this study, the potential of polycationic, amphiphilic cyclodextrin nanoparticles were evaluated in comparison to non-ionic amphiphilic cyclodextrins and core–shell type cyclodextrin nanoparticles for paclitaxel delivery to breast tumors. Pre-formulation studies were used as a basis for selecting the suitable organic solvent and surfactant concentration for the novel polycationic cyclodextrin nanoparticles. The nanoparticles were then extensively characterized with particle size distribution, polydispersity index, zeta potential, drug loading capacity, in vitro release profiles and cytotoxicity studies.

Results: Paclitaxel-loaded cyclodextrin nanoparticles were obtained in the diameter range of 80−125 nm (depending on the nature of the cyclodextrin derivative) where the smallest diameter nanoparticles were obtained with polycationic (PC) βCDC6. A strong positive charge also helped to increase the loading capacity of the nanoparticles with paclitaxel up to 60%. Interestingly, cyclodextrin nanoparticles were able to stabilize paclitaxel in aqueous solution for 30 days. All blank cyclodextrin nanoparticles were demonstrated to be non-cytotoxic against L929 mouse fibroblast cell line. In addition, paclitaxel-loaded nanoparticles have a significant anticancer effect against MCF-7 human breast cancer cell line as compared with a paclitaxel solution in DMSO.

Conclusion: According to the results of this study, both amphiphilic cyclodextrin derivatives provide suitable nanometer-sized drug delivery systems for safe and efficient intravenous paclitaxel delivery for chemotherapy. In the light of these studies, it can be said that amphiphilic cyclodextrin nanoparticles of different surface charge can be considered as a promising alternative for self-assembled nanometer-sized drug carrier systems for safe and efficient chemotherapy.

Introduction

Paclitaxel (PCX) is an effective wide-spectrum anticancer agent which is isolated from the bark of the tree *Taxus brevifolia* and further obtained semi-synthetically [1]. Its unique antimitotic mechanism depends on inducing the microtubule stabilization and inhibiting the depolymerization of microtubules [2]. PCX binds to N-terminal 31 amino acids of the β-tubulin proteins in microtubules and stabilizes (instead of inhibiting) microtubule assembly to prevent cell division. On the other hand, PCX causes cells to remain in G2/M phase. Microtubules formed by the action of PCX are also dysfunctional and cause cell death [3]. In spite of its promising antitumor activity, the drug has presented considerable difficulties related to its intravenous administration to patients. The most important of these challenges is the very low solubility of PCX in water (0.3 μg/mL) [4]. To overcome poor solubility of PCX in water, the current commercial injectable formulation consists of a 1:1 mixture of anhydrous ethanol and Cremophor EL®, which is known to be the cause of severe side effects including nephrotoxicity, neurotoxicity and hypersensitivity reactions [5,6]. Other major problems encountered in the clinical administration of PCX are rapid recrystallization of the drug as a result of dilution in isotonic saline or dextrose solution, leading to severe necrosis and pain at injection site as well as reported incompatibility with intravenous (iv) infusion sets [7]. In order to overcome these side effects of PCX in clinical applications, alternative approaches are developed and evaluated to increase safety and efficacy of chemotherapy with PCX.

A promising step was taken with the FDA approval of albumin nanoparticle bound PCX (Abraxane®) in 2005 for breast cancer treatment with a significantly lower dose [8]. This was considered a breakthrough in PCX formulation development as it avoided the use of solubilizers, delivering the drug bound to the nanocarriers in a considerably lower dose to target tissue.

Cyclodextrins (CDs) are cyclic oligosaccharides obtained through enzymatic degradation of starch. The most frequently used CDs in the pharmaceutical field are α-CD, β-CD and γ-CD having 6, 7 and 8 subunits, respectively [9]. These molecules have drawn attention as drug carrier systems for several years because of their unique molecular structures and supramolecular capabilities. CDs, although hydrophilic in the external surface, have hydrophobic cavity and this compartment allows them to form strong inclusion complexes with non-polar drugs or active molecules [10]. CDs are easily able to modulate physicochemical properties of guest molecules, including solubility and/or stability in biological medium. Despite all the advantages, CDs have some challenges. For instance, it is well known that β-CD has low solubility in water and causes haemolysis on blood cells when administered parenterally [11,12]. To overcome these challenges, natural CDs are modified with different chemical groups to alter their structure and improve their biocompatibility [13-16].

Amphiphilic CDs have been synthesized to overcome problems of natural CDs which enhance the interaction with drug molecules and biological membranes [17,18]. Most importantly, amphiphilic CDs possess the ability to spontaneously form nanoparticles at the interface, depending on the preparation method and physical and chemical properties of CD [19-22]. In the literature, amphiphilic CDs were reported to spontaneously self-assemble in the form of nanospheres or nanocapsules and overcome haemolytic activity on blood cells for eventual injectable nanoparticulate drug delivery [23-25].

The aim of this study was to evaluate and compare the potential of polycationic amphiphilic CD nanoparticles as delivery systems for effective and safe delivery of PCX in comparison to its non-ionic or core–shell analogues. For this reason, two different cyclodextrin derivatives were used in this context, namely the non-ionic 6OCaproβCD (M_W: 1813 g/mol) (Figure 1a) and the polycationic PC βCDC6 (3178 g/mol) (Figure 1b). 6OCaproβCD is non-ionic as no charged groups are present in the structure in the normal pH window (2–13) and it was used to prepare negatively charged nanoparticles. 6OCaproβCD possesses 7 lipophilic groups on the primary face whilst the polycationic PC βCDC6 has 7 cationic groups on the primary face and 14 lipophilic groups on the secondary face. Both nanoparticles were prepared by a nanoprecipitation technique which is based on spherical crystallites of the polymer while precipitation occurs at the interface. In addition, chitosan (Figure 1c) was used to coat the surface of the 6OCaproβCD nanoparticles. Chitosan-coated 6OCaproβCD nanoparticles (CS-6OCaproβCD) were also prepared and characterized. It was aimed to increase the efficacy of PCX (Figure 1d) as a model drug. All blank amphiphilic CD nanoparticles were optimized for selection of organic solvent, ratio of organic phase to aqueous phase and surfactant concentration to obtain monodis-

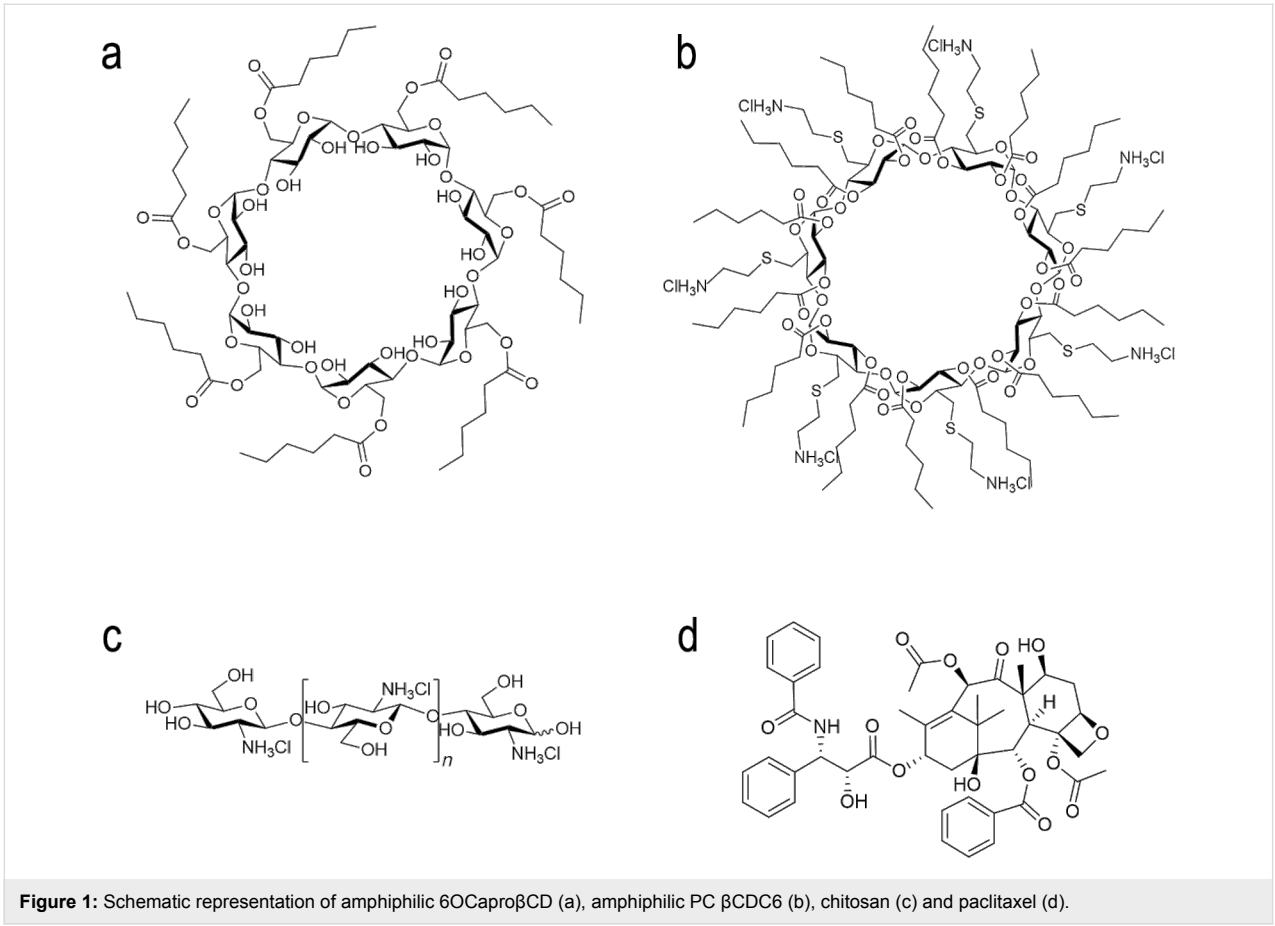

Figure 1: Schematic representation of amphiphilic 6OCaproβCD (a), amphiphilic PC βCDC6 (b), chitosan (c) and paclitaxel (d).

perse particles with a diameter range around 80 to 125 nm. Intended as chemotherapeutic nanocarriers, various PCX-loaded amphiphilic CD nanoparticles were also evaluated for their drug encapsulation, release profile and anticancer activity on MCF-7 human breast cancer cell line in particular. Safety and apoptotic efficacy of blank and PCX-loaded cationic or anionic amphiphilic CD nanoparticles were evaluated with cell culture studies against a series of healthy and cancer cells.

The amphiphilic, cationic PC βCDC6 derivative was used as the anticancer drug carrier delivery system for PCX for the first time in this study. There are various studies in which this derivative is used as a gene transfer delivery system; however, there is only example where this derivative was used as a drug delivery system. This was a study regarding the non-polar anxiolytic drug diapezam realized by Mendez-Ardoy et al. [22]. Our goal is to evaluate the potential of the polycationic CD nanoparticles as an anticancer drug delivery system. In fact, these polycationic CDs were evaluated for their intrinsic apoptotic effect in our first paper [26] in unloaded blank nanoparticle form. This study focuses on the nanocarrier properties and drug delivery system potential of the polycationic CD nanoparticles for PCX, which is an anticancer drug with several serious bioavaibility and toxicity problems. PCX was selected as the target drug in this study also for the fact that it is available on the market in nanomedicine form, known as Abraxane®.

Results and Discussion

Pre-formulation studies

Nanoparticles are promising carriers for drugs due to their tunable dimensions and shape. There are several factors that influence the particle size, particle distribution, surface charge, homogeneity and shape of nanometer-sized drug delivery systems. These factors have a subsequent influence on the biodistribution and the fate of the nanomedicine in the body [27]. In this case, the formulation parameters play an important role on the mean diameter of the nanoparticles. Our primary concern was to obtain an optimal particle size distribution with a diameter less than 200 nm and a polydispersity index lower than 0.2; therefore, the corresponding parameters were thoroughly assessed.

The effect of different organic solvents used in the organic phase on the mean particle size and polydispersity index (PDI) of blank amphiphilic CD nanoparticles is given in Table 1. It is clearly seen that among the various water-miscible solvents (re-

Table 1: Effect of organic solvent on mean particle size, PDI and zeta potential values of formulations (CD amount is 0.5 mg/mL in all formulations) (n = 3, ± standard deviation (SD)).

Nanoparticle formulations	Solvent	Particle diameter ± SD (nm)	PDI ± SD	Zeta potential (mV) ± SD
6OCaproβCD	acetone	164 ± 5	0.62 ± 0.05	−26 ± 2.9
	ethanol	104 ± 1	0.13 ± 0.02	−24 ± 0.3
	methanol	367 ± 2	0.15 ± 0.03	−26 ± 1.4
CS-6OCaproβCD	acetone	285 ± 5	0.34 ± 0.06	+57.2 ± 2.3
	ethanol	122 ± 4	0.23 ± 0.03	+69.1 ± 1.6
	methanol	399 ± 2	0.35 ± 0.03	+61 ± 3.1
PC βCDC6	acetone	124 ± 4	0.32 ± 0.05	+76 ± 0.2
	ethanol	75 ± 2	0.16 ± 0.02	+61 ± 1.4
	methanol	121 ± 6	0.51 ± 0.02	+65 ± 1.3

quired for the nanoprecipitation technique), ethanol is the optimal solvent in this study in terms of mean diameter and PDI for all CD nanoparticle formulations. The nanoprecipitation method is mainly based on interfacial turbulence between a miscible organic phase and an aqueous phase [28]. In nanoprecipitation, the polymer and drug is dissolved in a water-miscible organic solvent, which diffuses from the organic phase into the aqueous phase. Meanwhile, polymers in the organic phase tend to spontaneously aggregate, forming spherical crystals, and thus nanoparticles form rapidly [27,29].

As seen in Table 1, the mean particle size of the nanoparticles varies greatly in the range between 75 to 400 nm for different solvents, and ethanol gives the smallest diameter for all CD nanoparticles. The effect of organic solvent selection on nanoparticle diameter was found to follow the order of methanol > acetone > ethanol for 6OCaproβCD nanoparticles and CS-6OCaproβCD nanoparticles, and acetone > methanol > ethanol for PC βCDC6 nanoparticles. It is worth noting that ethanol also gave the most monodisperse particles with an acceptable polydispersity index (<0.2) (Table 1).

As expected, the core–shell nanoparticles CS-6OCaproβCD had the largest size due to the chitosan coating on its surface, and the PC βCDC6 nanoparticles were the smallest, probably resulting from the likely electrostatic destabilization of larger particles.

As is known, nanoparticle homogeneity is based on the properties of the organic solvent in the nanoprecipitation technique. It is shown that ethanol is the optimum organic solvent for amphiphilic CDs in this study. In the nanoprecipitation technique, nanoparticle formation occurs as a result of interfacial turbulence between two unequilibrated liquid phases. For the formation of turbulence, the liquid phases (organic phase and liquid phase) used in this method must be miscible with each other. Galindo-Rodriguez et al. investigated the influence of the different solvent types on NP formation in the nanoprecipitation technique [30]. The solvent and solubility parameters were calculated by using the dispersion force component, the polar component, and the hydrogen bonding component. It was reported that the smaller the difference between the solubility of solute and solvent, the higher the affinity and the smaller the particle size. They emphasized that the difference in polarity between ethanol/water is the smallest compared to the difference between the other solvents/water, and the smallest particle size is obtained in the formulation using ethanol [30]. In another study, Khan et al. prepared gelatine nanoparticles by the nanoprecipitation technique with different organic solvents (methanol, ethanol, acetone, *n*-propanol and acetonitrile) concluding that only methanol and ethanol led to nanometer-sized particles among those solvents that were studied. Furthermore, ethanol was reported to provide the smallest particle size (250 nm) between these two organic solvents [31] in parallel to the findings presented in Table 1.

As another major parameter influencing particle formation and size, the effect of surfactant presence and concentration was determined by investigating the mean particle size of amphiphilic CD nanoparticles for 0, 0.1 and 0.5% w/v pluronic F68 (PF68) dissolved in aqueous phase. Table 2 shows that the mean particle size increases in proportion with concentration of PF68.

The smallest particle size was obtained without the surfactant for all nanoparticle formulations. This is found to be in accordance with previous studies reported in the literature proving that amphiphilic CDs are able to form nanoparticles without the presence of surfactants [21,22,24,32-34] due to their favorable self-alignment properties at air–water or oil–water interface [35]. The mean particle size of amphiphilic CD nanoparticles increased linearly with concentration of surfactant. Bilensoy et al. evaluated the effect of the presence of PF68 in CD nanopar-

Table 2: Effect of surfactant concentration on nanoparticle diameter and dispersity in ethanol (CD amount is 0.5 mg/mL in all formulations) (n = 3, ± SD).

Nanoparticle formulations	PF68 concentration (% w/v)	Particle diameter ± SD (nm)	PDI ± SD
6OCaproβCD	0	104 ± 1	0.13 ± 0.02
	0.1	190 ± 4	0.17 ± 0.03
	0.5	208 ± 5	0.23 ± 0.02
CS-6OCaproβCD	0	122 ± 4	0.23 ± 0.03
	0.1	168 ± 6	0.15 ± 0.03
	0.5	185 ± 4	0.33 ± 0.06
PC βCDC6	0	75 ± 2	0.16 ± 0.02
	0.1	110 ± 7	0.37 ± 0.01
	0.5	175 ± 5	0.47 ± 0.04

ticle formulations on cytotoxicity on L929, a healthy mouse fibroblast cell line. According to these results, it was suggested that PF68 has no significant effect on size and drug loading capacity of nanoparticles but dose-dependent toxicity could occur on L929 fibroblast cells [36]. In another study, a polycationic, amphiphilic, cyclodextrin derivative was used to prepare nanospheres and nanocapsules as drug delivery systems. When the results are compared with this study in terms of particle size, it can be concluded that the use of surfactant is linearly correlated with the particle size [22].

Characterization of PCX-loaded amphiphilic CD nanoparticles

According to pre-formulation studies described and discussed in the previous section, it was decided that the most suitable solvent is ethanol for all CD formulations. Each PCX-loaded nanoparticle formulation was prepared with ethanol and without any surfactant (PF68).

Delivering the therapeutic load to the target site and maintaining therapeutic blood levels for the drug in an effective dose is the most important objective for targeted nanomedicines. Drug encapsulation efficiency is highly affected by the nature of the polymer/polysaccharide used to prepare the nanoparticles. Therefore, in order to determine the effect of surface charge on drug loading capacity of nanoparticles, PCX was chosen as a model anticancer drug frequently used in chemotherapy for patients with breast cancer. The encapsulation efficiency of amphiphilic CD nanoparticles is given in Table 3. The quantity of loaded PCX was determined directly with a validated HPLC method and entrapment efficiency or associated drug percentage were calculated with Equation 1 or Equation 2, as described later in the Experimental section. As seen in Table 3, the drug loading capacity of the nanoparticles was strongly related to the surface charge of the CD nanoparticles. As is known, PCX itself is negatively charged, so encapsulation due to electrostatic interactions is favored for the cationic CD nanoparticles, CS-6OCaproβCD and PC βCDC6, resulting in a 1.5-fold higher loading for this drug in cationic nanoparticles compared to the negatively charged 6OCaproβCD nanoparticles as seen in Table 3.

According to these results, the CS coating increased drug loading capacity of anionic 6OCaproβCD nanoparticles by approximately 50%. In addition, the CS coating may provide more efficient encapsulation area for PCX from aqueous media. It can be said that this hypothesis is also valid for PC βCDC6 nanoparticles. This amphiphilic CD derivative has long aliphatic chains terminated with amine groups. PC βCDC6 nanoparticles are believed to encapsulate PCX not only in the hydrophobic cavity but also between the long cationic aliphatic chains of the cyclodextrin as PCX and CD are co-nanoprecipitated during the preparation method.

Table 4 shows the final mean particle size, PDI and zeta potential values of PCX-loaded amphiphilic CD nanoparticles. The

Table 3: Associated drug (%) and entrapment drug quantity (μg/mg) of amphiphilic CD nanoparticles for PCX (CD amount is 0.5 mg/mL and initial PCX amount is 0.05 mg/mL in all formulations) (n = 3, ± SD).

Nanoparticle formulations	Percentage associated drug ± SD	Entrapment drug quantity ± SD (μg/mg)
6OCaproβCD	41 ± 2	4.4 ± 0.4
CS-6OCaproβCD	62 ± 5	5.6 ± 1.3
PC βCDC6	64 ± 2	6.3 ± 0.7

mean diameter of PCX-loaded nanoparticles varies in the range of 82 to 125 nm according to the type of CD used. They also exhibit a narrow distribution as the preparation technique nanoprecipitation was kept standard for all formulations.

Table 4: Mean particle size, PDI and zeta potential of PCX-loaded nanoparticles (CD amount is 0.5 mg/mL and initial PCX amount is 0.05 mg/mL in all formulations) (n = 3, ± SD).

Nanoparticle formulations	Particle size ± SD (nm)	PDI ± SD	Zeta potential ± SD (mV)
6OCaproβCD	113 ± 4	0.13 ± 1	−29 ± 2
CS-6OCaproβCD	125 ± 2	0.22 ± 4	+44 ± 3
PC βCDC6	82 ± 2	0.16 ± 5	+62 ± 1

In addition, drug loading did not cause significant changes in mean diameter of the nanoparticles except that an increase in diameter was observed for all nanoparticles. This suggests that the drug is partially adsorbed as a layer on the nanoparticle surface and partially encapsulated in the matrix due to charge interactions since PCX is a molecular entity with a carboxilic acid end, thereby anionic at neutral pH. Although the differences between the particle sizes of the blank and drug-loaded nanoparticles are not statistically significant, the smallest difference is seen in the CS-coated nanoparticles. The difference between the particle sizes of the blank and drug-loaded nanoparticles may be related to the localization of the drug. When the nanoparticles were prepared, the drug and cyclodextrins were dissolved together in the organic phase. Meanwhile, some of the drug is encapsulated by the hydrophobic cavity of the cyclodextrins and some of the drug is adsorbed on the surface of nanoparticles. This drug on the surface of the nanoparticles changes the particle size. For CS-coated nanoparticles, the drug and cyclodextrin were dissolved in the organic phase and then added to the CS-containing water. The presence of chitosan in the aqueous phase may cause a charge interaction between the adsorbed drug on the surface of the nanoparticles and the chitosan, resulting in a more rigid structure. In another previous study, it was reported that the new amphiphilic CD derivative PC βCDC6 is suitable to form stable nanoparticles with small particle size [26]. The particle size of nanoparticulate drug delivery systems play a direct and important role on cellular uptake, systemic circulation, toxicity and stability of nanoparticles [37,38]. It was reported that nanoparticles smaller than 200 nm can escape recognition by the mononuclear phagocytic system (MPS) [39]. The prolonged circulation time for nanoparticles, t, is needed to escape from MPS uptake in order to reach the tumor tissue. The MPS is one of the most important factors in preventing the prolonged circulation, affecting the biodistribution of nanoparticles. In this way, more effective and safe therapy can be provided with lower drug dose.

Zeta potential measurements indicate that 6OCaproβCD has a negative surface charge unlike the other formulations. In this study, PC βCDC6 has a strong positive surface charge owing to polycationic amino groups. This amphiphilic CD derivative was previously used for gene delivery studies due to net positive surface charge, facilitating the condensation of negatively charged DNA to form polyplexes [40,41]. In addition, CS-6OCaproβCD nanoparticles are also positively charged due to coating with cationic polymer. It is known that chitosan is a natural bioactive cationic polysaccharide derived from deacetylation of chitin and is well-characterized for its mucosal penetration enhancer property and apoptotic activity against cancer cells [42]. To alter the surface charge of nanomaterials, chitosan can be used as coating material in nanoparticles [43,44]. As a result of the surface coating with chitosan, the zeta potential value of 6OCaproβCD nanoparticles increased from −29 mV to +44 mV as seen in Table 3. Unal et al., prepared uncoated and CS-coated 6OCaproβCD nanocapsules for oral camptothecin delivery. They reported that the CS coating increased the zeta potential of nanocapsules from −11 to +10 mV [45,46].

Both CS-coated CD and PC βCDC6 were able to render a net positive charge to the nanoparticles while 6OCaproβCD had a charge around −25 mV. Nanoparticles with zeta potential between −10 and +10 mV are classified as neutral. Nanoparticles with zeta potential greater than +30 mV and less than −30 mV are considered as strongly charged [47]. According to this classification, two net positive nanoparticle formulations and a net negative nanoparticle formulation were used as a nanometer-sized drug delivery system for PCX in this study. These differences between the surface charge of CD nanoparticles allowed the comparison of the effect of surface charge on drug loading capacity, stability and anticancer activity in this study.

Furthermore, mean particle size distributions and PDI of the blank and PCX-loaded nanoparticles were followed for one month in aqueous form to determine the physical stability of PCX-loaded amphiphilic CD nanoparticle dispersions. Figure 2,

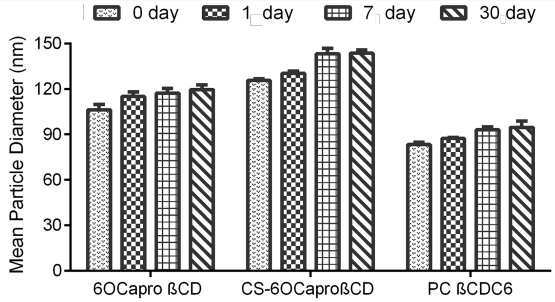

Figure 2: Time-dependent variation of particle size (nm) of PCX-loaded amphiphilic CD nanoparticles stored in aqueous dispersion form, (n = 3, ± SD).

Figure 3 and Figure 4 show that there is no significant difference for particle size, PDI and zeta potential of PCX-loaded and blank CD nanoparticle formulations ($p > 0.05$). PCX-loaded nanoparticles maintained their stability for 30 days in ultrapure water. This data shows that PCX crystals are not formed in aqueous dilution, which is believed to improve the safety of the drug delivery system.

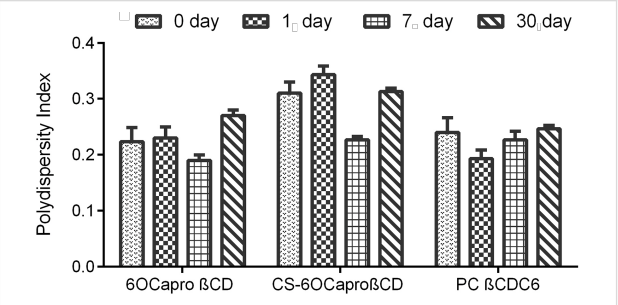

Figure 3: Time-dependent variation of the PDI value of PCX-loaded amphiphilic CD nanoparticles stored in aqueous dispersion form (n = 3, ± SD).

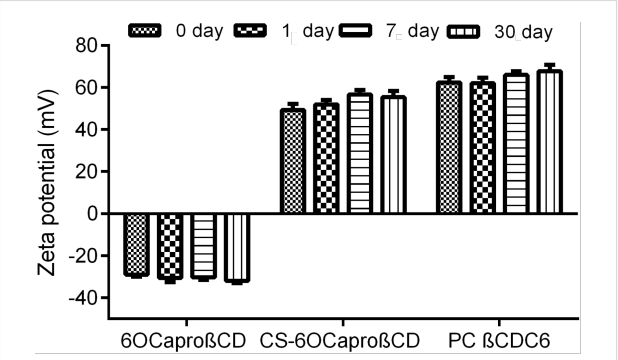

Figure 4: Time-dependent variation of the zeta potential value of PCX-loaded amphiphilic CD nanoparticles stored in aqueous dispersion form (n = 3, ± SD).

PCX exists in a crystal form in aqueous media due to hydrophobic interaction between lipophilic groups [48,49]. Due to this phenomenon, PCX is recrystallized in minutes as a result of dilution in isotonic saline solution for intravenous (iv) infusion, which is the preferred delivery route for chemotherapy. This is one of the main problems of clinical application of PCX. In the light of the physical stability studies depicted in Figures 2–4, it can be said that all amphiphilic CD nanoparticles maintained PCX in dispersed form within their hydrophobic matrix and thus, ensured stability of drug in aqueous media, which is also supported by previous studies for 6OCaproβCD nanocapsules and nanospheres [24].

The in vitro release profile of PCX from CD nanoparticles was determined using the dialysis bag method with HPLC as detailed in the Experimental section. As seen in Figure 5, PCX release from PC βCDC6 exhibited a markedly slower release profile of up to 42 h compared with other formulations. The release profiles indicated that in the first 5 h approximately 50% of PCX was released from the CS-6OCaproβCD and 70% from anionic 6OCaproβCD nanoparticles formulations, which can be attributed to desorption of surface PCX. Meanwhile, a 50% release time for PCX was found to be 8 h from PC βCDC6 nanoparticles. In addition, the release profile of PCX was found to reach plateau levels at 8, 12 and 42 h for 6OCaproβCD, CS-6OCaproβCD and PC βCDC6 nanoparticles, respectively.

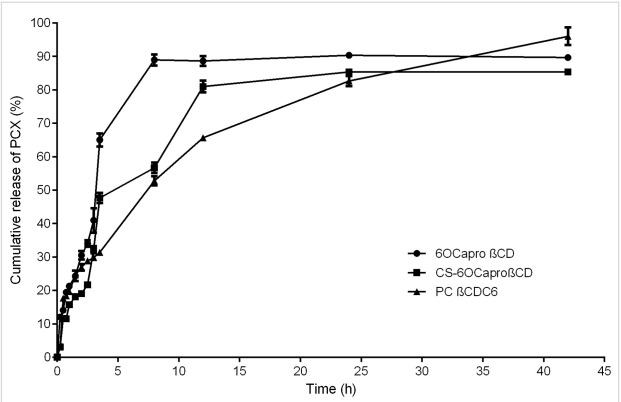

Figure 5: Cumulative release profile of PCX from different amphiphilic CD nanoparticles at pH 7.4 phosphate buffer solution under sink conditions (n = 3, ± SD).

PCX carries a negative charge and therefore has a stronger interaction with the positively charged CD, thus PCX release from PC βCDC6 is slower than other formulations. The CS coating of 6OCaproβCD nanoparticles also relatively slows down the release. However, the core–shell approach is believed to be insufficient to prolong the release of PCX as a result of both the hydrophobic nanoparticle matrix and the strong positive charge due to the negative charge of PCX.

It was reported in the literature that large nanoparticles result in a slower release profile than smaller nanoparticles [50]. However, in this study, PC βCDC6 nanoparticles have the smallest particle size and the longer release profile, as seen in Figure 5. It can therefore be suggested that the surface charge of nanoparticle is directly effective on the drug release profile.

Cell culture studies

In order to determine the safety of blank amphiphilic CD nanoparticles and the anticancer efficacy of PCX-loaded amphiphilic CD nanoparticles, L929 mouse fibroblast cells and MCF-7 human breast cancer cell lines were used, respectively. Both cell lines were grown and incubated in appropriate conditions (see Experimental section for full experimental details).

The cytotoxicity of blank amphiphilic CD nanoparticles was determined on L929 mouse fibroblast cells with MTT assay. This cell line is recommended by the U.S. Pharmacopeial Convention (USP) for the cytotoxicity evaluation of polymeric systems and was therefore used. According to MTT assay, cell viability for L929 cells is given in Figure 6.

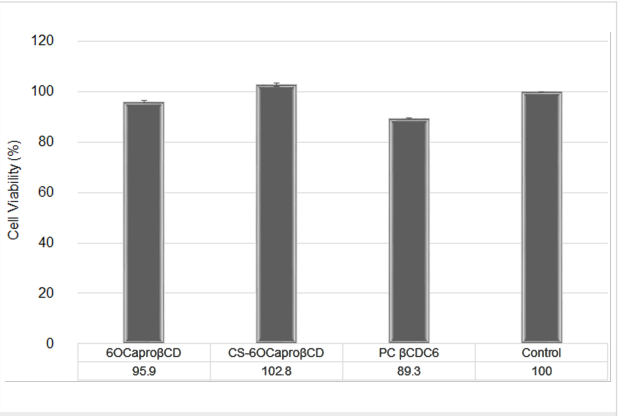

Figure 6: Cytotoxicity of unloaded amphiphilic CD nanoparticles on L929 mouse fibroblast cell line with MTT assay (CD concentration is 0.5 mg/mL in all formulation) (n = 3, ± SD).

It is clearly shown that all blank amphiphilic CD nanoparticle formulations are non-cytotoxic on L929 fibroblast cells compared with the control group ($p > 0.05$). It can therefore be concluded that blank amphiphilic CD nanoparticles have no cytotoxic effect on healthy cells. It was previously reported that toxicity of blank amphiphilic CD nanocapsules and nanospheres are concentration dependent and that they are also non-hemolytic [24,45]. Therefore, these nanoparticles may be safe on healthy cells as drug carrying systems.

To optimize the concentration of CD nanoparticles for cell culture studies, the inhibitory concentration 50 (IC_{50}) value of PCX was calculated on MCF-7 human breast cancer cell line. For this purpose, MCF-7 cells were incubated with different concentrations of PCX in dimethyl sulfoxide (DMSO). Non-treated cells were incubated with DMEM alone and were used as control group. Cell proliferation was determined and the IC_{50} value of PCX was calculated and the results are given in Figure 7.

As seen in Figure 7, the IC_{50} of PCX is 250 nM for the MCF-7 cell line. This result agrees with the literature [51]. According to the IC_{50} study results, nanoparticles loaded with 250 nM PCX were further used for cell culture studies.

The anticancer activity of PCX-loaded nanoparticles was determined on MCF-7 cell lines. After an incubation period, cell viability was calculated, as shown in Figure 8.

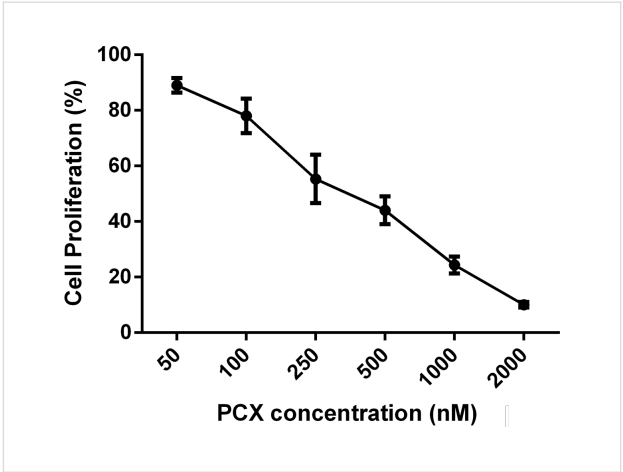

Figure 7: IC_{50} value of PCX solution in DMSO on MCF-7 human breast cancer cell line (n = 3, ± SD).

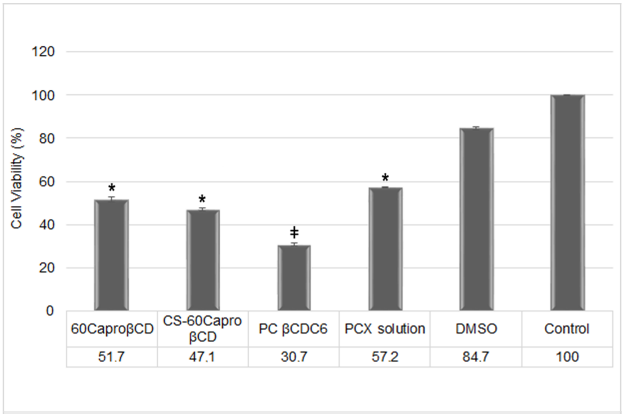

Figure 8: Anticancer activity of PCX-loaded amphiphilic CD nanoparticle formulations and PCX solution in DMSO on MCF-7 human breast cancer cell line after 48 h of incubation (All CD nanoparticle formulations and PCX solution contain 250 nM PCX) (n = 3, ± SD). Note that: * $p < 0.05$ as compared with the control, and ‡ $p < 0.05$ as compared with other CD nanoparticle formulations.

According to the results of anticancer activity studies on MCF-7, PCX-loaded amphiphilic CD nanoparticles have higher cytotoxicity than PCX solution in DMSO ($p < 0.05$). The amphiphilic CD nanoparticles and the drug solution carry an equivalent amount of PCX (250 nM) during the cell culture study. The cell viability in loaded CD nanoparticles is significantly different from the PCX solution ($p < 0.05$). Moreover, the effect of surface charge on viability of cancer cells can be clearly seen in Figure 8. Anticancer activity increases with increasing surface charge of nanoparticles. It was known that the cell membrane is negatively charged so that cationic nanoparticles enhance interaction with the biological membrane. Positively charged nanoparticles can bind with negatively charged molecules (e.g., sialic acid, cholesterol, phospholipid) on cell membrane easier than anionic nanoparticles [26,52]. In addition, the surface charge of nanoparticles play an important role on cellular

uptake and subcellular localization [53,54]. Another reason for the cell viability differences of CD nanoparticles may be related with drug release profiles. PCX shows anticancer activity by stabilizing microtubules and blocking the cell in G2 or M phase in cell cycle [55,56]. The duration of drug release of PCX-loaded amphiphilic CD nanoparticles increases in the order of 6OCaproβCD < CS-6OCaproβCD < PC βCDC6. Therefore, the amphiphilic CD nanoparticles carried different drug amounts when they were taken up by MCF-7 cells. This can explain the difference in the cell viability between CD nanoparticle formulations.

Conclusion

In this study, 6OCaproβCD, CS-6OCaproβCD and PC βCDC6 nanoparticles were prepared and used as nanometer-sized delivery systems and compared in terms of mean particle size, zeta potential, drug loading capacity and drug release profile for PCX, which is an effective anticancer agent over the wide spectrum various types of cancer. The findings strongly suggest that positive charge can improve drug loading capacity, slow down drug release and improve cellular interaction due to the negative charge of the cell membrane. Furthermore, unloaded or loaded nanoparticle cytotoxic effects were demonstrated with MTT assay in this study. In the light of the results of this study, it is clearly demonstrated that anionic and cationic CD nanoparticles are suitable carriers for PCX. Moreover, PC βCDC6 was used to prepare nanoparticulate, anticancer drug delivery systems for the first time in literature. Cationic CD nanoparticles can be considered as promising carriers for PCX as well as other lipophilic anticancer drugs for cancer therapy. In addition, by formulating with anionic and cationic amphiphilic CDs, it will be possible to enhance anticancer activity of drugs, overcoming the problem of surfactant-induced toxicity. Finally, it can be said that polycationic amphiphilic CDs are favorable, nanoparticulate, drug delivery systems for the delivery of anticancer agents.

Experimental

Materials

Anionic 6OCapro βCD and PC βCDC6 were synthetized as described previously in University of Sevilla, Spain [26]. PCX (≥97% powder, M_W: 853.91 g/mol) was purchased from Sigma-Aldrich, Germany. The chitosan used for coating the nanoparticles (Protasan UP G-113; M_W: <200 kDa, viscosity: <20 mPa·s), was purchased from Novamatrix, Norway. Cellulose membrane dialysis tubing (avgerage flat width 25 mm, MWCO: 14,000 Da) was purchased from Sigma-Aldrich, Germany. All other chemicals used were of analytical grade and obtained from Sigma-Aldrich. Ultrapure water was obtained from a Millipore Simplicity 185 Ultrapure water system (Millipore, France).

Methods

Preparation of unloaded or PCX-loaded amphiphilic CD nanoparticles

PC βCDC6 nanoparticles and anionic 6OCaproβCD nanoparticles were prepared according to the nanoprecipitation method as described previously [26,28]. Briefly, 1 mg of PC βCDC6 or 6OCaproβCD was dissolved in 1 mL of organic solvent (ethanol, methanol or acetone) (0.1% w/v). This organic phase was added dropwise into aqueous phase (2 mL) containing PF68 (0–0.5% w/v) under magnetic stirring at room temperature. Then, the organic phase was evaporated under vacuum at 40 °C to the desired final volume of 2 mL. To prepare CS-coated 6OCaproβCD nanoparticles, the same technique was employed in the presence of protosan (0.025%, w/v) in the aqueous phase. According to the results of the pre-formulation studies, optimal formulation parameters were selected for PCX-loaded amphiphilic CD nanoparticles. To prepare drug-loaded nanoparticles, PCX (0.1 mg) and cyclodextrin (1 mg) were co-nanoprecipitated in 1 mL organic solvent and then organic phase was poured in 2 mL ultrapure water using the conditions previously given.

Mean particle size distribution and surface charge

The mean particle diameter (nm), PDI and zeta potential (mV) of amphiphilic CD nanoparticles were determined by dynamic light scattering (DLS) (NanoZS, Malvern Instruments, UK). All formulations were measured at an angle of 173° for particle size measurements and 12° for zeta potential measurements. All formulations were measured at room temperature in triplicate for thesize and zeta potential analysis.

Drug loading capacity and in vitro release profile of PCX-loaded amphiphilic CD nanoparticles

The content of PCX in amphiphilic CD nanoparticle formulations was quantified directly with a validated HPLC method [32] (HP Agilent 1100 HPLC system, Germany). Briefly, PCX-loaded nanoparticle formulations were lyophilized for 24 h following centrifugation at 10,000 rpm for 15 min to remove free PCX. The supernatant was collected and freeze-dried. The lyophilized nanoparticle powder was dissolved in dichloromethane (DCM) to quantify nanoparticle-bound PCX (μg/mL).

The HPLC system consisted of reverse phase C18 column (Hichrom 5, 250 × 4.6 mm, U.K.) and acetonitrile: ultrapure water (70:30 v/v) as a mobile phase was delivered at a flow rate of 1.00 mL/min. A 50 μL aliquot of sample was injected for analysis. PCX was quantified by UV detection (λ = 227.4 nm) at 25 °C. Drug loading was expressed as described in Equation 1 and Equation 2 to clearly express the drug percentage bound to nanoparticles as well as drug entrapped per unit polymer.

$$\text{Associated drug}(\%) = \frac{\text{Experimental drug loading (μmol)}}{\text{Initial drug quantity (μmol)}} \times 100 \quad (1)$$

$$\text{Entrapment Drug Quantity} = \frac{\text{Experimental loaded drug (μg)}}{\text{Cyclodextrin amount (mg)}} \quad (2)$$

The in vitro cumulative release profile of PCX from CD nanoparticles was determined with the dialysis membrane technique under sink conditions in a shaking water bath at 37 °C in PBS pH 7.4. Briefly, drug-loaded nanoparticle dispersions were added in the dialysis membrane (Sigma, cellulose membrane, MWCO: 100,000 Da, Sigma Chemicals). The nanoparticle-containing dialysis bags, closed with stoppers on both ends, were placed in PBS pH 7.4 containing 0.1% Tween 80 at 37 °C to provide sink conditions. The samples were taken from the medium at specific time intervals and replaced with fresh PBS at the same volume and temperature. The PCX amount in the samples was determined with HPLC as described previously.

Physical stability of blank or drug-loaded nanoparticles

In order to determine the physical stability of PCX in the nanoparticles, drug-loaded nanoparticles were stored in ultrapure water at 4 °C and the mean particle size, PDI values and zeta potential were obtained periodically for 30 days in aqueous dispersion form to elucidate whether PCX crystals are formed or any aggregation/precipitation is observed upon storage of the nanoparticle dispersions.

Cell culture studies

In order to determine safety or anticancer efficacy of blank amphiphilic CD nanoparticles, L929 mouse fibroblast cells or MCF-7 human breast carcinoma cell lines were used, respectively. Both cell lines were cultured in the same conditions as a monolayer in Dulbecco's modified Eagle's medium (DMEM) supplemented with 10% fetal bovine serum (FBS), penicillin (100 units/mL) and streptomycin (100 μg/mL). The cultures were maintained at 37 °C in a humidified 5% CO_2 incubator. The cell lines were seeded in 96-well tissue culture plates at a density of 1×10^3 cells/well in DMEM (100 μL), separately.

After the L929 cells reached confluence, DMEM was removed from the cells and fresh medium containing blank amphiphilic CD nanoparticles was replaced and incubated for 48 h. In order to determine cell viability, 3-(4,5-dimethylthiazol-2-yl)-2,5-diphenyltetrazolium bromide (MTT) assay was applied. For this purpose, 20 μL of MTT solution in PBS (5 mg/mL) was added in each well and incubated for 4 h. After incubation, 100 mL of DMSO was added per well to dissolve formazan crystals. The optical density (OD) was determined by a microplate reader (Molecular Devices, USA) at 450 nm.

In order to determine the anticancer activity of loaded nanoparticles, the IC_{50} value of PCX was calculated firstly. For this purpose, after the MCF-7 cells reached full confluence, DMEM was replaced with different concentrations of a PCX solution in DMSO (50, 100, 250, 500, 1000 and 2000 nM) and incubated for 48 h. After the incubation time, the MTT assay was applied described above. According to the IC_{50} study, amphiphilic CD nanoparticles were prepared and diluted with DMEM to contain 250 nM PCX. The control group consisted of cells incubated in DMEM alone for two groups and PCX solution in DMSO for the MCF-7 cell line. After that, using MTT assay, the cell viability was determined.

Statistical Analysis

All statistical analyses were performed by Student's *t*-test using GraphPad Prism version 6 (San Diego, CA, USA). A value of $p < 0.05$ was considered to denote a statistically significant difference.

Acknowledgements

The authors wish to thank the TUBITAK Scientific Research Project 112S538 for financial support of this study. Gamze Varan is a recipient of a grant from the TUBITAK BIDEB National Scholarship Programme for PhD Students (2211-C).

References

1. Howat, S.; Park, B.; Oh, I. S.; Jin, Y.-W.; Lee, E.-K.; Loake, G. J. *New Biotechnol.* **2014,** *31,* 242–245. doi:10.1016/j.nbt.2014.02.010
2. Weaver, B. A.; Bement, W. *Mol. Biol. Cell* **2014,** *25,* 2677–2681. doi:10.1091/mbc.E14-04-0916
3. Mukhtar, E.; Adhami, V. M.; Mukhtar, H. *Mol. Cancer Ther.* **2014,** *13,* 275–284. doi:10.1158/1535-7163.MCT-13-0791
4. Shah, M.; Shah, V.; Ghosh, A.; Zhang, Z.; Minko, T. *J. Pharm. Pharmacol.* **2014,** *2,* 8. doi:10.13188/2327-204X.1000011
5. Gelderblom, H.; Verweij, J.; Nooter, K.; Sparreboom, A. *Eur. J. Cancer* **2001,** *37,* 1590–1598. doi:10.1016/S0959-8049(01)00171-X
6. Surapaneni, M. S.; Das, S. K.; Das, N. G. *ISRN Pharmacol.* **2012,** *2012,* 623139. doi:10.5402/2012/623139
7. Šmejkalová, D.; Nešporová, K.; Hermannová, M.; Huerta-Angeles, G.; Čožíková, D.; Vištejnová, L.; Šafránková, B.; Novotný, J.; Kučerík, J.; Velebný, V. *Int. J. Pharm.* **2014,** *466,* 147–155. doi:10.1016/j.ijpharm.2014.03.024
8. Miele, E.; Spinelli, G. P.; Miele, E.; Tomao, F.; Tomao, S. *Int. J. Nanomed.* **2009,** *4,* 99–105.
9. Jambhekar, S. S.; Breen, P. *Drug Discovery Today* **2016,** *21,* 356–362. doi:10.1016/j.drudis.2015.11.017
10. Gidwani, B.; Vyas, A. *BioMed Res. Int.* **2015,** *2015,* 198268. doi:10.1155/2015/198268
11. Onodera, R.; Motoyama, K.; Okamatsu, A.; Higashi, T.; Arima, H. *Sci. Rep.* **2013,** *3,* No. 1104. doi:10.1038/srep01104
12. Kiss, T.; Fenyvesi, F.; Bácskay, I.; Váradi, J.; Fenyvesi, E.; Iványi, R.; Szente, L.; Tósaki, A.; Vecsernyés, M. *Eur. J. Pharm. Sci.* **2010,** *40,* 376–380. doi:10.1016/j.ejps.2010.04.014

13. Erdogar, N.; Varan, G.; Bilensoy, E. *Curr. Top. Med. Chem. (Sharjah, United Arab Emirates)* **2017,** *17,* 1521–1528. doi:10.2174/1568026616666161222101104
14. Lakkakula, J. R.; Macedo Krause, R. W. *Nanomedicine* **2014,** *9,* 877–894. doi:10.2217/nnm.14.41
15. RodrÍguez-Lavado, J.; de la Mata, M.; Jiménez-Blanco, J. L.; Garcia-Moreno, M. I.; Benito, J. M.; Díaz-Quintana, A.; Sánchez-Alcázar, J. A.; Higaki, K.; Nanba, E.; Ohno, K.; Suzuki, Y.; Ortiz Mellet, C.; Garcia Fernández, J. M. *Org. Biomol. Chem.* **2014,** *12,* 2289–2301. doi:10.1039/c3ob42530d
16. Benito, J. M.; Gómez-Garcia, M.; Ortiz Mellet, C.; Baussanne, I.; Defaye, J.; Garcia Fernández, J. M. *J. Am. Chem. Soc.* **2004,** *126,* 10355–10363. doi:10.1021/ja047864v
17. Bilensoy, E.; Hincal, A. A. *Expert Opin. Drug Delivery* **2009,** *6,* 1161–1173. doi:10.1517/17425240903222218
18. Sallas, F.; Darcy, R. *Eur. J. Org. Chem.* **2008,** *2008,* 957–969. doi:10.1002/ejoc.200700933
19. Roux, M.; Perly, B.; Djedaïni-Pilard, F. *Eur. Biophys. J.* **2007,** *36,* 861–867. doi:10.1007/s00249-007-0207-6
20. Zerkoune, L.; Angelova, A.; Lesieur, S. *Nanomaterials* **2014,** *4,* 741–765. doi:10.3390/nano4030741
21. Ravoo, B. J.; Darcy, R. *Angew. Chem., Int. Ed.* **2000,** *39,* 4324–4326. doi:10.1002/1521-3773(20001201)39:23<4324::AID-ANIE4324>3.0.CO;2-O
22. Mendez-Ardoy, A.; Gomez-Garcia, M.; Geze, A.; Putaux, J. L.; Wouessidjewe, D.; Ortiz Mellet, C.; Defaye, J.; Garcia Fernandez, J. M.; Benito, J. M. *Med. Chem.* **2012,** *8,* 524–532. doi:10.2174/157340612801216265
23. Memişoğlu, E.; Bochot, A.; Özalp, M.; Sen, M.; Duchêne, D.; Hincal, A. A. *Pharm. Res.* **2003,** *20,* 117–125. doi:10.1023/A:1022263111961
24. Bilensoy, E.; Gürkaynak, O.; Doğan, A. L.; Hıncal, A. A. *Int. J. Pharm.* **2008,** *347,* 163–170. doi:10.1016/j.ijpharm.2007.06.051
25. Quaglia, F.; Ostacolo, L.; Mazzaglia, A.; Villari, V.; Zaccaria, D.; Sciortino, M. T. *Biomaterials* **2009,** *30,* 374–382. doi:10.1016/j.biomaterials.2008.09.035
26. Varan, G.; Öncül, S.; Ercan, A.; Benito, J. M.; Ortiz Mellet, C.; Bilensoy, E. *J. Pharm. Sci.* **2016,** *105,* 3172–3182. doi:10.1016/j.xphs.2016.06.021
27. Rao, J. P.; Geckeler, K. E. *Prog. Polym. Sci.* **2011,** *36,* 887–913. doi:10.1016/j.progpolymsci.2011.01.001
28. Fessi, H.; Puisieux, F.; Devissaguet, J. P.; Ammoury, N.; Benita, S. *Int. J. Pharm.* **1989,** *55,* R1–R4. doi:10.1016/0378-5173(89)90281-0
29. Kumari, A.; Yadav, S. K.; Yadav, S. C. *Colloids Surf., B* **2010,** *75,* 1–18. doi:10.1016/j.colsurfb.2009.09.001
30. Galindo-Rodriguez, S.; Allemann, E.; Fessi, H.; Doelker, E. *Pharm. Res.* **2004,** *21,* 1428–1439. doi:10.1023/B:PHAM.0000036917.75634.be
31. Khan, S. A.; Schneider, M. *Macromol. Biosci.* **2013,** *13,* 455–463. doi:10.1002/mabi.201200382
32. Bilensoy, E.; Gürkaynak, O.; Ertan, M.; Şen, M.; Hıncal, A. A. *J. Pharm. Sci.* **2008,** *97,* 1519–1529. doi:10.1002/jps.21111
33. Bilensoy, E. *Adv. Exp. Med. Biol.* **2015,** *822,* 201. doi:10.1007/978-3-319-08927-0_24
34. Erdoğar, N.; Esendağlı, G.; Nielsen, T. T.; Şen, M.; Öner, L.; Bilensoy, E. *Int. J. Pharm.* **2016,** *509,* 375–390. doi:10.1016/j.ijpharm.2016.05.040
35. Ringard-Lefebvre, C.; Bochot, A.; Memisoğlu, E.; Charon, D.; Duchêne, D.; Baszkin, A. *Colloids Surf., B* **2002,** *25,* 109–117. doi:10.1016/S0927-7765(01)00297-1
36. Memisoglu-Bilensoy, E.; Doğan, A. L.; Hincal, A. A. *J. Pharm. Pharmacol.* **2006,** *58,* 585–589. doi:10.1211/jpp.58.5.0002
37. Couvreur, P.; Vauthier, C. *Pharm. Res.* **2006,** *23,* 1417–1450. doi:10.1007/s11095-006-0284-8
38. Acharya, S.; Sahoo, S. K. *Adv. Drug Delivery Rev.* **2011,** *63,* 170–183. doi:10.1016/j.addr.2010.10.008
39. Kulkarni, S. A.; Feng, S.-S. *Pharm. Res.* **2013,** *30,* 2512–2522. doi:10.1007/s11095-012-0958-3
40. Díaz-Moscoso, A.; Le Gourriérec, L.; Gómez-García, M.; Benito, J. M.; Balbuena, P.; Ortega-Caballero, F.; Guilloteau, N.; Di Giorgio, C.; Vierling, P.; Defaye, J.; Ortiz Mellet, C.; García Fernández, J. M. *Chemistry* **2009,** *15,* 12871–12888. doi:10.1002/chem.200901149
41. Gallego-Yerga, L.; Blanco-Fernández, L.; Urbiola, K.; Carmona, T.; Marcelo, G.; Benito, J. M.; Mendicuti, F.; Tros de Ilarduya, C.; Ortiz Mellet, C.; García Fernández, J. M. *Chem. – Eur. J.* **2015,** *21,* 12093–12104. doi:10.1002/chem.201501678
42. Rudzinski, W. E.; Aminabhavi, T. M. *Int. J. Pharm.* **2010,** *399,* 1–11. doi:10.1016/j.ijpharm.2010.08.022
43. Agnihotri, S. A.; Mallikarjuna, N. N.; Aminabhavi, T. M. *J. Controlled Release* **2004,** *100,* 5–28. doi:10.1016/j.jconrel.2004.08.010
44. Jayakumar, R.; Menon, D.; Manzoor, K.; Nair, S. V.; Tamura, H. *Carbohydr. Polym.* **2010,** *82,* 227–232. doi:10.1016/j.carbpol.2010.04.074
45. Ünal, H.; Öztürk, N.; Bilensoy, E. *Beilstein J. Org. Chem.* **2015,** *11,* 204–212. doi:10.3762/bjoc.11.22
46. Ünal, H.; d'Angelo, I.; Pagano, E.; Borrelli, F.; Izzo, A.; Ungaro, F.; Quaglia, F.; Bilensoy, E. *J. Nanopart. Res.* **2015,** *17,* 42. doi:10.1007/s11051-014-2838-8
47. Clogston, J. D.; Patri, A. K. Zeta Potential Measurement. In *Characterization of Nanoparticles Intended for Drug Delivery;* McNeil, S. E., Ed.; Methods in Molecular Biology, Vol. 697; Humana Press: New York, NY, U.S.A., 2011; pp 63–70. doi:10.1007/978-1-60327-198-1_6
48. Vella-Zarb, L.; Baisch, U.; Dinnebier, R. E. *J. Pharm. Sci.* **2013,** *102,* 674–683. doi:10.1002/jps.23404
49. Mognetti, B.; Barberis, A.; Marino, S.; Berta, G.; De Francia, S.; Trotta, F.; Cavalli, R. *J. Inclusion Phenom. Macrocyclic Chem.* **2012,** *74,* 201–210. doi:10.1007/s10847-011-0101-9
50. Mora-Huertas, C. E.; Fessi, H.; Elaissari, A. *Int. J. Pharm.* **2010,** *385,* 113–142. doi:10.1016/j.ijpharm.2009.10.018
51. Motiwala, M. N.; Rangari, V. D. *Synergy* **2015,** *2,* 1–6. doi:10.1016/j.synres.2015.04.001
52. Verma, A.; Stellacci, F. *Small* **2010,** *6,* 12–21. doi:10.1002/smll.200901158
53. He, C.; Hu, Y.; Yin, L.; Tang, C.; Yin, C. *Biomaterials* **2010,** *31,* 3657–3666. doi:10.1016/j.biomaterials.2010.01.065
54. Asati, A.; Santra, S.; Kaittanis, C.; Perez, J. M. *ACS Nano* **2010,** *4,* 5321–5331. doi:10.1021/nn100816s
55. Schiff, P. B.; Horwitz, S. B. *Proc. Natl. Acad. Sci. U. S. A.* **1980,** *77,* 1561–1565. doi:10.1073/pnas.77.3.1561
56. Yardley, D. A. *J. Controlled Release* **2013,** *170,* 365–372. doi:10.1016/j.jconrel.2013.05.041

BEILSTEIN JOURNAL OF NANOTECHNOLOGY

Calcium fluoride based multifunctional nanoparticles for multimodal imaging

Marion Straßer[*,‡1,2], Joachim H. X. Schrauth[‡3,4], Sofia Dembski[1,5,6], Daniel Haddad[3,7], Bernd Ahrens[8,9], Stefan Schweizer[8,9], Bastian Christ[5], Alevtina Cubukova[5], Marco Metzger[5,6], Heike Walles[5,6], Peter M. Jakob[3,4] and Gerhard Sextl[1,2]

Full Research Paper

Open Access

Address:
[1]Fraunhofer Institute for Silicate Research ISC, Neunerplatz 2, 97082 Wuerzburg, Germany, [2]Department of Chemical Technology of Materials Synthesis, University of Wuerzburg, Roentgenring 11, 97070 Wuerzburg, Germany, [3]MRB Research Center for Magnetic Resonance Bavaria, Am Hubland, 97074 Wuerzburg, Germany, [4]Department of Experimental Physics 5 (Biophysics), University of Wuerzburg, Am Hubland, 97074 Wuerzburg, Germany, [5]Translational Center Wuerzburg “Regenerative Therapies for Oncology and Musculosceletal Diseases”, Branch of Fraunhofer Institute for Interfacial Engineering and Biotechnology IGB, 97070 Wuerzburg, Germany, [6]University Hospital Wuerzburg, Chair Tissue Engineering and Regenerative Medicine, Roentgenring 11, 97070 Wuerzburg, Germany, [7]Magnetic Resonance and X-ray Imaging Department of Fraunhofer Development Center X-ray Technology EZRT, a division of Fraunhofer Institute for Integrated Circuits IIS, Am Hubland, 97074 Wuerzburg, Germany, [8]South Westphalia University of Applied Sciences, Luebecker Ring 2, 59494 Soest, Germany and [9]Fraunhofer Application Center for Inorganic Phosphors, Branch Lab of Fraunhofer Institute for Microstructure of Materials and Systems IMWS, Luebecker Ring 2, 59494 Soest, Germany

Email:
Marion Straßer[*] - marion.strasser@isc.fraunhofer.de

* Corresponding author ‡ Equal contributors

Keywords:
calcium fluoride nanoparticles; magnetic resonance imaging (MRI); multifunctional nanoparticles; multimodal imaging; photoluminescence

Beilstein J. Nanotechnol. **2017,** *8,* 1484–1493.
doi:10.3762/bjnano.8.148

Received: 31 March 2017
Accepted: 22 June 2017
Published: 18 July 2017

This article is part of the Thematic Series "Nanomaterial-based cancer theranostics".

Guest Editor: V. Sivakov

Abstract

New multifunctional nanoparticles (NPs) that can be used as contrast agents (CA) in different imaging techniques, such as photoluminescence (PL) microscopy and magnetic resonance imaging (MRI), open new possibilities for medical imaging, e.g., in the fields of diagnostics or tissue characterization in regenerative medicine. The focus of this study is on the synthesis and characterization of CaF_2:(Tb^{3+},Gd^{3+}) NPs. Fabricated in a wet-chemical procedure, the spherical NPs with a diameter of 5–10 nm show a crystalline structure. Simultaneous doping of the NPs with different lanthanide ions, leading to paramagnetism and fluorescence, makes them suitable for MR and PL imaging. Owing to the Gd^{3+} ions on the surface, the NPs reduce the MR T_1 relaxation time constant as a function of their concentration. Thus, the NPs can be used as a MRI CA with a mean relaxivity of about $r = 0.471$ mL·mg^{-1}·s^{-1}.

Repeated MRI examinations of four different batches prove the reproducibility of the NP synthesis and determine the long-term stability of the CAs. No cytotoxicity of NP concentrations between 0.5 and 1 $mg \cdot mL^{-1}$ was observed after exposure to human dermal fibroblasts over 24 h. Overall this study shows, that the CaF_2:(Tb^{3+},Gd^{3+}) NPs are suitable for medical imaging.

Introduction

In recent years, medical imaging has become an important approach in the fields of diagnostics, therapy and regenerative medicine. Besides the classical technology of X-ray examination, contrast-rich methods such as computed tomography (CT), magnetic resonance imaging (MRI), positron emission tomography (PET) and ultrasonic techniques are being used increasingly for imaging soft tissue, e.g., cartilage imaging in progressive osteoarthritis. Advantages of different imaging techniques are used individually or combined to obtain a more detailed answer for medical questions and, thus, to reach a rapid and precise diagnosis. CT and MRI provide essentially morphological information and information on tissue structures and changes. Nuclear medicine procedures such as PET visualize metabolic processes and provide information on biochemical parameters. The optical imaging techniques such as fluorescence (PL) microscopy allow for a direct transfer of biological knowledge about cells in the in vivo application, e.g., endogenous regulation of transcription [1]. In this context, greater treatment success can be achieved through the combination of several detection methods. Contrast agents (CAs) are used to improve representation of structures and functions of the body by increasing the sensitivity and reducing the ambiguity in imaging techniques. Since the imaging techniques are based on different physical principles, different CAs are required. For the patient, this is associated with extended examination times, multiple injections and repeated contact with chemical substances. This results in an increased workload for the medical staff and an uncomfortable screening procedure for the patient. Therefore, it is desirable to develop a combined CA that is injected only once and then detected using different diagnostic methods with a higher comparability.

The production of CAs on the basis of nanoparticles (NPs) shows promise, as already examined on the infected myocardium [1-3]. Each imaging modality has its advantages and disadvantages. The integration of multiple functions into one NP system yields synergies and allows for a precise and fast diagnosis of diseases. Recently, various multimodal imaging probes on the basis of different functional NPs were fabricated for more accurate imaging and diagnosis [2]. One possibility is the synthesis of core/shell-structured NPs. Core and shell materials can be matched individually to specific detection methods. For example, the coating of a magnetic core with silicates or polymer shells doped with organic fluorophores or quantum dots (QDs) allows for the detection of NPs by MRI and PL [4]. Several successive shells can be designed of different inorganic materials. In this context, the following particle systems may be mentioned $Gd_2O(CO_3)_2 \cdot H_2O/SiO_2$/Au, Fe_3O_4/C/Ag and Fe_3O_4/SiO_2/Y_2O_3:(Yb^{3+},Er^{3+}) core/shell NPs [5-7]. Another possibility is to create multifunctional NPs by precipitation and simultaneous doping of the NP matrix with various ions [8,9]. Due to their co-doping with lanthanide ions, NPs on the basis of calcium phosphate or gadolinium oxide are also detectable by MRI and PL [10-13].

In recent years, fluorides have attracted considerable interest owing to their unique optical properties [14]. Fluoride NPs were used in lighting, optical amplification and lasing [14] and are well-known strategic materials in optical and photonic technologies in general. Furthermore, they combine high quantum efficiency with favorable chemical and mechanical properties. They seem to be perfect materials as fluorescence host matrix owing to their low phonon energies and they subsequently minimize the quenching of the excited state of rare-earth ions. In contrast to chloride or bromide hosts, fluorides are completely air stable materials [15,16].

Other than fluoride NP systems doped with rare earth elements, such as LaF_3:Ln^{3+}, CeF_3:Tb^{3+}, $NaYF_4$:(Yb^{3+},Er^{3+}), $NaGdF_4$:(Yb^{3+},Er^{3+}), which were actively investigated during last decades for biomedical applications [17-22], alkaline earth metal fluorides such as CaF_2 received little attention. There are only sporadic suggestions for the synthesis and application of this NP system as a labeling material. To date, CaF_2 has attracted most attention with respect to UV lithography, UV-transparent optical lenses, the surface conditioning of glass, the promotion of biocompatible agents for bone and teeth reconstruction [23]. Calcium fluoride exhibits a wide transparent spectral window (190–1100 nm), large band gap (approx. 12 eV), low refractive index and low phonon energy [14].

Because of the high stability and flexibility of the fluorite structure, a number of various ionic substitutions can also be integrated in the CaF_2 lattice [24]. Various methods have been reported for the preparation of rare-earth doped CaF_2 NPs such as co-precipitation [14,15,24-26], hydrothermal methods [27-29], flame synthesis [30], microemulsion methods [31,32] and a fluorolytic sol–gel process [33]. The stability and biocompatibility of CaF_2 makes it an attractive material for biomedical applications [28,29]. In addition, due to the high capacity to

accept lanthanide ions, CaF_2 is suitable for the preparation of CAs for multimodal imaging [24].

In this study, we report on synthesis and characterization of multifunctional NPs based on CaF_2. These NPs are produced by wet-chemical synthesis and doped with multiple ions leading to paramagnetism and fluorescence, making them suitable for T_1-weighted MRI and PL microscopy. The characterization of the resulting NPs is carried out by using transmission electron microscopy (TEM), X-ray diffraction (XRD) analysis, inductively coupled plasma optical emission spectrometry (ICP-OES), and photoluminescence (PL) spectroscopy. The capability of these NPs to be used as positive CAs for MRI was also investigated. In addition, the cytotoxicity of the NPs was tested by a cell culture based viability assay.

Results and Discussion

Synthesis and characterization of the multifunctional nanoparticles

The synthesis of the CaF_2:(Tb^{3+},Gd^{3+}) NPs was carried out in analogy to the reported wet-chemical procedure that is based on a co-precipitation process in ethanol [26]. Moreover, the NPs were doped with different lanthanide ions (Tb^{3+}, Gd^{3+}; 1 mol % based on Ca content) to guarantee a PL and MR activity. $CaCl_2$, $Tb(NO_3)_3{\cdot}5H_2O$, $GdCl_3{\cdot}6H_2O$ and NH_4F were used as reactants to prepare the NPs by a low-temperature single-step approach. $CaCl_2$ and NH_4F exhibit a significant solubility in water, but CaF_2 is insoluble in water and precipitates from aqueous solution. It is difficult to control the particle growth in aqueous solution and therefore the synthesis of the doped NPs is carried out in ethanol. This solvent contains a very low F^- ion concentration because of the low solubility of NH_4F in an ethanol solution and therefore the particle growth is slower [26].

The inset in Figure 1 shows the TEM micrograph of the CaF_2:(Tb^{3+},Gd^{3+}) NPs. The NPs possess a spherical shape with an average diameter of 5–10 nm. The results of the dynamic light scattering (DLS) show that these NPs are non-agglomerated and exhibit a narrow size distribution and a hydrodynamic particle diameter of 25–30 nm (number- and volume-weighted, Figure 1, see also DLS of the stabilized NPs, Figure S1, Supporting Information File 1 (number-weighted)).

For the determination of the MR relaxivity of the NPs, we use the hydrodynamic particle diameter from the DLS, because the correlation time between them and the surrounding water molecules depends on the tumbling of the NPs, which is influenced by their size and their morphology.

Figure 2 displays a selected XRD pattern of the crystalline CaF_2:(Tb^{3+},Gd^{3+}) NPs, all other samples exhibit the same tendency. The phase analysis indicates that the obtained product shows prominent peaks well accordant with the JCPDS standard card (Joint Committee on Powder Diffraction Standards, Powder Diffraction File: 035-0816) of fluorite (CaF_2). Moreover, there are reflexes of NH_4Cl detectable which come from the educts. Doping with multiple ions does not have influence on the formation of calcium fluoride crystal lattice.

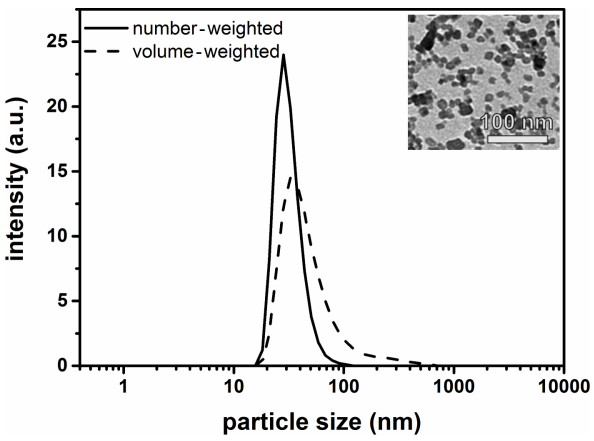

Figure 1: DLS measurement of the CaF_2:(Tb^{3+},Gd^{3+}) NPs (number- and volume-weighted). Inset: TEM micrograph of the same particles. The size of the NPs is in the range of 5–10 nm and they have a spherical shape.

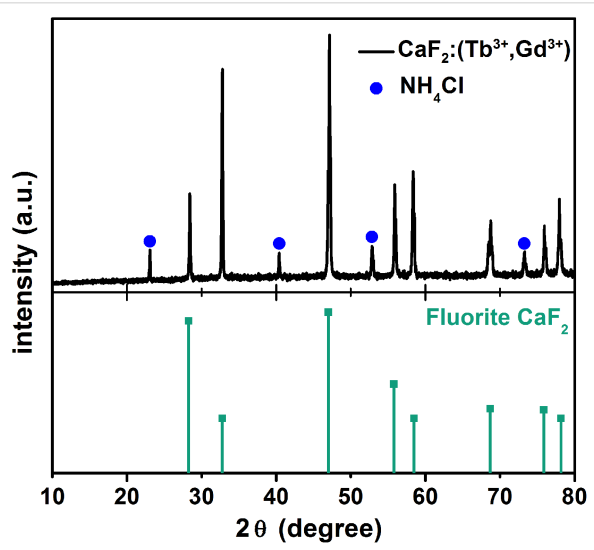

Figure 2: In the upper part, the XRD pattern of the CaF_2:(Tb^{3+},Gd^{3+}) NPs (d = 5–10 nm, doping concentration of Tb^{3+} and Gd^{3+}: 1 mol %) is plotted. Below a reference spectrum from the database JCPDS (Joint Committee on Powder Diffraction Standards, Powder Diffraction File: 035-0816) is shown. The reflexes of both spectra appear at the same diffraction angles 2θ, which indicates the crystalline structure (CaF_2 = fluorite) of the NPs. The blue points mark the peaks of NH_4Cl.

Since the XRD measurement only implies that the NPs have the crystalline structure of fluorite and nothing about the incorpora-

tion of the lanthanide ions, we analyze the composition of our nanoparticles further by means of ICP-OES. Table 1 shows the outcome of a representative sample.

Table 1: Representative outcome of an ICP-OES measurement of CaF_2:(Tb^{3+},Gd^{3+}) NPs.

element	amount of substance (mol)	doping (mol %)
F	0.46	
Ca	0.20	
Tb	0.02	0.87
Gd	0.02	0.92

The obtained ratio of calcium and the lanthanide ions to fluoride ((Ca+Ln)/F = 0.52) is an additional confirmation of the crystalline structure of fluorite with a composition of CaF_2. The doping levels are in the intended range of 1 mol %. However, there is a lower content of Tb^{3+} and Gd^{3+} (total amount of 1.83 mol %), which indicates a higher reaction rate of calcium compared to the dopants. This could be correlated to the different ion radii.

Photoluminescence spectroscopy

With respect to a later usage of our NPs as a contrast agent for PL we have also investigated the optical properties. Since terbium and its optical properties are extensively described in the literature [34-37], we use it as a model system in order to proof the integration of the ions in the calcium fluoride lattice (proof of principle). For a later clinical usage certainly we have to exchange terbium for a NIR dye or something similar because of the high sensitivity of living tissues towards UV light. In Figure 3 the emission spectrum of CaF_2:(Tb^{3+},Gd^{3+}) NPs at an excitation wavelength of λ_{exc} = 254 nm is shown. There are several maxima (490, 542, 586 and 622 nm), which represent the Tb^{3+}-related transitions from the $^5D_4$ excited state to the energy levels indicated [34,35]. The main emission line can be assigned to the $^5D_4 \rightarrow {}^7F_5$ transition of Tb^{3+} and causes an intense emission in the green spectral range (λ = 542 nm, Figure 3) [36,37]. Additionally, to XRD and ICP-OES measurements this was a confirmation of a successful integration of the Tb^{3+} ions in the calcium fluoride host lattice.

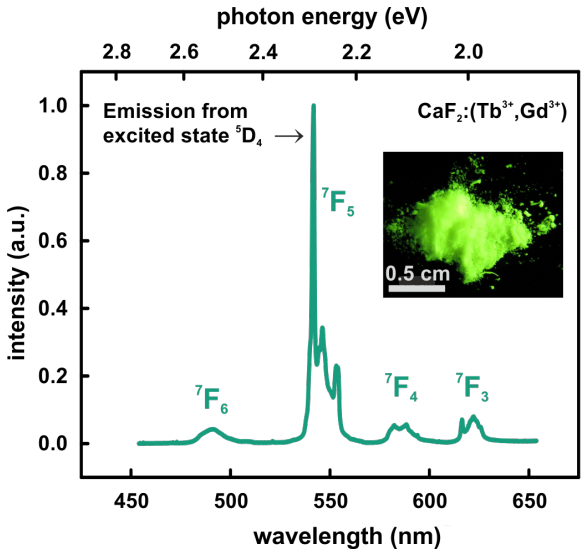

Figure 3: Normalized photoluminescence spectrum of CaF_2:(Tb^{3+},Gd^{3+}) NPs at an excitation wavelength of λ_{exc} = 254 nm. The emission spectrum shows several maxima (490, 542, 586 and 622 nm), which represent the Tb^{3+}-related transitions from the $^5D_4$ excited state to the energy levels indicated. The maximum intensity occurs in the green spectral range at a wavelength of λ = 542 nm. Inset: CaF_2:(Tb^{3+},Gd^{3+}) NP powder under UV light excitation (λ_{exc} = 254 nm). The green luminescence matches the maximum of the emission spectrum.

Magnetic resonance imaging

MRI is a non-invasive method that is optimized for soft tissue imaging in daily clinical use. Paramagnetic CAs are often used to reduce the measurement period or to gain higher signal-to-noise-ratios (SNR) which allows for improved diagnosis. Within this study, the capability of CaF_2:(Tb^{3+},Gd^{3+}) NPs to be used as positive CAs for MRI was investigated. To this end, different NP samples dispersed in water were characterized by MRI. To determine the contrast effect, NP dispersions of various concentrations (0.4–18.2 mg·mL^{-1}) were analyzed.

CaF_2:(Tb^{3+},Gd^{3+}) NPs as MRI contrast agent

Doping with Gd^{3+} ions leads to paramagnetism of the CaF_2 NPs. Because of this the NPs can be used as a T_1 CA. Additionally, there should be also an attenuation of the CT signal, which allows for the application as a CT CA. This property is already closer investigated in an ongoing study and will be shown in an additional publication in the future.

The T_1-weighted image of the CaF_2:(Tb^{3+},Gd^{3+}) NPs with concentrations in the range from 0.4 to 18.2 mg·mL^{-1} is shown in Figure 4a. Due to the different concentrations of the samples, the T_1 relaxation time constants vary and therefore, different signal intensities are observable at different time points.

To evaluate the potential CA not only on a qualitative basis, it is required to determine the efficiency quantitatively. First, it is necessary to measure the signal intensity at different time points and fit these intensities with a mono-exponential function. A T_1-map can be calculated (cf. Figure 4b). In this batch, the T_1 values of the NPs vary from 137 to 1633 ms with decreasing concentrations. Plotting the relaxation rate R_1 (inverse relaxation time T_1) over the concentration of the samples, the relax-

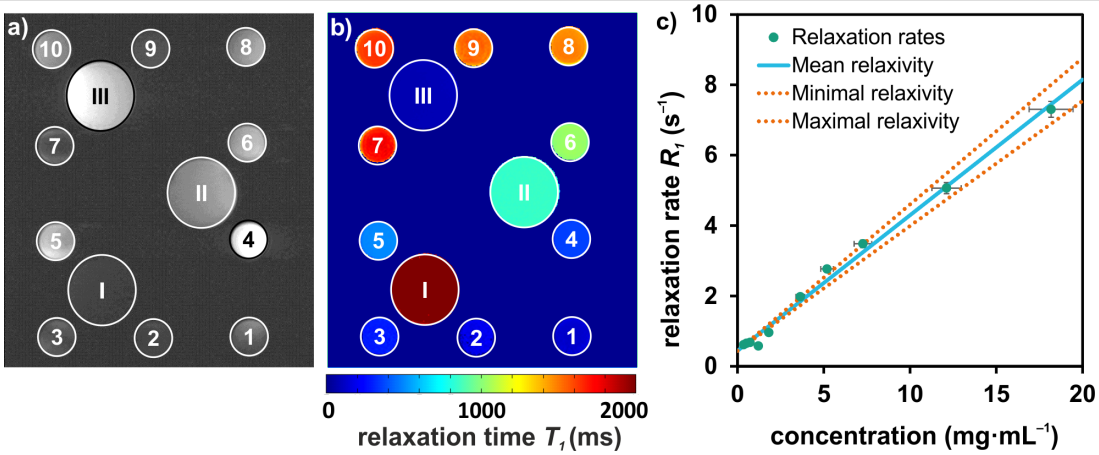

Figure 4: a) T_1-weighted MR image of the CaF_2:(Tb^{3+},Gd^{3+}) NPs with different concentrations in the range from 0.4 to 18.2 $mg \cdot mL^{-1}$ (1–10). I–III are reference samples of water and two concentrations of Magnevist. The different concentrations result in observable differences of the signal intensities. In b) the following T_1-map with a corresponding color range from 0 to 2000 ms is shown. c) The relaxivity (r = 0.385 ± 0.030 $mL \cdot mg^{-1} \cdot s^{-1}$) arises from the slope by plotting the relaxation rates over the concentrations. The errors of the relaxivity are given by the minimal and maximal slope.

ivity r arises from the slope of the linear fit (cf. Equation 1, Figure 4c).

$$R_1(c) = R_1(c=0) + r \cdot c. \quad (1)$$

The relaxivity indicates the efficiency of the CA. The most common CA in clinical applications is Magnevist (gadopentetate dimeglumine) with a relaxivity of 4.89 $mL \cdot mg^{-1} \cdot s^{-1}$ [38]. In this study, Magnevist was used as a reference in each measurement. Generally, the relaxivity is given in liters per mole per second. To compare the obtained relaxation rates from our NP dispersions with the relaxation rate from Magnevist we should convert the units because Magnevist is a complex with only one Gd^{3+} ion. In contrast, there are many Gd^{3+} ions in one NP evoking the MR activity. Unfortunately, we cannot quantify by now the exact amount of Gd^{3+} ions on the surface. The ICP-OES measurements (cf. Table 1) tell us how many Gd^{3+} ions are within the NPs in total, but most probably only the Gd^{3+} on the surface are responsible for the contrasting effect. Therefore, we convert the units into milliliters per milligram per second (for the calculation see Figure S2, Supporting Information File 1).

The relaxation rates obtained have a standard deviation of 3.1%. This value is used for the uncertainty of the MRI measurement itself and therefore also for the relaxation rates of the NPs. For acquiring the relaxivity of the NPs, an additional source of error is the uncertainty of the concentration of each sample. Determining the concentration, a gravimetrical measurement was carried out three times for each sample. The maximum deviation of the values was about ±7%, because of different error sources such as weighing or pipetting of the small sample volumes. The error of the relaxivity is given by the resulting minimal and maximal slope (Figure 4c).

Reproducibility of the MR relaxivity

To test the reproducibility of the CA efficiency, four batches of NPs were produced and their relaxivities were determined. These results are shown in Table 2 and Figure 5.

The first row of Table 2 and the green bars of Figure 5 represent the results of the measurements directly after fabrication. All results overlap with their error bars and additionally the mean value lies also within the ranges of all batches. Therefore, the relaxivities of all batches are comparable with each other indicating a high reproducibility of the synthesis procedure. This matches to the above described results of TEM, DLS and ICP-OES examinations.

Long-term stability

The long-term stability of the relaxivity over time was examined. All batches were investigated nine months after fabrica-

Table 2: Relaxivities of four different batches: as prepared (row 1) and nine months after fabrication (row 2).

	batches	1	2	3	4
relaxivity r [$mL \cdot mg^{-1} \cdot s^{-1}$]	as prepared	0.438 ± 0.044	0.443 ± 0.044	0.522 ± 0.052	0.451 ± 0.045
	nine months after fabrication	0.385 ± 0.038	0.388 ± 0.039	0.467 ± 0.046	0.400 ± 0.040

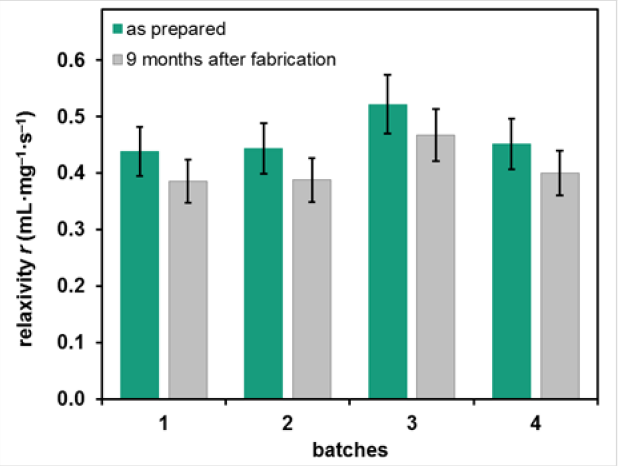

Figure 5: Relaxivity values of the four batches as prepared (green) and nine months (grey) after fabrication. Considering the error bars, the measured relaxivities directly after the preparation overlap with each other. After nine months a decrease of the relaxivity of each batch can be observed.

tion. These results are also shown in Table 2 and Figure 5. It is apparent that all relaxivities decrease over time. The difference between both groups (all batches as prepared and nine months after fabrication), which was tested with a *t*-test, is highly significant ($p < 0.01$). This decrease of the relaxivities cannot be explained with the deviation of the MR measurements. More likely, this trend is triggered by an agglomeration of the NPs. This results in a lower concentration of Gd^{3+} on the surface of the NPs, which leads to a lower interaction with the surrounding protons, implying a higher relaxation time constant and consequently a lower relaxivity. On average, all batches decrease about 11.6% after nine months. Through an examination of the vertical distribution of the T_1 relaxation time constants in the probing tubes a sedimentation of the NPs or a decrease of the relaxivity can be excluded. Also, a decomposition of the NPs, resulting in an increase of the free Gd^{3+} concentration within the solution and therefore an increase of the relaxivity, does not take place. This is another very important property of our CA, because of the toxicity of free Gd^{3+} ions.

Biocompatibility

In general, NPs without appropriate surface modification have a disposition to agglomerate and sediment subsequently under physiological conditions because of their pH value and salt content [39-41]. One crucial requirement for the application of NPs in cell-culture experiments or animal testing is the stabilization in physiological media. In contrast to an electrostatically stabilization of the NPs, for example by capping the CaF_2 NPs surface with citrate groups [28], we ensure the stability of the NPs in serum-containing cell-culture media in an electrosterical way. To this end, a polymer consisting of a polycarboxylate ether backbone and polyethylene oxide side chains bound to the backbone as esters (Melpers®2450), which can be considered as non-toxic [42], is adsorbed via Coulomb attraction between the negatively charged backbone on the positively charged NP surface [43]. As shown in photographs of bare and Melpers®2450-stabilized NPs dispersed in cell-culture medium containing fetal calf serum (FCS) (cf. Figure 6a), bare NPs start to sediment after 24 h and the stabilized sample remains clear. Additionally, the colloidal stability was monitored by UV–vis spectroscopy. The absorbance measurements (λ_{abs} = 700 nm) of stabilized and non-stabilized CaF_2:(Tb^{3+},Gd^{3+}) NPs in FCS-containing cell-culture medium over a period of 24 h is shown in Figure 6b. In contrast to non-stabilized NPs, the stabilized sample shows hardly any change in absorbance over a period of 24 h. The measured curve of non-stabilized NPs decreases within 2 h because of light scattering on NP agglomerates. Light-microscopy images of dispersions of stabilized and non-stabilized CaF_2:(Tb^{3+},Gd^{3+}) NPs in FCS-containing cell-culture medium are given in Figure S3 (Supporting Information File 1).

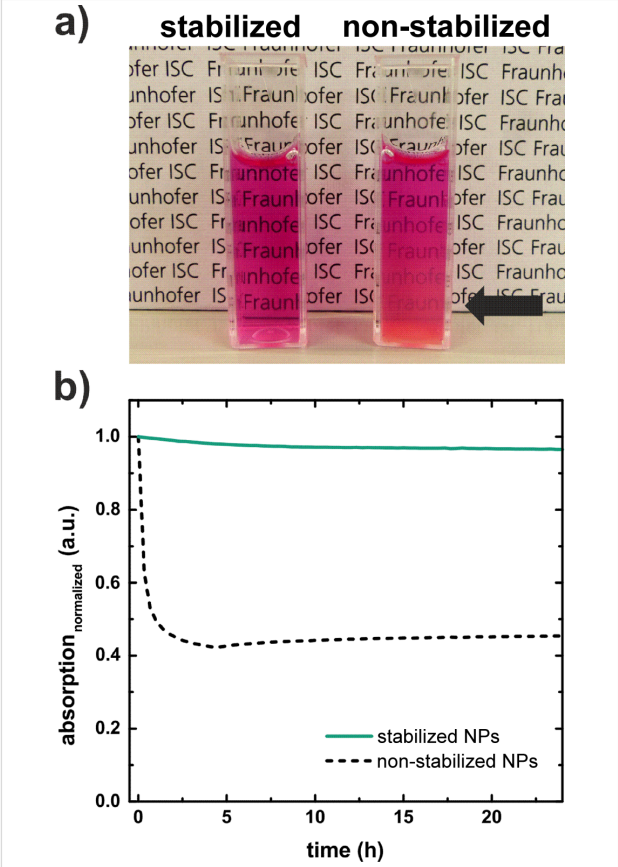

Figure 6: Sedimentation study of the CaF_2:(Tb^{3+},Gd^{3+}) NPs (5 mg·mL^{-1}) in Dulbecco's Modified Eagle's Medium (DMEM) with 10% FCS stabilized with Melpers®2450 and non-stabilized:
a) photographs of the stabilized NPs and the non-stabilized NPs 24 h after dispersing the NPs in FCS-containing cell-culture medium and
b) absorbance measurement (λ_{abs} = 700 nm) of the samples over a period of 24 h.

Finally, the viability of human dermal fibroblasts (hdF) after treatment with the NPs stabilized with Melpers®2450 for 24 h was evaluated. Therefore, the CellTiter-Glo assay was used [44], a method that is based on the quantification of adenosine-5′-triphosphate (ATP), which signals the presence of metabolically active cells. Adding the CellTiter-Glo reagent directly to hdF results in cell lysis and generates a luminescent signal directly proportional to the amount of the ATP concentration. The particle samples with a cellular viability over 80% can be classified as biocompatible. We have chosen concentrations of CaF_2:(Tb^{3+},Gd^{3+}) NPs between 0.5 and 1 mg·mL^{-1} for the assay because in this concentration range we have observed a good MR activity. Figure 7a shows a representative microscopic image of the hdF 24 h after treatment with the NPs (c = 1 mg·mL^{-1}). There is clear evidence that the cells treated with the NPs compared to untreated cells kept their typically morphology and proliferated normally under standard culture conditions. The granular structures in the picture arise from FCS (cf. untreated cells, Figure S4, Supporting Information File 1). The results of a CellTiter-Glo assay show the viability of hdF 24 h after treatment of these cells with the NP dispersions (cf. Figure 7b). NP concentrations of 0.5, 0.75 and 1.0 mg·mL^{-1} yield cell viabilities of more than 80% with respect to the positive control. Thus in this concentration range no cytotoxicity of CaF_2:(Tb^{3+},Gd^{3+}) NPs is observed on hdF.

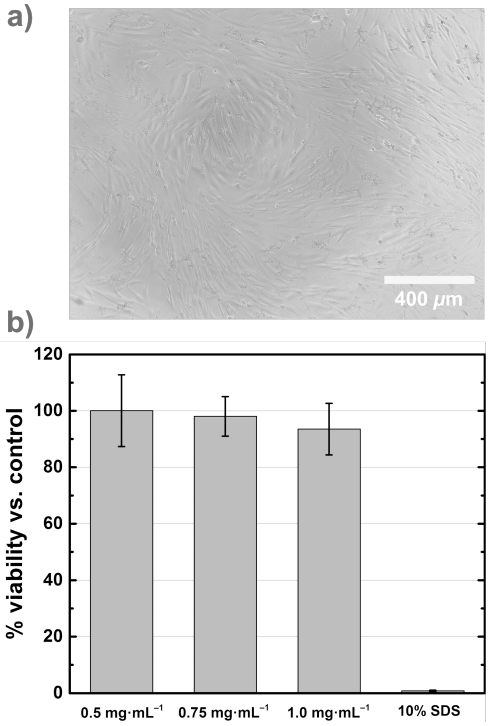

Figure 7: a) Representative microscopic image of hdF 24 h after treatment with the NPs (c = 1 mg·mL^{-1}). b) Cell viability 24 h after adding CaF_2:(Tb^{3+},Gd^{3+}) NPs at concentrations between 0.5 and 1 mg·mL^{-1} to hdF. 10% SDS was used for the positive control. All samples have cell viabilities over 80% and therefore the NPs can be classified as non-cytotoxic (n = 3).

Conclusion

In summary, we have demonstrated a new multifunctional particle system CaF_2:(Tb^{3+},Gd^{3+}), which was fabricated via a co-precipitation process. TEM, DLS, XRD and ICP-OES examinations deliver a consistent characterization of the NPs. According to TEM and DLS measurements, the mean size of the NPs is in the range of 5–10 nm and they have a spherical shape. In the XRD diffractogram the crystalline structure of fluorite CaF_2 is observable. The outcome of ICP-OES shows a congruent composition of the NPs in all different batches. Hence the results of these characterization methods evidence that the used synthesis was successful and capable of producing the desired particle system. The assumption is that doping with the rare-earth ions Tb^{3+} and Gd^{3+} leads to a PL and MR activity. The Tb^{3+} emission spectrum shows maxima at the expected wavelengths (489, 542, 585, 621 and 667 nm). This signifies the successful Tb^{3+} doping and thus, the NPs are suitable for use as a PL CA. With the second investigated imaging technique MRI we verified the integration of the Gd^{3+} ions in the CaF_2 lattice and the reproducibility of the NP synthesis procedure. Furthermore, we investigated the long-term stability of the relaxivities. In fact, the results for all batches show a decrease of the relaxivity of about 11.6% after nine months. Finally, the cell viability of the NPs stabilized with Melpers®2450 was evaluated in hdF and we can show that the NP system is biocompatible and non-toxic.

Overall, we have developed a very promising particle system CaF_2:(Tb^{3+},Gd^{3+}), which can be used as a multimodal CA for two different imaging methods and therefore allows for a more reliable, precise and time efficient diagnosis of diseases.

Experimental

Materials

Calcium chloride ($CaCl_2$, ≥95%), ammonium fluoride (NH_4F, p.a.), terbium(III) nitrate pentahydrate ($Tb(NO_3)_3{\cdot}5H_2O$, 99.9%) and gadolinium(III) chloride hexahydrate ($GdCl_3{\cdot}6H_2O$, 99%) were purchased from Sigma-Aldrich and used without further purification.

Synthesis of CaF_2:(Tb^{3+},Gd^{3+}) NPs

Following Wang et al., 3.72 g (33.5 mmol) $CaCl_2$, 146 mg (340 μmol, 1 mol % based on Ca content) $Tb(NO_3)_3{\cdot}5H_2O$ and 121 mg (340 μmol, 1 mol % based on Ca content) $GdCl_3{\cdot}6H_2O$ were dissolved in 420 mL ethanol [26]. 2.5 g (67.5 mmol) of ammonium fluoride were added under sonification. Subsequently, the solution was stirred at room temperature for 12 h. The resulting precipitate was collected by centrifugation and

washed with ethanol and deionized water for three times to remove possible impurities such as $CaCl_2$. Then the precipitate was dried at 60 °C for 12 h and collected for characterization.

Characterization

The morphology of the NPs was studied by TEM on a Zeiss EM 900 transmission electron microscope at an acceleration voltage of 200 kV. Samples were prepared by dipping 200 mesh copper grids coated with a thin carbon film (Quantifoil Micro Tools GmbH) into aggregate-free NP dispersions. The size of the particles was determined by the measurement tools of Fiji. The DLS was measured with a Zetasizer Nano-ZS from Malvern Instruments. The DLS measurement was carried out in aqueous solutions. X-ray diffraction measurements were carried out on a Phillips PW 1730/10 employing Cu Kα radiation. The composition of the NPs was determined by ICP-OES using a Varian Wista Pro spectrometer. The crystallinity of the powder samples was analyzed with a Philips PW 1152. For photoluminescence measurements, a custom-built photospectrometer (S&I Spectroscopy & Imaging FluoroVista) was used. The excitation of the Tb^{3+}-related emission spectra was carried out with a 254 nm UV lamp (Vilber Lourmat VL-4.LC), the emission was detected with a high-speed silicon CCD camera (Princeton Instruments PIXIS256). The spectra were not corrected for the spectral sensitivity of the experimental setup.

MRI measurements

To guarantee a homogenous distribution within each sample, all tubes were sonicated for five minutes and vortexed afterwards. The MRI examinations took place within the following hour. All measurements were performed at a 1.5 T system (Magnetom Avanto, Siemens) in combination with a 4 + 4 channel multifunctional coil array (NORAS MRI products). The relaxation time constant T_1 was obtained through a segmented 2D IRSnapshotFlash method (T_R/T_E = 8.7 ms/4.8 ms, matrix: 256 × 176, inplane resolution: 0.7 × 0.7 mm^2, slice thickness: 20 mm, number of segments: 44, number of echoes: 128, T_A = 4.75 min) [45,46]. Image reconstruction, data fitting and a manually segmentation of the tubes was done offline using Matlab R2012b (The Mathworks). The program used for the statistical analysis was PASW Statistics 18 (IBM).

Biocompatibility

CaF_2:(Tb^{3+},Gd^{3+}) NPs were stabilized by shaking the particles in a 20 vol % Melpers®2450 dispersion in water for 18 h. Afterwards the NPs were centrifuged, washed two times with DI water and finally redispersed in DMEM with 10% FCS.

The sedimentation studies over 24 h were carried out by monitoring the absorbance at 700 nm as a function of time (Shimadzu, UV-3100). The sample (5 $mg \cdot mL^{-1}$ NPs in DMEM with 10% FCS, with or without Melpers®2450) was placed into a polystyrene micro cuvette and the absorbance was measured in 20 min time intervals. As the measurement beam entered the cuvette approximately 1.5 cm from the bottom of the cuvette, the supernatant of the sedimenting sample was measured. As a reference DMEM with 10% FCS was used. The first measurement was taken as 1.0 and the reference as 0.

The cell toxicity of the CaF_2:(Tb^{3+},Gd^{3+}) NPs was investigated in 96-well plates on a subconfluent monolayer culture of hdF. With the CellTiter-Glo luminescent cell viability assay (Promega), based on the quantification of the ATP concentration, the cell viability was examined. The cell line was seeded into 96-well cell-culture plates at a number of $1.47 \cdot 10^4$ cells per square centimeter. Dilutions of CaF_2:(Tb^{3+},Gd^{3+}) NP samples in the concentration range of 0.5–1 $mg \cdot mL^{-1}$ in DMEM with 10% FCS were added in triplicate. Wells containing 10% sodium dodecyl sulfate (SDS) and untreated hdF in DMEM with 10% FCS were used as positive and negative control, respectively. After 24 h of incubation, the CellTiter-Glo reagent was administered per well according to the instructions of the manufacturer. Briefly, the test solutions were removed by washing with PBS buffer, the cells in each well were overlaid with 100 µL of basal medium and 100 µL of CellTiter-Glo reagent and luminescence was measured after two minutes of shaking and ten minutes incubation at room temperature in a TECAN plate reader (infinite M200, TECAN, Maennedorf, Switzerland). According to DIN EN ISO 10993-5, a more than 20% deviation of measurement values of treated cells compared to the untreated control was defined as cytotoxic.

Supporting Information

Supporting Information File 1

Additional figures and data.
[http://www.beilstein-journals.org/bjnano/content/supplementary/2190-4286-8-148-S1.pdf]

Acknowledgements

M. Straßer and J. H. X. Schrauth contributed equally to this work. We thank Prof. Dr. Georg Krohne (Department of Biology, University of Wuerzburg, Germany) for providing the electron microscopy and Kevin Duscher for the support while stabilizing the NPs.

References

1. Doubrovin, M.; Serganova, I.; Mayer-Kuckuk, P.; Ponomarev, V.; Blasberg, R. G. *Bioconjugate Chem.* **2004,** *15,* 1376–1388. doi:10.1021/bc0498572

2. Park, J.; Yang, J.; Lee, J.; Lim, E.-K.; Suh, J.-S.; Huh, Y.-M.; Haam, S. *J. Colloid Interface Sci.* **2009,** *340,* 176–181. doi:10.1016/j.jcis.2009.08.015
3. Sosnovik, D. E.; Nahrendorf, M.; Deliolanis, N.; Novikov, M.; Aikawa, E.; Josephson, L.; Rosenzweig, A.; Weissleder, R.; Ntziachristos, V. *Circulation* **2007,** *115,* 1384–1391. doi:10.1161/CIRCULATIONAHA.106.663351
4. Corr, S. A.; Rakovich, Y. P.; Gun'ko, Y. K. *Nanoscale Res. Lett.* **2008,** *3,* 87–104. doi:10.1007/s11671-008-9122-8
5. Hu, K.-W.; Jhang, F.-Y.; Su, C.-H.; Yeh, C.-S. *J. Mater. Chem.* **2009,** *19,* 2147–2153. doi:10.1039/b815087g
6. Probst, J.; Dembski, S.; Milde, M.; Rupp, S. *Expert Rev. Mol. Diagn.* **2012,** *12,* 49–64. doi:10.1586/erm.11.86
7. Chen, J.; Guo, Z.; Wang, H.-B.; Gong, M.; Kong, X.-K.; Xia, P.; Chen, Q.-W. *Biomaterials* **2013,** *34,* 571–581. doi:10.1016/j.biomaterials.2012.10.002
8. Zheng, W.; Zhou, S.; Chen, Z.; Hu, P.; Liu, Y.; Tu, D.; Zhu, H.; Li, R.; Huang, M.; Chen, X. *Angew. Chem., Int. Ed.* **2013,** *52,* 6671–6676. doi:10.1002/anie.201302481
9. Zheng, W.; Zhou, S.; Chen, Z.; Hu, P.; Liu, Y.; Tu, D.; Zhu, H.; Li, R.; Huang, M.; Chen, X. *Angew. Chem.* **2013,** *125,* 6803–6808. doi:10.1002/ange.201302481
10. Lebugle, A.; Pellé, F.; Charvillat, C.; Rousselot, I.; Chane-Ching, J. Y. *Chem. Commun.* **2006,** 606–608. doi:10.1039/b515164c
11. Kim, E. J.; Choi, S.-W.; Hong, S.-H. *J. Am. Ceram. Soc.* **2007,** *90,* 2795–2798. doi:10.1111/j.1551-2916.2007.01791.x
12. Petoral, R. M., Jr.; Söderlind, F.; Klasson, A.; Suska, A.; Fortin, M. A.; Abrikossova, N.; Selegård, L.; Käll, P.-O.; Engström, M.; Uvdal, K. *J. Phys. Chem. C* **2009,** *113,* 6913–6920. doi:10.1021/jp808708m
13. Ashokan, A.; Menon, D.; Nair, S.; Koyakutty, M. *Biomaterials* **2010,** *31,* 2606–2616. doi:10.1016/j.biomaterials.2009.11.113
14. Pandurangappa, C.; Lakshminarasappa, B. N. *Opt. Commun.* **2012,** *285,* 2739–2742. doi:10.1016/j.optcom.2012.01.054
15. Wang, J.; Miao, W.; Li, Y.; Yao, H.; Li, Z. *Mater. Lett.* **2009,** *63,* 1794–1796. doi:10.1016/j.matlet.2009.05.047
16. Pandey, C.; Bhasin, J. K.; Dhopte, S. M.; Muthal, P. L.; Moharil, S. V. *Mater. Chem. Phys.* **2009,** *115,* 804–807. doi:10.1016/j.matchemphys.2009.02.027
17. Lim, S. F.; Riehn, R.; Ryu, W. S.; Khanarian, N.; Tung, C.-k.; Tank, D.; Austin, R. H. *Nano Lett.* **2006,** *6,* 169–174. doi:10.1021/nl0519175
18. Wang, Z. L.; Quan, Z. W.; Jia, P. Y.; Lin, C. K.; Luo, Y.; Chen, Y.; Fang, J.; Zhou, W.; O'Connor, C. J.; Lin, J. *Chem. Mater.* **2006,** *18,* 2030–2037. doi:10.1021/cm052360x
19. Zeng, J.-H.; Su, J.; Li, Z.-H.; Yan, R.-X.; Li, Y.-D. *Adv. Mater.* **2005,** *17,* 2119–2123. doi:10.1002/adma.200402046
20. Wei, Y.; Lu, F.; Zhang, X.; Chen, D. *Chem. Mater.* **2006,** *18,* 5733–5737. doi:10.1021/cm0606171
21. Park, Y. I.; Kim, J. H.; Lee, K. T.; Jeon, K.-S.; Na, H. B.; Yu, J. H.; Kim, H. M.; Lee, N.; Choi, S. H.; Baik, S.-I.; Kim, H.; Park, S. P.; Park, B.-J.; Kim, Y. W.; Lee, S. H.; Yoon, S.-Y.; Song, I. C.; Moon, W. K.; Suh, Y. D.; Hyeon, T. *Adv. Mater.* **2009,** *21,* 4467–4471. doi:10.1002/adma.200901356
22. Chen, Z.; Liu, Z.; Liu, Y.; Zheng, K.; Qin, W. *J. Fluorine Chem.* **2012,** *144,* 157–164. doi:10.1016/j.jfluchem.2012.08.009
23. Feldmann, C.; Roming, M.; Trampert, K. *Small* **2006,** *2,* 1248–1250. doi:10.1002/smll.200600140
24. Zhi, G.; Song, J.; Mei, B.; Zhou, W. *J. Alloys Compd.* **2011,** *509,* 9133–9137. doi:10.1016/j.jallcom.2011.06.084
25. Kumar, G. A.; Chen, C. W.; Riman, R. E. *Appl. Phys. Lett.* **2007,** *90,* 93123. doi:10.1063/1.2392284
26. Wang, F.; Fan, X.; Pi, D.; Wang, M. *Solid State Commun.* **2005,** *133,* 775–779. doi:10.1016/j.ssc.2005.01.014
27. Zahedifar, M.; Sadeghi, E.; Harooni, S. *Nucl. Instrum. Methods Phys. Res., Sect. B* **2012,** *291,* 65–72. doi:10.1016/j.nimb.2012.09.013
28. Dong, N.-N.; Pedroni, M.; Piccinelli, F.; Conti, G.; Sbarbati, A.; Ramírez-Hernández, J. E.; Maestro, L. M.; Iglesias-de la Cruz, M. C.; Sanz-Rodriguez, F.; Juarranz, A.; Chen, F.; Vetrone, F.; Capobianco, J. A.; Solé, J. G.; Bettinelli, M.; Jaque, D.; Speghini, A. *ACS Nano* **2011,** *5,* 8665–8671. doi:10.1021/nn202490m
29. Wang, G.; Peng, Q.; Li, Y. *J. Am. Chem. Soc.* **2009,** *131,* 14200–14201. doi:10.1021/ja906732y
30. Grass, R. N.; Stark, W. J. *Chem. Commun.* **2005,** 1767–1769. doi:10.1039/b419099h
31. Tian, Y.; Yu, J.-C.; Qi, X.-H.; Wu, X.-W.; Hua, R.-N.; Fan, S.-D. *J. Mater. Sci.: Mater. Electron.* **2009,** *20,* 439–444. doi:10.1007/s10854-008-9748-4
32. Bensalah, A.; Mortier, M.; Patriarche, G.; Gredin, P.; Vivien, D. *J. Solid State Chem.* **2006,** *179,* 2636–2644. doi:10.1016/j.jssc.2006.05.011
33. Ritter, B.; Krahl, T.; Rurack, K.; Kemnitz, E. *J. Mater. Chem. C* **2014,** *2,* 8607–8613. doi:10.1039/C4TC01073F
34. Binnemans, K.; Van Deun, R.; Görller-Walrand, C.; Adam, J. L. *J. Non-Cryst. Solids* **1998,** *238,* 11–29. doi:10.1016/S0022-3093(98)00540-7
35. Hou, Z.; Wang, L.; Lian, H.; Chai, R.; Zhang, C.; Cheng, Z.; Lin, J. *J. Solid State Chem.* **2009,** *182,* 698–708. doi:10.1016/j.jssc.2008.12.021
36. Gaft, M.; Panczer, G.; Reisfeld, R.; Uspensky, E. *Phys. Chem. Miner.* **2001,** *28,* 347–363. doi:10.1007/s002690100163
37. Boutinaud, P.; Mahiou, R.; Cousseins, J. C. *J. Lumin.* **1997,** *72–74,* 318–320. doi:10.1016/S0022-2313(96)00172-X
38. Reichenbach, J. R.; Hackländer, T.; Harth, T.; Hofer, M.; Rassek, M.; Mödder, U. *Eur. Radiol.* **1997,** *7,* 264–274. doi:10.1007/s003300050149
39. Allouni, Z. E.; Cimpan, M. R.; Høl, P. J.; Skodvin, T.; Gjerdet, N. R. *Colloids Surf., B* **2009,** *68,* 83–87. doi:10.1016/j.colsurfb.2008.09.014
40. Ji, Z.; Jin, X.; George, S.; Xia, T.; Meng, H.; Wang, X.; Suarez, E.; Zhang, H.; Hoek, E. M. V.; Godwin, H.; Nel, A. E.; Zink, J. I. *Environ. Sci. Technol.* **2010,** *44,* 7309–7314. doi:10.1021/es100417s
41. Bihari, P.; Vippola, M.; Schultes, S.; Praetner, M.; Khandoga, A. G.; Reichel, C. A.; Coester, C.; Tuomi, T.; Rehberg, M.; Krombach, F. *Part. Fibre Toxicol.* **2008,** *5,* 14. doi:10.1186/1743-8977-5-14
42. Koch, S.; Kessler, M.; Mandel, K.; Dembski, S.; Heuzé, K.; Hackenberg, S. *Colloids Surf., B* **2016,** *143,* 7–14. doi:10.1016/j.colsurfb.2016.03.010
43. Vaisman, L.; Wagner, H. D.; Marom, G. *Adv. Colloid Interface Sci.* **2006,** *128–130,* 37–46. doi:10.1016/j.cis.2006.11.007
44. Promega 2012, Technical Bulletin of CellTiter-Glo® Luminescent Cell Viability Assay. https://www.promega.de/-/media/files/resources/protocols/technical-bulletins/0/celltiter-glo-luminescent-cell-viability-assay-protocol.pdf (accessed June 22, 2017).
45. Haase, A.; Frahm, J.; Matthael, D.; Hänicke, W.; Merboldt, K.-D. *J. Magn. Reson.* **1986,** *67,* 258–266. doi:10.1016/0022-2364(86)90433-6
46. Haase, A. *Magn. Reson. Med.* **1990,** *13,* 77–89. doi:10.1002/mrm.1910130109

BEILSTEIN JOURNAL OF NANOTECHNOLOGY

A nanocomplex of C_{60} fullerene with cisplatin: design, characterization and toxicity

Svitlana Prylutska*[1], Svitlana Politenkova[1], Kateryna Afanasieva[1], Volodymyr Korolovych[2], Kateryna Bogutska[1], Andriy Sivolob[1], Larysa Skivka[1], Maxim Evstigneev*[3,4], Viktor Kostjukov[4], Yuriy Prylutskyy[1] and Uwe Ritter[5]

Full Research Paper

Open Access

Address:
[1]Taras Shevchenko National University of Kyiv, Volodymyrska Str., 64, 01601 Kyiv, Ukraine, [2]School of Materials Science and Engineering, Georgia Institute of Technology, Atlanta, USA, [3]Belgorod State University, Pobedy Str. 85, 308015 Belgorod, Russia, [4]Department of Physics, Sevastopol State University, Sevastopol 299053, Crimea and [5]Technical University of Ilmenau, Institute of Chemistry and Biotechnology, Weimarer Str., 25, 98693 Ilmenau, Germany

Email:
Svitlana Prylutska* - psvit@bigmir.net; Maxim Evstigneev* - max_evstigneev@mail.ru

* Corresponding author

Keywords:
atomic force microscopy; C_{60} fullerene; cisplatin; comet assay; computer simulation; dynamic light scattering; flow cytometry; human lymphocytes; toxicity in vitro

Beilstein J. Nanotechnol. **2017,** *8,* 1494–1501.
doi:10.3762/bjnano.8.149

Received: 08 March 2017
Accepted: 30 June 2017
Published: 20 July 2017

This article is part of the Thematic Series "Nanomaterial-based cancer theranostics".

Guest Editor: V. Sivakov

Abstract

The self-organization of C_{60} fullerene and cisplatin in aqueous solution was investigated using the computer simulation, dynamic light scattering and atomic force microscopy techniques. The results evidence the complexation between the two compounds. The genotoxicity of C_{60} fullerene, Cis and their complex was evaluated in vitro with the comet assay using human resting lymphocytes and lymphocytes after blast transformation. The cytotoxicity of the mentioned compounds was estimated by Annexin V/PI double staining followed by flow cytometry. The results clearly demonstrate that water-soluble C_{60} fullerene nanoparticles (0.1 mg/mL) do not induce DNA strand breaks in normal and transformed cells. C_{60} fullerene in the mixture with Cis does not influence genotoxic Cis activity in vitro, affects the cell-death mode in treated resting human lymphocytes and reduces the fraction of necrotic cells.

Introduction

The water-soluble inorganic bi-valent platinum derivative, cisplatin (*cis*-[Pt(II)$(NH_3)_2Cl_2$], Cis), is currently one of the most effective therapeutic agents used against cancer deceases, in particular, ovarian cancer, bladder cancer, esophagus cancer, lung cancer, and cancer of head and neck [1]. As an antitumor metal-containing agent Cis exerts an alkylating action and binds

covalently to DNA. In tumor cells Cis induces the selective inhibition of DNA synthesis and replication [2]. However, the action of Cis is accompanied by side effects that limit the use of Cis in anticancer chemotherapy. Cis-induced nephro-, hepato- and cardiotoxicity, as well as disorders of the central nervous system and sensory organs were reported [1]. Hence, there is a search for new drugs including nanodimensional compounds that could lower the side effects of Cis action, deliver Cis to the region of pathological process in a targeted manner, manage the curing at cell level, increase solubility in bioavailable form and protect Cis from degradation [3-9]. The carbon allotrope C_{60} fullerene could act as such a potent agent.

Pristine C_{60} fullerenes have no acute or sub-acute toxicity in vitro [10-12] and in vivo [13] (at least at low physiological concentrations), exerting strong antioxidant properties due to their high activity as free radical acceptors [14,15]. Water-soluble pristine C_{60} fullerenes penetrate through plasma membranes and are located in the central part of tumor cells [16]. Thereby, C_{60} fullerenes can be used for treatment of cancer [17,18], including combination chemotherapy [19] and photodynamic therapy [20-22]. They are also applied for the targeted delivery of drugs into tumor cells [23-25].

However, there are several conflicting reports in the literature regarding the genotoxicity of C_{60} fullerene [26]. Thus, a strong correlation between the genotoxic response and the concentration of an aqueous suspension of nC_{60} (178 nm in size) was observed at 2.2 μg/L in human lymphocytes using a single-cell gel electrophoresis assay [27]. In contrast, with stable C_{60} fullerene suspensions in 0.1% carboxymethylcellulose sodium or 0.1% Tween 80 aqueous solution no positive mutagenic response was observed up to the dose of 1 mg/plate with any tester strain in the bacterial genotoxicity tests in vitro and in vivo [28].

The aqueous suspension of C_{60} fullerenes caused positive responses in two bacterial genotoxicity tests, namely the Bacillus subtilis Rec-assay and umu test, up to concentrations of 0.048 mg/L and 0.43 mg/L, respectively. In [29], bulky DNA adducts could not be found by ^{32}P-postlabeling/polyacrylamide gel electrophoresis assay, suggesting that an aqueous suspension of C_{60} fullerenes has the potential to damage DNA. By use of a comet assay it was also demonstrated that an aqueous suspension of C_{60} fullerenes (0.1–1 mg/L) causes a concentration-dependent increase in DNA strand breaks in haemocytes [30].

The in vivo genotoxicity of C_{60} fullerene was estimated with a comet assay in lung cells of rats. After a single and repeated instillation inflammatory responses were observed in the lungs, suggesting that C_{60} fullerene has no potential for DNA damage even at inflammation causing doses [31]. Thus, it may be concluded that the genotoxicity of C_{60} fullerene in vitro and in vivo systems may strongly depend on its concentration in biomedium, dose administration, type of cells and time of exposure.

Since the biological action of C_{60} fullerene significantly differs from the action of traditional drugs by the mechanism of penetration inside cells and biodistribution [23-25,32-35], the conjugation of C_{60} molecules with drugs is currently considered a perspective biomedical strategy. The formation of a stable non-covalent nanocomplex of C_{60} fullerene with doxorubicin (C_{60}+Dox) in aqueous solution was confirmed theoretically and experimentally [23,34,36]. The antitumor action of the C_{60}+Dox nanocomplex was reported to be stronger than the sole action of Dox or C_{60} fullerene in vivo [23,24]. Moreover, recently it was found that C_{60} fullerene in C_{60}+Dox nanocomplex prevents cyto- and genotoxic effects of Dox on lymphocytes in vitro [37,38]. Based on these results it was suggested that the mechanism of complexation could induce biological synergy for other drugs administered together with C_{60} fullerene as well [19,23]. Taking into account the importance of Cis in chemotherapy of cancer, this drug could be a candidate molecule for study. A recent extended physico-chemical study has confirmed the formation of non-covalent entropically driven nanocomplexes between Cis and C_{60} fullerene in physiological solution (i.e., the adsorption of Cis in C_{60} fullerene clusters) [25,39]. Hence, it is reasonable to expect the biological interaction of these drugs. In order to testify this hypothesis in the present study we evaluated and compared in vitro cytotoxic action of C_{60} fullerene, Cis and their complex on lymphocytes from healthy persons, as well as their genotoxic effects towards resting lymphocytes and lymphocytes after blast transformation.

Experimental

Materials preparation

A highly stable reproducible aqueous colloid solution of pristine C_{60} fullerene (C_{60}FAS) with a maximum concentration of 0.15 mg/mL was prepared according to the protocol [40,41]. The initial stock solution of Cis (“Cisplatin-TEVA”, Pharmachemie B.V.) was prepared with a concentration of 0.5 mg/mL and was further diluted to the required concentrations used in particular experiments.

Immobilization of Cis on C_{60} fullerene was accomplished according to the following protocol: C_{60}FAS and Cis solution were mixed in a molar ratio of 1:2.4 (typically 0.1 mM C_{60} fullerene and 0.24 mM Cis). The obtained mixture was subjected to ultrasonic treatment in dispersant for 20 min, followed by magnetic stirring over 12 h at room temperature.

Computer simulation

The spatial structure of the C_{60} fullerene was built according to [http://www-jmg.ch.cam.ac.uk/data/molecules/misc/c60.html]. The spatial structure of Cis was built with the aid of HyperChem 8.0 according to Wysokiński et al. [42] and then optimizated in Gaussian 09W at the mPW1PW hybrid level of theory [43] in LanL2DZ basis set [44]. This level of theory and basis set is considered to be optimal for quantum-mechanical calculations of the molecules containing platinum atoms, in particular for Cis [42]. The spatial structure of the C_{60}+Cis nanocomplex was built according to Kostjukov et al. [45] with the aid of the XPLOR software (version 3.851 [46] with CHARMM27 force field). The plane of the Cis molecule was located parallel to the surface of the C_{60} fullereneat a distance of ca. 3.4 Å. Geometry optimization of the C_{60}+Cis nanocomplex was accomplished by means of molecular mechanics in X-PLOR. The modeling of the aqueous environment was carried out by water molecules in the form of TIP3P placed in a cubic box with a side length of 35 Å (1423 molecules).

DLS study

Measurement of the hydrodynamic size distribution was performed by dynamic light scattering (DLS) on a Zetasizer Nano ZS (Malvern Ins. Ltd) with upload of multiple narrow modes (high resolution) at room temperature. The instrument is equipped with a He–Ne gas laser (max. output power 5 mW) operating at a wavelength of 633 nm. The measurements were performed at a 173° scattering angle (NIBS technology). The autocorrelation function of the scattered light intensity was analyzed by the Malvern Zetasizer software.

The zeta potential was measured with a Zetasizer Nano ZS (Malvern Ins. Ltd) using a universal dip cell in disposable cuvettes. The Smoluchowski approximation was used to convert the electrophoretic mobility to the zeta potential.

AFM study

The surface morphology of the particles was examined using atomic force microscopy (AFM). AFM images were collected using an Integra Spectra microscope (NTMDT, Russia) in the "light" tapping mode according to the well-established procedure. For the sample preparation, a drop of solution was placed onto a pre-cleaned microscope glass slide and dried in air prior to AFM imaging.

Cell isolation and cultivation

Human peripheral blood from healthy donors was collected into a heparinized medical syringe. Lymphocytes were separated by centrifugation in a density gradient (Histopaque 1077, Sigma, USA) according to instructions of the manufacturer and washed twice: control lymphocytes in 0.15 M NaCl, lymphocytes that were intended for blast transformation reaction in RPMI 1640 medium. To induce the blast transformation the lymphocyte suspension was cultivated in RPMI 1640 medium with 10% FBS and 1000 units/mL IL-2α at 37 °C for 20 h. After cultivation the cells were washed in 0.15 M NaCl. Aliquots of the suspension were used for cytological analysis to evaluate the level of blast transformation (the fraction of lymphoblasts).

Incubation of lymphocytes and lymphoblasts

The cell suspension in RPMI 1640 medium (cell concentration in the range of 1×10^5 to 5×10^5 cells per mL) was incubated in the presence of either C_{60} fullerene (0.1 mg/mL), anticancer drug Cis (0.01, 0.1 or 0.15 mg/mL) or the complex of C_{60} fullerene with Cis (Cis concentration was 0.1 or 0.15 mg/L, the C_{60} fullerene to Cis molar ratio was equal to 1:2.4) for 1.5 h at 37 °C, washed once in 0.15 M NaCl, and then used for the comet assay. Five to seven independent repeats of the experiments were performed. As shown before [25], the molar ratio of 1:2.4 yields the highest anticancer activity of the C_{60}+Cis complex and was therefore used in the experiments.

Comet assay

To obtain lysed cells (nucleoids) 20 µL of the cell suspension was mixed with 40 µL of 1% low-melting agarose (Sigma, USA) at ca. 37 °C. 20 µL of the mixture were used to prepare a microscope slide previously covered with 1% high-melting agarose. After agarose polymerization, the slides were placed in the lysis solution consisting of 2.5 M NaCl, 100 mM EDTA, 10 mM Tris-HCl (pH 7.5), and 1% Triton X-100 (Ferak, Germany), which was added before use. Cells were exposed to lysis solution for 2 h at 4 °C. After the lysis, slides were washed with TBE buffer (89 mM Tris-borate, 2 mM EDTA, pH 7.5) and electrophoresed in the same buffer for 20 min at 4 °C (1 V/cm, 300 mA).

After electrophoresis, the slides were stained with 1.3 µg/mL of DAPI (Sigma, USA) and immediately analyzed under a fluorescence microscope (LOMO, Russia) connected with Canon A570 camera (a total 200 to 300 cells on each slide were analyzed). The relative amount of DNA in the comet tail, the parameter that reflects the level of DNA damages, was determined using the image analysis software programs Comet Assay IV (Perspective Instruments, UK) and CometScore (TriTec Corp., USA).

Cell-death assay

Apoptosis was assessed by staining cells with Annexin V–fluorescein isothiocyanate (FITC) and counterstaining with propidium iodide (PI) with the use Annexin V-FITC Apoptosis Detection Kit (Dojindo EU GmbH, Munich, Germany) according to the instructions of the manufacturer. Briefly, 2×10^5 cells

were placed into wells of a 96-well flat-bottom plate and were treated with C_{60} fullerene (sample 1), Cis (sample 2) and C_{60}+Cis nanocomplex (sample 3) for 24 h. All additives were used at the concentration of 0.15 mg/mL. Untreated cells were used as a control (sample 4). Afterwards cells were washed twice with PBS and incubated in the Annexin V binding buffer containing 1/50 volume of FITC-conjugated Annexin V solution and PI (50 µg/mL) for 10 min at room temperature in the dark. Cells from each sample were then analyzed by FacsCalibur flow cytometer (BD Biosciences). The data were analyzed using CELLQuest software (BD). PI detects cells that have lost CPM integrity (i.e., necrotic and secondary necrotic cells), whereas Annexin V detects early apoptotic cells.

Statistics

Statistical analysis was performed by conventional methods of variation statistics. Significance of the differences between the control and experimental measurements was estimated within the framework of the Student's t-test using Origin 8.0 software (OriginLab Corporation, USA). The difference between the compared values was considered to be significant at $p < 0.05$.

Results and Discussion

Characterization of the C_{60}+Cis mixture

The freshly prepared mixture of C_{60} fullerene with Cis was characterized by conventional physico-chemical methods, namely DLS and AFM. The monitoring of the morphology of nanoparticles in solution is important not only for checking the quality of solution for study, but also to control the degree of aggregation which may influence their biodistribution and toxicity [47].

Figure 1 shows DLS data of C_{60}FAS and C_{60}+Cis mixture at room temperature. It is seen that C_{60}FAS contains C_{60} fullerene nanoparticles with hydrodynamic sizes ranging from 65 to 105 nm. The C_{60}+Cis nanocomplex exhibits hydrodynamic sizes from 91 to 164 nm. The *Z*-average size of the C_{60}+Cis nanocomplex is about 122 nm. These results are in accordance with AFM data (Figure 2), as well as with previous study of C_{60}+Cis complexation [39].

The zeta potential of the C_{60}+Cis mixture measured in this work equals to −16.8 mV at room temperature. It is known from previous studies that C_{60} fullerene clusters not containing any guest molecules have a zeta potential equal to −23 mV in water solution [41]. Addition of neutral Cis molecules into C_{60}FAS results in their adsorption into the C_{60} fullerene clusters and causes a lowering of the absolute value of the zeta potential. The stability of such negatively charged clusters in water is determined by two opposite forces, viz., electrostatic repulsion of negatively charged C_{60} molecules and attraction of the

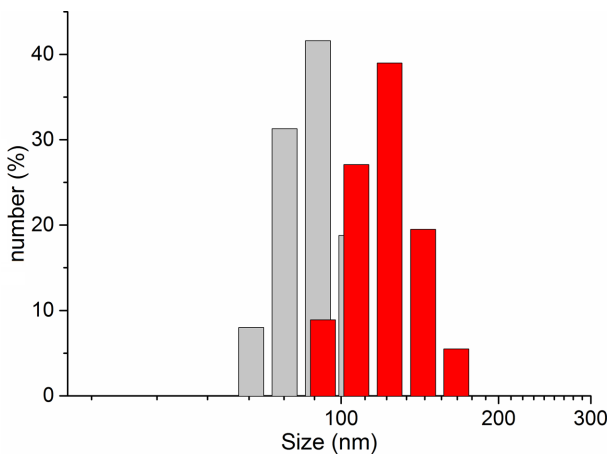

Figure 1: DLS (hydrodynamic size) results of C_{60}FAS (grey; concentration 0.15 mg/mL) and C_{60}+Cis mixture (red; molar ratio of 1:2.4).

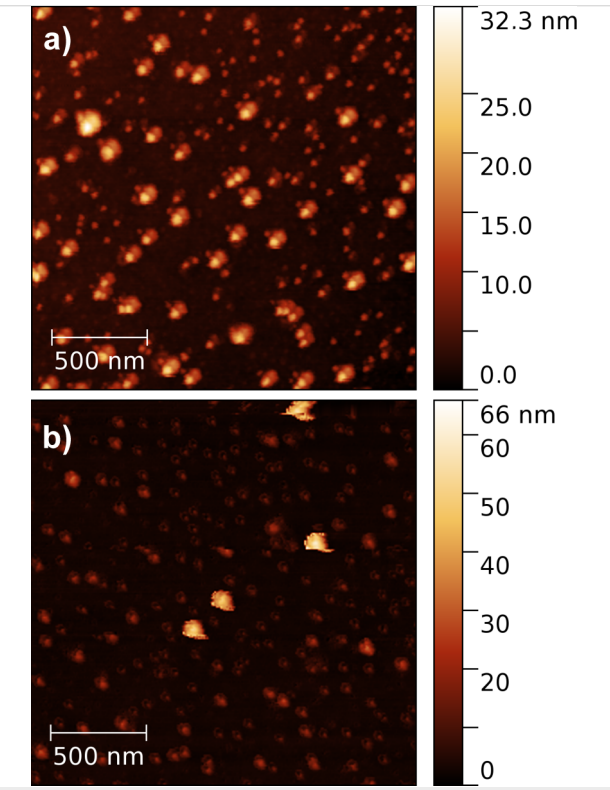

Figure 2: AFM images of a) nanoparticles in C_{60}FAS (concentration 0.15 mg/mL) and b) C_{60}+Cis mixture (molar ratio as 1:2.4).

C_{60} fullerenes due to hydrophobic and van der Waals forces. Thereby, the negative potential of C_{60}+Cis clusters is an important factor responsible for the stabilization of this aqueous system.

The structural and energetic peculiarities of C_{60}+Cis complexation were investigated by calculating the energy-minimized spatial structure of their complex, shown in Figure 3.

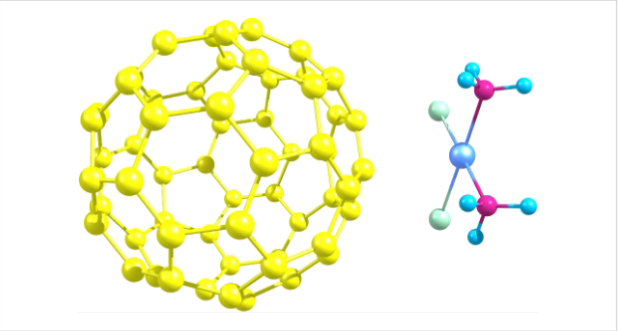

Figure 3: The calculated energy-optimized structure of the C_{60}+Cis nanocomplex in aqueous solution.

The initial location coordinates of Cis above the C_{60} fullerene surface were taken from the ab initio structure [39]. Then we performed the molecular dynamics simulation of this nanocomplex in aqueous environment and calculated the time-averaged energies of interaction. The net van der Waals, electrostatic and hydrophobic energies were obtained as follows, $\Delta G_{vdw} \approx -0.6$ kJ/mol, $\Delta G_{el} \approx 0.9$ kJ/mol and $\Delta G_{hyd} \approx -9.0$ kJ/mol, respectively. The near-zero magnitudes of the net 'vdw' and 'el' terms are quite expected and originate from compensatory nature of the enthalpic interaction with water environment and between the interacting molecules (discussed in more detail in [36,39]). The 'hyd' term outweighs any other interactions indicating the predominantly entropic character of C_{60}+Cis complexation. The obtained results fully agree with previous calorimetric measurements of the same system [39] reporting the purely hydrophobic nature of interaction between these molecules. Moreover, the same conclusion was made regarding the aggregation of C_{60} fullerene in solution [48], C_{60} fullerene complexation with Dox [36] and landomycin A [49], and seems to reveal a general pattern of complexation of small molecules in water [45].

Estimation of genotoxic effects

Figure 4 shows typical images of the comet assay obtained after 20 min of electrophoresis of lysed cells. For both lymphocytes and lymphoblasts, either the control cells or cells treated with the agents studied, we did not observe any differences in the comet appearance.

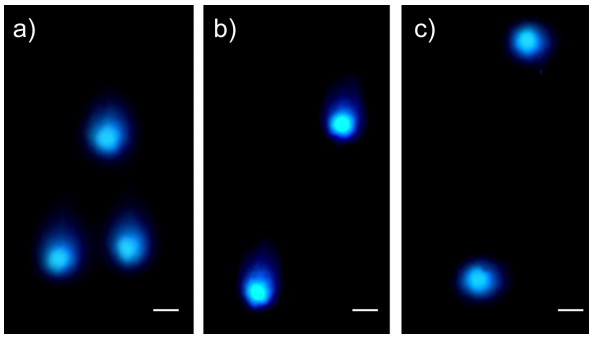

Figure 4: The representative comet-assay images obtained after 20 min of electrophoresis of a) control cells, b) cells incubated with C_{60} fullerene at concentration of 0.1 mg/mL, and c) cells treated with Cis at 0.15 mg/mL. The bars correspond to 10 μm.

The average amount of DNA in the comet tails in control experiments, when the isolated lymphocytes or lymphoblasts were incubated in RPMI 1640 medium without any agents, was ca. 0.11 for both cell types (Figure 5). This value, which appears to

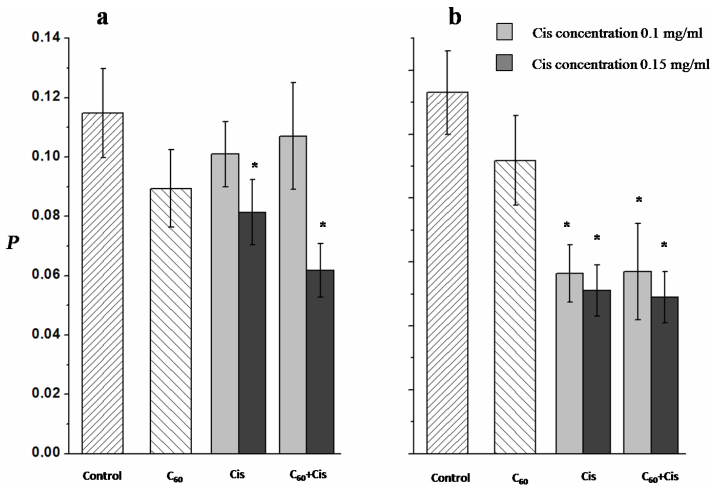

Figure 5: The relative amount of DNA in the comet tails (*P*) after 20 min of electrophoresis of a) lymphocytes and b) lymphoblasts treated with Cis, C_{60} fullerene or C_{60}+Cis nanocomplex. Control: cells were incubated in RPMI 1640 medium without any additional agents. The average values of 5–7 independent experiments are presented. The error bars represent the standard deviations. *Statistically significant ($p < 0.05$) with respect to control cells.

be slightly higher than that usually observed for intact cells (the typical value is 0.06–0.07) [50], may indicate that a small amount of DNA strand breaks occurred in the cells. We did not observe any significant changes in the average amount of DNA in the comet tails after cell treatment with C_{60} fullerene (Figure 5). Thus, C_{60} fullerene nanoparticles do not induce the DNA breaks in the cells.

At a low Cis concentration (0.01 mg/mL) the Cis-treated lymphocytes and lymphoblasts showed a DNA amount in the tails comparable to that of control cells. The same picture was observed for lymphocytes treated with Cis at 0.1 mg/mL (Figure 5a), but a significant decrease in the DNA fraction in the comet tails was detected for lymphoblasts incubated with Cis at this concentration. To explain this result it is worth remembering the mechanism of Cis action. After penetration into cell nuclei Cis may induce coordinate bonds between Pt and guanine bases in DNA that leads to intra- and inter-strand crosslinking. In addition, Cis interaction with nuclear proteins induces DNA–protein crosslinking. After cell lysis these crosslinks remain in nucleoids, which hamper DNA migration in the comet tail under electrophoretic conditions, i.e., the lower the fraction of DNA in the tail, the stronger the mutagenic action of Cis. Thus, lymphoblasts appear to be more sensitive to Cis action than lymphocytes. During cultivation with IL-2α (when lymphocytes are transformed into lymphoblast) a large set of genes are activated to allow the entry of cells in the G1 phase of the cell cycle [51]. Probably, such transformation that never occurs in vivo in lymphocytes under normal conditions, leads to an increase in the cells' sensitivity to the anticancer drug Cis.

The increase of the Cis concentration up to 0.15 mg/mL causes significant decrease in the DNA fraction in the comet tails for both cell types, viz., the average amount of DNA in the tail was 0.08 ± 0.01 for lymphocytes and 0.05 ± 0.01 for lymphoblasts. At the same time, we did not observe any differences in DNA fraction in the comet tail between cells treated with Cis only or with its nanocomplex with C_{60} fullerene. Hence, C_{60} fullerene in the nanocomplex does not influence the Cis activity.

Comparative evaluation of the cytotoxic effects

Genotoxic effect of Cis is mostly associated with apoptotic cell death. However, mechanism of Cis cytotoxic action involves multiple signaling pathways inducing not only apoptosis but also necrotic cell death [52-55]. Nephrotoxicity is considered to be the most important side effect of Cis and is mainly caused by tubular epithelial cell necrosis induced by extensive reactive oxygen species (ROS) generation [56,57]. According to Kaeidi et al. [58], preconditioning with mild oxidative stress may enhance some endogenous defense mechanisms and stimulate cellular adaptation to subsequent severe oxidative stress after the treatment with Cis. C_{60} fullerene can either consume ROS or induce their generation [59]. Taking into account this fact we have hypothesized that C_{60} fullerene in the nanocomplex with Cis can affect mode of cell death induced by Cis. In order to testify this hypothesis, Annexin V/PI double staining of human healthy lymphocytes treated with either C_{60} fullerene, Cis or their nanocomplex was conducted. As shown in Figure 6, the total number of dead lymphocytes from healthy persons after the treatment with C_{60} fullerene was 13.8% vs 32.4% and 36.7% in samples of cells treated with Cis and C_{60}+Cis nanocomplex, respectively.

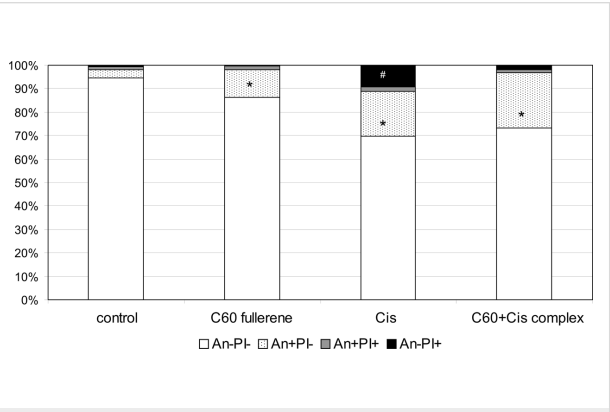

Figure 6: C_{60} fullerene, Cis and their nanocomplex induce apoptosis as well as necrosis of lymphocytes from healthy persons. Cells were treated with mentioned compounds at the concentration of 0.15 mg/mL for 24 h. After culturing, cells were stained with annexin V (AnnV)/ propidium iodide (PI) and analyzed by flow cytometry. Control: cells were incubated without any additional agents. The average values for four independent experiments are presented. $^{*}p < 0.05$ compared with untreated cells; $^{\#}p < 0.05$ compared with cells treated with C_{60}+Cis nanocomplex.

Analysis of cell death using an Annexin V-FITC/PI assay allows one to differentiate the stages of apoptosis and to reveal necrotic cells. The treatment of human healthy resting lymphocytes with C_{60} fullerene resulted in significant increase of early apoptotic cells (An+PI−) to 11.8%, and raise of late apoptotic (An+PI+) to 1.7% on average, as well as necrotic cells (An−PI+) to 0.3%. Apoptosis to necrosis ratio in these samples was 6:1 (on average). In cell samples treated with Cis we noticed significantly more necrotic cells (9.2%), wherein apoptosis to necrosis ratio was 2:1. C_{60}+Cis nanocomplex induced mainly apoptosis in resting lymphocytes, and apoptosis to necrosis ratio was 7:1.

Conclusion

1. The computer simulation, DLS and AFM data confirmed the ability of C_{60} fullerene to form non-covalent nanocomplex with Cis in aqueous solution.

2. C_{60} fullerene nanoparticles do not induce DNA strand breaks in the normal (lymphocytes) and transformed (lymphoblasts) cells as revealed by the comet assay.

3. C_{60} fullerene in the C_{60}+Cis nanocomplex does not influence the genotoxic activity of Cis in vitro.

4. C_{60} fullerene in the C_{60}+Cis nanocomplex affects the cell death mode in treated resting lymphocytes from healthy persons and reduces the fraction of necrotic cells.

Acknowledgements

S.V.P. is grateful to the Academician Platon Kostyuk Foundation for financial support. This work was partially supported by STCU project N 6256.

References

1. Florea, A.-M.; Büsselberg, D. *Cancer* **2011,** *3,* 1351–1371. doi:10.3390/cancers3011351
2. Cepeda, V.; Fuertes, M. A.; Castilla, J.; Alonso, C.; Quevedo, C.; Pérez, J. M. *Anti-Cancer Agents Med. Chem.* **2007,** *7,* 3–18. doi:10.2174/187152007779314044
3. Dong, X.-P.; Xiao, T.-H.; Dong, H.; Jiang, N.; Zhao, X.-G. *Asian Pac. J. Cancer Prev.* **2013,** *14,* 3079–3083. doi:10.7314/APJCP.2013.14.5.3079
4. Pandey, A.; Sarangi, S.; Chien, K.; Sengupta, P.; Papa, A.-L.; Basu, S.; Sengupta, S. *Nanotechnology* **2014,** *25,* 445101. doi:10.1088/0957-4484/25/44/445101
5. Liao, L.; Liu, J.; Dreaden, E. C.; Morton, S. W.; Shopsowitz, K. E.; Hammond, P. T.; Johnson, J. A. *J. Am. Chem. Soc.* **2014,** *136,* 5896–5899. doi:10.1021/ja502011g
6. Alam, N.; Khare, V.; Dubey, R.; Saneja, A.; Kushwaha, M.; Singh, G.; Sharma, N.; Chandan, B.; Gupta, P. N. *Mater. Sci. Eng., C* **2014,** *38,* 85–93. doi:10.1016/j.msec.2014.01.043
7. Guo, S.; Miao, L.; Wang, Y.; Huang, L. *J. Controlled Release* **2014,** *174,* 137–142. doi:10.1016/j.jconrel.2013.11.019
8. Yoong, S. L.; Wong, B. S.; Zhou, Q. L.; Chin, C. F.; Li, J.; Venkatesan, T.; Ho, H. K.; Yu, V.; Ang, W. H.; Pastorin, G. *Biomaterials* **2014,** *35,* 748–759. doi:10.1016/j.biomaterials.2013.09.036
9. He, C.; Liu, D.; Lin, W. *Biomaterials* **2015,** *36,* 124–133. doi:10.1016/j.biomaterials.2014.09.017
10. Prylutska, S. V.; Matyshevska, O. P.; Golub, A. A.; Prylutskyy, Y. I.; Potebnya, G. P.; Ritter, U.; Scharff, P. *Mater. Sci. Eng., C* **2007,** *27,* 1121–1124. doi:10.1016/j.msec.2006.07.009
11. Prylutska, S. V.; Grynyuk, I. I.; Grebinyk, S. M.; Matyshevska, O. P.; Prylutskyy, Y. I.; Ritter, U.; Siegmund, C.; Scharff, P. *Materialwiss. Werkstofftech.* **2009,** *40,* 238–241. doi:10.1002/mawe.200900433
12. Tolkachov, M.; Sokolova, V.; Loza, K.; Korolovych, V.; Prylutskyy, Y.; Epple, M.; Ritter, U.; Scharff, P. *Materialwiss. Werkstofftech.* **2016,** *47,* 216–221. doi:10.1002/mawe.201600486
13. Baati, T.; Bourasset, F.; Gharbi, N.; Njim, L.; Abderrabba, M.; Kerkeni, A.; Szwarc, H.; Moussa, F. *Biomaterials* **2012,** *33,* 4936–4946. doi:10.1016/j.biomaterials.2012.03.036
14. Gharbi, N.; Pressac, M.; Hadchouel, M.; Szwarc, H.; Wilson, S. R.; Moussa, F. *Nano Lett.* **2005,** *5,* 2578–2585. doi:10.1021/nl051866b
15. Prylutska, S. V.; Grynyuk, I. I.; Matyshevska, O. P.; Prylutskyy, Y. I.; Ritter, U.; Scharff, P. *Fullerenes, Nanotubes, Carbon Nanostruct.* **2008,** *16,* 698–705. doi:10.1080/15363830802317148
16. Prylutska, S.; Bilyy, R.; Overchuk, M.; Bychko, A.; Andreichenko, K.; Stoika, R.; Rybalchenko, V.; Prylutskyy, Y.; Tsierkezos, N. G.; Ritter, U. *J. Biomed. Nanotechnol.* **2012,** *8,* 522–527. doi:10.1166/jbn.2012.1404
17. Prylutska, S. V.; Burlaka, A. P.; Prylutskyy, Y. I.; Ritter, U.; Scharff, P. *Exp. Oncol.* **2011,** *33,* 162–164.
18. Didenko, G.; Prylutska, S.; Kichmarenko, Y.; Potebnya, G.; Prylutskyy, Y.; Slobodyanik, N.; Ritter, U.; Scharff, P. *Materialwiss. Werkstofftech.* **2013,** *44,* 124–128. doi:10.1002/mawe.201300082
19. Prylutska, S.; Grynyuk, I.; Matyshevska, O.; Prylutskyy, Y.; Evstigneev, M.; Scharff, P.; Ritter, U. *Drugs R&D* **2014,** *14,* 333–340. doi:10.1007/s40268-014-0074-4
20. Scharff, P.; Carta-Abelmann, L.; Siegmund, C.; Matyshevska, O. P.; Prylutska, S. V.; Koval, T. V.; Golub, A. A.; Yashchuk, V. M.; Kushnir, K. M.; Prylutskyy, Y. I. *Carbon* **2004,** *42,* 1199–1201. doi:10.1016/j.carbon.2003.12.055
21. Davydenko, M. O.; Radchenko, E. O.; Yashchuk, V. M.; Dmytruk, I. M.; Prylutskyy, Y. I.; Matyshevska, O. P.; Golub, A. A. *J. Mol. Liq.* **2006,** *127,* 145–147. doi:10.1016/j.molliq.2006.03.046
22. Jiao, F.; Liu, Y.; Qu, Y.; Li, W.; Zhou, G.; Ge, C.; Li, Y.; Sun, B.; Chen, C. *Carbon* **2010,** *48,* 2231–2243. doi:10.1016/j.carbon.2010.02.032
23. Panchuk, R. R.; Prylutska, S. V.; Chumak, V. V.; Skorokhyd, N. R.; Lehka, L. V.; Evstigneev, M. P.; Prylutskyy, Y. I.; Berger, W.; Heffeter, P.; Scharff, P.; Ritter, U.; Stoika, R. S. *J. Biomed. Nanotechnol.* **2015,** *11,* 1139–1152. doi:10.1166/jbn.2015.2058
24. Prylutska, S. V.; Skivka, L. M.; Didenko, G. V.; Prylutskyy, Y. I.; Evstigneev, M. P.; Potebnya, G. P.; Panchuk, R. R.; Stoika, R. S.; Ritter, U.; Scharff, P. *Nanoscale Res. Lett.* **2015,** *10,* 499. doi:10.1186/s11671-015-1206-7
25. Prylutska, S.; Panchuk, R.; Gołuński, G.; Skivka, L.; Prylutskyy, Y.; Hurmach, V.; Skorohyd, N.; Borowik, A.; Woziwodzka, A.; Piosik, J.; Kyzyma, O.; Garamus, V.; Bulavin, L.; Evstigneev, M.; Buchelnikov, A.; Stoika, R.; Berger, W.; Ritter, U.; Scharff, P. *Nano Res.* **2017,** *10,* 652–671. doi:10.1007/s12274-016-1324-2
26. Wallin, H.; Jacobsen, N. R.; White, P. A.; Gingerich, J.; Møller, P.; Loft, S.; Vogel, U. *J. Biomed. Nanotechnol.* **2011,** *7,* 29. doi:10.1166/jbn.2011.1185
27. Dhawan, A.; Taurozzi, J. S.; Pandey, A. K.; Shan, W.; Miller, S. M.; Hashsham, S. A.; Tarabara, V. V. *Environ. Sci. Technol.* **2006,** *40,* 7394–7401. doi:10.1021/es0609708
28. Shinohara, N.; Matsumoto, K.; Endoh, S.; Maru, J.; Nakanishi, J. *Toxicol. Lett.* **2009,** *191,* 289–296. doi:10.1016/j.toxlet.2009.09.012
29. Matsuda, S.; Matsui, S.; Shimizu, Y.; Matsuda, T. *Environ. Sci. Technol.* **2011,** *45,* 4133–4138. doi:10.1021/es1036942
30. Al-Subiai, S. N.; Arlt, V. M.; Frickers, P. E.; Readman, J. W.; Stolpe, B.; Lead, J. R.; Moody, A. J.; Jha, A. N. *Mutat. Res.* **2012,** *745,* 92–103. doi:10.1016/j.mrgentox.2011.12.019
31. Ema, M.; Tanaka, J.; Kobayashi, N.; Naya, M.; Endoh, S.; Maru, J.; Hosoi, M.; Nagai, M.; Nakajima, M.; Hayashi, M.; Nakanishi, J. *Regul. Toxicol. Pharmacol.* **2012,** *62,* 419–424. doi:10.1016/j.yrtph.2012.01.003
32. Zakharian, T. Y.; Seryshev, A.; Sitharaman, B.; Gilbert, B. E.; Knight, V.; Wilson, L. J. *J. Am. Chem. Soc.* **2005,** *127,* 12508–12509. doi:10.1021/ja0546525

33. Lu, F.; Haque, S. A.; Yang, S.-T.; Luo, P. G.; Gu, L.; Kitaygorodskiy, A.; Li, H.; Lacher, S.; Sun, Y.-P. *J. Phys. Chem. C* **2009,** *113,* 17768–17773. doi:10.1021/jp906750z
34. Evstigneev, M. P.; Buchelnikov, A. S.; Voronin, D. P.; Rubin, Y. V.; Belous, L. F.; Prylutskyy, Y. I.; Ritter, U. *ChemPhysChem* **2013,** *14,* 568–578. doi:10.1002/cphc.201200938
35. Skamrova, G. B.; Laponogov, I.; Buchelnikov, A. S.; Shckorbatov, Y. G.; Prylutska, S. V.; Ritter, U.; Prylutskyy, Y. I.; Evstigneev, M. P. *Eur. Biophys. J.* **2014,** *43,* 265–276. doi:10.1007/s00249-014-0960-2
36. Prylutskyy, Y. I.; Evstigneev, M. P.; Pashkova, I. S.; Wyrzykowski, D.; Woziwodzka, A.; Gołuński, G.; Piosik, J.; Cherepanov, V. V.; Ritter, U. *Phys. Chem. Chem. Phys.* **2014,** *16,* 23164–23172. doi:10.1039/C4CP03367A
37. Prylutska, S. V.; Didenko, G. V.; Potebnya, G. P.; Bogutska, K. I.; Prylutskyy, Y. I.; Ritter, U.; Scharff, P. *Biopolym. Cell* **2014,** *30,* 372–376. doi:10.7124/bc.0008B4
38. Afanasieva, K. S.; Prylutska, S. V.; Lozovik, A. V.; Bogutska, K. I.; Sivolob, A. V.; Prylutskyy, Y. I.; Ritter, U.; Scharff, P. *Ukr. Biochem. J.* **2015,** *87,* 91–98. doi:10.15407/ubj87.01.091
39. Prylutskyy, Y. I.; Cherepanov, V. V.; Evstigneev, M. P.; Kyzyma, O. A.; Petrenko, V. I.; Styopkin, V. I.; Bulavin, L. A.; Davidenko, N. A.; Wyrzykowski, D.; Woziwodzka, A.; Piosik, J.; Kaźmierkiewicz, R.; Ritter, U. *Phys. Chem. Chem. Phys.* **2015,** *17,* 26084–26092. doi:10.1039/C5CP02688A
40. Prylutskyy, Y. I.; Durov, S. S.; Bulavin, L. A.; Adamenko, I. I.; Moroz, K. O.; Geru, I. I.; Dihor, I. N.; Scharff, P.; Eklund, P. C.; Grigorian, L. *Int. J. Thermophys.* **2001,** *22,* 943–956. doi:10.1023/A:1010791402990
41. Ritter, U.; Prylutskyy, Y. I.; Evstigneev, M. P.; Davidenko, N. A.; Cherepanov, V. V.; Senenko, A. I.; Marchenko, O. A.; Naumovets, A. G. *Fullerenes, Nanotubes, Carbon Nanostruct.* **2015,** *23,* 530–534. doi:10.1080/1536383X.2013.870900
42. Wysokiński, R.; Michalska, D. *J. Comput. Chem.* **2001,** *22,* 901–912. doi:10.1002/jcc.1053
43. Adamo, C.; Barone, V. *J. Chem. Phys.* **1998,** *108,* 664–675. doi:10.1063/1.475428
44. Hay, P. J.; Wadt, W. R. *J. Chem. Phys.* **1985,** *82,* 299–310. doi:10.1063/1.448975
45. Kostjukov, V. V.; Khomytova, N. M.; Hernandez Santiago, A. A.; Tavera, A.-M. C.; Alvarado, J. S.; Evstigneev, M. P. *J. Chem. Thermodyn.* **2011,** *43,* 1424–1434. doi:10.1016/j.jct.2011.04.014
46. Brunger, A. T. *X–PLOR. A system for X–ray crystallography and NMR;* Yale University Press: New Haven, CT, USA, 1992.
47. Cataldo, F.; Da Ros, T., Eds. *Medicinal Chemistry and Pharmacological Potential of Fullerenes and Carbon Nanotubes;* Springer: Netherlands, 2008. doi:10.1007/978-1-4020-6845-4
48. Voronin, D. P.; Buchelnikov, A. S.; Kostjukov, V. V.; Khrapatiy, S. V.; Wyrzykowski, D.; Piosik, J.; Prylutskyy, Y. I.; Ritter, U.; Evstigneev, M. P. *J. Chem. Phys.* **2014,** *140,* 104909. doi:10.1063/1.4867902
49. Prylutskyy, Y. I.; Cherepanov, V. V.; Kostjukov, V. V.; Evstigneev, M. P.; Kyzyma, O. A.; Bulavin, L. A.; Ivankov, O.; Davidenko, N. A.; Ritter, U. *RSC Adv.* **2016,** *6,* 81231–81236. doi:10.1039/C6RA18807A
50. Afanasieva, K.; Chopei, M.; Zazhytska, M.; Vikhreva, M.; Sivolob, A. *Biochim. Biophys. Acta* **2013,** *1833,* 3237–3244. doi:10.1016/j.bbamcr.2013.09.021
51. Mzali, R.; Seguin, L.; Liot, C.; Auger, A.; Pacaud, P.; Loirand, G.; Thibault, C.; Pierre, J.; Bertoglio, J. *FASEB J.* **2005,** *19,* 1911–1930. doi:10.1096/fj.05-4030fje
52. Godoy, L. C.; Anderson, C. T. M.; Chowdhury, R.; Trudel, L. J.; Wogan, G. N. *Proc. Natl. Acad. Sci. U. S. A.* **2012,** *109,* 20373–20378. doi:10.1073/pnas.1218938109
53. Zhang, M. N.; Long, Y.-T.; Ding, Z. *J. Inorg. Biochem.* **2012,** *108,* 115–122. doi:10.1016/j.jinorgbio.2011.11.010
54. Hong, J.-Y.; Kim, G.-H.; Kim, J.-W.; Kwon, S.-S.; Sato, E. F.; Cho, K.-H.; Shim, E. B. *BMC Syst. Biol.* **2012,** *6,* No. 122. doi:10.1186/1752-0509-6-122
55. Zhang, J.; Lou, X.; Jin, L.; Zhou, R.; Liu, S.; Xu, N.; Liao, D. J. *Oncoscience* **2014,** *1,* 407–422. doi:10.18632/oncoscience.61
56. Sancho-Martínez, S. M.; Piedrafita, F. J.; Cannata-Andía, J. B.; López-Novoa, J. M.; López-Hernández, F. J. *Toxicol. Sci.* **2011,** *122,* 73–85. doi:10.1093/toxsci/kfr098
57. Sancho-Martínez, S. M.; Prieto-García, L.; Prieto, M.; López-Novoa, J. M.; López-Hernández, F. J. *Pharmacol. Ther.* **2012,** *136,* 35–55. doi:10.1016/j.pharmthera.2012.07.003
58. Kaeidi, A.; Rasoulian, B.; Hajializadeh, Z.; Pourkhodadad, S.; Rezaei, M. *Renal Failure* **2013,** *35,* 1382–1386. doi:10.3109/0886022X.2013.829406
59. Kong, L.; Zepp, R. G. *Environ. Toxicol. Chem.* **2012,** *31,* 136–143. doi:10.1002/etc.711

License and Terms

BEILSTEIN JOURNAL OF NANOTECHNOLOGY

Development of an advanced diagnostic concept for intestinal inflammation: molecular visualisation of nitric oxide in macrophages by functional poly(lactic-*co*-glycolic acid) microspheres

Kathleen Lange[*,‡1,§], Christian Lautenschläger[‡1], Maria Wallert[2], Stefan Lorkowski[3], Andreas Stallmach[1] and Alexander Schiller[4]

Letter

Open Access

Address:
[1]Jena University Hospital, Department of Internal Medicine IV (Gastroenterology, Hepatology, Infectiology), Am Klinikum 1, 07743 Jena, Germany, [2]Atherothrombosis and Vascular Laboratory, Baker Heart and Diabetes Institute, Melbourne, Australia, [3]Competence Cluster for Nutrition and Cardiovascular Health (nutriCARD) Halle–Jena–Leipzig and Friedrich Schiller University of Jena, Institute of Nutrition, Department of Nutritional Biochemistry, Dornburger Straße 25, 07743 Jena, Germany and [4]Friedrich Schiller University Jena, Institute for Inorganic and Analytical Chemistry, Humboldtstr. 8, 07743 Jena, Germany

Email:
Kathleen Lange[*] - kathleen.lange@med.uni-jena.de

* Corresponding author ‡ Equal contributors
§ Phone: +49 3641 9324641

Keywords:
functional imaging; intestinal inflammation; microparticle; molecular imaging; nitric oxide

Beilstein J. Nanotechnol. **2017,** *8,* 1637–1641.
doi:10.3762/bjnano.8.163

Received: 01 April 2017
Accepted: 04 July 2017
Published: 08 August 2017

This article is part of the Thematic Series "Nanomaterial-based cancer theranostics".

Guest Editor: V. Sivakov

Abstract

We here describe a new approach to visualise nitric oxide (NO) in living macrophages by fluorescent NO-sensitive microspheres based on poly(lactic-*co*-glycolic acid) (PLGA). PLGA microspheres loaded with NO550 dye were prepared through a modified solvent-evaporation method. Microparticles were characterized by a mean hydrodynamic diameter of 3000 nm, zeta potential of −26.000 ± 0.351 mV and a PDI of 0.828 ± 0.298. Under abiotic conditions, NO release was triggered through UV radiation (254 nm) of 10 mM sodium nitroprusside dehydrate (SNP). After incubation, AZO550 microspheres exhibited an about 8-fold increased emission at 550 nm compared to NO550 particles. For biotic NO release, RAW 264.7 murine macrophages were activated with lipopolysaccharide (LPS) of *Salmonella typhimurium*. After treatment with NO550 microparticles, only activated cells caused a green particle fluorescence and could be detected by laser scanning microscopy. NO release was confirmed indirectly with Griess reaction. Our functional NO550 particles enable a simple and early evaluation of inflammatory and immunological processes. Furthermore, our results on particle-based NO sensing and previous studies in targeting intestinal inflammation via (PLGA)-based microspheres demonstrate that an advanced concept for visualizing intestinal inflammation is tangible.

Introduction

Inflammation and malignancies are fundamental aspects of many human diseases. Nitric oxide (NO) has been proposed to be an important mediator of inflammation and carcinogenesis. Chronic inflammation, as found in inflammatory bowel diseases, seems to be maintained by high levels of nitric oxide (NO) due to an abnormal immune response against endogenous flora and luminal antigens in genetically susceptible individuals. High levels of NO become noxious to mucosal tissue. As NO levels even correlate with severity of disease, imaging of mucosal NO concentrations improves the assessment of disease activity and even may contribute to predict disease progression before mucosal damage continues. The visualisation of molecular processes that drive mucosal inflammation is of great interest in life sciences. NO is synthesised and released on demand, it is not stored and is highly diffusible. In vivo detection of NO in real time is difficult, because NO rapidly diffuses and reacts with cellular components. NO quantification with chemiluminescence or amperometry is often complicated by low spatio-temporal resolution and complex experimental setups prone to interferences [1]. Hence, the development of highly sensitive fluorescent sensors for NO imaging may improve its visualisation in vivo significantly [2]. Furthermore, molecular imaging of NO enables a better visualisation of intestinal functionalities, including irregular mucosal patterns and vascular lesions [3].

We developed a novel polymeric microparticle made of biodegradable poly(lactic-*co*-glycolic acid) (PLGA), which accumulates selectively in inflamed mucosa of patients with inflammatory bowel disease without interfering with the healthy mucosa. This approach is based on the epithelial barrier dysfunction of the intestine during intestinal inflammation. The intestinal barrier shows an increased permeability by disabled tight junction proteins, alterations in the thickness and composition of the mucus. Thus, particles penetrate and accumulate only into the inflamed mucosa [4]. Previously, we have shown that polymeric particles penetrate and accumulate selectively within the inflamed mucosa proving that a particle-based approach is feasible [5,6]. Now, we introduce a cutting-edge strategy to visualise NO in living macrophages as first step, and to visualise these cells in NO-mediated intestinal inflammation in vivo by fluorescent particle-based diagnostics in a second step.

Here, we used a NO-sensitive dye, namely NO550, as a model molecule to proof the concept of a particle-based diagnostic as part of an advanced diagnostic concept for detecting intestinal inflammation. NO550 is a chemical sensor for the cellular imaging of NO, while being inert to other reactive oxygen and nitrogen species (ROS/RNS), and is characterized by high specificity and low background signals [7]. We prepared and characterized NO550-loaded PLGA microspheres to study NO in abiotic and biotic experiments. To our knowledge, this is the first time of visualisation of NO at different concentrations via fluorescence-emitting NO550-PLGA microspheres.

Results and Discussion

Physicochemical characterisation of microspheres

The preparation of NO550-loaded microspheres was a reliable and reproducible process (for more experimental data please see Section 1 and Section 2 of Supporting Information File 1). The particles showed a mean hydrodynamic diameter of 3000 nm, a zeta potential of −26.000 ± 0.351 mV and a PDI of 0.828 ± 0.298. Furthermore, NO550-loaded microspheres were characterised by a slightly more irregular surface with small pores compared to blank microspheres (Figure 1). In contrast, blank microspheres showed a mean hydrodynamic diameter of 3000 nm, a zeta potential of −1.250 ± 0.132 mV and a PDI of 0.253 ± 0.042. The blank microspheres are similarly sized spherical particles with smooth, uniform and pore-free surfaces (Figure 1). The influence of NO550 leads to a higher PDI, a

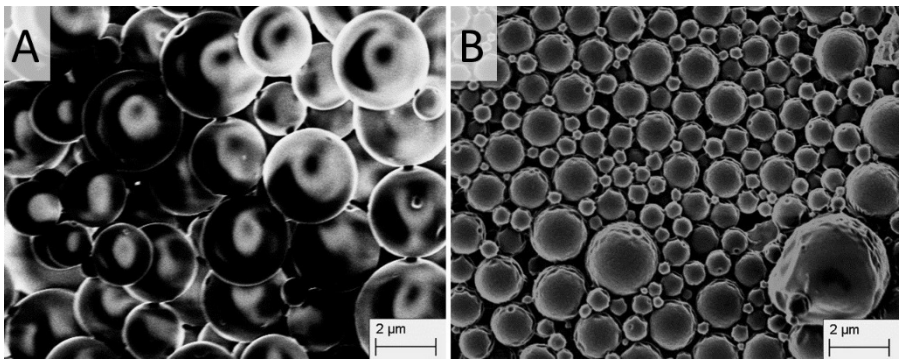

Figure 1: Scanning electron microscopic images of blank (A) and NO550-loaded (B) polymeric microspheres.

shift of the zeta potential and an irregular surface compared to blank microspheres.

Abiotic nitric oxide sensing studies

In this study, we used sodium nitroprusside (SNP) as an exogenous NO donor. SNP in aqueous medium is highly photosensitive and releases NO in a constant manner when irradiated with UV light. This experimental approach allows for abiotic NO sensing studies. After 2 minutes of incubation of NO550-loaded microspheres with UV-irradiated SNP (10 mM, 2 min, 254 nm) we observed an up to 8-fold increased fluorescence signal at 550 nm compared to inactive NO550-loaded microspheres (see Section 3 of Supporting Information File 1 for further experimental data). Thus, NO550-loaded particles could sense abiotic NO by reacting with the encapsulated NO550. The conversion into the fluorescent AZO550 was detected photometrically (Figure 2).

Biotic nitric oxide sensing studies

In our studies, we used the murine RAW264.7 macrophage cell line as an established model to analyse the endogenous formation of NO. This experimental approach allows for biotic NO sensing studies with NO550-loaded microspheres. LPS from *Salmonella typhimurium* was used to induce NO production in these macrophages. The pathogen *Salmonella typhimurium* causes severe intestinal inflammations, in some cases even leading to bacteraemia. LPS increased cellular production and release of NO in RAW264.7 macrophages up to 50 µM after 24 h of stimulation compared to non-stimulated macrophages. The incubation (1 h) of LPS-treated RAW264.7 with microspheres resulted in a slight increase in NO formation in the range of about 1 µM, while native untreated cells displayed basal NO levels of approximately 0.6 µM. Microscopic investigation of untreated macrophages confirmed this by a low fluorescence signal of NO550-loaded microspheres (Figure 3). In contrast, NO550-loaded microspheres revealed in LPS-stimulated macrophages a strong fluorescence signal at 550 nm. Due to the polymeric encapsulation of NO550, no fluorescent background was observed. The microspheres showed a clear round shape with homogenous fluorescence. Some smaller microspheres were located within macrophages, likely because of endocytic uptake by the RAW264.7 macrophages (Figure 3). These results clearly show that NO550-loaded particles can be used to sense biotic NO by the reaction of NO with the encapsulated NO550. The conversion of NO550 into the fluorescent AZO550 molecule can be detected chemically and spectrometrically. Furthermore, the fluorescence intensity of the microspheres in the supernatants of the cells can be measured using a plate reader. In the same supernatants, we determined NO release using the Griess reaction (see Section 4 and Section 5 of Supporting Information File 1 for experimental data). These experiments showed that the fluorescence intensity of the supernatants coincided with the amount of nitrite in the supernatant of LPS-stimulated cells as determined by the Griess reaction (Figure 4).

Conclusion

We demonstrated the possibility of molecular imaging of NO at different concentrations and under different conditions using NO550-loaded PLGA microspheres in living macrophages. NO550 is converted by NO into an azo dye, which emits green fluorescence in an NO concentration-dependent manner. Thus, this approach provides a novel approach for the early spatio-temporal evaluation of inflammatory processes in IBD. The intestinal distribution and signal intensity of the microspheres can be easily analysed by fluorescence-based microscopy. A

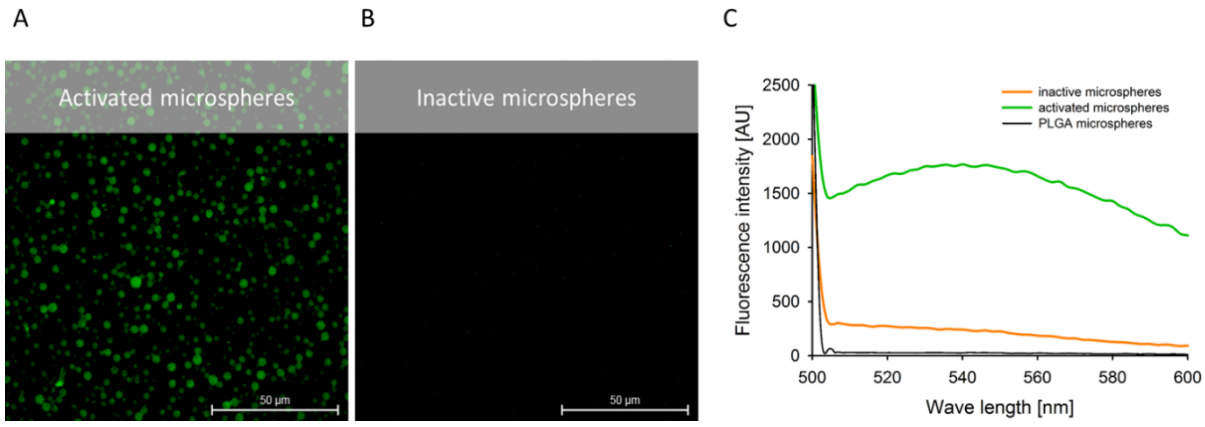

Figure 2: NO-releasing sodium nitroprusside (SNP) leads to light emission of NO550-loaded microspheres. Confocal laser scanning microscopy (CLSM) images of activated (A) and inactivated (B) NO550-loaded polymeric microspheres in DPBS including fluorescence emission spectra (C) of the microspheres are shown. UV-irradiated SNP (10 mM, 2 min, 254 nm) was used for 2 minutes to activate NO550-loaded microspheres. During the incubation with SNP, NO550 is converted to AZO550 that emits green fluorescence at 550 nm.

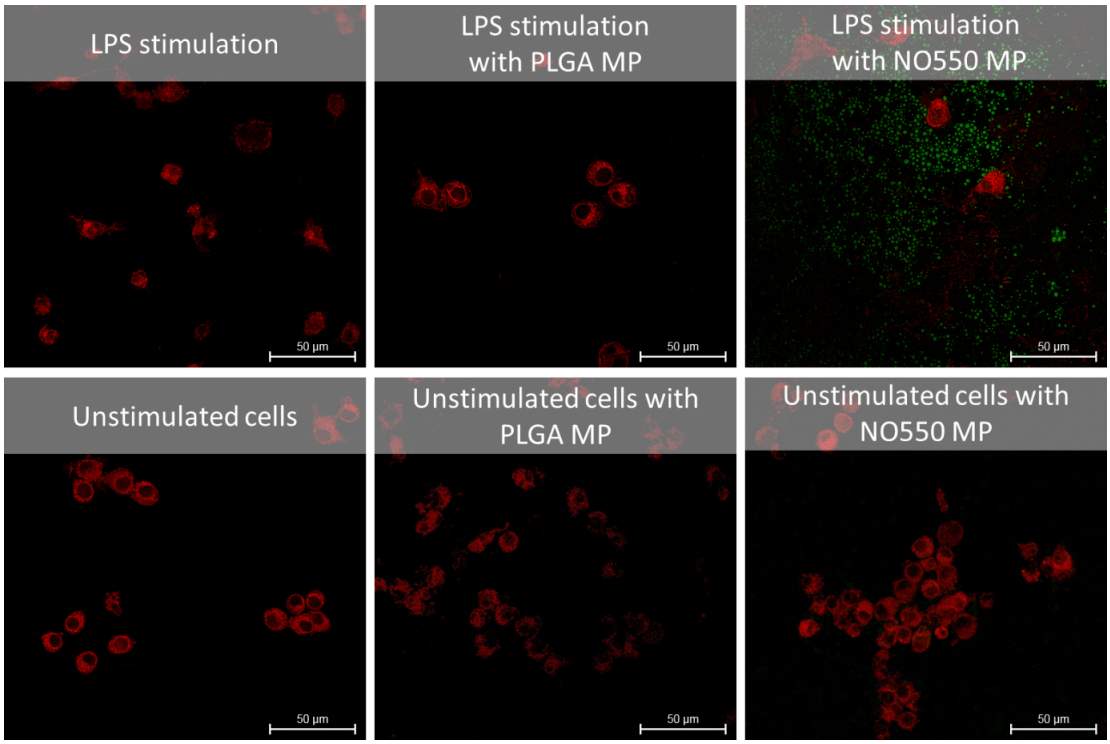

Figure 3: NO550-loaded microspheres detect the inflammatory response of murine macrophage-like RAW 264.7 cells. CLSM images of LPS-stimulated and non-stimulated RAW 264.7 cells are shown. Cells were stained with Cell Mask deep red. The treatment of RAW 264.7 cells with LPS increased formation and release of NO which in turn converted NO550 into AZO550 within the NO550-loaded microspheres. NO formation is visualised as green fluorescence signal during LPS stimulation.

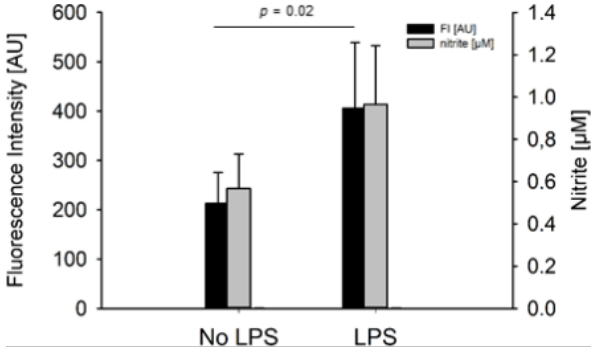

Figure 4: Quantification of NO release with NO550-loaded microspheres in inflamed cells. LPS-stimulated murine RAW 264.7 macrophages led to significantly higher fluorescence intensity (FI) signals using NO550-loaded microspheres than in unstimulated cells (p = 0.02). The signal coincide with nitrite concentrations estimated by Griess reaction. AU: arbitrary units.

next step will be to adopt our approach for the use with fluorescence-based endoscopy and for the visualisation of NO release in mucosal biopsies obtained from patients with chronic intestinal inflammation. Furthermore, our results on particle-based NO-sensing and previous works in targeting intestinal inflammation via PLGA microspheres demonstrate that an advanced concept for visualizing intestinal inflammation is tangible.

Supporting Information

Supporting Information File 1

Additional experimental data.
[http://www.beilstein-journals.org/bjnano/content/supplementary/2190-4286-8-163-S1.pdf]

References

1. Hetrick, E. M.; Schoenfisch, M. H. *Annu. Rev. Anal. Chem.* **2009,** *2,* 409–433. doi:10.1146/annurev-anchem-060908-155146
2. Li, H.; Wan, A. *Analyst* **2015,** *140,* 7129–7141. doi:10.1039/C5AN01628B
3. Schmidt, C.; Lautenschläger, C.; Petzold, B.; Sakr, Y.; Marx, G.; Stallmach, A. *Br. J. Anaesth.* **2013,** *111,* 996–1003. doi:10.1093/bja/aet219
4. Lautenschläger, C.; Schmidt, C.; Fischer, D.; Stallmach, A. *Adv. Drug Delivery Rev.* **2014,** *71,* 58–76. doi:10.1016/j.addr.2013.10.001
5. Lautenschläger, C.; Schmidt, C.; Lehr, C.-M.; Fischer, D.; Stallmach, A. *Eur. J. Pharm. Biopharm.* **2013,** *85,* 578–586. doi:10.1016/j.ejpb.2013.09.016

6. Schmidt, C.; Lautenschlaeger, C.; Collnot, E.-M.; Schumann, M.; Bojarski, C.; Schulzke, J.-D.; Lehr, C.-M.; Stallmach, A. *J. Controlled Release* **2013,** *165,* 139–145. doi:10.1016/j.jconrel.2012.10.019
7. Ghebremariam, Y. T.; Huang, N. F.; Kambhampati, S.; Volz, K. S.; Joshi, G. G.; Anslyn, E. V.; Cooke, J. P. *J. Vasc. Res.* **2014,** *51,* 68–79. doi:10.1159/000356445

License and Terms

BEILSTEIN JOURNAL OF NANOTECHNOLOGY

Methionine-mediated synthesis of magnetic nanoparticles and functionalization with gold quantum dots for theranostic applications

Arūnas Jagminas*[1,§], Agnė Mikalauskaitė[1], Vitalijus Karabanovas[2] and Jūrate Vaičiūnienė[1]

Full Research Paper

Open Access

Address:
[1]State Research Institute Center for Physical Sciences and Technology, Sauletekio Ave. 3, LT- 10222, Vilnius, Lithuania and [2]National Cancer Institute, Baublio 3b, LT- 08406, Vilnius, Lithuania

Email:
Arūnas Jagminas* - arunas.jagminas@ftmc.lt

* Corresponding author
§ Tel: +370 5648891

Keywords:
functionalization; gold; magnetic nanoparticles; quantum dots; theranostics

Beilstein J. Nanotechnol. **2017,** *8,* 1734–1741.
doi:10.3762/bjnano.8.174

Received: 24 March 2017
Accepted: 02 August 2017
Published: 22 August 2017

This article is part of the Thematic Series "Nanomaterial-based cancer theranostics".

Guest Editor: V. Sivakov

Abstract

Biocompatible superparamagnetic iron oxide nanoparticles (NPs) through smart chemical functionalization of their surface with fluorescent species, therapeutic proteins, antibiotics, and aptamers offer remarkable potential for diagnosis and therapy of disease sites at their initial stage of growth. Such NPs can be obtained by the creation of proper linkers between magnetic NP and fluorescent or drug probes. One of these linkers is gold, because it is chemically stable, nontoxic and capable to link various biomolecules. In this study, we present a way for a simple and reliable decoration the surface of magnetic NPs with gold quantum dots (QDs) containing more than 13.5% of Au^{+}. Emphasis is put on the synthesis of magnetic NPs by co-precipitation using the amino acid methionine as NP growth-stabilizing agent capable to later reduce and attach gold species. The surface of these NPs can be further conjugated with targeting and chemotherapy agents, such as cancer stem cell-related antibodies and the anticancer drug doxorubicin, for early detection and improved treatment. In order to verify our findings, high-resolution transmission electron microscopy (HRTEM), atomic force microscopy (AFM), FTIR spectroscopy, inductively coupled plasma mass spectroscopy (ICP-MS), and X-ray photoelectron spectroscopy (XPS) of as-formed $CoFe_2O_4$ NPs before and after decoration with gold QDs were applied.

Introduction

In current nanomedicine, biocompatible iron oxide-based NPs have attracted particular interest due to their size-dependent magnetic, optical and chemical properties that allow for the design of NPs for multimodal imaging and photothermal therapy of cancer cells [1]. Dual-imaging probes, capable to perform simultaneously magnetic resonance and fluorescent imaging, allow for a more rapid and precise screening of the oncological disease sites. This is frequently achieved by covering magnetic NPs with shells containing luminescent quantum dots (QDs) [2-6]. The target molecules can be attached to the surface of magnetic NPs through biocompatible links such as Au–S– [7]. Iron oxide NPs can be coated with polymeric or silica shells containing incorporated gold NPs [8-10]. However, in this case the size of the magnetic NPs increases up to ten times [9], resulting in a significant decrease in the saturation magnetization value of the magnetic core. To eliminate this drawback, several methods for the deposition of the gold directly onto the surface of magnetic NPs have been proposed that are based on the reduction of Au(III) species by the typical reducing agents such as borohydride, ascorbic acid and citric acid [11-14]. However, the direct-deposition protocols are mainly suitable for covering γ-Fe_2O_3 NPs. The formation of a gold shell on magnetite (Fe_3O_4) or ferrite surfaces through reduction of chloroauric acid by citrates or borohydride is usually problematic due to the formation of pure gold crystallites in the solution [5,15]. The deposition of gold onto the surface of magnetic iron oxide-based NPs can also be achieved via their impregnation with hydroxylamine [16], vitamin C [17] or methionine [18,19], which are capable to reduce the gold ions at the surface of NPs. However, in this case, uniform coating of magnetic NPs can only be obtained via precise control of the precursor content and all steps of the multistep process [17,18]. As a result, this way is time-consuming and it does not fully prevent the formation of gold crystallites in the plating solution. Moreover, to avoid the aggregation of magnetic NPs during or at the end of the synthesis they must be covered with capping materials such as acid anions [20,21], surfactants [22] or proteins [23]. Besides, for in vivo and in vitro applications of magnetic NPs their capping materials should be biocompatible and allow for the attachment of gold species. In recent publications amino acids such as methionine [19] and lysine [24] have been reported to be effective capping agents to control the size of magnetite [19] and Co ferrite [24] NPs during co-precipitation synthesis [25]. The main goal of the methionine capping was the application of Fe_3O_4@Met NPs for the adsorption of water pollutants.

In this study, we report a novel synthesis protocol for superparamagnetic cobalt ferrite NPs capped with a biocompatible methionine shell ($CoFe_2O_4$@Met), which in turn is capable to reduce and attach the gold species. In this way, hybrid magnetoplasmonic cobalt ferrite NPs decorated with Au^0/Au^{1+} quantum dots (QDs) were formed for the first time. The formation of plasmonic gold QDs at the surface of iron oxide-based NPs was confirmed by HRTEM, AFM, FTIR, XPS and chemical analysis.

Results and Discussion

Synthesis and characterization of methionine-functionalized cobalt ferrite nanoparticles

A hydrothermal approach was applied to synthesize the superparamagnetic cobalt ferrite NPs stabilized with methionine. The proposed approach differs from the reported one [19] in the nature of magnetic NPs, the composition of the aqueous solution applied, synthesis atmosphere and modes. It involves the preparation of an alkaline aqueous solution containing $CoCl_2$, $FeCl_3$, methionine, and NaOH up to pH 12.4, followed by autoclaving at 130 °C for 10 h. To the best of our knowledge, methionine has not been applied before for hydrothermal synthesis and stabilization of cobalt ferrite NPs as the capping ligand and reducing agent of gold ions. The interest in NPs capped with methionine was based on the current understanding that methionine can reduce chloroauric acid from alkaline solutions anchoring Au^0 at the surface of the NPs [18]. As-synthesized NPs were characterized by TEM, XRD, FTIR and magnetic measurements. Figure 1a depicts the TEM image of the as-grown NPs that have been carefully rinsed and reveals their spherical shape and a size distribution in the range of (3.0 – 8.5) nm with a mean value of 5.7 nm (Figure 1b). Furthermore, the stabilization of cobalt ferrite NPs with metionine molecules confers them strong non-fouling properties not allowing aggregate. The XRD pattern of these NPs (Figure 1c) implied the formation of pure, inverse spinel structure $CoFe_2O_4$, as all diffraction peaks at 2Θ positions: 18.29 (111), 30.08 (220), 35.44 (311), 43.06 (400), 53.45 (422), 56.97 (511) 62.59 (440), and 74.01 (533) match well with the standard polycrystalline $CoFe_2O_4$ diffraction data summarized in the PDF Card No. 00.022-1086. The average size of as-grown Nps, calculated by the Scherrer formula [26] from the (311) XRD line broadening ~ 6.0 nm, it is a close proximity to the one calculated from the TEM data (5.8 nm, Figure 1b).

Magnetization measurements were further performed to evaluate the gold deposition onto the surface of cobalt ferrite NPs. Figure 1d shows the room-temperature magnetization plots as a function of applied magnetic field for $CoFe_2O_4$@Met NPs before (1) and after (2) their sonication in the chloroauric acid solution. It was found that the saturation magnetization value of

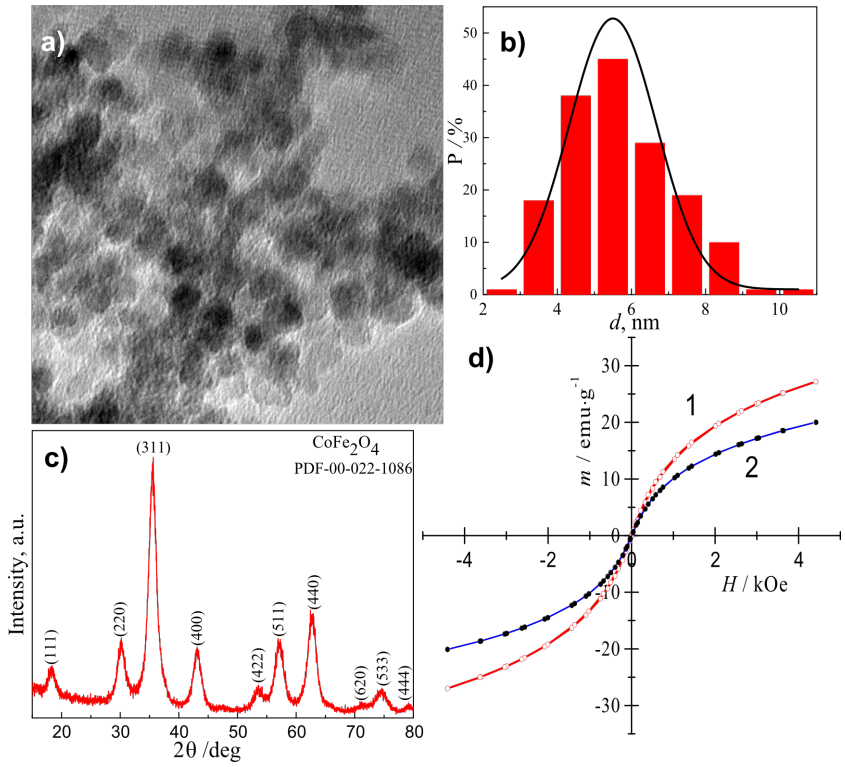

Figure 1: a) TEM image of cobalt ferrite NPs synthesized hydrothermally in a solution containing 25.0 mmol·L^{-1} $CoCl_2$, 50 mmol·L^{-1} $FeCl_3$, 0.2 mol·L^{-1} methionine, and NaOH to pH 12.4 at 130 °C for 10 h. The size distribution histogram and XRD pattern of the as-formed NPs are shown in panels b) and c), respectively. In panel d) the magnetic responses of as-formed (1) and sonicated NPs in a 10 mmol·L^{-1} $HAuCl_4$ solution, kept at a pH 12.2, at 37 °C for 4 h (2) are presented.

$CoFe_2O_4$@Met NPs decreases from 27 to 21 emu·g^{-1} (at H_{max} = 4.4 kOe) upon sonication supporting the claim that gold species are deposited but the NPs remain superparamagnetic. The high-resolution TEM image of the $CoFe_2O_4$@Met NPs after gold deposition with methionine and the EDX spectrum of these NPs are shown in Figure 2.

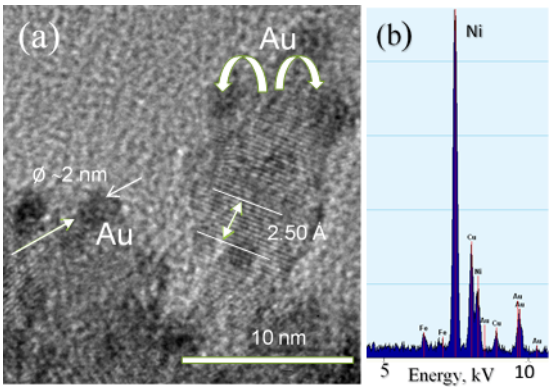

Figure 2: HRTEM image of $CoFe_2O_4$@Met NPs after sonication in 15 mmol·L^{-1} $HAuCl_4$ solution at 37 °C for 4 h (a) and their EDX spectrum (b).

The HRTEM image shows the formation of numerous gold species at the surface of methionine-stabilized $CoFe_2O_4$@Met NPs. In accordance with HRTEM image and EDX spectrum, the ICP-MS analysis of the gold plating solution performed before and after 30 min of sonication of the NPs indicated the reduction of ca. 99.3% of gold ions. From the HRTEM inspection, however, it was difficult to determine the size distribution of the attached gold species, although some of them seemed to be spherical with a diameter of ca. 2.0 nm. More precise results were obtained by the determination of the size of gold species that were removed from the NP surface by the ultrasonic agitation of 10 mg $CoFe_2O_4$@Met/Au NPs probe in 10 mmol·L^{-1} methionine solution. As a result a reddish-pink solution was obtained after 20 min processing (see inset in Figure 3). This process is most likely due to the stronger capping of Au NPs with methionine molecules than with $CoFe_2O_4$@Met/Au NPs. Note that no fluorescence was seen under UV and blue-light excitation of this solution. Typical UV–vis absorption spectra of aqueous methionine, tetrachlorauric acid and gold species solution are shown in Figure 3.

The pure methionine solution does not exhibit any absorption peaks in the measured spectral range. For the chloroauric acid

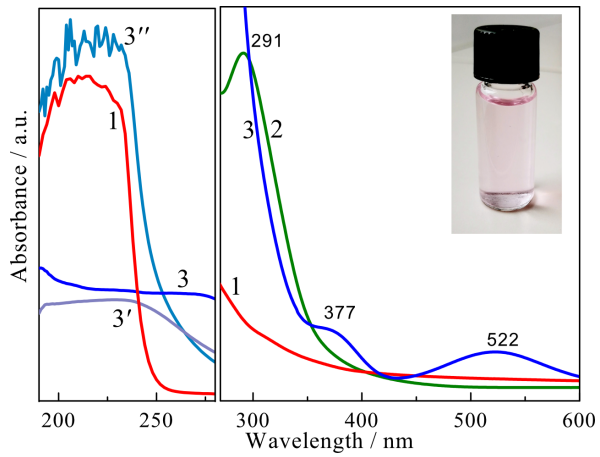

Figure 3: Absorption spectra of methionine (1), tetrachlorauric acid (2) and reddish-pink colored solution of gold species (inset) collected from the $CoFe_2O_4$@Met–Au nanoparticles initially (3) and after dilution to one half (3′) and to on quarter (3″).

solution, however, a clearly resolved absorption peak at 291 nm is observed. The UV–vis absorption spectrum of the solution containing the gold species collected from the surface of the cobalt ferrite NPs (Figure 3, plot 3) exhibits two absorption shoulders at 522 and 377 nm. The former seems to be originated from the surface plasmon absorption of metallic Au [27-29]. The position of this band mainly depends on the size of Au species [30]. So the absorption position of this peak indicates that the size of the methionine-stabilized gold species is extremely small. This assumption was further verified by AFM of gold species spread on a freshly cleaved mica substrate (Figure 4a).

According to these investigations, the shape and size of gold species attached to the surface of magnetic NPs were estimated. The vast majority of species are 1–2 nm sized gold quantum dots (QDs) (Figure 4b). Control experiments demonstrated that the gold species detached from the surface of magnetic NPs coalesced upon dilution of the analyzed Au@Met solution. Consequently, it can be assumed that a significant part of the NPs larger than 2–3 nm are coalesced ultra-small gold QDs.

The state of gold species formed and attached to the surface of methionine-stabilized cobalt ferrite NPs was also investigated using X-ray photoelectron spectroscopy (XPS). The surface chemical composition of the $CoFe_2O_4$@Met–Au NPs is presented in Table 1, whereas the typical core-level spectrum of the deposited gold is presented in Figure 5. As shown, the main Au $4f_{7/2}$ photoelectron peak is located at a binding energy (BE)

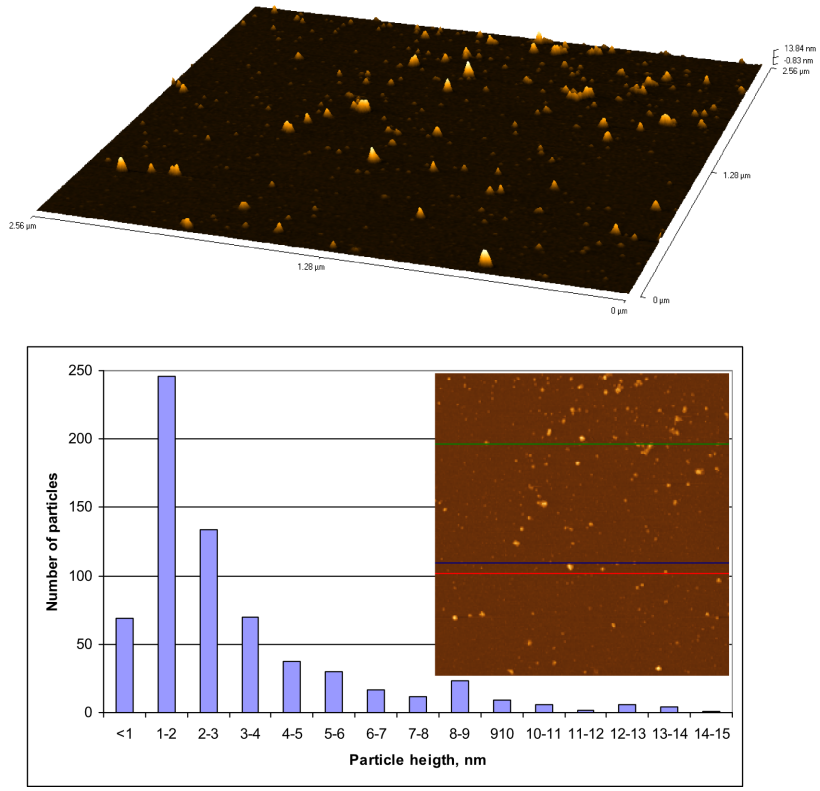

Figure 4: a) AFM 3D image and b) size distribution histogram b) of Au species removed from the surface of $CoFe_2O_4$@Met–Au NPs.

Table 1: Elemental composition of $CoFe_2O_4$@Met–Au NPs.

name	peak BE (eV)	FWHM (eV)	peak area (arb. un.)	atom %
Au 4f	83.94	1.96	12435.07	1.39
C 1s	284.87	2.88	18041.56	36.02
N 1s	399.98	2.24	2647.25	3.02
O 1s	530.21	3.03	55974.26	40.37
Fe 2p	710.75	3.70	63210.72	12.68
Co 2p	780.67	3.29	36815.35	6.47

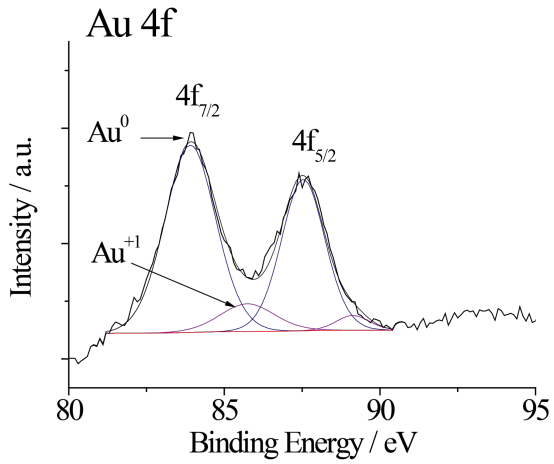

Figure 5: Deconvoluted X-ray photoelectron spectrum (XPS) of Au 4f.

value of 83.94 eV, typical of pure metallic Au^0 species [31]. The fitting of the Au 4f core-level spectrum is performed further by using two spin–orbit split Au $4f_{7/2}$ and Au $4f_{5/2}$ components, separated by 3.56 eV. Surprisingly, the Au 4f curve fitting shows an additional shoulder peaked at 85.74 eV indicating the presence of Au^+ species [31,32]. Their relative distribution reveals a fraction of about 13.7% of Au^+ on the NPs surface of the total deposited gold content of 1.39% (Table 1). It is noticeable that plasmonic gold NPs upon excitation with nanosecond laser light the wavelength of which corresponds to the maximum absorption peak can create hot electrons in the conductive band of gold and, as a result, generate especially active singlet oxygen ($^1O_2$), $^{\cdot}OH$ and O_2^- [33,34].

FTIR spectra

Figure 6 compares the infrared spectra of cobalt ferrite NPs grown via the methionine-assisted hydrothermal approach, and methionine as well as methionine sulfoxide. The FTIR spectrum of the same NPs sonicated in an aqueous solution of chloroauric acid at 37 °C for 4 h is presented. The characteristic peaks of methionine are at 1582 cm^{-1}, assigned to antisymmetric $\nu_{as}(COO)$ and symmetric $\nu_s(COO)$ stretching vibrations of the COO^- group, whereas the bands in the spectral region of 1277–1341 cm^{-1} are due to the coupled vibration of CH_2 antisymmetric deformation and CH deformation modes [35,36]. According to the literature data [27], the band at 1516 cm^{-1} is

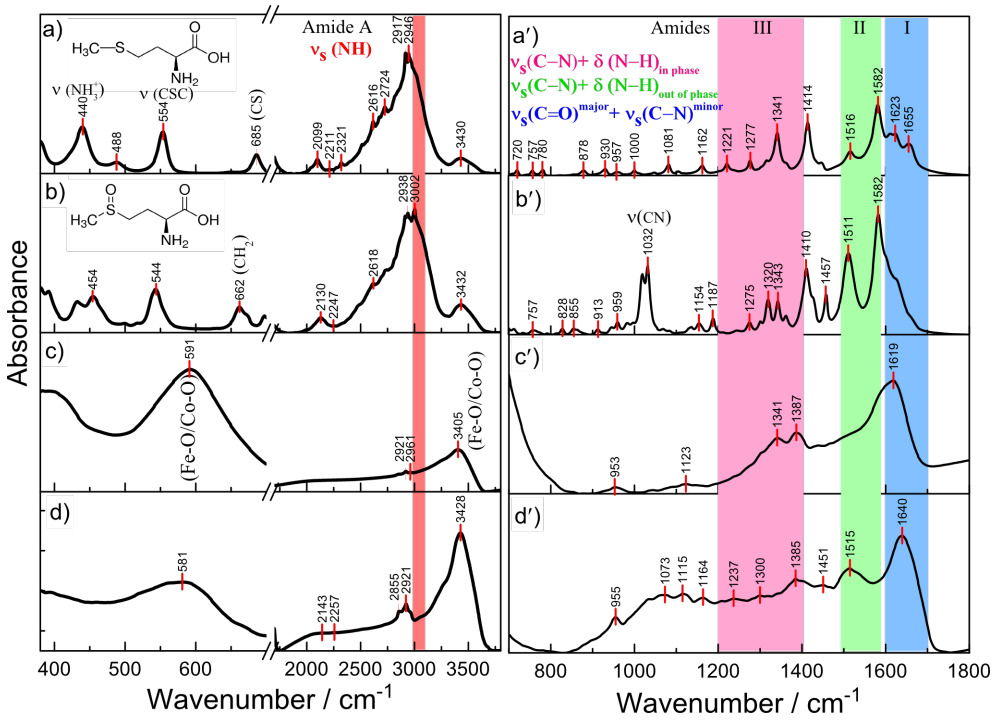

Figure 6: FTIR spectra of methionine (a, a′), methionine sulfoxide (b, b′), cobalt ferrite NPs stabilized with methionine (c, c′), and the same NPs after decoration with gold (d, d′) within the indicated wavenumbers.

associated with the symmetric deformation vibration of NH_3^+, $\delta_s(NH_3)$. Besides, the typical methionine S–C stretching mode at 685 cm^{-1} [37,38] and a clear resolved C–S–C stretching mode, ν(CSC), peaked at 554 cm^{-1} [39] are present in the spectrum. In the FTIR spectra of methionine and methionine sulfoxide a broad and strong band peaked at 2950–3002 cm^{-1} belongs to the symmetric stretching of NH_3^+ ions [40]. In the spectrum of Co ferrite NPs, presented in Figure 6c, the intense and broad band peaked at 591 cm^{-1} belongs to Fe–O/Co–O stretching vibrations in the tetrahedral metal complex [41]. The broad band, peaked near 1515 cm^{-1}, belongs to $\delta_s(NH_3)$ mode and is indicative of the presence of charged amino groups [35,37]. The symmetric C–H deformation mode is also observed at 1341 cm^{-1} in the FTIR spectra of both pure methionine and $CoFe_2O_4$@Met. The attachment of methionine molecules during the synthesis of NPs can also be proven by the presence of the vibration modes in the frequency range of 2961–2855 cm^{-1}, attributable to the symmetric stretching of NH_3^+ ions [42]. The frequency of $\nu_s(COO)$ downshifts from 1414 to 1387 cm^{-1} upon stabilization of ferrite NPs with methionine molecules. The band near 1515 cm^{-1}, however, can only be seen in the $CoFe_2O_4$@Met FTIR spectrum after sonication of NPs in the chloroauric acid-containing solution. The well-resolved band peaked at 1385 cm^{-1} is also characteristic for the FTIR spectrum of NPs after their sonication in the chloroauric acid solution (Figure 6d). As has been previously reported, such frequency downshift is due to the direct interaction of the carboxylate group of the amino acid with the NP surface [43]. We also suspect that the appearance of the significantly stronger symmetric vibration mode in the FTIR spectrum of gold decorated NPs at 1515 cm^{-1} due to cooperative vibrations of $–CH_3$ and $–NH_2$ groups is indicative of the oxidation of methionine to methionine sulfoxide. However, this mechanism requires more specific evidence and needs to be studied.

Conclusion

Superparamagnetic methionine-coated cobalt ferrite nanoparticles with an average size of ca. 6 nm were hydrothermally synthesized via co-precipitation. Then the stabilizing shell of methionine molecules attached to Np surface was successfully applied for the reduction of the chloroauric acid. The formation of ultra-small Au^0/Au^+ QDs with a mean size of ca. 1.5 nm at the surface of magnetic NPs, which retains their magnetic, binding and conjugation properties, has been confirmed by HRTEM, AFM, XPS and magnetic investigations. Contrary to the previous works reported on the formation of Au^0 nanoparticulate shells with thicknesses above 10 nm, we obtained numerous Au^0/Au^+ QDs at the surface of magnetic NPs stabilized with a biocompatible methionine shell. In this way, the initial saturation magnetization of the $CoFe_2O_4$@Met NPs (ca. 27 emu·g^{-1}) decreased by ca. 22%. Besides, the formation of more than 13.5% of extremely active Au^+ species of the total gold content at the surface can have a dramatic effect on the formation of the surface protein corona in the bloodstream that affects $CoFe_2O_4$@Met–Au NPs passive targeting and uptake into tumor cells.

The elaborated functionalization of magnetic NPs with gold QDs represents a promising multi-task platform for linking magnetic NPs with specific targeting ligands, such as aptamers and antibodies. This synthesis way may also be explored in future to design superparamagnetic, methionine-stabilized plasmonic magnetite NPs decorated with Au^0/Au^{+1} QDs.

Experimental

Chemicals: All chemicals, including Co(II) and Fe(III) chlorides, and $HAuCl_4·4H_2O$ were of analytical grade, purchased from Aldrich and used without further purification. NaOH was purchased from Poch SA (Poland) and purified by preparation of a saturated solution, which lead to crystallization of other sodium salts. D,L-methionine (99% purity) and D,L-methionine sulfoxide (≥99.0% purity) were purchased from Sigma-Aldrich Co. Distilled water was used throughout the experiments.

Synthesis of Co-ferrite nanoparticles: Superparamagnetic cobalt ferrite nanoparticles were synthesized by a hydrothermal approach in an alkaline solution (40 mL) of Co(II) and Fe(III) chlorides, at a molar ratio 1:2, at 130 °C for 10 h using a 10 K·min^{-1} ramp. The total metal salt concentration was 75 mmol·L^{-1}. Methionine (0.2 mol·L^{-1}) was used as the reducing and capping additive. The pH value of the solution was kept at 12.4 by addition of 2.0 mol·L^{-1} NaOH solution. The required quantity of NaOH solution was determined by an additional blank experiment. In the subsequent experiment, this quantity was placed in the reactor, and mixed with the other components, during several seconds under vigorous stirring. The as-grown products were collected by centrifugation at 8500 rpm for 3 min and carefully rinsed 5 times using fresh portions (10 mL) of H_2O. Afterwards, the NPs were dried at 60 °C. The collected NPs were studied and subjected to further processing within the following two days.

Gold deposition: The deposition of gold onto the Co ferrite surface was carried out through the methionine-induced chemical reduction of $HAuCl_4$. Briefly, 3.5 mL of NP solution was diluted to 5 mL under ultrasonic agitation for 10 min and 2.0 mL of $HAuCl_4$ (10 mmol·L^{-1}) was introduced into the reaction medium under ultrasound agitation. The solution was alkalized to the required pH value by addition of 2.0 mol·L^{-1} NaOH under vigorous stirring. The deposition process was performed at 37 °C for 4 h under mild mixing conditions. The products ob-

tained were collected by magnetic separation, carefully rinsed several times with deionized water and re-dispersed in ethanol for further examinations. For TEM observations, a drop of NPs suspension was placed onto a lacey grid, whereas for FTIR and magnetic investigations the suspension was dried at 60 °C.

Analysis: The concentration of gold remaining in the deposition solution was determined by inductively coupled plasma mass spectrometry. Measurements were made on emission peaks at λ_{Au} = 267.595 nm, λ_{Au} = 242.795 nm, λ_{Co} = 228.616 nm and λ_{Fe} = 238.204 nm using an OPTIMA 7000DV (Perkin Elmer, USA) spectrometer. Calibration curves were made using dissolved standards (1 to 50 ppm) in the same acid matrix as the unknown samples.

Characterization: The morphology of as-grown products was investigated using a transmission electron microscope (TEM, model MORGAGNI 268) operated at an accelerating voltage of 72 keV. The average size of nanoparticles was estimated from at least 150 species observed in the TEM images. High-resolution transmission electron microscopy (HRTEM) studies of as-synthesized products were performed using a LIBRA 200 FE at an accelerating voltage of 200 keV. X-ray powder diffraction experiments were performed on a D8 diffractometer (Bruker AXS, Germany), equipped with a Göbel mirror as a primary beam monochromator for Cu Kα radiation. Upgraded vacuum generator (VG) ESCALAB MKII spectrometer, fitted with a new XR4 twin anode, was used for XPS investigations. The non-monochromatised Mg Kα X-ray source was operated at $h\nu$ = 1253.6 eV with 300 W power (20 mA/15 kV) and the pressure in the analysis chamber was lower than 5×10^{-7} Pa during spectral acquisition. The spectra were acquired with an electron analyzer pass energy of 20 eV and resolution of 0.05 eV and with a pass energy of 100 eV. All spectra were recorded at a 90° take-off angle and the binding energies (BE) scale was calibrated by measuring of the C 1s peak at 284.6 eV. The spectra calibration, processing and fitting routines were done using Avantage software (5.918) provided by Thermo VG Scientific. Core-level peaks of Fe 2p, Co 2p, Au 4f, C 1s and O 1s were analyzed using a nonlinear Shirley-type background and the calculation of the elemental composition was performed on the basis of Scofield's relative sensitivity factors. The FTIR spectra were recorded in transmission mode with a Bruker Vertex 70v vacuum FTIR spectrometer over the wavenumber range of 4000–400 cm^{-1}. A 7 mm thick KBr discs were prepared under high pressure by mixing the powdered samples with KBr powder. Samples for AFM measurements were prepared by casting a drop (20 µL) of gold NP solution on freshly cleaved V-1 grade muscovite mica (SPI supplies, USA). The drop of solution was removed after 60s by spinning the sample at 1000 rpm. The commercially available atomic force microscope (AFM) diInnova (Veeco instruments inc., USA) was used to take three-dimensional (3D) images of gold nanoparticles. TESPA-V2 cantilevers (Veeco Instruments Inc., USA) with a tip curvature of 8 nm were used. Measurements were performed in the tapping mode in air. Images were acquired at the scan rate of 1 Hz per line with the 512 × 512 pixel image resolution. Image processing included flattening (2nd order) to remove the background slope caused by the irregularities of the piezoelectric scanner. The analysis was performed using the SpmLabAnalysis software (Veeco Instruments Inc., USA).

Magnetization measurements were accomplished using a vibrating-sample magnetometer calibrated by a Ni sample of similar dimensions as the studied sample. The magnetometer was composed of the vibrator, the lock-in amplifier, and the electromagnet. The magnetic field was measured by a testameter FH 54 (Magnet-Physics Dr. Steingrover GmbH).

Acknowledgements

The authors are thankful to Drs. Saulius Tumėnas, Vitalija Jasulaitiene, Kęstutis Mažeika, and Vilius Poderys for FTIR and XPS spectra, magnetic measurements and AFM tests, respectively.

References

1. Demirer, G. S.; Okur, A. C.; Kizilela, S. *J. Mater. Chem. B* **2015,** *3,* 7831–7849. doi:10.1039/C5TB00931F
2. Acharaya, A. J. *Nano Sci. Nano Technol.* **2013,** *13,* 3753–3768. doi:10.1166/jnn.2013.7460
3. Mashhadizadeh, M. H.; Amoli-Diva, M. *J. Nanomed. Nanotechnol.* **2012,** *3,* 2–8. doi:10.4172/2157-7439.1000139
4. Viswanathan, K. *Colloids Surf., A* **2011,** *386,* 11–15. doi:10.1016/j.colsurfa.2011.06.017
5. Lu, H.; Yi, G.; Zhao, S.; Chen, D.; Guo, L.-H.; Chen, J. *J. Mater. Chem.* **2004,** *14,* 1336–1341. doi:10.1039/b315103d
6. Salgueiriño-Maceira, V.; Correa-Duarte, M. A.; Spasova, M.; Liz-Marzán, L. M.; Farle, M. *Adv. Funct. Mater.* **2006,** *16,* 509–514. doi:10.1002/adfm.200500565
7. Cai, H.; Li, K.; Shen, M.; Wen, S.; Luo, Y.; Peng, C.; Zhang, G.; Shi, X. *J. Mater. Chem.* **2012,** *22,* 15110. doi:10.1039/c2jm16851k
8. An, P.; Zuo, F.; Li, X.; Wu, Y.; Zhang, J.; Zheng, Z.; Ding, X.; Peng, Y. *Nano* **2013,** *8,* 1350061. doi:10.1142/S1793292013500616
9. Wu, A.; Ou, P.; Zeng, L. *Nano* **2010,** *05,* 245–270. doi:10.1142/S1793292010002165
10. Deng, Y.-H.; Wang, C.-C.; Hu, J.-H.; Yang, W.-L.; Fu, S.-K. *Colloids Surf., A* **2005,** *262,* 87–93. doi:10.1016/j.colsurfa.2005.04.009
11. Larsen, B. A.; Haag, M. A.; Serkova, N. J.; Shroyer, K. R.; Stoldt, C. R. *Nanotechnology* **2008,** *19,* 265102. doi:10.1088/0957-4484/19/26/265102
12. Cui, Y.; Wang, Y.; Hui, W.; Zhang, Z.; Xin, X.; Chen, C. *Biomed. Microdevices* **2005,** *7,* 153–156. doi:10.1007/s10544-005-1596-x
13. Tamer, U.; Gündoğlu, Y.; Boyacı, İ. H.; Pekmez, K. *J. Nanopart. Res.* **2010,** *12,* 1187–1196. doi:10.1007/s11051-009-9749-0

14. Fan, Z.; Shelton, M.; Singh, A. K.; Senapati, D.; Khan, S. A.; Ray, P. C. *ACS Nano* **2012,** *6,* 1065–1073. doi:10.1021/nn2045246
15. Chen, M.; Yamamuro, S.; Farrell, D.; Majetich, S. A. *J. Appl. Phys.* **2003,** *93,* 7551–7553. doi:10.1063/1.1555312
16. Brown, K. R.; Walter, D. G.; Natan, M. J. *Chem. Mater.* **2000,** *12,* 306–313. doi:10.1021/cm980065p
17. Jagminas, A.; Mažeika, K.; Kondrotas, R.; Kurtinaitienė, M.; Jagminienė, A.; Mikalauskaitė, A. *Nanomater. Nanotechnol.* **2014,** *4,* 11. doi:10.5772/58453
18. Mikalauskaitė, A.; Kondrotas, R.; Niaura, G.; Jagminas, A. *J. Phys. Chem. C* **2015,** *119,* 17398–17407. doi:10.1021/acs.jpcc.5b03528
19. Belachew, N.; Rama Devi, D.; Basavaiah, K. *J. Mol. Liq.* **2016,** *224,* 713–720. doi:10.1016/j.molliq.2016.10.089
20. Sun, C.; Zhou, R.; Jianan, E.; Sun, J.; Su, Y.; Ren, H. *RSC Adv.* **2016,** *6,* 10633–10640. doi:10.1039/C5RA22491H
21. Coelgo, B. C. P.; Siqueira, E. R.; Ombredane, A. S.; Joanitti, G. A.; Chaves, S. B.; da Silva, S. W.; Chaker, J. A.; Longo, J. P. F.; Azevedo, R. B.; Morais, P. C.; Sousa, M. H. *RSC Adv.* **2017,** *7,* 11223–11232. doi:10.1039/C6RA27539G
22. Kim, D. K.; Zhang, Y.; Voit, W.; Rao, K. V.; Muhammed, M. *J. Magn. Magn. Mater.* **2001,** *225,* 30–36. doi:10.1016/S0304-8853(00)01224-5
23. Berry, C. C.; Wells, S.; Charles, S.; Curtis, A. S. G. *Biomaterials* **2003,** *24,* 4551–4557. doi:10.1016/S0142-9612(03)00237-0
24. Žalnėravičius, R.; Paškevičius, A.; Mažeika, K.; Jagminas, A. *Appl. Surf. Sci.* **2017,** submitted.
25. Massart, R. *IEEE Trans. Magn.* **1981,** *17,* 1247–1248. doi:10.1109/TMAG.1981.1061188
26. Guinier, A.; Lorrain, P.; Lorrain, D. S.-M. X-Ray Diffraction. *Crystals, Imperfect Crystals and Amorphous Bodies;* Freeman, W. H. & Co.: San Francisco, CA, U.S.A., 1963; p 356.
27. Hains, W.; Thanh, N. T. K.; Aveyard, J.; Fernig, D. G. *Anal. Chem.* **2007,** *79,* 4215–4221. doi:10.1021/ac0702084
28. Amendola, V.; Meneghetti, M. *J. Phys. Chem. C* **2009,** *113,* 4277–4285. doi:10.1021/jp8082425
29. Njoki, P. N.; Lim, I-I. S.; Mott, D.; Park, H. Y.; Khan, B.; Mishra, S.; Sujakumar, R.; Luo, J.; Zhong, C.-J. *J. Phys. Chem. C* **2007,** *111,* 14664–14669. doi:10.1021/jp074902z
30. Wang, L.; Luo, J.; Fan, Q.; Suzuki, M.; Suzuki, I. S.; Engerlhard, M. H.; Lin, Y.; Kim, N.; Wang, J. Q.; Zhong, C.-J. *J. Phys. Chem. B* **2005,** *109,* 21593–21601. doi:10.1021/jp0543429
31. Moulder, J. F.; Stickle, W. F.; Sobol, P. E.; Bomben, K. D. In *Handbook of X-Ray Photoelectron Spectroscopy;* Chastain, J.; King, R. C., Eds.; Physical Electronics: Eden Prairee, MN, U.S.A., 1995.
32. Venezia, A. M.; Pantaleo, G.; Longo, A.; Di Carlo, G.; Casaletto, M. P.; Liotta, L.; Deganello, G. *J. Phys. Chem. B* **2005,** *109,* 2821–2827. doi:10.1021/jp045928i
33. Misawa, M.; Takahashi, J. *Nanomedicine* **2011,** *7,* 604–614. doi:10.1016/j.nano.2011.01.014
34. Zhang, W.; Li, Y.; Niu, J.; Chen, Y. *Langmuir* **2013,** *29,* 4647–4651. doi:10.1021/la400500t
35. Ito, A.; Honda, H.; Kobayashi, T. *Cancer Immunol. Immunother.* **2006,** *55,* 320–328. doi:10.1007/s00262-005-0049-y
36. Saha, K.; Agasti, S. S.; Kim, C.; Li, X.; Rotello, V. M. *Chem. Rev.* **2012,** *112,* 2739–2779. doi:10.1021/cr2001178
37. Abadeer, N. S.; Murphy, C. J. *J. Phys. Chem. C* **2016,** *120,* 4691–4716. doi:10.1021/acs.jpcc.5b11232
38. Paiva, F. M.; Batista, J. C.; Rego, F. S. C.; Lima, J. A., Jr.; Freire, P. T. C.; Melo, F. E. A.; Mendes Filho, J.; de Menezes, A. S.; Nogueira, C. E. S. *J. Mol. Struct.* **2017,** *1127,* 419–426. doi:10.1016/j.molstruc.2016.07.067
39. Wolpert, M.; Hellwig, P. *Spectrochim. Acta, Part A* **2006,** *64,* 987–1001. doi:10.1016/j.saa.2005.08.025
40. Pandiarajan, S.; Umadevi, M.; Briget Mary, M.; Rajaram, R. K.; Ramakrishnan, V. *J. Raman Spectrosc.* **2004,** *35,* 907–913. doi:10.1002/jrs.1224
41. Safi, R.; Ghasemi, A.; Shoja-Razavi, R.; Tavousi, M. *J. Magn. Magn. Mater.* **2015,** *396,* 288–294. doi:10.1016/j.jmmm.2015.08.022
42. Zor, S.; Kandemirli, F.; Bingul, M. *Prot. Met. Phys. Chem. Surf.* **2009,** *45,* 46–53. doi:10.1134/S2070205109010079
43. Dagys, M.; Lamberg, P.; Shleev, S.; Niaura, G.; Bachmatova, I.; Marcinkeviciene, L.; Meskys, R.; Kulys, J.; Arnebrant, T.; Ruzgas, T. *Electrochim. Acta* **2014,** *130,* 141–147. doi:10.1016/j.electacta.2014.03.014

License and Terms

The definitive version of this article is the electronic one which can be found at: doi:10.3762/bjnano.8.174

BEILSTEIN JOURNAL OF NANOTECHNOLOGY

Synthesis and functionalization of $NaGdF_4$:Yb,Er@$NaGdF_4$ core–shell nanoparticles for possible application as multimodal contrast agents

Dovile Baziulyte-Paulaviciene[1], Vitalijus Karabanovas[*2,3,§], Marius Stasys[2,4], Greta Jarockyte[2,4], Vilius Poderys[2], Simas Sakirzanovas[1,5] and Ricardas Rotomskis[2,4]

Full Research Paper

Open Access

Address:
[1]Faculty of Chemistry and Geosciences, Vilnius University, Naugarduko str. 24, Vilnius LT-03225, Lithuania, [2]Biomedical Physics Laboratory, National Cancer Institute, Baublio str. 3b, Vilnius 2, Lithuania, [3]Department of Chemistry and Bioengineering, Vilnius Gediminas Technical University, Sauletekio Ave. 11, Vilnius, LT-10223, Lithuania, [4]Biophotonics group of Laser Research Center, Faculty of Physics, Vilnius University, Sauletekio Ave. 9, Vilnius LT-10222, Lithuania and [5]Institute of Chemistry, Center for Physical Sciences and Technology, Sauletekio Ave. 3, Vilnius, LT-10222, Lithuania

Email:
Vitalijus Karabanovas* - vitalijus.karabanovas@nvi.lt

* Corresponding author
§ Tel. +370 5 2190902

Keywords:
cancer theranostics; core–shell structure; luminescence; multimodal; nanoparticles; upconverting nanoparticles; upconversion

Beilstein J. Nanotechnol. **2017,** *8,* 1815–1824.
doi:10.3762/bjnano.8.183

Received: 29 March 2017
Accepted: 02 August 2017
Published: 01 September 2017

This article is part of the Thematic Series "Nanomaterial-based cancer theranostics".

Guest Editor: V. Sivakov

Abstract

Upconverting nanoparticles (UCNPs) are promising, new imaging probes capable of serving as multimodal contrast agents. In this study, monodisperse and ultrasmall core and core–shell UCNPs were synthesized via a thermal decomposition method. Furthermore, it was shown that the epitaxial growth of a $NaGdF_4$ optical inert layer covering the $NaGdF_4$:Yb,Er core effectively minimizes surface quenching due to the spatial isolation of the core from the surroundings. The mean diameter of the synthesized core and core–shell nanoparticles was ≈8 and ≈16 nm, respectively. Hydrophobic UCNPs were converted into hydrophilic ones using a nonionic surfactant Tween 80. The successful coating of the UCNPs by Tween 80 has been confirmed by Fourier transform infrared (FTIR) spectroscopy. Scanning electron microscopy (SEM), powder X-ray diffraction (XRD), photoluminescence (PL) spectra and magnetic resonance (MR) T1 relaxation measurements were used to characterize the size, crystal structure, optical and magnetic properties of the core and core–shell nanoparticles. Moreover, Tween 80-coated core–shell nanoparticles presented enhanced optical and MR signal intensity, good colloidal stability, low cytotoxicity and nonspecific internalization into two different breast cancer cell lines, which indicates that these nanoparticles could be applied as an efficient, dual-modal contrast probe for in vivo bioimaging.

Introduction

Lanthanide-doped multimodal upconverting nanoparticles (UCNPs), which can convert near-infrared (NIR) radiation into visible light, have been extensively investigated due to the advantages associated with their unique optical properties [1]. Compared with traditional semiconductor quantum dots (QDs) or organic fluorophores, UCNPs show superior features such as sharp emission peaks, low toxicity, high photochemical stability, high resistance to photobleaching, and long emission lifetime [2,3]. As a unique class of luminescent phosphors, UCNPs show great promise in a broad range of applications ranging from bioimaging, biosensors, drug delivery, to photodynamic therapy [4-8]. Through combination with biologically active molecules, UCNPs could be multifunctional in both therapy and diagnostics (theranostics) [9]. However, biomedical applications require ultrasmall multifunctional nanoparticles to be hydrophilic, biocompatible and have intense upconversion emission and efficient paramagnetic properties. Hexagonal phase sodium gadolinium fluoride β-$NaGdF_4$ is an ideal matrix for the creation optical/magnetic dual-modal bioprobes, but upconversion luminescence (UCL) efficiency of this host material is still low and needs to be improved. A major method to enhance the UCL intensity is to use a core–shell structure, where the nonactive shell protects the luminescent rare earth ions in the core from quenching caused by surface defects and organic ligands [10]. A wide variety of studies were performed to synthesize dual functional core–shell UCNPs [11-13]. However, it remains difficult to obtain hexagonal phase $NaGdF_4$ (a host material exhibiting about an order of magnitude higher upconversion luminescence efficiency compared to cubic ones) with great optical and magnetic properties while maintaining a small size (<20 nm).

The next problem is that those nanoparticles are often synthesized in an organic phase and stabilized with hydrophobic ligands, such as oleic acid. Consequently, they can only be dispersed in nonpolar solvents (e.g., toluene, cyclohexane). In the past few years, several methods including surface silanization [14], ligand exchange [15], ligand oxidation [16], ligand removal [17], and amphiphilic polymer coating [18] have been developed in order to transfer nanoparticles with hydrophobic surfaces into aqueous media. Furthermore, the multimodal UCNP surface modification field still lacks reference materials and established protocols for functionalization and targeting. Some studies showed that the nonionic surfactant Tween 80 helps different nanoparticles (gold, silver and iron oxide) to become well-dispersed in aqueous solution even in the presence of biological molecules, such as different serum proteins [19-21]. However, information about Tween 80-coated gadolinium-based UCNPs behavior in biological systems and biocompatibility/nanotoxicity is still limited. The study of Cascales et al. showed that ultrasmall Yb:Er:$NaGd(WO_4)_2$ UCNPs could be successfully covered with Tween 80 and are internalized by human mesenchymal stem cells without triggering their metabolic activity, but still no information has been presented about uptake of these nanoparticles into different types of cancer cells [22]. Although different gadolinium chelates are widely used in clinics as contrast agents for magnetic resonance imaging (MRI), the literature for the last two years shows increased awareness of the effects of gadolinium toxicity [23,24]. Moreover, the possible influence of gadolinium-based UCNPs on cells is not yet investigated and understood.

In this work, we focus on studies of multimodal core–shell $NaGdF_4$:Yb,Er coated with $NaGdF_4$ ($NaGdF_4$:Yb,Er@$NaGdF_4$) UCNPs synthesis and demonstrate the effective surface modification method that uses a surfactant polysorbate 80 (Tween 80, polyoxyethylene sorbitan laurate). Hexagonal phase β-$NaGdF_4$ was chosen as host lattice for its ability to combine optical and MRI. Tween 80 was used to make the UCNPs colloidally stable and dispersible in water while protecting the surface from nonspecific adsorption of biomolecules. Our results show that Tween 80-coated $NaGdF_4$:Yb,Er@$NaGdF_4$ core–shell nanoparticles exhibit excellent dispersibility in a biological medium and are photostable. We also do not observe any changes in the overall upconversion (UC) emission intensity of Tween 80-coated nanoparticles in comparison with oleic acid coated UCNPs. In addition, the nonspecific uptake and distribution of non-targeted Tween 80-coated UCNPs in human MCF-7 and MDB-MA-231 breast cancer cells was visualized by using confocal fluorescence microscopy. Our results showed that Tween 80-coated UCNPs exhibited low cytotoxicity even at a high-dose concentration.

Results and Discussion

The SEM images of the $NaGdF_4$:Yb,Er core and $NaGdF_4$:Yb,Er@$NaGdF_4$ core–shell nanoparticles are shown in Figure 1. Core nanoparticles are monodisperse, and have a spherical shape with an average diameter of approximately 8 nm with polydispersity index (PDI) of 1.02. The resulting core–shell nanoparticles are polydisperse and have an average diameter of ≈16 nm with PDI of 1.16. This indicates that polydispersity occurred from secondary nucleation during the shell growth process. However, an increase of the size suggests that the $NaGdF_4$ has been successfully epitaxial grown on the $NaGdF_4$:Yb,Er core nanoparticles. The diffraction peaks of the core (Figure 2a) and core–shell (Figure 2b) nanoparticles can be indexed as pure hexagonal β-$NaGdF_4$ phase (JCPDS, Card No. 27-0699), indicating no change in the crystalline phase during the shell growth.

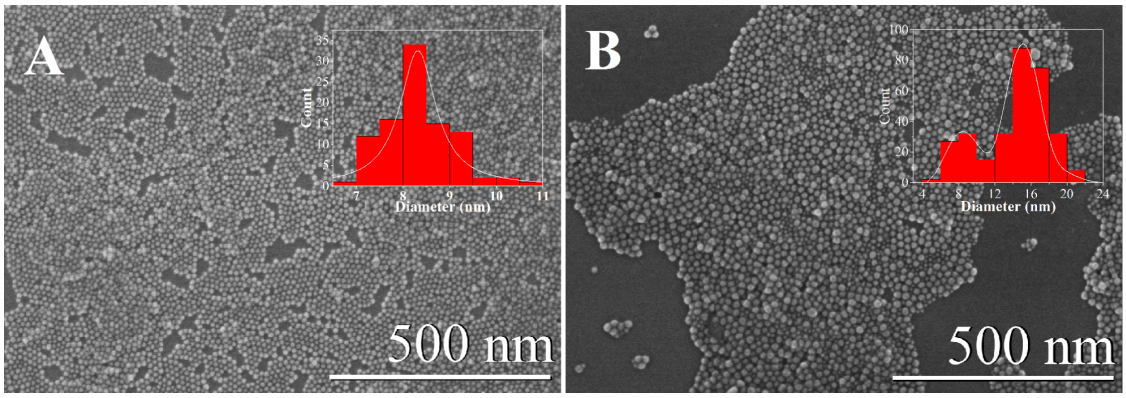

Figure 1: SEM images of the core $NaGdF_4$:Yb,Er (A) and core@shell $NaGdF_4$:Yb,Er@$NaGdF_4$ (B) nanoparticles. The insets display the UCNP diameter distributions.

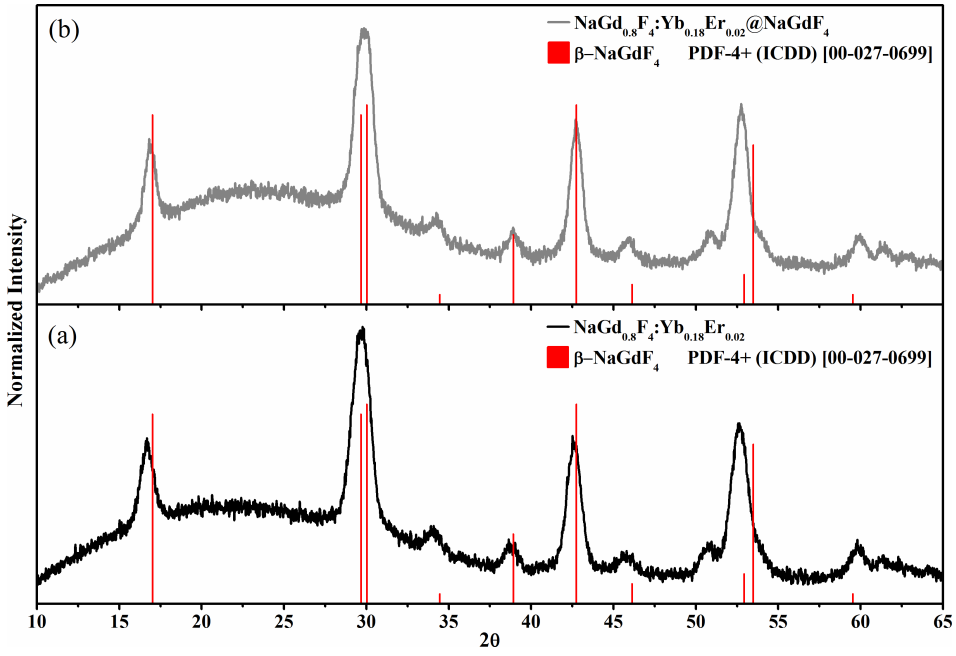

Figure 2: XRD pattern of $NaGdF_4$:Yb,Er core only (a), and $NaGdF_4$:Yb,Er@$NaGdF_4$ core–shell (b) nanoparticles.

The as-obtained core and core–shell UCNPs were hydrophobic as they were stabilized by oleic acid molecules. In this work, hydrophobic core and core–shell nanoparticles were converted into hydrophilic ones using a nonionic surfactant Tween 80.

The presence of the Tween 80 coating was verified by comparing its FTIR spectra to that of pure oleic acid, oleate ligands coated particles, pure Tween 80, and the final coated nanoparticles (Figure 3). $NaGdF_4$:Yb,Er UCNPs prepared in the presence of oleic acid shows characteristic absorption peaks of oleate ligands. The absorption peak at 1710 cm^{-1} (Figure 3f) corresponds to the stretching vibration of C=O in pure oleic acid (Figure 3a) which is replaced by two carboxylate stretching bands (1560 and 1447 cm^{-1} in Figure 3e), which indicates oleate ligand adsorption on the UCNP surface.

Tween 80 is composed of three building blocks: aliphatic ester chains, three-terminal hydroxyl groups and an aliphatic chain (Figure 3b). The aliphatic chain can be adsorbed on the hydrophobic surface by hydrophobic interactions of UCNPs as synthesized in oleic acid [25]. The strong band around 3400 cm^{-1} can be assigned to the O–H stretching vibrations (Figure 3d) from terminal hydroxyl groups of Tween 80 (Figure 3b) and the remaining moisture in the samples. The bands centred at 2922

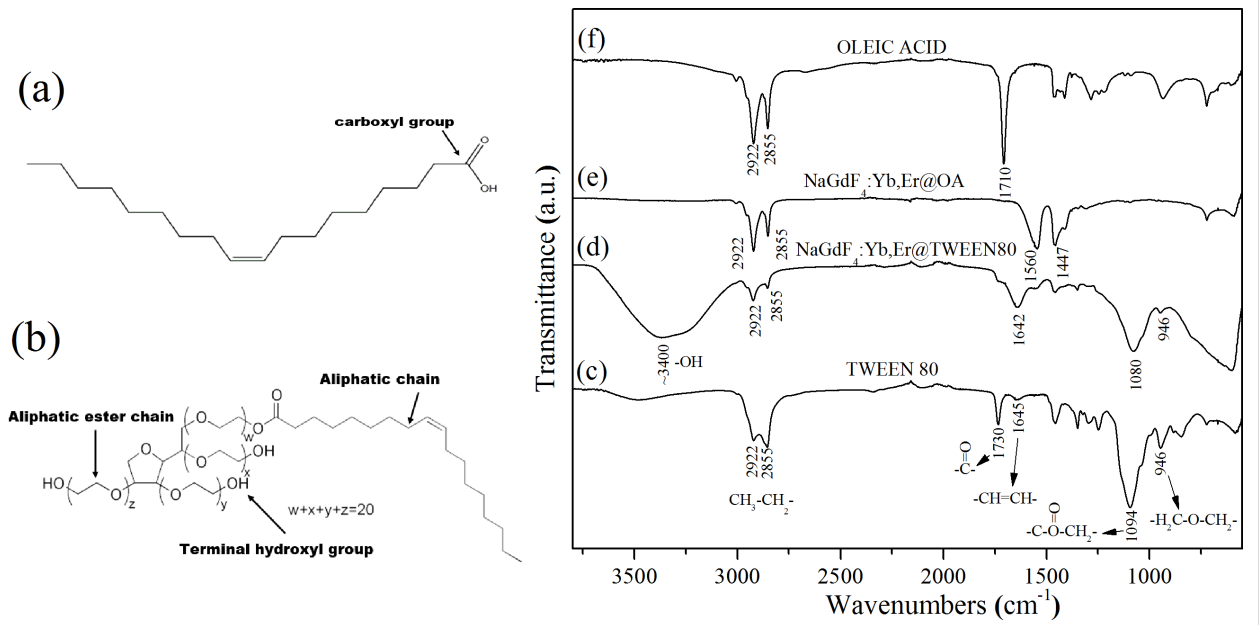

Figure 3: The structure of (a) oleic acid (OA) and (b) Tween 80. FTIR spectra of (c) pure Tween 80, (d) $NaGdF_4$:Yb,Er@Tween80, (e) $NaGdF_4$:Yb,Er@OA, and (f) pure OA.

and 2855 cm^{-1} are associated with the asymmetric (vas) and symmetric (vs) stretching vibrations of methylene (–CH2), respectively. The adsorption peaks at 1730 and 1094 cm^{-1} are attributed to the ester group stretching. The band at 946 cm^{-1} is present, which corresponds to the ether bond from the aliphatic ester chains (Figure 3c). The FTIR data of UCNPs@Tween80 (Figure 3d) is highly comparable with that of pure Tween 80 (Figure 3c), indicating that the Tween 80 was successfully coated onto the UCNPs. Additionally, dynamic light scattering (DLS) was employed to measure the hydrodynamic diameter of Tween-coated UCNPs in the cell culture medium as well as their surface zeta potential. The measured mean hydrodynamic diameter of the Tween-coated core $NaGdF_4$:Yb,Er UCNPs was 38 nm and the core–shell $NaGdF_4$:Yb,Er@$NaGdF_4$ particles was 48 nm. The zeta potential of Tween 80-coated core nanoparticles was about 26 mV and for core–shell nanoparticles it was slightly higher at about 33 mV. More detailed information about the DLS results is presented in the Supporting Information File 1.

The upconversion emission spectra of different NaGdF4:Yb,Er@NaGdF4@Tween80 core–shell and $NaGdF_4$:Yb,Er@Tween80 core nanoparticles dispersed in water are shown in Figure 4a. The major emissions located at 381, 408, 521, 540, 654 and 756 nm can be attributed to radiative transitions from $^4G_{11/2}$ $^2H_{9/2}$, $^2H_{11/2}$, $^4S_{3/2}$, $^4F_{9/2}$ and $^4I_{9/2}$ levels to the $^4I_{15/2}$ level of Er^{3+} (Figure 4b), respectively. The comparison with the core-only nanoparticles showed that coating the $NaGdF_4$:Yb^{3+},Er^{3+} core with a shell that has the same crystal lattice structure reduce the effects of luminescence quenching from the addition of ligands and/or surface defects and therefore a significant increase in the UCL can be observed. For the core-only nanoparticles, lanthanide dopants are exposed to surface deactivations owing to the high surface-to-volume ratio at the nanometer dimension, thus yielding UCL at low efficiency. The integrated intensity (521 nm) of the core–shell $NaGdF_4$:Yb,Er@$NaGdF_4$ nanoparticles was estimated to be about two magnitudes higher than the core-only $NaGdF_4$:Yb,Er UCNPs. The results indicate that the core–shell structure can effectively spatially isolate lanthanide dopants from being quenched, and also negate the influence of surface defects. The results correlate well with what is presented in the literature. Yi et al. reported that the UC emissions of hexagonal phase $NaYF_4$:Yb^{3+},Er^{3+} were enhanced by as much as seven times by growth of a 2 nm layer of $NaYF_4$ [26]. In a later publication, the same conclusion was independently verified in core–shell UCNPs of $NaGdF_4$:Yb^{3+},Tm^{3+}@$NaGdF_4$ and $KGdF_4$:Yb^{3+},Tm^{3+}@$KGdF_4$ when compared to the core under 980 nm excitation [11,12,27].

As shown in Figure 5 (inset), a positive enhancement for the magnetic resonance (MR) signal was observed for all the UCNPs samples when compared to water. Moreover, with the increase of the concentration of UCNPs, the T1-weighted MRI signal intensity (SI) continuously increased, resulting in brighter images for both types of UCNPs. The MR SI values of UCNPs are presented in Figure 5. The maximum MR signal enhancement was of approximately 3.5-fold compared with the refer-

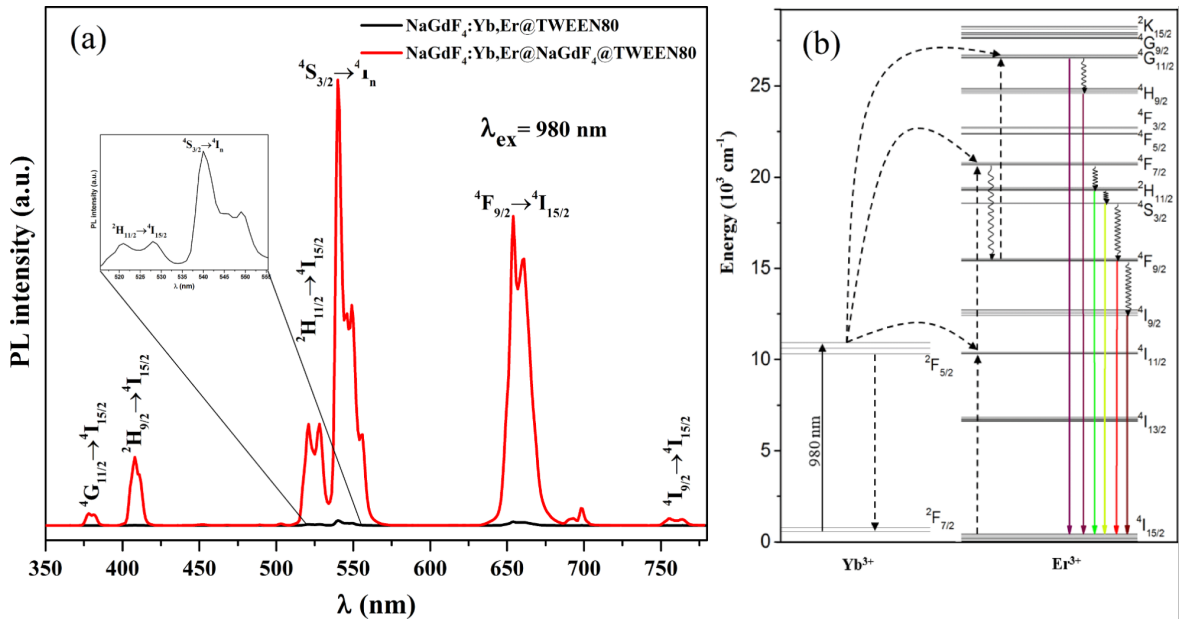

Figure 4: (a) Upconversion luminescence spectra of Tween 80-coated UCNPs upon 980 nm excitation [28] and (b) energy level diagram of Yb^{3+} and Er^{3+} ions.

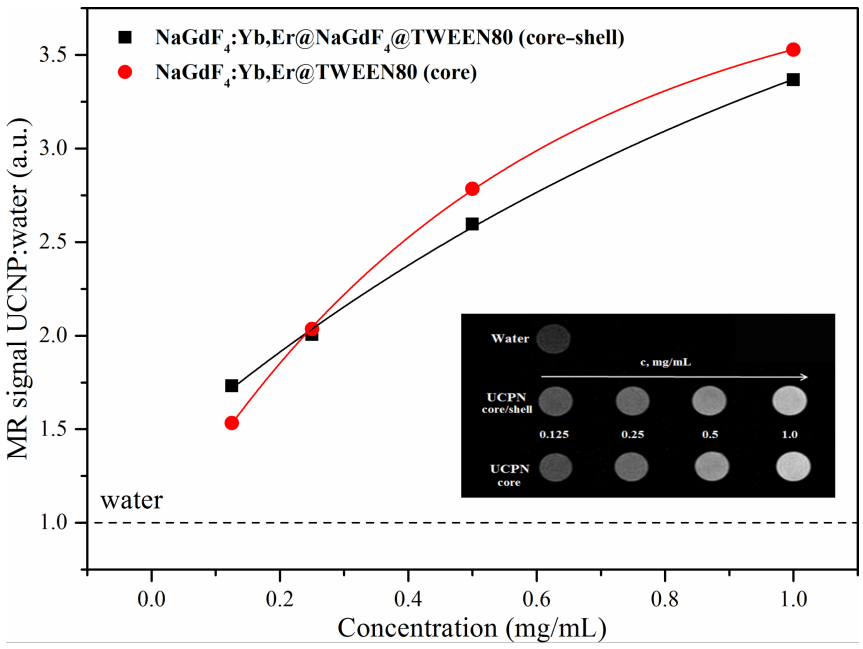

Figure 5: Magnetic resonance (MR) signal intensity (SI) plot of core (red dots) and core–shell (black squares) UCNPs of different concentrations of aqueous solutions. Water SI is marked as a dashed line as a reference; Inset: T1-weighted MR in vitro images of core and core–shell UCNPs at different concentrations of aqueous solutions.

ence. There was no significant difference observed in MR signal enhancement between the core and core–shell UCNPs. Therefore, it can be concluded that the UCNP coating does not affect the favorable MRI properties of UCNPs. That signifies that the Gd^{3+} ions in the shell of the UCNPs are the major contributors toward the relaxation of water protons, and the UCNP core does not show any significant effect towards relaxivity enhancement. However, it has been shown in the literature that reduced water access to the Gd^{3+} ions may yield reduced values for MR signal enhancement [29,30]. These observations

indicate that both core and core–shell UCNPs could be applied as efficient MRI contrast agents as they both present enhanced MR signal intensity.

The as-prepared Tween 80-coated core–shell $NaGdF_4$:Yb,Er@$NaGdF_4$ nanoparticles were studied to evaluate their application to biological imaging using MDA-MB-231 breast cancer cells. The confocal image of MDA-MB-231 breast cancer cells after 24 h incubation with UCNPs is shown in Figure 6A. The scatter of excitation light by intracellular cell structures was marked with red color. This was obtained by excitation at 514 nm and detected at 500–530 nm. Tween 80-coated core–shell UCNPs were marked with green color (excitation was continuous wave at 980 nm and detection at 500–530 nm). The cell nuclei were labeled with DAPI and imaged using an excitation of 405 nm and detected at using a bandpass filter with a center wavelength of 450 nm and bandwidth of 35 nm. As seen from Figure 6A, the luminescence of the UCNPs came from the intracellular region, suggesting that Tween 80-coated nanoparticles were non-specifically internalized into cells and concentrated within the cytoplasm. The similar localization of Tween 80-coated nanoparticles was observed in MCF-7 cells as well. The same results of endocytic NP accumulation in cells was demonstrated in different studies with UCNPs [31], quantum dots [32], magnetic nanomaterials [33] and noble metal nanoparticles [34].

Cell viability assay XTT was performed to measure the cellular metabolic activity of human breast cancer MCF-7 and MDA-MB-231 cell lines after 24 h treatment with core–shell Tween 80-coated UCNPs (Figure 6B). Untreated cells were used as a control group. After 24 h of incubation in the UCNP concentration range from 5 to 100 μg/mL, the viability of human breast cancer MCF-7 cells remained over 92–100% and the viability of MDA-MB-231 cells remained 85–93%. These results clearly express that core–shell gadolinium-based UCNPs have low cytotoxicity and are in good agreement with previous studies [35,36].

Conclusion

In summary we have successfully synthesized ultrasmall, monodisperse, hexagonal phase core $NaGdF_4$:Yb,Er nanoparticles and polydisperse, core–shell $NaGdF_4$:Yb,Er@$NaGdF_4$ nanoparticles.

Oleate-capped core $NaGdF_4$:Yb,Er nanoparticles and core–shell $NaGdF_4$:Yb,Er@$NaGdF_4$ nanoparticles were successfully transferred to aqueous solutions after surface modification with the surfactant Tween 80. The core–shell UCNPs presented enhanced upconversion intensity and MR signal intensity, which indicates that these nanoparticles could be applied as an efficient dual optical, MRI contrast agent. Moreover, an in vitro uptake and cytotoxicity evaluation study showed that the UCNPs internalized into breast cancer cell lines and possessed low cytotoxicity and good biocompatibility. All these findings indicate that Tween 80-coated $NaGdF_4$:Yb,Er@$NaGdF_4$ UCNPs are a promising nanomaterial platform for imaging and detection in oncology.

Experimental

Materials: All of the chemicals used in our experiments were of analytical grade and used without further purification. Ln

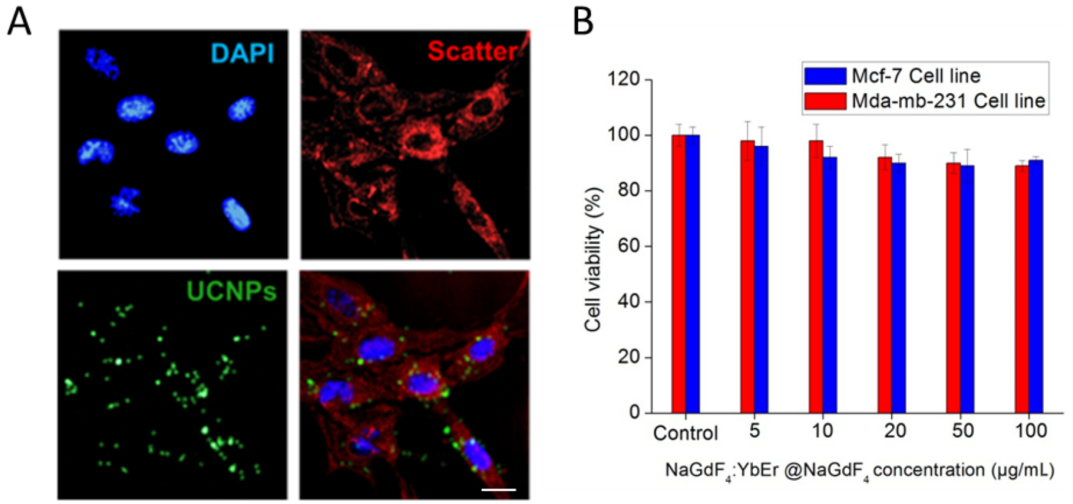

Figure 6: A) Confocal images of MDA-MB-231 cells after 24 h treatment with Tween 80-coated core–shell UCNPs (10 μg/mL); UCNPs are green, DAPI staining is blue, the red color represents excitation scattering from intracellular structures. Scale bar equals 10 μm. B) Viability of MCF-7 and MDA-MB-213 cells, treated with different concentrations of UCNPs for 24 h. Toxicity of UCNPs was investigated using XTT cell viability assay.

oxides (Ln_2O_3, 99.99%, Ln: Gd, Yb, Er) were obtained from Treibacher Industrie AG (Germany). Oleic acid (OA, 90%) was purchased from Fisher Scientific, 1-octadecene (ODE, 90%) was obtained from Sigma-Aldrich. Tween 80 (polysorbate 80) was purchased from Merck Millipore. Other chemicals including hydrochloric acid, sodium hydroxide, ammonium fluoride, methanol, chloroform, cyclohexane and acetone were obtained from Reachem Slovakia.

Synthesis of core β-$NaGdF_4$:Yb,Er nanoparticles: The synthesis of β-$NaGdF_4$:Yb,Er NPs was developed via a modified procedure from the literature [11]. In a typical experiment, 1.6 mmol Gd_2O_3, 0.36 mmol Yb_2O_3 and 0.04 mmol Er_2O_3 were dissolved in HCl at an elevated temperature (≈80 °C) to prepare the rare earth chloride stock solution. Metal chlorides were mixed with 12 mL oleic acid (OA) and 30 mL 1-octadecene (ODE) in three-neck round-bottom flask and then heated to 150 °C for 40 min. 10 mL of methanol solution containing NaOH (5 mmol) and NH_4F (8 mmol) was slowly introduced and the solution was stirred at 50 °C for 30 min. After the methanol was evaporated, the solution was heated to 300 °C for 1 h under argon atmosphere. The resultant nanoparticles were precipitated by hexane/acetone (1:4 v/v), collected by centrifugation, washed with acetone and DI water several times, and finally redispersed in cyclohexane.

Synthesis of core–shell β-$NaGdF_4$:Yb,Er@$NaGdF_4$ nanoparticles: The subsequent deposition of the $NaGdF_4$ shell followed a similar process for the preparation of $NaGdF_4$:Yb,Er core particles. 1 mmol Gd_2O_3 was dissolved in HCl at an elevated temperature (≈80 °C) to prepare a 2 mmol gadolinium chloride stock solution. 2 mmol gadolinium chloride was added to a three-neck round-bottom flask containing 8 mL OA and 30 mL ODE and then heated to 150 °C for 40 min under argon atmosphere to form a homogeneous solution and then cooled to room temperature. 10 mL of cyclohexane solution of 0.66 mmol $NaGdF_4$:Yb,Er nanoparticles was added dropwise into the solution. The mixture was degassed at 100 °C for 10 min to remove cyclohexane and cooled to room temperature. Then 10 mL methanol solution of NaOH (5 mmol) and NH_4F (8 mmol) was added and stirred at 50 °C for 30 min. After the methanol evaporated, the solution was heated to 300 °C for 1 h under argon atmosphere. The resultant core–shell nanoparticles were precipitated by hexane/acetone (1:4 v/v), collected by centrifugation, washed with acetone and DI water several times, and finally redispersed in cyclohexene.

Tween modification of oleate-capped β-$NaGdF_4$:Yb,Er and β-$NaGdF_4$:Yb,Er@$NaGdF_4$ nanoparticles: The surface modification of β-$NaGdF_4$:Yb,Er and β-$NaGdF_4$:Yb,Er@$NaGdF_4$ nanoparticles was carried out following a literature protocol with slight modifications [37]. In a typical experiment, 400 µL of Tween 80 was added into a round-bottom flask containing ≈20 mg of β-$NaGdF_4$:Yb,Er (β-$NaGdF_4$:Yb,Er@$NaGdF_4$) and 8 mL of $CHCl_3$, and the solution was stirred for 1 h at room temperature. 20 mL of deionized water was poured in the flask and the dispersion was kept in a 80 °C water bath for 3 h. During this period, the $CHCl_3$ was evaporated and the hydrophobic UCNPs were gradually converted into hydrophilic ones. A principle mechanism by which the Tween 80 surfactant stabilizes the UCNPs is shown in Figure 7.

Characterization: The polydispersity index of UCNPs was calculated by finding the weight (D_w) and number-average diameter (D_n) ratio using the following equations:

$$D_n = \sum n_i D_i / \sum n_i \quad (1)$$

$$D_w = \sum n_i D_i^4 / \sum n_i D_i^3 \quad (2)$$

where n_i and D_i are the number and diameter of the particle, respectively.

Dynamic light scattering (DLS) was used to determine the hydrodynamic particle diameter and zeta potential. These exper-

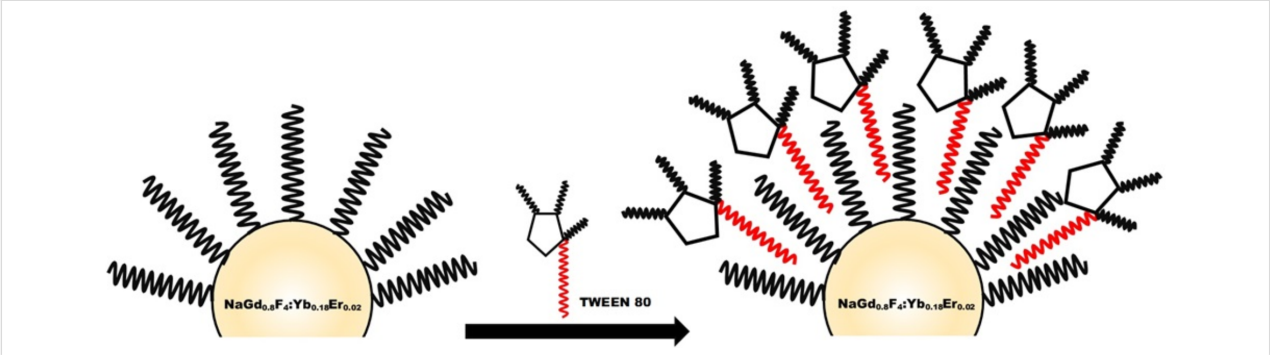

Figure 7: Formation of water-soluble core and core–shell UCNPs by coating with Tween 80.

iments were performed with Brookhaven ZetaPALS zeta potential analyzer (Brookhaven Instruments, USA). Powder X-ray diffraction (XRD) analysis has been carried out by employing a Rigaku MiniFlex II diffractometer working in the Bragg–Brentano (θ/2θ) geometry. The data were collected within a 2θ angle from 10° to 65° at a step of 0.01° and scanning speed of 10 °/min using the Ni-filtered Cu Kα line. The particle morphology was characterized using a field emission scanning electron microscope (SU-70 Hitachi, FE-SEM) at an acceleration voltage of 10 kV. The UC luminescence spectra were recorded using an Edinburgh Instruments FLS980 spectrometer equipped with a double emission monochromator, a cooled (−20 °C) single-photon counting photomultiplier (Hamamatsu R928), and a 1 W continuous wavelength 980 nm laser diode. The emission slit was set to 1 nm, the step size was 1 nm, and the integration time was 0.1 s with 5 scans to gain more intensity. The emission spectra were corrected by a correction file obtained from a tungsten incandescent lamp certified by National Physics Laboratory, UK. The measurements were performed in standard 1 cm quartz cuvettes at room temperature. Fourier transform infrared (FTIR) spectra were recorded on an infrared spectrometer (Perkin Elmer Spectrum).

Cell culturing and imaging: Human breast cancer cell lines MDA-MB-231 and MCF-7 were obtained from the American Type Culture Collection (ATCC HTB-26™; ATCC HTB-22™). MDA-MB-231 and MCF-7 cells were cultured in cell growth medium (DMEM, Gibco, US), supplemented with 10% (v/v) fetal bovine serum (FBS) (Gibco, US), 100 U/mL penicillin and 100 mg/mL streptomycin. The cells were maintained at 37 °C in a humidified atmosphere containing 5% of CO_2. The cells were routinely subcultured 2–3 times a week in 25 cm^2 culture dishes. Prior to the UCNP experimentation, the uptake cells were seeded and allowed to grow for 24 h and then treated with 10 μg/mL of Tween 80-coated core–shell UCNPs for 24 h. Then the cells were fixed with 4% paraformaldehyde and stained with DAPI. The high-resolution imaging system for UCNP imaging was based on a confocal microscopy system Nikon C1si (Japan). A 980 nm continuous wave laser with an intensity control module was introduced into the confocal microscopy system for excitation of samples in the NIR spectral region. 450/35 nm, 515/30 nm and 605/75 nm band pass filters (where the first value is the center/peak wavelength and the second refers to the bandwidth of the filter) were used to block detectors from reflected and scattered NIR light.

Cell viability assay: MCF-7 and MDA-MB-231 human breast cancer cells were seeded on a 96-well plate at a density of 20,000 cells/well. After 24 h, the old medium was replaced with a fresh medium containing 5, 10, 20, 50 and 100 μg/mL core–shell UCNPs. 12 wells were left without upconverting particles to serve as the control group. After 24 h of treatment, the cell growth medium with nanoparticles was aspirated and cells were washed with DPBS (pH 7.0) three times. To prepare an XTT solution, 0.1 mL activation solution (*N*-methyl dibenzopyrazine methyl sulfate) was mixed with 5 mL XTT reagent (tetrazolium derivative). 100 μL of a fresh medium and 50 μL of the reaction solution were added to each well and the plate was incubated for 5 h in an incubator at 37 °C. After incubation, optical density values at 490 nm were measured using the Biotek (USA) microplate reader. Values obtained from measuring optical density were recalculated as percentage values of viability. The absorbance value of the control group was set to 100% and the rest of the values were recalculated accordingly.

in vitro MR imaging: The MR signal enhancement measurements were carried out on a 1.5 T clinical MRI scanner (Achieva, Philips Medical Systems, Best, The Netherlands) in conjunction with a Sense Flex-M coil (Philips Medical Systems, Best, The Netherlands). Dilutions of core and core–shell UCNPs (0.125, 0.25, 0.5, 1.0 mg/mL) in deionized water were prepared for T1-weighted MR imaging and T1-weighted contrast enhancement. A series of aqueous solutions of UCNPs were placed in an array of 2.0 mL Eppendorf tubes with the order of UCNP concentrations and deionized water (0 mg/mL) was used as the reference. The parameters for T1-weighted MR imaging sequence was set as follows: echo time (TE) = 15.0 ms, repetition time (TR) = 500 ms, number of averages (NSA) = 8, matrix = 1024 × 1024, FOV = 200 × 200 mm, and slice thickness = 1.5 mm. The MR signal intensity (SI) in the tubes was determined by the average intensity in the defined regions of interests (ROIs). The resulting SI values in ROIs were plotted as a ratio of UCNP:water against the concentration of UCNPs.

Statistical analysis: Data are shown as the representative result or as mean of at least three independent experiments ±SD. Statistical analyses were performed using the two-tailed Student's *t*-test; differences were considered significant at $p < 0.05$.

Supporting Information

Supporting Information File 1

The hydrodynamic particle size and zeta potential.
The results representing hydrodynamic size distribution of UCNPs and their zeta potential that were measured using dynamic light scattering method (DLS).
[http://www.beilstein-journals.org/bjnano/content/supplementary/2190-4286-8-183-S1.pdf]

Acknowledgements

This work was supported by the grant "Study of optical properties and biocompatibility of $Na(Gd/Y)F_4$ nanoparticles" (No.MIP-030/2014) from the Research Council of Lithuania. A part of this work has been presented at the International Conference of Lithuanian Society of Chemistry on April 28–29, 2016.

References

1. Wang, M.; Abbineni, G.; Clevenger, A.; Mao, C.; Xu, S. *Nanomedicine: NBM* **2011,** *7,* 710–729. doi:10.1016/j.nano.2011.02.013
2. Mader, H. S.; Kele, P.; Saleh, S. M.; Wolfbeis, O. S. *Curr. Opin. Chem. Biol.* **2010,** *14,* 582–596. doi:10.1016/j.cbpa.2010.08.014
3. Liu, C.; Gao, Z.; Zeng, J.; Hou, Y.; Fang, F.; Li, Y.; Qiao, R.; Shen, L.; Lei, H.; Yang, W.; Gao, M. *ACS Nano* **2013,** *7,* 7227–7240. doi:10.1021/nn4030898
4. Deng, R.; Qin, F.; Chen, R.; Huang, W.; Hong, M.; Liu, X. *Nat. Nanotechnol.* **2015,** *10,* 237–242. doi:10.1038/nnano.2014.317
5. Sun, Y.; Feng, W.; Yang, P.; Huang, C.; Li, F. *Chem. Soc. Rev.* **2015,** *44,* 1509–1525. doi:10.1039/C4CS00175C
6. Zhou, J.; Liu, Z.; Li, F. *Chem. Soc. Rev.* **2012,** *41,* 1323–1349. doi:10.1039/C1CS15187H
7. Wang, F.; Banerjee, D.; Liu, Y.; Chen, X.; Liu, X. *Analyst* **2010,** *135,* 1839–1854. doi:10.1039/c0an00144a
8. Wang, F.; Liu, X. *Chem. Soc. Rev.* **2009,** *38,* 976–989. doi:10.1039/b809132n
9. Guanying, C.; Gang, H. *Theranostics* **2013,** *3,* 289–291. doi:10.7150/thno.6382
10. Qiu, H.; Yang, C.; Shao, W.; Damasco, J.; Wang, X.; Ågren, H.; Prasad, P. N.; Chen, G. *Nanomaterials* **2014,** *4,* 55. doi:10.3390/nano4010055
11. Liu, Y.; Tu, D.; Zhu, H.; Li, R.; Luo, W.; Chen, X. *Adv. Mater.* **2010,** *22,* 3266. doi:10.1002/adma.201000128
12. Wang, F.; Wang, J.; Liu, X. *Angew. Chem.* **2010,** *49,* 7456. doi:10.1002/anie.201003959
13. Chen, D.; Lei, L.; Yang, A.; Wang, Z.; Wang, Y. *Chem. Commun.* **2012,** *48,* 5898–5900. doi:10.1039/c2cc32102e
14. Liu, F.; He, X.; Liu, L.; You, H.; Zhang, H.; Wang, Z. *Biomaterials* **2013,** *34,* 5218–5225. doi:10.1016/j.biomaterials.2013.03.058
15. Cao, T.; Yang, T.; Gao, Y.; Yang, Y.; Hu, H.; Li, F. *Inorg. Chem. Commun.* **2010,** *13,* 392–394. doi:10.1016/j.inoche.2009.12.031
16. Chen, Z.; Chen, H.; Hu, H.; Yu, M.; Li, F.; Zhang, Q.; Zhou, Z.; Yi, T.; Huang, C. *J. Am. Chem. Soc.* **2008,** *130,* 3023–3029. doi:10.1021/ja076151k
17. Bogdan, N.; Vetrone, F.; Ozin, G. A.; Capobianco, J. A. *Nano Lett.* **2011,** *11,* 835–840. doi:10.1021/nl1041929
18. Cheng, L.; Yang, K.; Zhang, S.; Shao, M.; Lee, S.; Liu, Z. *Nano Res.* **2010,** *3,* 722–732. doi:10.1007/s12274-010-0036-2
19. Zhao, Y.; Wang, Z.; Zhang, W.; Jiang, X. *Nanoscale* **2010,** *2,* 2114–2119. doi:10.1039/c0nr00309c
20. Huang, Y.; Zhang, B.; Xi, S.; Yang, B.; Xu, Q.; Tan, J. *ACS Appl. Mater. Interfaces* **2016,** *8,* 11336–11341. doi:10.1021/acsami.6b02838
21. Baalousha, M.; Arkill, K. P.; Romer, I.; Palmer, R. E.; Lead, J. R. *Sci. Total Environ.* **2015,** *502,* 344–353. doi:10.1016/j.scitotenv.2014.09.035
22. Cascales, C.; Paíno, C. L.; Bazán, E.; Zaldo, C. *Nanotechnology* **2017,** *28,* 185101. doi:10.1088/1361-6528/aa6834
23. Rogosnitzky, M.; Branch, S. *BioMetals* **2016,** *29,* 365–376. doi:10.1007/s10534-016-9931-7
24. Swaminathan, S. *Magn. Reson. Imaging* **2016,** *34,* 1373–1376. doi:10.1016/j.mri.2016.08.016
25. Park, S.; Mohanty, N.; Suk, J. W.; Nagaraja, A.; An, J.; Piner, R. D.; Cai, W.; Dreyer, D. R.; Berry, V.; Ruoff, R. S. *Adv. Mater.* **2010,** *22,* 1736–1740. doi:10.1002/adma.200903611
26. Yi, G.-S.; Chow, G.-M. *Chem. Mater.* **2007,** *19,* 341. doi:10.1021/cm062447y
27. Wong, H.-T.; Vetrone, F.; Naccache, R.; Chan, H. L. W.; Hao, J.; Capobianco, J. A. *J. Mater. Chem.* **2011,** *21,* 16589. doi:10.1039/c1jm12796a
28. Baziulyte, D.; Karabanovas, V.; Stalnionis, M.; Jurciukonis, I.; Sakirzanovas, S. In *Book of abstracts of the "Chemistry and Chemical Technology,* International Conference of Lithuanian Society of Chemistry; 2016; p 150.
29. Johnson, N. J. J.; Oakden, W.; Stanisz, G. J.; Scott Prosser, R.; van Veggel, F. C. J. M. *Chem. Mater.* **2011,** *23,* 3714–3722. doi:10.1021/cm201297x
30. Hou, Y.; Qiao, R.; Fang, F.; Wang, X.; Dong, C.; Liu, K.; Liu, C.; Liu, Z.; Lei, H.; Wang, F.; Gao, M. *ACS Nano* **2013,** *7,* 330–338. doi:10.1021/nn304837c
31. Vetrone, F.; Naccache, R.; de la Fuente, A. J.; Sanz-Rodriguez, F.; Blazquez-Castro, A.; Rodriguez, E. M.; Jaque, D.; Solé, J. G.; Capobianco, J. A. *Nanoscale* **2010,** *2,* 495–498. doi:10.1039/B9NR00236G
32. Karabanovas, V.; Zitkus, Z.; Kuciauskas, D.; Rotomskis, R.; Valius, M. *J. Biomed. Nanotechnol.* **2014,** *10,* 775–786. doi:10.1166/jbn.2014.1770
33. Osman, O.; Zanini, L. F.; Frénéa-Robin, M.; Dumas-Bouchiat, F.; Dempsey, N. M.; Reyne, G.; Buret, F.; Haddour, N. *Biomed. Microdevices* **2012,** *14,* 947–954. doi:10.1007/s10544-012-9673-4
34. Wang, S.-H.; Lee, C.-W.; Chiou, A.; Wei, P.-K. *J. Nanobiotechnol.* **2010,** *8,* 33. doi:10.1186/1477-3155-8-33
35. Woźniak, A.; Noculak, A.; Gapiński, J.; Kociolek, D.; Boś-Liedke, A.; Zalewski, T.; Grześkowiak, B. F.; Kołodziejczak, A.; Jurga, S.; Banski, M.; Misiewicz, J.; Podhorodecki, A. *RSC Adv.* **2016,** *6,* 95633–95643. doi:10.1039/C6RA20415E
36. Guller, A. E.; Generalova, A. N.; Petersen, E. V.; Nechaev, A. V.; Trusova, I. A.; Landyshev, N. N.; Nadort, A.; Grebenik, E. A.; Deyev, S. M.; Shekhter, A. B.; Zvyagin, A. V. *Nano Res.* **2015,** *8,* 1546–1562. doi:10.1007/s12274-014-0641-6
37. Ren, W.; Tian, G.; Jian, S.; Gu, Z.; Zhou, L.; Yan, L.; Jin, S.; Yin, W.; Zhao, Y. *RSC Adv.* **2012,** *2,* 7037–7041. doi:10.1039/c2ra20855e

BEILSTEIN JOURNAL OF NANOTECHNOLOGY

Optical techniques for cervical neoplasia detection

Tatiana Novikova

Review

Open Access

Address:
LPICM, CNRS, Ecole polytechnique, University Paris Saclay, Palaiseau, France

Email:
Tatiana Novikova - tatiana.novikova@polytechnique.edu

Keywords:
cervical intraepithelial neoplasia; confocal endomicroscopy; Mueller polarimetry; nanotheranostics; optical coherence tomography; optical spectroscopy; Raman spectroscopy

Beilstein J. Nanotechnol. **2017,** *8,* 1844–1862.
doi:10.3762/bjnano.8.186

Received: 28 April 2017
Accepted: 09 August 2017
Published: 06 September 2017

This article is part of the Thematic Series "Nanomaterial-based cancer theranostics".

Guest Editor: V. Sivakov

Abstract

This paper provides an overview of the current research in the field of optical techniques for cervical neoplasia detection and covers a wide range of the existing and emerging technologies. Using colposcopy, a visual inspection of the uterine cervix with a colposcope (a binocular microscope with 3- to 15-fold magnification), has proven to be an efficient approach for the detection of invasive cancer. Nevertheless, the development of a reliable and cost-effective technique for the identification of precancerous lesions, confined to the epithelium (cervical intraepithelial neoplasia) still remains a challenging problem. It is known that even at early stages the neoplastic transformations of cervical tissue induce complex changes and modify both structural and biochemical properties of tissues. The different methods, including spectroscopic (diffuse reflectance spectroscopy, induced fluorescence and autofluorescence spectroscopy, Raman spectroscopy) and imaging techniques (confocal microscopy, optical coherence tomography, Mueller matrix imaging polarimetry, photoacoustic imaging), probe different tissue properties that may serve as optical biomarkers for diagnosis. Both the advantages and drawbacks of these techniques for the diagnosis of cervical precancerous lesions are discussed and compared.

Review

Introduction

Cervical cancer remains one of the major health issues, causing 266000 deaths of women worldwide in 2012 [1]. While the highest incidence rate of cervical cancers (approximately 70%) is observed in developed countries, the cervical cancer mortality rate is highest in low-income countries, where the regular screening by Papanicolaou (Pap) test, colposcopy, biopsy and curative treatment are not routinely available because of lack of health infrastructure, trained practitioners and necessary resources [2]. The high mortality rate of cervical cancer may be reduced by implementing the integrated strategy which includes the prevention, screening and treatment of the disease [3] (Figure 1).

There is conclusive evidence that the majority of cervical cancer cases (95–98%) is caused by the infection with cancerogenic strains of *human papillomavirus* (HPV) [4-6]. Most of these

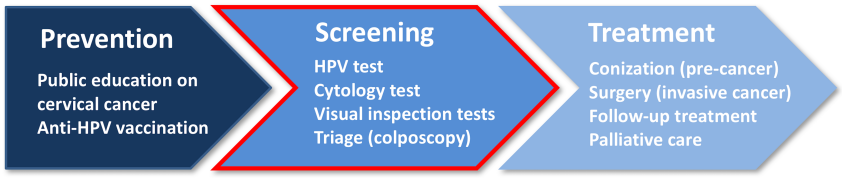

Figure 1: Key steps for addressing cervical cancer as public health concern. New optical technologies and innovative approaches for the improvement of early detection of cervical pre-cancer (second step) are discussed in this paper.

infections are cleared by the immune system within one to two years. If carcinogenic HPV infection is not cleared, the virus invades the cells at the junction of squamous epithelium of the ectocervix and columnar epithelium of endocervical canal (cervical squamocolumnar junction CSJ) [7-9]. The location of the squamocolumnar junction relative to the external orifice, or external os (cervix opening to the vagina, see Figure 2) shifts over the lifetime of a woman.

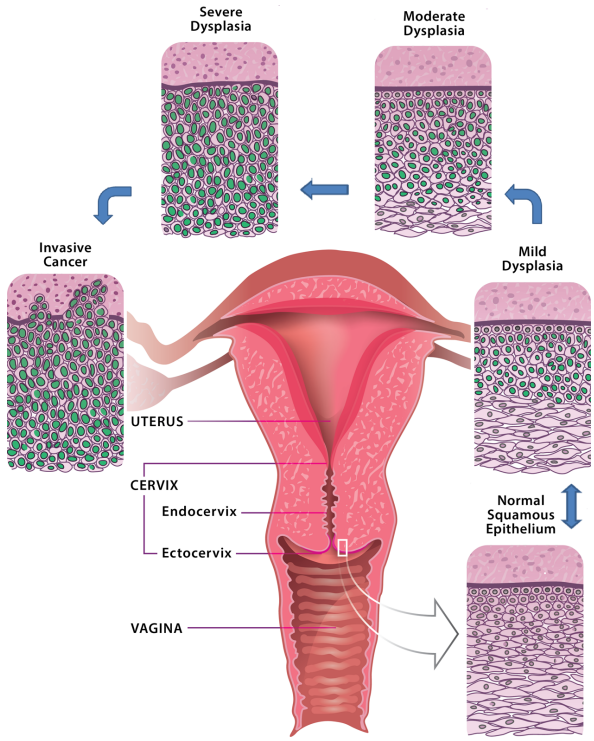

Figure 2: Cross-section of uterus and vagina; schematics of cervical intraepithelial neoplasia development.

The transformation zone, defined as an area limited by the positions of original and the active squamocolumnar junctions is most susceptible to HPV infection. When HPV gets a foothold and reproduces itself, it can invade the cells of the basal layer, which separates epithelium from underlying connective tissue and, eventually, rise to the epithelium surface with the mature squamous cells. The virus infection gradually induces severe damage. HPV-infected cells may become malignant if the virus inserts its cancer-causing genes into the DNA of the host cell.

The staging of the disease is based on morphological criteria and tissue architecture, namely, on the thickness of the involved epithelium layer (Figure 2). When one third of the epithelium is affected by disorganized growth and cytological atypia we talk about mild dysplasia or cervical intraepithelial neoplasia (CIN) of 1st grade (CIN 1). Such abnormality can regress and disappear on its own. Moderate (CIN 2) dysplasia involves two thirds of the epithelium, while severe dysplasia (CIN 3) spans over the whole epithelium depth. At this stage, it is already highly unlikely that precancerous epithelial lesions will clear spontaneously. According to the Bethesda system [10], the low-grade squamous intraepithelial lesion (LSIL) usually indicates mild dysplasia (CIN 1), high-grade squamous intraepithelial lesion (HSIL) refers to moderate and severe dysplasia (CIN 2–3). This classification system is used for reporting cervical cytological diagnostics and for choosing different treatment strategies for each group.

Left untreated, severe dysplasia will grow and break a basal membrane and eventually evolve into an invasive cancer. This process is very slow and may take over ten years after the infection. It makes cervical cancer perfectly suited for the effective management by screening according to criteria defined by the World Health Organization [11,12].

Recent discovery and subsequent mass use of the vaccines against HPV hold promise for the prevention of cervical cancer and will significantly improve the situation at large [13]. Those vaccines, however, need to be applied early in life, and cannot cure already existing conditions. Furthermore, none of those vaccines create complete immunity against all HPV types, and the price of these vaccines remains quite high. So, improvements in the management of HPV infection are still needed, especially for the population in low-income countries.

In high-resource settings a regular screening by the cytopathological Pap test is performed for an early detection and prevention of cervical cancer. Cells collected from the external os of

the cervix are studied under a microscope. If abnormal cells are detected, further diagnostic testing in the form of colposcopy is often recommended for the localization and marking out of metaplasia.

The visual examination of the cervix for metaplastic lesions with a colposcope is done after the application of acetic acid and then repeated after the application of iodine Lugol's solution (both work as contrast enhancing agents). Normally, the biopsies (removal of a small tissue sample for examination by a pathologist) are taken from the areas whitened by acetic acid and those which are not colored by iodine. If the analysis of histological cuts by pathologists ultimately confirms the presence of a high grade malignant lesion (CIN 2–3), the abnormal zone is surgically removed by cervical conization. This is a minimally invasive curative treatment which can completely eliminate the disease provided it was diagnosed at an early stage before the transformation into an invasive cancer. This treatment has minimal adverse effect on fertility and reproductive functions of women.

It is worth to mention that the results of colposcopy may also be affected by the presence of non-neoplastic cervical diseases and demographic factors such as age and parity. Thus, the accuracy of colposcopy strongly depends on the level of training and experience of clinicians performing the test. As stand-alone diagnostic method colposcopy has a quite high sensitivity (ratio of true positive over the sum of true positive and false negative diagnosis) of over 90% in detecting HSIL and cancer (CIN 2+). But the specificity (ratio of true negative over the sum of true negative and false positive diagnosis) of colposcopy for the detection of CIN 2–3 is reported to be relatively low (23–87%) [14-21]. Even if the diagnosis of a CIN 2–3 lesion is confirmed by histological analysis, an additional difficulty is the correct delimitation ("mapping") of the neoplasia zone for complete treatment. This problem arises because of the lack of contrast between healthy and neoplastic zones of the cervix in colposcopy images viewed by surgeon-gynecologists. Because of these drawbacks of conventional colposcopy there is an ongoing research and exploration of different optical techniques (spectral or imaging, wide-field or scanning) for the accurate detection of cervical neoplasia.

Current management of cervical cancer (implementation of screening, anti-HPV vaccination and treatment programs) has significantly decreased the mortality rate in highly developed countries during last decades. At the same time the incidence and mortality rates in the middle and low-income countries did not improve and remain significantly high due to insufficient awareness about cervical cancer among women and health providers, lack of access to HPV vaccination, absence of screening and treatment programs. This puts women at the increased risk of developing invasive cervical cancer (Figure 3).

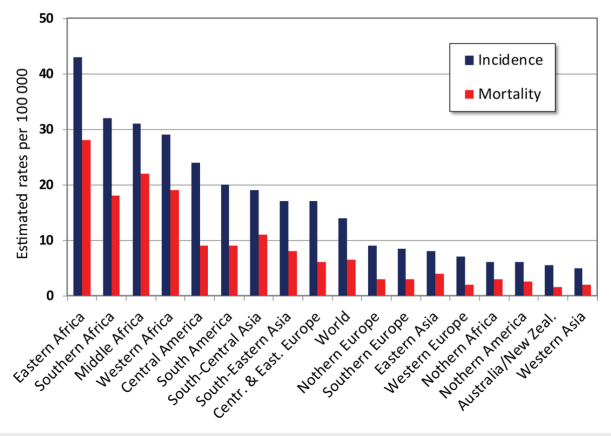

Figure 3: Cervical cancer estimated incidence, mortality and prevalence worldwide in 2012. Adapted from [22].

In current programs for screening and diagnosis of cervical cancer the critical issue is an increase of efficiency and accuracy of screening and diagnostics techniques. Typically it requires up to three visits to a medical professional and several weeks in total in order to obtain the diagnosis and treatment, if necessary [23]. The implementation of new optical techniques may bring an alternative to the Pap/HPV test for screening and an improvement of colposcopy for guiding the biopsy and diagnosis. The performance of new techniques is estimated in terms of accuracy, time and cost of diagnostics, combined with patient comfort, which is relevant to the rate of participation in screening programs.

Currently several optical methods such as diffuse reflectance spectroscopy, fluorescence spectroscopy, Raman spectroscopy, in vivo confocal microscopy, optical coherence tomography and multi-wavelength imaging Mueller polarimetry, as well as the combination of different techniques have been explored to improve the detection of cervical neoplasia. The results of these studies as well as current trends to miniaturization of diagnostic instruments will be discussed further.

Optical spectroscopy and imaging

In vivo diffuse reflectance optical spectroscopy (DRS) exploits the fact that abnormal zones of the cervical epithelium illuminated with a low-power broadband light source produce different backscattering spectra compared to normal cervical tissue in the visible wavelength range. Such difference in spectra detected by an optical sensor can be used in order to identify neoplastic lesions of the cervical epithelium. DRS is an indirect optical technique and may require either fitting of measured spectra with multi-parametric models describing the realistic

optical properties of tissue [24] or using an efficient classification algorithm of optical spectra for the detection of HSIL [25,26]. The propagation of light in a scattering medium is usually modeled by the Monte Carlo algorithm. The fit of the measured spectral data with the optical model of tissue provides the effective values of diagnostically relevant model parameters, e.g., reduced scattering coefficient and absorption coefficient. In the optical model of tissue these parameters are linked to the size and density of the scatterers, total hemoglobin (Hb) concentration and Hb saturation with oxygen, which can be used as optical markers to assess and grade CIN lesion. The principle of using diffuse reflectance and fluorescence spectroscopy for tissue diagnostics is illustrated in Figure 4.

It has been demonstrated that the total concentration of Hb, which is responsible for absorption in tissue in the visible wavelength range, was statistically higher in CIN 2–3 compared to normal cervical tissue [24,27]. This effect was attributed to an increased density of micro-vessels in the stroma of neoplastic tissue and stromal angiogenesis [28-30]. The observed drop in scattering in CIN 1–3 zones was attributed to the degradation of the stromal collagen matrix of the cervix related to both decomposition of collagen fibers and decrease in concentration of collagen cross-links [31,32].

Despite the observed common trends for DRS optical markers with the evolution of CIN lesions there is a significant variability of parameter values in different patients depending on their age as well as presence of non-neoplastic lesions [33]. The shortcomings of DRS as a tool for screening and diagnosis are related to the fact that the estimation of optical parameters may be degraded by both correlation of model parameters and instrument-dependent response. It increases the uncertainty of threshold parameter values used for diagnostics and choice of treatment strategy, when either watchful waiting accompanied by HPV/Pap tests or active treatment is further needed [34-38]. The use of spectra classification algorithms (e.g., Bayesian variable selection, neural networks, library approach, multivariate statistical analysis) may bring its own set of the problems: high-dimensionality of data, insufficient number of data for training, overtraining because of too many tuning parameters [25]. Moreover, Mirkovic et al. [39] reported that even in healthy cervical tissue a transformation zone (area of most probable location of HSILs) and squamous epithelium are spectroscopically different because of their anatomical differences. This effect can also have impact on the diagnostic parameters extracted from the spectroscopic measurements. Using optical spectroscopy as a complementary technique to colposcopy aims to examine the patients with inconclusive Pap test cytological results and to guide the biopsies [25,40].

Point-probe optical spectroscopic instruments may also be used for scanning the suspicious sites of the cervix. However, this approach is laborious and time-consuming and the possibility to miss the potential lesions is not negligible. Hence, these techniques are not suitable for CIN screening in real settings. The instruments that perform a multi-spectral wide-field imaging of the whole cervix are required to address these issues. Park et al. [41] developed an algorithm for the automated analysis of colposcopic images taken with a multispectral digital colposcope before (Figure 5a) and after (Figure 5b) application of acetic acid. They explored the ratio between the reflected intensities of green and red light and the changes in the reflectance images induced by acetic acid as optical markers for differentiating HSIL and cancer from LSIL and healthy cervical tissue. In their study of 29 patients a sensitivity of 79% and a specificity of 88% for HSIL detection were reported using histological analysis of excised cone biopsies (Figure 5c) as the gold-standard diagnosis technique.

The advanced version of the automated domain-specific image analysis algorithm for the detection of cervical precancerous lesions identified first the regions of squamous and columnar epithelium [42]. Transformation zone and external os were

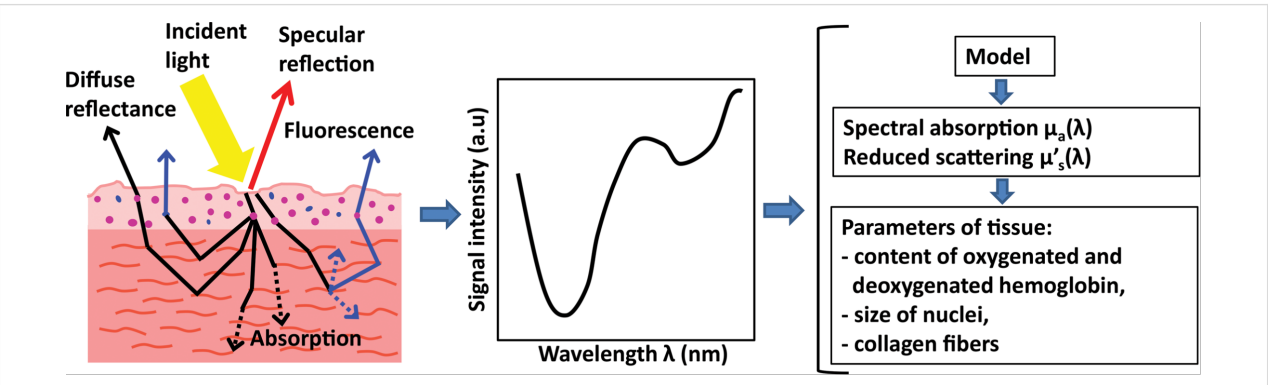

Figure 4: Diffuse reflectance and/or fluorescence spectroscopy for the optical analysis of tissue; λ is a wavelength. Adapted from [34].

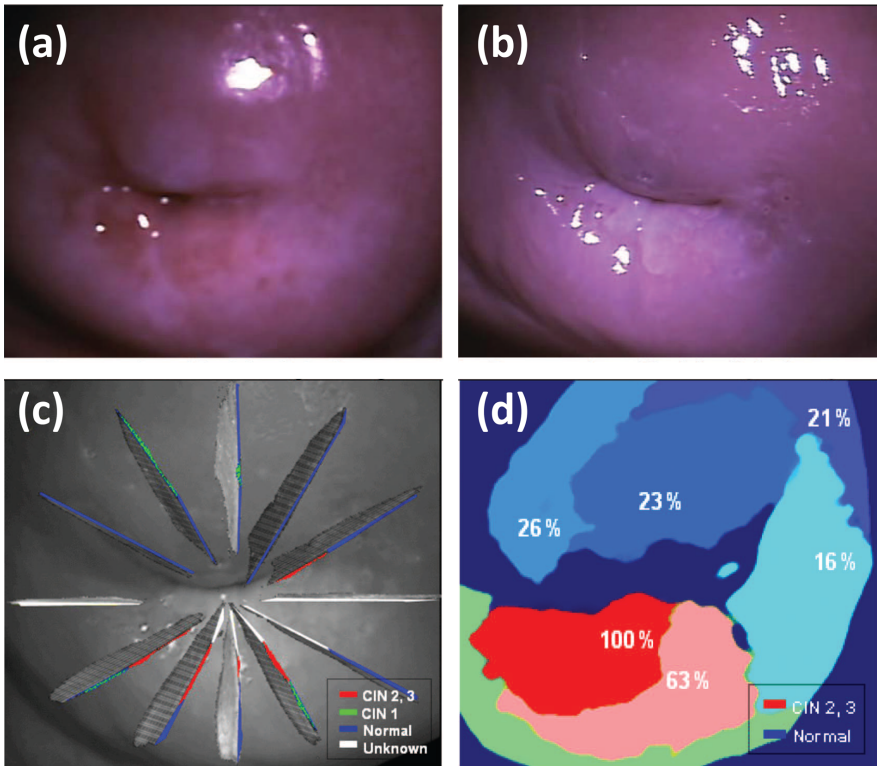

Figure 5: Reflectance colposcopic images (a) before and (b) after application of acetic acid; (c) reconstructed histological map of lesions CIN 1, 2, and 3; (d) diagnostic map of disease probability provided by an automated multi-classifier. Reproduced with permission from [41], copyright 2008 Society of Photo-optical Instrumentation Engineers.

delimited on the image taken before the application of acetic acid using color and texture information. Domain-specific anatomical features related to tissue types were integrated in the conditional random field probabilistic model for the segmentation of images taken after the application of acetic acid. The clinical data from 48 patients were examined with the proposed image analysis algorithm resulting in an average sensitivity of 70% and specificity of 80% in detecting neoplastic areas, when using histopathology analysis as gold-standard diagnosis. Lower average sensitivity compared to conventional colposcopy performance was attributed to the fact that during the patient-based colposcopy analysis a delimitation of abnormal zones in images was not carried out.

Fluorescence spectroscopy and imaging

While the scattering of light by biological tissue plays the main role in DRS, the absorption and emission of light by matter are the key steps in fluorescence spectroscopy. The use of fluorescence spectroscopy for the screening and diagnosis of cancer is related to the ability of this technique to probe the molecular composition of tissue and observe the distribution of specific molecules. When light of a chosen excitation wavelength illuminates the sample, the tissue molecules are exposed to light having an energy that may match a possible electronic transition within the molecule. Consequently, part of incident radiation will be absorbed as the electron is lifted to a higher energy orbital. During de-excitation (return of electron to the ground state) those molecules release energy in the form of light of a specific emission wavelength (usually different from the excitation wavelength), which can be measured by a detector. The fluorescence signal is a superposition of various emission signals of different wavelengths and intensities. It depends on the excitation wavelength and on the presence and concentration of fluorophore molecules in the tissue.

Depending on the type of investigated fluorophores (endogenous, i.e., intrinsically present in biological tissue or synthesized after introducing a precursor molecule, or exogenous, i.e., administrated as drugs) light-induced fluorescence spectroscopy can be classified either as autofluorescence spectroscopy or as induced fluorescence spectroscopy, respectively. The information on fluorescence lifetimes may be obtained using instruments with pulsed mode illumination and time-resolved detection [43]. The direct links between endogenous fluorophores and certain morphological and functional properties of living matter lead to distinguishable autofluorescence emission peaks and give an opportunity to monitor the state of biological tissues in vivo.

There is experimental evidence that the intensity of autofluorescence of normal cervical tissue is altered by the precancerous modifications of cervical epithelium [31]. The differences in fluorescence spectra of normal and precancerous cervical tissue are explained by the concomitance of two phenomena linked with the CIN progression. An increase in number of metabolically active mitochondria in epithelial cells with CIN development leads to the increase of epithelial fluorescence, while stromal fluorescence drops because of a decrease in density of the collagen matrix adjacent to neoplastic epithelium [31,44]. The overexpression of matrix metalloproteinases (enzymes responsible for the degradation of collagen cross-links, which are the main source of collagen autofluorescence) was found to be an early sign of malignant transformation in cervical neoplasia [45].

Chidananda et al. [46] studied about 1000 autofluorescence spectra of cervical tissue specimens taken from 62 patients with different cervical pathologies. They reported a sensitivity and specificity of over 95% for CIN diagnostics using total fluorescence spectra resulting from the emission of individual endogenous fluorophores (e.g., collagen and the reduced form of nicotinamide adenine dinucleotide (NADH), the main tissue fluorophores in the visible wavelength range). The excitation wavelength was 325 nm. Principal component analysis (PCA) of the spectra and the intensity ratio of curve resolved fluorescence peaks was applied (Figure 6). Recent studies of autofluorescence spectra of biopsied specimens taken during colposcopy from 46 patients demonstrated both a significant decrease in collagen fluorescence (peak around 400 nm) and increase in NADH fluorescence (peak around 460 nm) in dysplastic tissues [47].

Combining information about the fluorescence of stromal collagen and epithelial NADH, Pandey et al. [47] reported a sensitivity of 96.5% for cervical neoplasia diagnosis. In vivo fluorescence spectroscopy studies reported the decrease of emission intensity combined with the shift of emission peak towards longer emission wavelengths for precancerous zones compared to healthy squamous tissue of the ectocervix.

Apart from the changes in cellular metabolic processes and in the extracellular tissue matrix induced by CIN progression, both scattering and absorption of light in tissues may significantly influence the measured fluorescence spectra modifying the intensity and width of specific peaks. Georgakoudi et al. [48] suggested combining the information from DRS and fluorescence spectra in order to remove the distortion of fluorescence spectra caused by tissue scattering and absorption and to determine the fluorescence spectra of NAD(P)H and collagen in vivo. The intrinsic (undistorted) fluorescence spectra from 35 patients taken at different (normal and abnormal) sites of the cervix during the colposcopy were analyzed. The results of these studies also showed that high-grade dysplastic lesions are characterized by low collagen fluorescence and high NADH fluorescence compared to non-dysplastic tissues.

Despite a clinically significant increase in NADH fluorescence and decrease in collagen fluorescence in the spectra measured on dysplastic cervical tissue the age of the patient may affect the fluorescence-based diagnosis of CIN. Some age-related changes of cervical tissue modify the fluorescence spectra in a similar way as dysplasia [47,49]. Due to a wide inter- and intra-patient variability of fluorescence spectra there is a need for the development of advanced mathematical algorithms for the analysis of fluorescence signals to provide the consistent and reproducible diagnosis of cervical neoplastic lesions [46,50]. The preprocessing (filtering, co-registration) of reflectance and fluorescence images, the reduction of image data by PCA, the image clustering by the K-means clustering algorithm and the use of the nonparametric K-nearest neighbor (KNN) classifier for the image segmentation was implemented by Milbourne et al. [51]

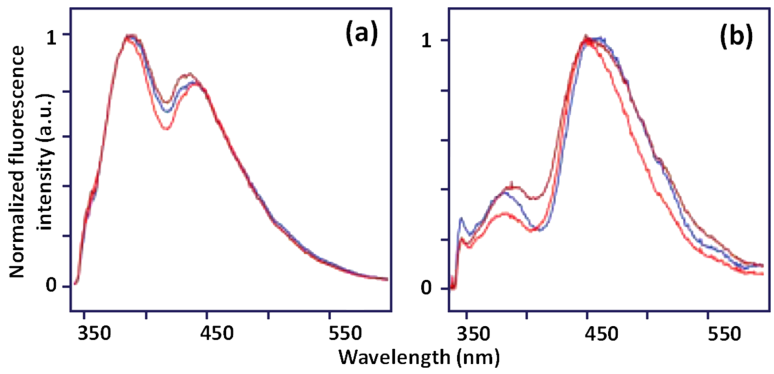

Figure 6: Site-to-site variations in fluorescence spectra measured at different pathologically confirmed (a) normal and (b) malignant tissue samples at 325 nm excitation wavelength. Reproduced with permission from [46], copyright 2006 Wiley-Liss, Inc.

for the diagnosis of high- and low-grade lesions of the cervix. The results of this pilot study in 46 patients showed that using an appropriate classifier on the multispectral digital colposcope data may produce algorithmic maps that correlate well with histopathologic mapping.

The accuracy of the detection of CIN lesions with spectral autofluorescence measurements depends on several factors including (i) changes in autofluorescence background, which may influence the quantum yield of fluorophore, (ii) inhomogeneities in the optical properties of tissue, (iii) alterations of the tissue architecture (e.g., variable thickness of epithelial layer), (iv) the spectral dependence of the absorption of light by non-fluorescent chromophores such as hemoglobin. Weingandt et al. [52] observed a similarity of autofluorescence response from zones of severe inflammation and of CIN. This made the diagnostics difficult and led to an increased number of false positive results.

Gu et al. [53] suggested using fluorescence-lifetime imaging microscopy (FLIM) on haematoxylin and eosin (H&E) stained histological cuts of cervical tissue and a neural network classifier for the automated diagnosis of CIN lesions. This technique can overcome the limitations of conventional fluorescence microscopy because FLIM results are insensitive to fluorophore concentration and excitation power of the laser.

The growth of tumor in mice, inoculated with highly tumorigenic TC-1 cells immortalized using HPV type 16 proteins, was studied as a model of cervical cancer by Bae and co-workers [54]. Using an optical imaging system they detected the enhancement of protoporphyrin IX (PpIX) autofluorescence in tumor regions. This endogenous protein tends to accumulate in tumor tissue, and may help in effective localization and visualization of tumor lesions by PpIX fluorescence imaging

An intrinsic problem of fluorescence spectroscopy is linked to the fact that both intensity and contrast of autofluorescence in tissue are quite low. Often the spectral difference between normal and pathological tissue can be enhanced by external administration of fluorophores or fluorophore precursors. The preferential accumulation of exogenous fluorophores in abnormal cells [55] results in contrast enhancement, which helps to detect and stage the lesions [56,57]. However, possible side effects and a low accumulation rate of exogenous fluorophores may impede the clinical use of the method.

Raman spectroscopy

During the interaction of light with matter a number of different processes may take place: reflection, transmission, absorption, elastic and inelastic scattering of incident radiation. Raman spectroscopy (RS) is an optical technique that relies on inelastic scattering of light. The sample is usually illuminated with a monochromatic laser beam that vibrationally excites molecular chemical bonds. The energy of inelastically scattered light is changed by those vibrations that are strictly related to the structure of molecules. A plot of intensity of inelastically scattered radiation as a function of the difference of its frequency from the frequency of the incident radiation is called Raman spectrum. Consequently, positions, shapes and relative intensities of the peaks in a Raman spectrum carry valuable information about both chemical composition and morphology of the sample. That is why RS performs well as a versatile optical technique for chemical and structural characterization of studied samples in a rapid and non-destructive manner (Figure 7).

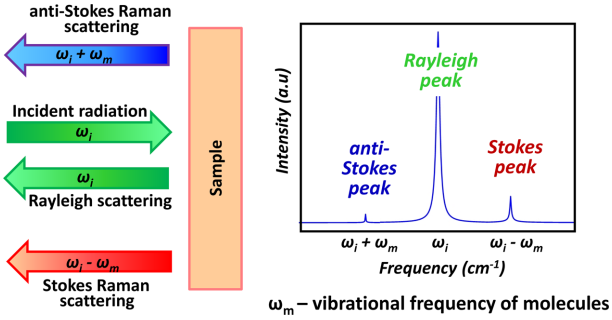

Figure 7: Raman vibrational spectroscopy for probing the molecular chemical bonds as well as crystal lattice vibrations. ω_i is the frequency of the incident radiation.

The biochemical components of tissue (e.g., proteins, lipids and carbohydrates) contribute to the measured Raman spectra by superposition of their individual Raman signals. The combinations of these components, which are specific for the different type and physiological status of tissue, produce a unique biochemical "signature" of the sample in the form of particular fingerprint-like spectral features in the Raman spectrum.

It suggests that Raman spectroscopy may be used as a tool to detect early biochemical changes at a molecular level that are associated with the precancerous modifications of tissue. During the last years the potential of RS as label-free diagnostics technique for the detection of different types of cancers has been studied by many research groups both in vivo and ex vivo [58-65].

In one study of 44 patients Raman spectra were acquired from 356 normal and 120 precancerous sites during the colposcopy in the fingerprint (FP, 800–1800 cm^{-1}) and high wavenumber (HW, 2800–3700 cm^{-1}) spectral regions [62]. Differences in Raman spectra of normal and dysplastic cervical tissue were observed at wavenumbers related to proteins, lipids, glycogen,

nucleic acids, and the water in tissue. The multivariate statistical analysis yielded a sensitivity of 85.0% and a specificity of 81.7% using integrated FP/HW Raman spectroscopy for the in vivo diagnosis of cervical precancerous lesions.

Results of studies of 79 patients showed that in vivo Raman spectroscopy combined with logistic regression can differentiate HSIL zones from benign conditions with a similar sensitivity of 89% and a higher specificity of 81% compared to colposcopy in expert hands [66].

The use of Raman spectroscopy for histological analysis of cervical tissue cuts is discussed in [60] and [64]. The Raman spectral mapping of the unstained histological cuts was performed with the spatial resolution of 18 μm. The spectral Raman data set was evaluated by K-means cluster analysis (KMCA). The regions with similar spectral and hence biochemical properties were clustered on a generated pseudo-color map.

In the spectrum averaged over the pixels from stromal layer cluster the Raman peaks at 853, 921, 938 and 1245 cm^{-1} were assigned to collagen, which is the major component of this layer. The accumulation of glycogen in the mature squamous cells of intermediate and/or superficial layers manifested itself by peaks at 480, 849 and 938 cm^{-1} in the spectrum averaged over the pixels from corresponding clusters. The differentiation of stromal, basal and superficial layers on a pseudo-color map of normal squamous cervical tissue was clearly observed [64]. The KMCA of Raman spectral data from cervical tissue with HSIL demonstrated the loss of differentiation of layers. The classifier clustered HSIL regions with basal layer. It proposes that cells of both regions of cervical tissue share common biochemical profiles.

The obvious advantages of Raman spectroscopy include (i) no specific requirements for sample preparation, (ii) the possibility to use this technique with fiber optics for ex vivo and in vivo measurements, (iii) a high spatial resolution suitable for imaging of subcellular components.

Typically, Raman scattering produces a very weak signal (with a spontaneous inelastic scattering cross-section of about 10^{-30} $cm^2 \cdot sr^{-1}$). So, one of the main difficulties of RS consists in separating the contribution of the weak intensity of the inelastically scattered light from the strong intensity of the Rayleigh scattering signal. Current solution consists in using notch or edge optical filters to cut the contribution of the Raman probing wavelength. To avoid the interference of the Raman signal with fluorescence emission, special attention should be paid to the selection of the laser excitation wavelength.

The improvement of the signal-to-noise ratio can be achieved by using ultrashort-pulsed laser sources (stimulated Raman scattering (SRS) and coherent anti-Stokes Raman scattering (CARS)) or metal nanoparticles (surface-enhanced Raman scattering, SERS). However, these improvements often increase the time of measurements and the complexity/cost of the instrument, which may hinder clinical applications of Raman spectroscopy. In addition, the spread of diagnostically relevant peaks across the Raman spectra requires the development of efficient classifiers, which can fully explore rich spectral information for accurate and reliable diagnostics. One of the promising applications of RS can be the monitoring of the patients undergoing chemotherapy. A priori knowledge of administrated drugs will help to detect the new Raman peaks. There will be no need for point-by-point scanning. Hence, the time of measurements can be significantly reduced.

High-resolution microscopy

The optical techniques for CIN diagnostics discussed so far focused on macroscopic imaging or spectral probing of tissue. It is known that CIN lesions are characterized by morphological changes, such as modified tissue architecture, increased size of cell nuclei and increased nuclear/cytoplasmic ratio. The assessment of these morphological changes is currently done through microscopic histological analysis of biopsies (gold-standard diagnostics). Screening and diagnostics can be significantly improved by the high-resolution optical imaging technologies that image subcellular structures in vivo, thus, replacing tissue removal, processing, and examination by pathologists [67].

In vivo confocal microscopy is an optical technology that can non-invasively reconstruct three-dimensional cell structures from successive microscopic images taken at different depths (around 300–400 μm) within a thick tissue (so called optical sectioning). A point illumination and a pinhole placed at the optically conjugate image plane in front of the detector isolate light reflected or fluorescent from a finite volume and block scattered and out-of-focus light. This increases optical resolution and image contrast compared to conventional optical microscopy. The sample plane is scanned by focused laser beam and confocal images are built up point-by-point. The fluorescence scanning confocal microscopy is typically used for imaging in the majority of biological applications [68-70]. The use of reflectance confocal microscopy for tissue imaging is limited, but sometimes it can provide additional information from the samples with significant spatial variation of refractive index [71,72]. It is worth to mention that optical sections are imaged in a focal plane tangential to the tissue surface. This is not a typical view seen by pathologists, because standard histological cuts are orthogonal to the tissue surface.

Confocal microscopy has been extensively used in different branches of medicine [69-72]. Due to its ability to provide real-time structural information on superficial layers of tissue this technique was also applied for the detection of precancerous lesions of the uterine cervix [73-76]. A fiber-optic reflectance confocal microscope was used by Carlson et al. [74] for in vivo imaging of cervix. They demonstrated an increase of nucleus-to-cytoplasm ratio with scanning depth in normal epithelium, but there was little change of this ratio from the upper layer to the basal layer in the images of dysplastic epithelium. Tan et al. [76] used fluorescence confocal endomicroscopy for in vivo microscopic imaging of cellular structures during colposcopy. Confocal imaging and histology of normal cervix tissue (Figure 8 a(ii), a(iii)) showed a uniform arrangement of epithelial cells through the full thickness of squamous epithelium.

CIN lesions were characterized by increased nuclear density and size, and the presence of atypical cells. Examination of a CIN 3 lesion with a confocal endomicroscopic imaging probe (site marked by the asterisk in the colposcopy image (Figure 8 b(i)) showed significant variation in nuclear size and shape (Figure 8 b(ii)). Histological analysis confirmed precancerous cell modifications over the full epithelial thickness (Figure 8 b(iii)). They reported a sensitivity of 97% for CIN detection, a specificity of 80% for predicting the grade of dysplasia for normal tissue to CIN 1 and 93% for CIN 2 to CIN 3 lesions.

A low-cost high-resolution microendoscope (HRME) was developed and used for the direct visualization of neoplastic biomarkers (increase in nucleus-to-cytoplasm ratio and nuclear density, pleomorphic nuclei) during colposcopy [77-79]. Grant et al. [79] performed HRME imaging by placing a fiber-optic probe tip in contact with colposcopically abnormal and normal sites. Before microendoscopic imaging a topical solution of proflavin (fluorescent DNA label that stains the nuclei and makes them appear brighter than the cytoplasm of the cell) was applied to the cervix. In pilot studies involving 59 women the HRME images were obtained from 84 colposcopically abnormal sites and 59 colposcopically normal sites. They reported a sensitivity of 92% and specificity of 77% for CIN 2+ detection using parameters calculated from HRME images of 59 abnormal sites (nucleus-to-cytoplasm ratio, mean nuclear area and median nuclear eccentricity). They acknowledged a lower specificity of HRME image-based diagnostics (67%) in their previous studies [77] where they used one parameter from HRME image (nucleus-to-cytoplasm ratio) alone for the diagnostics. The majority of the sites with false-positive diagnosis were affected by chronic inflammation.

A set of images from over 60 patients obtained by fluorescence confocal endomicroscopy was used for ex vivo and in vivo studies of four types of cervical tissue relevant for the diagnostics: normal columnar epithelium, normal and precancerous squamous epithelium, and stromal tissue [80]. Researchers ac-

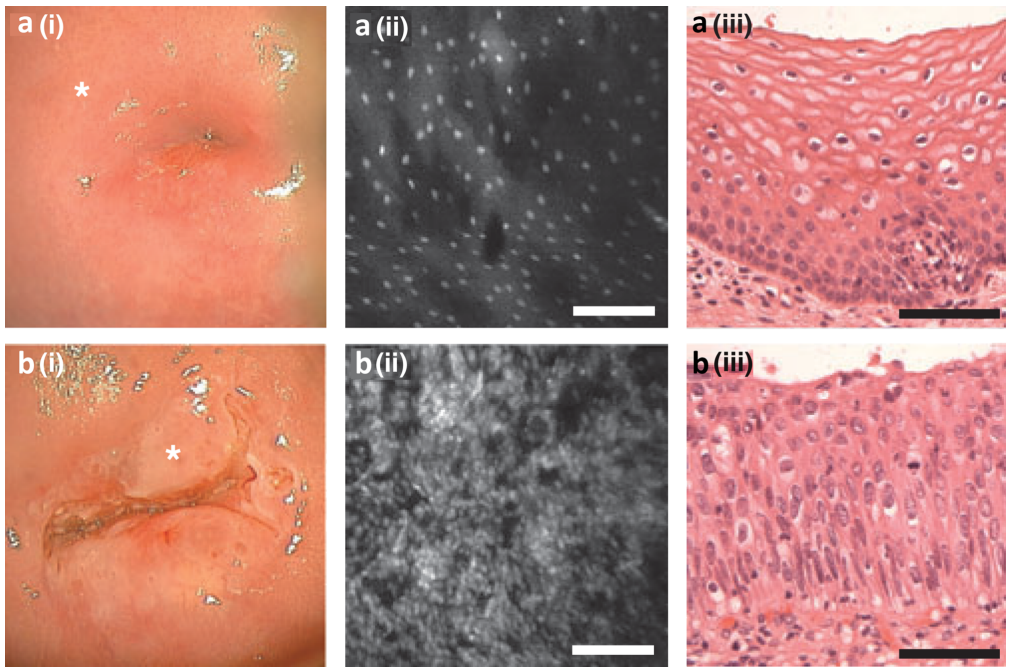

Figure 8: Cervical epithelium examined using (i) colposcopy, (ii) confocal endomicroscopy and (iii) conventional histology (H&E staining). (a) Normal cervix; (b) cervical CIN 3 lesion. *Confocal image site. Scale bars = 100 µm. Reproduced with permission from [76], copyright 2006 Wiley-Liss, Inc.

knowledged the challenge of reliable differentiation of all four types of cervical tissue by fluorescence endomicroscopy alone because of structural similarities of HSIL and stromal/columnar tissues in confocal endomicroscopic images. However, the capacity of confocal fluorescence microscopy to accurately discriminate between HSIL and LSIL/normal tissues at various imaging depths was confirmed [80,81].

Nanotheranostics

The rapid progress of nanotechnology had an important impact on cancer management research. The variety of new nanoscale platforms (gold nanoparticles, quantum dots, nanocages, carbon nanotubes) are used for cancer theranostics, which means the simultaneous diagnosis and treatment of diseases [82-86]. These nanoobjects can be used for a non-invasive monitoring of cellular processes at a molecular level. It has been confirmed that there is a strong interaction of nanoobjects with a size of less than 100 nm (i.e., which are much smaller than normal human cells) with biomolecules such as receptors, enzymes, and antibodies on the cell surface and inside the cell [87]. By surface coating, functionalization, and integration with different bioconjugated targeting agents those nanoparticles can be used for molecular-selective recognition of cancer biomarkers. The overexpression of specific biomarkers with cancer development will lead to the increase in concentration of optically active nanoobjects in the tumor zone and, consequently, to the diagnostic contrast enhancement (Figure 9).

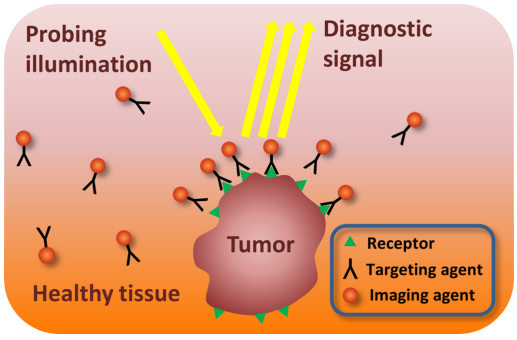

Figure 9: Illustration of optical molecular-targeted imaging with nanoparticles.

It is known that progression of CIN from mild dysplasia to invasive cancer is accompanied by the increase in level of epidermal growth factor receptor (EGFR). The overexpression of EGFR has been correlated to uncontrolled cell growth and inhibition of cell apoptosis. Hence, EGFR can be used as a unique molecular tumor marker [88].

The contrast agents consisting of a targeting agent conjugated with optically active labels (metal nanoparticles, quantum dots) can be used for in vivo imaging of this biomarker. Sokolov et al [89] reported the use of gold nanoparticles for the molecular targeted imaging of the specific biomarker of cervical cancer. The bioconjugates of gold nanoparticles (approximately 12 nm in diameter) with antibodies against EGFR have been used to increase the contrast during in vitro confocal reflectance and confocal fluorescence imaging of normal and abnormal cervical cells. The high affinity of antibodies to EGFR and the overexpression of EGFR in tumor cells lead to the agglomeration of gold nanoparticles in tumor zone. The scattering cross-section per particle increases when particles agglomerate. It leads to a non-linear enhancement in scattering resulting in a large optical contrast between isolated gold particles and agglomerated gold particles in tumor tissue in both confocal reflectance and confocal fluorescence images of cervical tissue specimens [89].

In recent years many research groups explored the potential of using quantum dots (QDs) as inorganic fluorophores for cellular imaging [57,83,85,90-93]. The unique optical properties of semiconductor quantum dots including quantum confinement effect, wide absorption spectrum (i.e., broad excitation band), and narrow emission spectrum (i.e., tunable fluorescence emission via QD bandgap engineering) combined with low toxicity and resistance to photo bleaching [93] make them ideal candidates for multi-wavelength cellular imaging. Because of the small size QDs can be effectively used for labeling molecular targets at both cellular and subcellular levels. Despite the above mentioned advantages of using QDs for molecular imaging in cancer theranostics the possible side effects (toxicity, disruption of cellular processes) also need to be considered [90].

Mueller polarimetry

There is an emerging set of optical techniques based on the detection of changes in the polarization of light instead of (or together with) intensity measurements. Apart from the intensity and wavelength of probing light its polarization can carry important information about the sample. Many research groups work in the field of biomedical applications of polarized light [94-103].

Even the simplest orthogonal state contrast (OSC) polarimetric techniques provide data about the polarimetric characteristics of the sample. Typically, the sample is illuminated with linearly or circularly polarized white light. Two set of measurements are performed, detecting the intensity of signal after interaction with sample through another linear or circular polarizer, set parallely ($I_{\parallel}$) and orthogonally ($I_{\perp}$) to the polarization state of the illuminating light. The OSC parameter is then calculated from these two measurements as $\mathrm{OSC} = \left(I_{\parallel} - I_{\perp}\right) / \left(I_{\parallel} + I_{\perp}\right)$. The diagnostic utility of this optical technique relies on the fact that polarized light loses its polarization when undergoing

multiple scattering events within biological tissue. The part of backscattered light that preserves its polarization was most probably scattered only once or reflected at the sample surface. Thus, the differential signal removes the contribution of light that has been diffused deeply within tissue and keeps the contribution of the superficial layer at which epithelial cancer starts.

The studies of spectra or images of OSC polarimetric measurements for the detection of colon cancerous polyps [94], skin cancer [95], and cervical precancerous lesions [104,105] revealed the enhancement of contrast between normal and pathological zones of tissue. Balas et al. [106] reported on using $I_{\perp}$ measurements for eliminating the surface reflectance component during time-resolved imaging of the whitening of cervical neoplasia after the application of acetic acid.

The OSC techniques make use of only two out of four components of the Stokes vector

$$\mathbf{S} = \left(I_{\mathrm{P}} + I_{\perp}, I_{\mathrm{P}} - I_{\perp}, I_{45^\circ} - I_{-45^\circ}, I_{\mathrm{L}} + I_{\mathrm{R}}\right)^{\mathrm{T}},$$

where I_{45° and I_{-45° denote the intensities which would be measured through ideal linear polarizers oriented along either +45° or −45°, respectively, in the plane perpendicular to the direction of light propagation and I_{L} and I_{R} are the intensities transmitted by left-handed or right-handed circular polarizers, respectively [107]. The linear transformation of the Stokes vector of incident light $\mathbf{S^i}$ interacting with a sample is described by the matrix equation $\mathbf{S^o} = \mathbf{MS^i}$, where $\mathbf{M}$ is the 4 × 4 real Mueller matrix of the sample. This matrix provides the most complete description of the polarimetric response of any medium (even partially or fully depolarizing) to the illumination with polarized light in the absence of non-linear effects. So, using the Stokes–Mueller formalism has proven to be necessary when dealing with biological samples. Rich polarimetric information about the sample properties is contained in the coefficients of the Mueller matrix. Currently, the phenomenological approach based on polar decomposition of the Mueller matrix by the Lu–Chipman algorithm [108] is widely accepted by many research groups [97,102,103,105,109,110] for the interpretation of basic polarimetric properties of the sample. The measured Mueller matrix $\mathbf{M}$ is decomposed into the product of three matrices: $\mathbf{M} = \mathbf{M_\Delta M_R M_D}$, where $\mathbf{M_\Delta}$, $\mathbf{M_R}$, and $\mathbf{M_D}$ are the Mueller matrices of depolarizer, retarder and diattenuator, respectively. Finally, the scalar values of depolarization, retardance and diattenuation, as well as the orientation of the optical axes of the retarder and the diattenuator can be obtained from the matrices $\mathbf{M_\Delta}$, $\mathbf{M_R}$, and $\mathbf{M_D}$. Strictly speaking, these parameters represent a set of "effective" optical markers of tissue. Lu–Chipman decomposition implies a sequential order of elementary polarimetric properties along the trajectory of the probing beam, whereas these polarimetric properties can be mixed within the volume of tissue. Nevertheless, these effective values of depolarization and retardance are found to be the important parameters for the polarimetric analysis.

Shukla et al. [109] obtained polarimetric images of histological slides of cervical tissue by applying Lu–Chipman decomposition of experimental Mueller matrices and analyzed them in order to discriminate normal tissue and CIN lesions. They found that values of scalar retardance drop in stromal areas adjacent to neoplastic epithelium. It can be explained by the structural reorganization of the extra-cellular collagen matrix accompanying early precancerous modifications of the epithelium [31,32]. The observed increase in depolarization power in neoplastic epithelial zones of tissue was attributed to an increasing scattering coefficient due to the increase of cell density.

During in vivo clinical studies linear OSC images of healthy uterine cervices acquired during colposcopy demonstrated a strong change of OSC contrasts with a 90° periodicity (i.e., a strong optical anisotropy) when the azimuth of the polarizer was varied [105]. Contrary to that the OSC contrasts in CIN zones, confirmed by following histological analysis of corresponding biopsies, showed no dependence on the azimuth variation. Consequently, CIN zones behaved as an isotropic depolarizer. The ex vivo polarimetric images of scalar retardance and depolarization power calculated from the Mueller matrix of a fresh cervical specimen measured at 550 nm are shown in Figure 10. None of studied cervical specimens demonstrated noticeable diattenuation. Healthy regions of cervix covered with squamous epithelium exhibited strong birefringence (optical index anisotropy), which vanished in precancerous regions even for LSIL. The orientation of the optical axis of retarder became completely random in CIN zones.

This effect was attributed to the degeneration of stromal collagen beneath the precancerous epithelial lesions [31,32]. The depolarization power is found to decrease monotonously with precancerous evolution. Combining both scalar retardance and depolarization power values it is possible to delimit the zone of benign modifications of cervical tissue (Figure 10a,b).

At first glance the trends in depolarization look contradictory to the results of Shukla et al. [109]. However, the imaging plane of a Mueller polarimeter is orthogonal to the plane of histological cuts of tissue seen by pathologists. Moreover, the images of thick tissue specimens were taken in backscattering configuration [105] compared to Mueller polarimetric transmission measurements of thin histological cuts by Shukla and co-workers [109]. It suggests that "effective" optical polarimetric biomark-

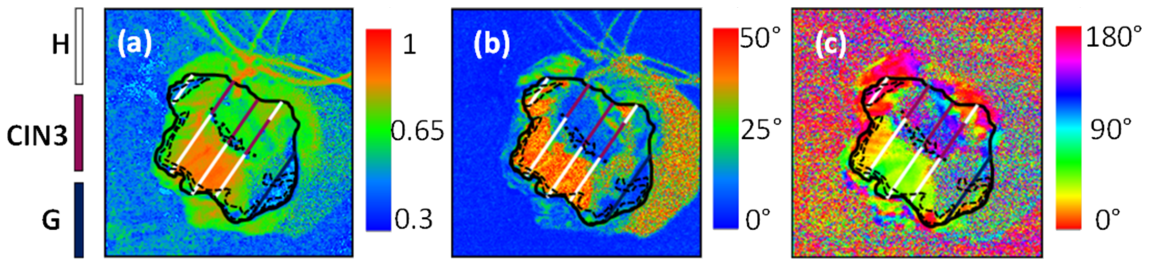

Figure 10: Polarimetric images of a cervical specimen taken at 550 nm: (a) depolarization (b) scalar retardance and (c) azimuth of optical axis. The colored lines show the position of cuts and results of histological analysis (white: healthy squamous epithelium (H), violet: CIN 3, black: glandular epithelium (G)). Reproduced with permission from [105], copyright 2013 Optical Society of America.

ers of tissue (scalar retardance, azimuthal angle of retarder optical axis and depolarization) extracted from in vivo Mueller polarimetric images in clinical settings will be sensitive not to precancerous epithelial transformations but rather to stromal modifications induced by CIN [111]. Hence, the decrease of depolarization power in CIN zones of thick tissue can be attributed to both a decrease of light scattering and an increase of absorption [112] due to reorganization of the collagen matrix and stromal angiogenesis [28-30].

Ex vivo studies of 17 fixed cervical specimens performed with a multi-spectral Muller imaging polarimeter [113] showed optimized values of sensitivity and specificity of about 83% for HSIL diagnosis when using both scalar retardance and depolarization power values as decision variables and histological analysis of pathologists as gold-standard diagnostics (Figure 11).

This suggests that Mueller polarimetry as wide-field imaging technique can greatly enhance colposcopy performance for the detection of CIN zones provided the raw data are processed by properly chosen algorithms. Finally, since polarimetric imaging is sensitive to the overall conditions of the collagen in the extracellular matrix (e.g., spatial organization, density and fiber length), it may also be relevant for the optical diagnostic of various gynecological pathologies involving connective tissues (e.g., preterm birth [114] and female genital prolapse [115,116]).

Optical coherence tomography

Optical coherence tomography (OCT) is an optical technique for non-invasive cross-sectional imaging of biological tissue. This technique makes use of low-coherence interferometry with a near-infrared light source to create two-dimensional images of tissue cross-sections by exploring elastic light scattering from internal tissue microstructures [117]. OCT provides depth-resolved images, where the contrast results from the spatial difference in refractive indices of layers and structures within the tissue. The high resolution of OCT (2–20 μm) and a depth of penetration up to 2 mm allow clinicians to visualize the subsurface tissue in real time at a spatial resolution better than that available with other optical diagnostics techniques. The depth resolution of OCT is decoupled from its transverse resolution.

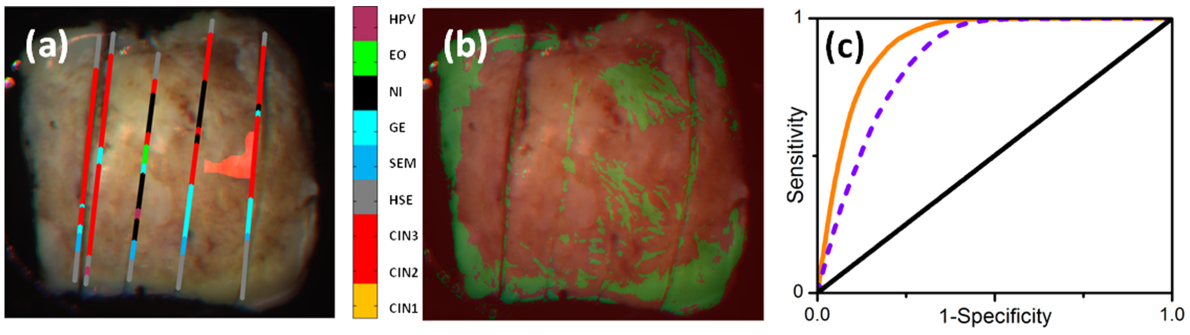

Figure 11: (a) Histological map (colored lines) superimposed on an RGB image of a conization sample; HPV: epithelium infected by HPV; EO: external os of cervix; NI: non-identified epithelial zones, GE: glandular epithelium; SEM: squamous epithelium metaplasia; HSE: healthy squamous epithelium; CIN 1–3: squamous intraepithelial neoplasia of grade 1–3; (b) diagnostic (red: CIN 2–3, green: all other conditions) image segmentation using a threshold of 10.1° for the value of scalar retardance *R* for measurements performed at 450 nm; (c) receiver operating characteristic (ROC) curves (violet dashed: diagnostics based on scalar retardance values only, orange: diagnostics based on combination of scalar retardance and depolarization power values). Images adapted from [113], copyright 2016 Society of Photo-optical Instrumentation Engineers.

Nowadays OCT is the reference technique in ophthalmology [118-121] and has been clinically tested in dermatology, otolaryngology and gastroenterology [122-125]. Recently OCT has been shown to be an efficient adjunct to colposcopy for the management of cervical neoplasia [126-128]. Because the resolution of OCT approaches the cellular tissue level, this optical technique demonstrated its potential for guiding biopsies during colposcopy and for monitoring CIN treatment [129].

Normal squamous cervical tissue exhibits a well-organized three-layer architecture [126]. Prior studies revealed that the lack of this specific structure in OCT images of squamous cervical tissue can be used as a fingerprint of malignancy, which allows for discriminating "benign" and "malignant" OCT images [129-131].

In the OCT image of healthy squamous cervical tissue a basement membrane (BM) is not resolved because of the lack of OCT resolution (Figure 12a). However, a sharp interface between the epithelium and stroma is clearly seen on OCT image. Both HSIL and invasive carcinoma are characterized by loss of layered tissue architecture and an increase in tissue microstructural disorder in OCT images (Figure 12 b,c). The stromal layer demonstrates columnar proliferation towards the surface of tissue in the OCT image of a CIN 3 lesion (Figure 12b). The invasive carcinoma manifests itself in the OCT image as unstructured homogeneous highly backscattering region with a complete loss of layered tissue architecture (Figure 12c). The basement membrane is broken and the microstructure of the tissue is no longer preserved.

Studies on using OCT for the detection of CIN and invasive carcinomas were carried by Gallwas and co-workers [131]. During the colposcopy in 60 women 610 OCT images were acquired from colposcopically abnormal and normal zones of the ectocervix. OCT images were independently evaluated by two experts and then matched to histological diagnoses of the corresponding biopsies. A sensitivity of 95% and a specificity of 46% for the detection of precancerous (CIN) and cancerous lesions were reported for OCT technique. A similar study in 120 women was performed for the evaluation of the accuracy and reproducibility of OCT diagnostics for both detection of CIN lesions and identification of CIN grades [126]. With the threshold at CIN 1 the sensitivity varied between 98% and 96%. Defining the threshold at CIN 2 the sensitivity calculated for both experts was 86% and 84%, respectively. A specificity of 39–41% was reported with the threshold at CIN 1. The specificity increased to 60–64% when the threshold was defined at CIN 2. These studies prove that OCT is highly sensitive in identifying precancerous lesions and invasive cancer of the uterine cervix. The relatively low specificity of OCT was attributed to the difficulties in distinguishing the OCT images of mild dysplasia (CIN 1) and tissue inflammation/benign modifications. It was shown that the mean brightness of the cervical epithelium layer in OCT images of squamous cervical tissue has the potential to become an optical marker for the differentiation between normal tissue, LSIL, HSIL and invasive cancer [132].

A study with 299 women on using OCT as adjunct to colposcopy for improving its sensitivity and specificity in a real-time clinical evaluation were conducted by Liu and co-workers [133]. They demonstrated that the specificity increased from 83% to 93% by adding OCT to colposcopy, but the sensitivity for CIN 2+ lesions decreased.

Gallwas et al. [134] suggested combining an OCT device with a microscope for the detection of CIN lesions. In that study 160 OCT images of excised cervical specimens were taken under microscopic guidance. The OCT images were independently analyzed by two experts and later compared to the histological gold-standard diagnosis, resulting in a sensitivity of 88% (second investigator 84%) and a specificity of 69% (65%) in detecting HSIL. They expect that the integration of an OCT instrument into the colposcope may be beneficial compared to scanning with the OCT probe and may improve the accuracy of colposcopic examinations of the cervix.

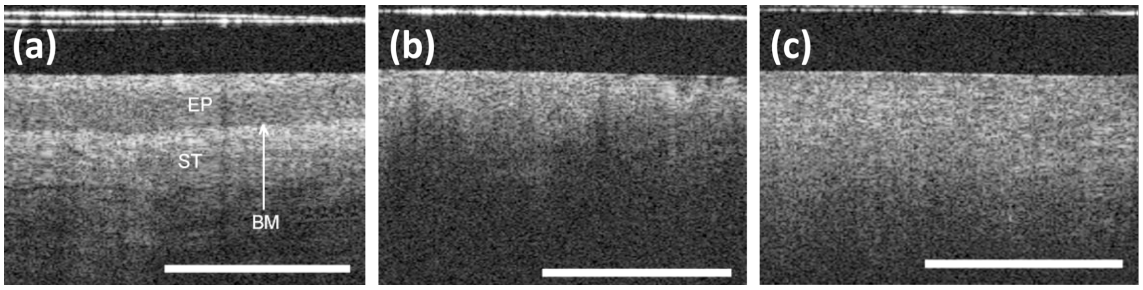

Figure 12: (a) OCT image of normal cervical tissue (BM: basement membrane, EP: epithelium, ST: stroma); (b) OCT image of a CIN 3 lesion; (c) OCT image of invasive carcinoma (length of white bar: 1 mm). Reproduced with permission from [131], copyright 2010 ISUOG.

Polarization-sensitive OCT (PS-OCT) combines the spatial information on the polarization state of light scattered from tissue with the recorded intensity of interference fringes [135]. Depth-resolved images of Stokes vector parameters allow for the determination of the degree of polarization and the orientation of the optical axis in anisotropic turbid media, thus providing additional contrast in cross-sectional OCT images of the sample.

Lee et al. [136] examined cervical conization specimens from 18 patients with PS-OCT (71 images were taken) for the detection of CIN lesions. It was demonstrated that PS-OCT can improve the specificity of diagnosis when interpreting "difficult" OCT intensity images. From the images of the degree of circular depolarization DOCP = S_3/S_0, the slope of axial decay of DOCP signal near the cervical epithelium was determined by a linear fitting procedure. Using the abovementioned slope as parameter for CIN diagnostics a sensitivity of 94.7% and a specificity of 71.2% was obtained for a slope threshold value of 1.8 mm^{-1}.

Combined techniques

Several studies reported using the combination of different optical (and non-optical) techniques to improve the performance of CIN diagnostics. Georgakoudi et al. [137] developed a trimodal spectroscopy (TMS) combining intrinsic fluorescence, diffuse reflectance, and light scattering spectroscopy for the detection and analysis of CIN lesions. During colposcopic examination a white light reflectance spectrum and autofluorescence spectra at ten excitation wavelengths were acquired using a flexible optical contact probe. Light scattering spectra were obtained by subtracting the contribution of diffuse reflectance from the measured reflectance. Intrinsic fluorescence spectra provided information about the metabolic state of the epithelium and adjacent stromal collagen. Information about scattering and absorption properties of epithelium and stroma was extracted from light scattering and diffuse reflectance spectra, respectively. Data collected from 44 patients demonstrated that the sensitivity and specificity of TMS was higher compared to the results of each individual technique alone.

Freeberg et al. [33] reported the results of a screening trial comprising 1000 patients and a diagnostic trail comprising 850 patients with combined fluorescence and reflectance spectroscopy using a fiber-optic probe for detecting cervical neoplasia. According to their analysis there is a distinguishable difference in mean intensity values measured on normal cervical tissue and HSIL. However, type of tissue (squamous or columnar) and patient age were confounding factors for the performance of combined fluorescence and reflectance spectroscopy diagnostics. The clinical trials on 227 patients with an optical detection system (ODS; combining scanning fluorescence spectroscopy, diffuse reflectance spectroscopy and video imaging) as an adjunct to colposcopy showed statistically significant improvement in the detection of histologically confirmed CIN 2–3 lesions compared to conventional colposcopy [138].

Weber et al. [139] measured in vivo reflectance and fluorescence spectra of normal and precancerous cervical tissue in 330 patients using a fiber-optic point-probe. By means of an analytical model they extracted diagnostically relevant parameters from the spectral data. They reported a sensitivity of 85% and a specificity of 51% of their technique relative to the gold standard of histopathology analysis.

A multimodal hyperspectroscopy (MHS) instrument that combines fluorescence and reflectance spectroscopy was tested in 1607 women at risk for cervical dysplasia [140]. The sensitivity of MHS for CIN 2+ lesions was 91.3%. The specificity was 38.9% for women with normal or benign histology and 30.3% for women with CIN 1 histology.

The comparative studies of diffuse reflectance and Raman spectroscopic measurements performed in vivo with a fiber-optic probe on 22 patients (67 tumor spectra and 22 normal cervix spectra) showed a slightly better diagnostic accuracy of Raman spectroscopy [141]. The sensitivity and specificity of RS were estimated as 91% and 96%, respectively, compared to a sensitivity of 85% and a specificity of 95% for DRS diagnostics. Some inherent features of Raman systems (price, complexity and dimensions) suggest using them in stationary settings, while compactness, portability and low cost of DRS systems can make them an instrument of choice for field applications.

A hybrid optical imaging modality that explores photoacoustic effect was used by Peng et al. [142] for the detection and grading of precancerous and cancerous lesions of the cervix (in vitro studies). The technique is based on the absorption of light by tissue, which creates a temperature gradient, and the associated raise of pressure, which generates ultrasonic waves. Acoustic detectors receive these waves and provide the signals to generate images. Optical absorption in tissue is mainly due to hemoglobin; hence, photoacoustic imaging provides an enhanced image contrast for vascular system, hemodynamics and oxygen metabolism, which all can be used as biomarkers for the detection of tissue malignancy. Using ultrasound as a response signal allows for a deeper penetration depth compared to pure optical imaging systems. It suggests photoacoustic imaging for the detection of lesions in the endocervix, which is not accessible for the direct observation under colposcopy [142].

The efficacy and advantages/disadvantages of new alternative technologies or technologies adjunct to colposcopy using multimodal hyperspectroscopy, dynamic spectral imaging, OCT, confocal microcolposcopy, electrical impedance spectroscopy and combined optical/electrical instruments are discussed in [143-147].

The use of all functionalities of smartphones for the wide-field imaging of the uterine cervix with white and green light sources and magnification lens for an enhanced visualization is suggested and being tested by MobileODT [148]. Another mobile battery-powered colposcope Gynocular by Gynius AB [149] was clinically tested for cervical examination in Sweden, Bangladesh, India and Uganda. These new instruments allow a medical practitioner to get relevant information on the spot, thus, making screening, diagnostics and treatment more effective and less expensive. Hence, the emerging techniques may also contribute to the reliable "screen-and-treat" cervical cancer programs in low- and middle-income countries wherever the Pap and/or HPV tests would be difficult to implement [150,151].

Conclusion

Current programs for cervical cancer screening still rely on Pap/HPV tests for the primary screening and on colposcopy for the diagnostics and guiding biopsies, if necessary. With more countries introducing HPV vaccination programs the prevalence of HSIL is expected to drop. The challenges for standard colposcopy will grow, since correct diagnosis depends to a large extent on the experience of the operator trained to recognize the high-grade cervical dysplasia on a sheer number of cases.

To maintain the satisfactory level of sensitivity and specificity of HSIL diagnostics we need to improve the instruments and advance the screening procedures. The innovative biomedical optical imaging and spectroscopic techniques provide clinicians the possibility to inspect the epithelial volume and underlying tissue non-invasively and to extract an accurate information regarding tissue morphological and biochemical states. The choice of the most appropriate optical technique will always involve a trade-off between the technical parameters (such as spatial and spectral resolution, acquisition time and field of view) and medical diagnostic outcome (specificity and sensitivity) that can be achieved.

Currently, new optical instruments and contrast enhancement techniques for the accurate and reliable diagnostics of cervical neoplasia are still at an exploratory stage and have not yet been widely accepted for routine screening and diagnostics. Commercially available instruments are being tested by medical practitioners in real-life settings, while other devices still undergo clinical trials for the confirmation and optimization of their diagnostic performance.

Modern trends in biomedical optical instrumentation require the development of portable and cost-effective versions of medical devices. In particular, these needs are driven by the necessity to support global transition, namely, to deploy and use these instruments in low-resource countries. This is the problem of paramount importance for the screening, diagnosis and treatment of cervical cancer. Ideally the wide-field imaging (polarimetric or fluorescent) should be combined with optical point-probe measurements (e.g., Raman spectroscopy, confocal microscopy, OCT) and different contrast-enhancing techniques to perform the optical biopsy of tissue. Such instruments might be considered for the first-line screening and triage by optical means during the same medical visit, thus, significantly reducing the cost of cervical cancer prevention programs.

Acknowledgements

Funding from ANR TWIST4NET grant and Campus France POLHIS project No. 38660WH (PHC RILA) is gratefully acknowledged. Special thanks to L. Fatykhova for the art work.

References

1. World Health Organization. Chapter 5.12. *World Cancer Report;* World Health Organization: Geneva, Switzerland, 2014; pp 465–481.
2. Catarino, R.; Petignat, P.; Dongui, G.; Vassilakos, P. *World J. Clin. Oncol.* **2015,** *6,* 281–290. doi:10.5306/wjco.v6.i6.281
3. WHO. Cervical cancer. http://www.who.int/cancer/prevention/diagnosis-screening/cervical-cancer/en/ (accessed Aug 8, 2017).
4. Lowy, D. R.; Solomon, D.; Hildesheim, A.; Schiller, J. T.; Schiffman, M. *Cancer* **2008,** *113* (Suppl. 7), 1980–1993. doi:10.1002/cncr.23704
5. Yang, E. J.; Quick, M. C.; Hanamornroongruang, S.; Lai, K.; Doyle, L. A.; McKeon, F. D.; Xian, W.; Crum, C. P.; Herfs, M. *Mod. Pathol.* **2015,** *28,* 994–1000. doi:10.1038/modpathol.2015.54
6. Reich, O.; Regauer, S. *Int. J. Cancer* **2015,** *137,* 2520–2521. doi:10.1002/ijc.29117
7. Herfs, M.; Yamamoto, Y.; Laury, A.; Wang, X.; Nucci, M. R.; McLaughlin-Drubin, M. E.; Münger, K.; Feldman, S.; McKeon, F. D.; Xian, W.; Crum, C. P. *Proc. Natl. Acad. Sci. U. S. A.* **2012,** *109,* 10516–10521. doi:10.1073/pnas.1202684109
8. Herfs, M.; Parra Herran, C.; Howitt, B. E.; Laury, A. R.; Nucci, M. R.; Feldman, S.; Jimenez, C. A.; McKeon, F. D.; Xian, W.; Crum, C. P. *Am. J. Surg. Pathol.* **2013,** *37,* 1311–1318. doi:10.1097/PAS.0b013e3182989ee2
9. Mirkovic, J.; Howitt, B. E.; Roncarati, P.; Demoulin, S.; Suarez-Carmona, M.; Hubert, P.; McKeon, F. D.; Xian, W.; Li, A.; Delvenne, P.; Crum, C. P.; Herfs, M. *J. Pathol.* **2015,** *236,* 265–271. doi:10.1002/path.4533
10. Nayar, R.; Solomon, D. *CytoJournal* **2004,** *1,* 4. doi:10.1186/1742-6413-1-4
11. Wilson, J. M.; Jungner, G. *The principles and practice of screening for disease;* World Health Organization: Geneva, Switzerland, 1966.

12. Safaeian, M.; Solomon, D.; Castle, P. E. *Obstet. Gynecol. Clin. North Am.* **2007,** *34,* 739–760. doi:10.1016/j.ogc.2007.09.004
13. European Centre for Disease Prevention and Control. *Introduction of HPV vaccines in EU countries – an update;* ECDC: Stockholm, Sweden, 2012.
14. Adamopoulou, M.; Kalkani, E.; Charvalos, E.; Avgoustidis, D.; Haidopoulos, D.; Yapijakis, C. *Anticancer Res.* **2009,** *29,* 3401–3410.
15. Agrawal, A.; Sharma, A.; Gupta, M.; Agarwal, N. *Int. J. Reprod. Contracept. Obstet. Gynecol.* **2016,** *5,* 3765–3769. doi:10.18203/2320-1770.ijrcog20163838
16. Orfanoudaki, I. M.; Kappou, D.; Sifakis, S. *Arch. Gynecol. Obstet.* **2011,** *284,* 1197–1208. doi:10.1007/s00404-011-2009-4
17. Underwood, M.; Arbyn, M.; Parry-Smith, W.; De Bellis-Ayres, S.; Todd, R.; Redman, C. W. E.; Moss, E. L. *BJOG* **2012,** *119,* 1293–1301. doi:10.1111/j.1471-0528.2012.03444.x
18. Cantor, S. B.; Cárdenas-Turanzas, M.; Cox, D. D.; Atkinson, E. N.; Nogueras-Gonzalez, G. M.; Beck, J. R.; Follen, M.; Benedet, J. L. *Obstet. Gynecol.* **2008,** *111,* 7–14. doi:10.1097/01.AOG.0000295870.67752.b4
19. Dalla Palma, P.; Giorgi Rossi, P.; Collina, G.; Buccoliero, A. M.; Ghiringhello, B.; Lestani, M.; Onnis, G.; Aldovini, D.; Galanti, G.; Casadei, G. P.; Aldi, M.; Giubilato, P.; Ronco, G.; NTCC Pathology Group. *Am. J. Clin. Pathol.* **2008,** *129,* 75–80. doi:10.1309/EWYGWFRRM8798U5P
20. Mitchell, M. F.; Schottenfeld, D.; Tortolero-Luna, G.; Cantor, S. B.; Richards-Kortum, R. *Obstet. Gynecol.* **1998,** *91,* 626–631.
21. Nam, K.; Chung, S.; Kwak, J.; Cha, S.; Kim, J.; Jeon, S.; Bae, D. *J. Lower Genital Tract Dis.* **2010,** *14,* 346–351. doi:10.1097/LGT.0b013e3181e9635b
22. GLOBOCAN Cancer Fact Sheets: Cervical cancer. http://globocan.iarc.fr/old/FactSheets/cancers/cervix-new.asp (accessed Aug 8, 2017).
23. Thekkek, N.; Richards Kortum, R. *Nat. Rev. Cancer* **2008,** *8,* 725–731. doi:10.1038/nrc2462
24. Arifler, D.; MacAulay, C. E.; Follen, M.; Richards-Kortum, R. R. *J. Biomed. Opt.* **2006,** *11,* 064027. doi:10.1117/1.2398932
25. Cantor, S. B.; Yamal, J.-M.; Guillaud, M.; Cox, D. D.; Atkinson, E. N.; Benedet, J. L.; Miller, D.; Ehlen, T.; Matisic, J.; van Niekerk, D.; Bertrand, M.; Milbourne, A.; Rhodes, H.; Malpica, A.; Staerkel, G.; Nader-Eftekhari, S.; Adler-Storthz, K.; Scheurer, M. E.; Basen-Engquist, K.; Shinn, E.; West, L. A.; Vlastos, A.-T.; Tao, X.; Beck, J. R.; MacAulay, C.; Follen, M. *Int. J. Cancer* **2011,** *128,* 1151–1168. doi:10.1002/ijc.25667
26. Prabitha, V. G.; Suchetha, S.; Jayanthi, J. L.; Baiju, K. V.; Rema, P.; Anuraj, K.; Mathews, A.; Sebastian, P.; Subhash, N. *Lasers Med. Sci.* **2016,** *31,* 67–75. doi:10.1007/s10103-015-1829-z
27. Chang, V. T.-C.; Cartwright, P. S.; Bean, S. M.; Palmer, G. M.; Bentley, R. C.; Ramanujam, N. *Neoplasia (Ann Arbor, MI, U. S.)* **2009,** *11,* 325–332. doi:10.1593/neo.81386
28. Lee, J. S.; Kim, H. S.; Jung, J. J.; Lee, M. C.; Park, C. S. *Anal. Quant. Cytol. Histol.* **2002,** *24,* 103–113.
29. Lee, J. S.; Choi, Y. D.; Lee, J. H.; Nam, J. H.; Choi, C.; Lee, M. C.; Park, C. S.; Juhng, S. W.; Kim, H. S.; Min, K. W. *Gynecol. Oncol.* **2004,** *95,* 523–529. doi:10.1016/j.ygyno.2004.08.036
30. Chang, V. T.-C.; Bean, S.; Cartwright, P. S.; Ramanujam, N. *J. Biomed. Opt.* **2010,** *15,* 057006. doi:10.1117/1.3495730
31. Pavlova, I.; Sokolov, K.; Drezek, R.; Malpica, A.; Follen, M.; Richards-Kortum, R. *Photochem. Photobiol.* **2003,** *77,* 550–555. doi:10.1562/0031-8655(2003)0770550MABOON2.0.CO2
32. Arifler, D.; Pavlova, I.; Gillenwater, A.; Richards-Kortum, R. *Biophys. J.* **2007,** *92,* 3260–3274. doi:10.1529/biophysj.106.089839
33. Freeberg, J. A.; Serachitopol, D. M.; McKinnon, N.; Price, R. L.; Atkinson, E. N.; Cox, D. D.; MacAulay, C. E.; Richards-Kortum, R. R.; Follen, M.; Pikkula, B. M. *J. Biomed. Opt.* **2007,** *12,* 034015. doi:10.1117/1.2750332
34. Yu, B.; Ferris, D. G.; Liu, Y.; Nagarajan, V. K. *Austin J. Biomed. Eng.* **2014,** *1,* 1007.
35. Nath, A.; Rivoire, K.; Chang, S. K.; Cox, D. D.; Atkinson, E. N.; Follen, M.; Richards-Kortum, R. R. *J. Biomed. Opt.* **2004,** *9,* 523–533. doi:10.1117/1.1695562
36. Reif, R.; Amorosino, M. S.; Calabro, K. W.; A'Amar, O. M.; Singh, S. K.; Bigio, I. J. *J. Biomed. Opt.* **2008,** *13,* 010502. doi:10.1117/1.2870115
37. Tabrizi, S. H.; Reza Aghamiri, S. M.; Farzaneh, F.; Amelink, A.; Sterenborg, H. J. C. M. *J. Biomed. Opt.* **2013,** *18,* 017002. doi:10.1117/1.JBO.18.1.017002
38. Chang, V. T.-C.; Merisier, D.; Yu, B.; Walmer, D. K.; Ramanujam, N. *Opt. Express* **2011,** *19,* 17908–17924. doi:10.1364/OE.19.017908
39. Mirkovic, J.; Lau, C.; McGee, S.; Yu, C.-C.; Nazemi, J.; Galindo, L.; Feng, V.; Darragh, T.; de Las Morenas, A.; Crum, C.; Stier, E.; Feld, M.; Badizadegan, K. *J. Biomed. Opt.* **2009,** *14,* 044021. doi:10.1117/1.3194142
40. Cardenas-Turanzas, M.; Freeberg, J. A.; Benedet, J. L.; Atkinson, E. N.; Cox, D. D.; Richards-Kortum, R.; MacAulay, C.; Follen, M.; Cantor, S. B. *Gynecol. Oncol.* **2007,** *107* (Suppl. 1), S138–S146. doi:10.1016/j.ygyno.2007.08.082
41. Park, S. Y.; Follen, M.; Milbourne, A.; Rhodes, H.; Malpica, A.; MacKinnon, N. B.; MacAulay, C. E.; Markey, M. K.; Richards-Kortum, R. R. *J. Biomed. Opt.* **2008,** *13,* 014029. doi:10.1117/1.2830654
42. Park, S. Y.; Sargent, D.; Lieberman, R.; Gustafsson, U. *IEEE Trans. Med. Imaging* **2011,** *30,* 867–878. doi:10.1109/TMI.2011.2106796
43. Wagnieres, G. A.; Star, W. M.; Wilson, B. C. *Photochem. Photobiol.* **1998,** *68,* 603–632. doi:10.1111/j.1751-1097.1998.tb02521.x
44. Chang, S. K.; Arifler, D.; Drezek, R. A.; Follen, M.; Richards-Kortum, R. R. *J. Biomed. Opt.* **2004,** *9,* 511–522. doi:10.1117/1.1695559
45. Talvensaari-Mattila, A.; Apaja-Sarkkinen, M.; Höyhtyä, M.; Westerlund, A.; Puistola, U.; Turpeenniemi-Hujanen, T. *Gynecol. Oncol.* **1999,** *72,* 306–311. doi:10.1006/gyno.1998.5157
46. Chidananda, S. M.; Satyamoorthy, K.; Rai, L.; Manjunath, A. P.; Kartha, V. B. *Int. J. Cancer* **2006,** *119,* 139–145. doi:10.1002/ijc.21825
47. Pandey, K.; Pradhan, A.; Agarwal, A.; Bhagoliwal, A.; Agarwal, N. *J. Obstet. Gynecol. India* **2012,** *62,* 432–436. doi:10.1007/s13224-012-0298-6
48. Georgakoudi, I.; Jacobson, B. C.; Muller, M. G.; Sheets, E. E.; Badizadegan, K.; Carr-Locke, D. L.; Crum, C. P.; Boone, C. W.; Dasari, R. R.; Van Dam, J.; Feld, M. S. *Cancer Res.* **2002,** *62,* 682–687.
49. Drezek, R. R.; Sokolov, K. V.; Utzinger, U.; Boiko, I.; Malpica, A.; Follen, M.; Richard-Kortum, R. R. *J. Biomed. Opt.* **2001,** *6,* 385–396. doi:10.1117/1.1413209
50. Ramanujam, N.; Mitchell, M. F.; Mahadevan, A.; Thomsen, S.; Malpica, A.; Wright, T.; Atkinson, N.; Richards-Kortum, R. *Lasers Surg. Med.* **1996,** *19,* 46–62. doi:10.1002/(SICI)1096-9101(1996)19:1<46::AID-LSM7>3.0.CO;2-Q

51. Milbourne, A.; Park, S. Y.; Benedet, J. L.; Miller, D.; Ehlen, T.; Rhodes, H.; Malpica, A.; Matisic, J.; Van Niekirk, D.; Atkinson, E. N.; Hadad, N.; MacKinnon, N.; MacAulay, C.; Richards-Kortum, R.; Follen, M. *Gynecol. Oncol.* **2005,** *99,* S67–S75. doi:10.1016/j.ygyno.2005.07.047
52. Weingandt, H.; Stepp, H.; Baumgartner, R.; Diebold, J.; Xiang, W.; Hillemanns, P. *BJOG* **2002,** *109,* 947–951. doi:10.1111/j.1471-0528.2002.01311.x
53. Gu, J.; Yaw Fu, C.; Koon Ng, B.; Razul, S. G.; Kim Lim, S. *J. Biophotonics* **2014,** *7,* 483–491. doi:10.1002/jbio.201200202
54. Miyasaka, N.; Egawa, M.; Isobe, M.; Inoube, Y.; Kubota, T. *J. Obstet. Gynaecol. Res.* **2016,** *42,* 1846–1853. doi:10.1111/jog.13139
55. Calatrava-Pérez, E.; Bright, S.; Achermann, S.; Moylan, C.; Senge, M.; Veale, E.; Williams, D. C.; Gunnlaugsson, T.; Scanlan, E. M. *Chem. Commun.* **2016,** *52,* 13086–13089. doi:10.1039/C6CC06451E
56. Castellanos, M. R.; Szerszen, A.; Gundry, S.; Pirog, E. C.; Maiman, M.; Rajupet, S.; Gomez, J. P.; Davidov, A.; Debata, P. R.; Banerje, P.; Fata, J. E. *Diagn. Pathol.* **2015,** *10,* 119. doi:10.1186/s13000-015-0343-8
57. Pierce, M. C.; Javier, D. J.; Richards-Kortum, R. *Int. J. Cancer* **2008,** *123,* 1979–1990. doi:10.1002/ijc.23858
58. McGregor, H. C.; Short, M. A.; McWilliams, A.; Shaipanich, T.; Ionescu, D. N.; Zhao, J.; Wang, W.; Chen, G.; Lam, S.; Zeng, H. *J. Biophotonics* **2017,** *10,* 98–110. doi:10.1002/jbio.201500204
59. Jermyn, M.; Desroches, J.; Aubertin, K.; St-Arnaud, K.; Madore, W.-J.; De Montigny, E.; Guiot, M.-C.; Trudel, D.; Wilson, B. C.; Petrecca, K.; Leblond, F. *Phys. Med. Biol.* **2016,** *61,* R370–R400. doi:10.1088/0031-9155/61/23/R370
60. Lyng, F. M.; Traynor, D.; Ramos, I. R. M.; Bonnier, F.; Byrne, H. J. *Anal. Bioanal. Chem.* **2015,** *407,* 8279–8289. doi:10.1007/s00216-015-8946-1
61. Lin, K.; Wang, J.; Zheng, W.; Ho, K. Y.; Teh, M.; Yeoh, K. G.; Huang, Z. *Cancer Prev. Res.* **2016,** *9,* 476–483. doi:10.1158/1940-6207.CAPR-15-0213
62. Duraipandian, S.; Zheng, W.; Ng, J.; Low, J. J. H.; Ilancheran, A. *Anal. Chem.* **2012,** *84,* 5913–5919. doi:10.1021/ac300394f
63. Li, X.; Yang, T.; Li, S.; Wang, D.; Song, Y.; Zhang, S. *Laser Phys.* **2016,** *26,* 035702. doi:10.1088/1054-660X/26/3/035702
64. Rashid, N.; Nawaz, H.; Poon, K. W. C.; Bonnier, F.; Bakhiet, S.; Martin, C.; O'Leary, J. J.; Byrne, H. J.; Lyng, F. M. *Exp. Mol. Pathol.* **2014,** *97,* 554–564. doi:10.1016/j.yexmp.2014.10.013
65. Kanter, E. M.; Majumder, S.; Vargis, E.; Robichaux-Viehoever, A.; Kanter, G. J.; Shappell, H.; Jones, H. W., III; Mahadevan-Jansen, A. *J. Raman Spectrosc.* **2009,** *40,* 205–211. doi:10.1002/jrs.2108
66. Robichaux-Viehoever, A.; Kanter, E.; Shappell, H.; Billheimer, D.; Jones, H.; Mahadevan-Jansen, A. *Appl. Spectrosc.* **2007,** *61,* 986–993. doi:10.1366/000370207781746053
67. Carignan, C. S.; Yagi, Y. *Diagn. Pathol.* **2012,** *7,* 98. doi:10.1186/1746-1596-7-98
68. Paull, P. E.; Hyatt, B. J.; Wassef, W.; Fischer, A. H. *Arch. Pathol. Lab. Med.* **2011,** *135,* 1343–1348. doi:10.5858/arpa.2010-0264-RA
69. Iovieno, A.; Longo, C.; De Luca, M.; Piana, S.; Fontana, L.; Ragazzi, M. *Am. J. Ophthalmol.* **2016,** *168,* 207–216. doi:10.1016/j.ajo.2016.06.001
70. Goetz, M.; Kiesslich, R. *Anticancer Res.* **2008,** *28,* 353–360.
71. Jabbour, J. M.; Cheng, S. N.; Malik, B. H.; Cuenca, R.; Jo, J. A.; Wright, J.; Cheng, Y.-S. L.; Maitland, K. C. *J. Biomed. Opt.* **2013,** *18,* 046012. doi:10.1117/1.JBO.18.4.046012
72. Hoogedoorn, L.; Gerritsen, M. J. P.; Wolberink, E. A. W.; Peppelman, M.; van de Kerkhof, P. C. M.; van Erp, P. E. J. *J. Eur. Acad. Dermatol. Venereol.* **2016,** *30,* 1308–1314. doi:10.1111/jdv.13627
73. Drezek, R. A.; Collier, T.; Brookner, C. K.; Malpica, A.; Lotan, R.; Richards-Kortum, R. R.; Follen, M. *Am. J. Obstet. Gynecol.* **2000,** *182,* 1135–1139. doi:10.1067/mob.2000.104844
74. Carlson, K.; Pavlova, I.; Colliera, T.; Descourb, M.; Follen, M.; Richards-Kortum, R. *Gynecol. Oncol.* **2005,** *99* (Suppl. 3), S84–S88. doi:10.1016/j.ygyno.2005.07.049
75. Collier, T. G.; Guillaud, M.; Follen, M.; Malpica, A.; Richards-Kortum, R. R. *J. Biomed. Opt.* **2007,** *12,* 024021. doi:10.1117/1.2717899
76. Tan, J.; Quinn, M. A.; Pyman, J. M.; Delaney, P. M.; McLaren, W. J. *BJOG* **2009,** *116,* 1663–1670. doi:10.1111/j.1471-0528.2009.02261.x
77. Pierce, M. C.; Guan, Y.; Quinn, M. K.; Zhang, X.; Zhang, W.-H.; Qiao, Y.-L.; Castle, P.; Richards-Kortum, R. *Cancer Prev. Res.* **2012,** *5,* 1273–1279. doi:10.1158/1940-6207.CAPR-12-0221
78. Quinn, M. K.; Bubi, T. C.; Pierce, M. C.; Kayembe, M. K.; Ramogola-Masire, D.; Richards-Kortum, R. *PLoS One* **2012,** *7,* e44924. doi:10.1371/journal.pone.0044924
79. Grant, B. D.; Fregnani, J. H. T. G.; Possati Resende, J. C.; Scapulatempo-Neto, C.; Matsushita, G. M.; Mauad, E. C.; Quang, T.; Stoler, M. H.; Castle, P. E.; Schmeler, K. M.; Richards-Kortum, R. R. *Eur. J. Cancer Prev.* **2017,** *26,* 63–70. doi:10.1097/CEJ.0000000000000219
80. Schlosser, C. L.; Bodenschatz, N.; Lam, S. F.; Lee, M.; McAlpine, J. N.; Miller, D. M.; Van Niekerk, D. J. T.; Follen, M.; Guillaud, M.; MacAulay, C. E.; Lane, P. M. *J. Biomed. Opt.* **2016,** *21,* 126011. doi:10.1117/1.JBO.21.12.126011
81. Sheikhzadeh, F.; Ward, R. K.; Carraro, A.; Yang Chen, Z.; van Niekerk, D.; Miller, D.; Ehlen, T.; MacAulay, C. E.; Follen, M.; Lane, P. M.; Guillaud, M. *BioMed. Eng. OnLine* **2015,** *14,* 96. doi:10.1186/s12938-015-0093-6
82. Cuenca, A. G.; Jiang, H.; Hochwald, S. N.; Delano, M.; Cance, W. G.; Grobmyer, S. R. *Cancer* **2006,** *107,* 459–466. doi:10.1002/cncr.22035
83. Thakur, M.; Mewada, A.; Pandey, S.; Bhori, M.; Singh, K.; Sharon, M.; Sharon, M. *Mater. Sci. Eng., C* **2016,** *67,* 468–477. doi:10.1016/j.msec.2016.05.007
84. Fan, Z.; Fu, P. P.; Yu, H.; Ray, P. C. *J. Food Drug Anal.* **2014,** *22,* 3–17. doi:10.1016/j.jfda.2014.01.001
85. Xu, Y.; Wu, M.; Liu, Y.; Feng, X.-Z.; Yin, X.-B.; He, X.-W.; Zhang, Y.-K. *Chem. – Eur. J.* **2013,** *19,* 2276–2283. doi:10.1002/chem.201203641
86. Tolstik, E.; Osminkina, L. A.; Akimov, D.; Gongalsky, M. B.; Kudryavtsev, A. A.; Timoshenko, V. Yu.; Heintzmann, R.; Sivakov, V.; Popp, J. *Int. J. Mol. Sci.* **2016,** *17,* 1536–1550. doi:10.3390/ijms17091536
87. Ahmed, N.; Fessi, H.; Elaissari, A. *Drug Discovery Today* **2012,** *17,* 928–934. doi:10.1016/j.drudis.2012.03.010
88. Kersemaekers, A. M.; Kenter, G. G.; Van den Broek, L. J.; Uljee, S. M.; Hermans, J.; Van de Vijver, M. J. *Clin. Cancer Res.* **1999,** *5,* 577–586.
89. Sokolov, K.; Follen, M.; Aaron, J.; Pavlova, I.; Malpica, A.; Lotan, R.; Richards-Kortum, R. *Cancer Res.* **2003,** *63,* 1999–2004.

90. Nida, D. L.; Rahman, M. S.; Carlson, K. D.; Richards-Kortum, R.; Follen, M. *Gynecol. Oncol.* **2005,** *99,* S89–S94. doi:10.1016/j.ygyno.2005.07.050
91. Rahman, M.; Abd-El-Barr, M.; Mack, V.; Tkaczyk, T.; Sokolov, K.; Richards-Kortum, R.; Descour, M. *Gynecol. Oncol.* **2005,** *99* (Suppl. 3), S112–S115. doi:10.1016/j.ygyno.2005.07.053
92. Xu, X.; Zhang, K.; Zhao, L.; Li, C.; Bu, W.; Shen, Y.; Gu, Z.; Chang, B.; Zheng, C.; Lin, C.; Sun, H.; Yang, B. *ACS Appl. Mater. Interfaces* **2016,** *8,* 32706–32716. doi:10.1021/acsami.6b12252
93. Ye, H.-L.; Cai, S.-J.; Li, S.; He, X.-W.; Li, W.-Y.; Li, Y.-H.; Zhang, Y. K. *Anal. Chem.* **2016,** *88,* 11631–11638. doi:10.1021/acs.analchem.6b03209
94. Gurjar, R. S.; Backman, V.; Perelman, L. T.; Georgakoudi, I.; Badizadegan, K.; Itzkan, I.; Dasari, R. R.; Feld, M. S. *Nat. Med.* **2001,** *7,* 1245–1248. doi:10.1038/nm1101-1245
95. Jacques, S. L.; Ramella-Roman, J. C.; Lee, K. *J. Biomed. Opt.* **2002,** *7,* 329–340. doi:10.1117/1.1484498
96. Soni, J.; Purwar, H.; Lakhotia, H.; Chandel, S.; Banerjee, C.; Kumar, U.; Ghosh, N. *Opt. Express* **2013,** *21,* 15475–15489. doi:10.1364/OE.21.015475
97. Du, E.; He, H.; Zeng, N.; Sun, M.; Guo, Y.; Wu, J.; Liu, S.; Ma, H. *J. Biomed. Opt.* **2014,** *19,* 076013. doi:10.1117/1.JBO.19.7.076013
98. Novikova, T.; Meglinski, I.; Ramella-Roman, J. C.; Tuchin, V. V. *J. Biomed. Opt.* **2016,** *21,* 071001. doi:10.1117/1.JBO.21.7.071001
99. Alali, S.; Vitkin, I. A. *J. Biomed. Opt.* **2015,** *20,* 061104. doi:10.1117/1.JBO.20.6.061104
100. Ghassemi, P.; Lemaillet, P.; Ramella-Roman, J. C.; Shupp, J. W.; Venna, S. S.; Boisvert, M. E.; Flanagan, K.; Jordan, M. H.; Germer, T. A. *J. Biomed. Opt.* **2012,** *17,* 076014. doi:10.1117/1.JBO.17.7.076014
101. Kunnen, B.; Macdonald, C.; Doronin, A.; Jacques, S.; Eccles, M.; Meglinski, I. *J. Biophotonics* **2015,** *8,* 317–323. doi:10.1002/jbio.201400104
102. Qi, J.; Elson, D. S. *Sci. Rep.* **2016,** *6,* 25953. doi:10.1038/srep25953
103. Novikova, T.; Pierangelo, A.; De Martino, A.; Benali, A.; Validire, P. *Opt. Photonics News* **2012,** *23,* 26–32. doi:10.1364/OPN.23.10.000026
104. Anastasiadou, M.; De Martino, A.; Clement, D.; Liège, F.; Laude-Boulesteix, B.; Quang, N.; Dreyfuss, J.; Huynh, B.; Nazac, A.; Schwartz, L.; Cohen, H. *Phys. Status Solidi C* **2008,** *5,* 1423–1426. doi:10.1002/pssc.200777805
105. Pierangelo, A.; Nazac, A.; Benali, A.; Validire, P.; Cohen, H.; Novikova, T.; Haj Ibrahim, B.; Manhas, S.; Fallet, C.; Antonelli, M.-R.; De Martino, A. *Opt. Express* **2013,** *21,* 14120–14130. doi:10.1364/OE.21.014120
106. Balas, C. *IEEE Trans. Biomed. Eng.* **2001,** *48,* 96–104. doi:10.1109/10.900259
107. Huard, S. *Polarization of Light;* Wiley: New York, NY, U.S.A., 1997.
108. Lu, S.-Y.; Chipman, R. A. *J. Opt. Soc. Am. A* **1996,** *13,* 1106–1113. doi:10.1364/JOSAA.13.001106
109. Shukla, P.; Pradhan, A. *Opt. Express* **2009,** *17,* 1600–1609. doi:10.1364/OE.17.001600
110. Chue-Sang, J.; Bai, Y.; Stoff, S.; Straton, D.; Ramaswamy, S.; Ramella-Roman, J. C. *J. Biomed. Opt.* **2016,** *21,* 71109. doi:10.1117/1.JBO.21.7.071109
111. Nazac, A.; Bancelin, S.; Teig, B.; Ibrahim, B. H.; Fernandez, H.; Schanne-Klein, M. C.; De Martino, A. *Microsc. Res. Tech.* **2015,** *78,* 723–730. doi:10.1002/jemt.22530
112. Novikova, T.; Pierangelo, A.; Manhas, S.; Benali, A.; Validire, P.; Gayet, B.; De Martino, A. *Appl. Phys. Lett.* **2013,** *102,* 241103. doi:10.1063/1.4811414
113. Rehbinder, J.; Haddad, H.; Deby, S.; Teig, B.; Nazac, A.; Novikova, T.; Pierangelo, A.; Moreau, F. *J. Biomed. Opt.* **2016,** *21,* 071113. doi:10.1117/1.JBO.21.7.071113
114. Stoff, S.; Chue-Sang, J.; Holness, N. A.; Gandjbakhche, A.; Chernomordik, V.; Ramella-Roman, J. *Proc. SPIE* **2016,** *9689,* 968947. doi:10.1117/12.2213387
115. Pannu, H. K.; Genadry, R.; Kaufman, H. S.; Fishman, E. K. *J. Comput. Assisted Tomogr.* **2003,** *27,* 779–785. doi:10.1097/00004728-200309000-00016
116. Kerkhof, M. H.; Hendriks, L.; Brölmann, H. A. M. *Int. Urogynecol. J.* **2009,** *20,* 461–474. doi:10.1007/s00192-008-0737-1
117. Fercher, A. F.; Drexler, W.; Hitzenberger, C. K.; Lasser, T. *Rep. Prog. Phys.* **2003,** *66,* 239–303. doi:10.1088/0034-4885/66/2/204
118. Cennamo, G.; Romano, M. R.; Breve, M. A.; Velotti, N.; Reibaldi, M.; de Crecchio, G.; Cennamo, G. *Eye (London, U. K.)* **2017,** *31,* 906–915. doi:10.1038/eye.2017.14
119. Ehlers, J. P.; Tao, Y. K.; Srivastava, S. K. *Curr. Opin. Ophthalmol.* **2014,** *25,* 221–227. doi:10.1097/ICU.0000000000000044
120. Pircher, M.; Hitzenberger, C. K.; Schmidt-Erfurthn, U. *Prog. Retinal Eye Res.* **2011,** *30,* 431–451. doi:10.1016/j.preteyeres.2011.06.003
121. Gabriele, M. L.; Wollstein, G.; Ishikawa, H.; Kagemann, L.; Xu, J.; Folio, L. S.; Schuman, J. S. *Invest. Ophthalmol. Visual Sci.* **2011,** *52,* 2425–2436. doi:10.1167/iovs.10-6312
122. Wessels, R.; De Bruin, D. M.; Faber, D. J.; Van Leeuwen, T. G.; Van Beurden, M.; Ruers, T. J. M. *Lasers Med. Sci.* **2014,** *29,* 1297–1305. doi:10.1007/s10103-013-1291-8
123. Sattler, E. C.; Kästle, R.; Welzel, J. *J. Biomed. Opt.* **2013,** *18,* 061224. doi:10.1117/1.JBO.18.6.061224
124. DeCoro, M.; Wilder-Smith, P. *Expert Rev. Anticancer Ther.* **2010,** *10,* 321–329. doi:10.1586/era.09.191
125. Kirtane, T. S.; Wagh, M. S. *Gastroenterol. Res. Pract.* **2014,** *2014,* 376367. doi:10.1155/2014/376367
126. Gallwas, J. K. S.; Turk, L.; Stepp, H.; Mueller, S.; Ochsenkuehn, R.; Friese, K.; Dannecker, C. *Lasers Surg. Med.* **2011,** *43,* 206–212. doi:10.1002/lsm.21030
127. Zuluaga, A. F.; Follen, M.; Boiko, I.; Malpica, A.; Richards-Kortum, R. *Am. J. Obstet. Gynecol.* **2005,** *193,* 83–88. doi:10.1016/j.ajog.2004.11.054
128. Escobar, P. F.; Rojas-Espaillat, L.; Tisci, S.; Enerson, C.; Brainard, J.; Smith, J.; Tresser, N. J.; FeldchteinI, F. I.; Rojas, L. B.; Belinson, J. L. *Int. J. Gynecol. Cancer* **2006,** *16,* 1815–1822. doi:10.1111/j.1525-1438.2006.00665.x
129. Panteleeva, O. G.; Kuznetsova, I. A.; Kachalina, O. V.; Eliseeva, D. D.; Grebenkina, E. V.; Gamayunov, S. V.; Kuznetsov, S. S.; Yunusova, E. E.; Gubarkova, E. V.; Kirillin, M. Yu.; Shakhova, N. M. *Mod. Technol. Med.* **2015,** *7,* 89–96. doi:10.17691/stm2015.7.1.12
130. Shakhova, N. M.; Feldchtein, F. I.; Sergeev, A. M. Applications of Optical Coherence Tomography in Gynecology. In *Handbook of Optical Coherence Tomography;* Bouma, B. E.; Tearney, G. I., Eds.; CRC Press: Boca Raton, FL, U.S.A., 2002; pp 649–671. doi:10.1201/b14024-25
131. Gallwas, J.; Turk, L.; Friese, K.; Dannecker, C. *Ultrasound Obstet. Gynecol.* **2010,** *36,* 624–629. doi:10.1002/uog.7656

132. Belinson, S. E.; Ledford, K.; Rasool, N.; Rollins, A.; Wilan, N.; Wang, C.; Rong, X.; Zhang, W.; Zhu, Y.; Tresser, N.; Wu, R.; Belinson, J. L. *J. Lower Genital Tract Dis.* **2013,** *17,* 160–166. doi:10.1097/LGT.0b013e31825d7bf0
133. Liu, Z.; Belinson, S. E.; Li, J.; Yang, B.; Wulan, N.; Tresser, N. J.; Wang, C.; Mohr, M.; Zhang, L.; Zhou, Y.; Weng, L.; Wu, R.; Belinson, J. L. *Int. J. Gynecol. Cancer* **2010,** *20,* 283–287. doi:10.1111/IGC.0b013e3181cd1810
134. Gallwas, J.; Jalilova, A.; Ladurner, R.; Kolben, T. M.; Kolben, T.; Ditsch, N.; Homann, C.; Lankenau, E.; Dannecker, C. *J. Biomed. Opt.* **2017,** *22,* 16013. doi:10.1117/1.JBO.22.1.016013
135. de Boer, J. F.; Milner, T. E. *J. Biomed. Opt.* **2002,** *7,* 359–371. doi:10.1117/1.1483879
136. Lee, S.-W.; Yoo, J.-Y.; Kang, J.-H.; Kang, M.-S.; Jung, S.-H.; Chong, Y.; Cha, D.-S.; Han, K.-H.; Kim, B.-M. *Opt. Express* **2008,** *16,* 2709–2719. doi:10.1364/OE.16.002709
137. Georgakoudi, I.; Sheets, E. E.; Müller, M. G.; Backman, V.; Crum, C. P.; Badizadegan, K.; Dasari, R. R.; Feld, M. S. *Am. J. Obstet. Gynecol.* **2002,** *186,* 374–382. doi:10.1067/mob.2002.121075
138. Alvarez, R. D.; Wright, T. C., Jr.; Optical Detection Group. *Gynecol. Oncol.* **2007,** *106,* 23–28. doi:10.1016/j.ygyno.2007.02.028
139. Weber, C. E. R.; Schwarz, R. A.; Atkinson, E. N.; Cox, D. D.; MacAulay, C. E.; Follen, M.; Richards-Kortum, R. R. *J. Biomed. Opt.* **2008,** *13,* 064016. doi:10.1117/1.3013307
140. Twiggs, L. B.; Chakhtoura, N. A.; Ferris, D. G.; Flowers, L. C.; Winter, M. L.; Sternfeld, D. R.; Lashgari, M.; Burnett, A. F.; Raab, S. S.; Wilkinson, E. J. *Gynecol. Oncol.* **2013,** *130,* 147–151. doi:10.1016/j.ygyno.2013.04.012
141. Shaikh, R.; Prabitha, V. G.; Kumar Dora, T.; Chopra, S.; Maheshwari, A.; Deodhar, K.; Rekhi, B.; Sukumar, N.; Krishna, C. M.; Subhash, N. *J. Biophotonics* **2017,** *10,* 242–252. doi:10.1002/jbio.201500248
142. Peng, K.; He, L.; Wang, B.; Xiao, J. *Biomed. Opt. Express* **2015,** *6,* 135–143. doi:10.1364/BOE.6.000135
143. Drezek, R. A.; Richards-Kortum, R.; Brewer, M. A.; Feld, M. S.; Pitris, C.; Ferenczy, A.; Faupel, M. L.; Follen, M. *Cancer* **2003,** *98* (Suppl. S9), 2015–2027. doi:10.1002/cncr.11678
144. Leeson, S. *Eur. J. Obstet. Gynecol. Reprod. Biol.* **2014,** *182,* 140–145. doi:10.1016/j.ejogrb.2014.09.016
145. Wade, R.; Spackman, E.; Corbett, M.; Walker, S.; Light, K.; Naik, R.; Sculpher, M.; Eastwood, A. *Health Technol. Assess.* **2013,** *17*. doi:10.3310/hta17080
146. Louwers, J. A.; Kocken, M.; ter Harmsel, W. A.; Verheijen, R. H. M. *BJOG* **2009,** *116,* 220–229. doi:10.1111/j.1471-0528.2008.02047.x
147. Tan, J. H. J.; Wrede, C. D. H. *Best Pract. Res. Clin. Obstet. Gynaecol.* **2011,** *25,* 667–677. doi:10.1016/j.bpobgyn.2011.05.005
148. MobileODT - MobileODT. http://www.mobileodt.com/ (accessed Aug 8, 2017).
149. Gynocular Colposcopes – Gynius AB. http://www.gynius.se/the-gynocular/ (accessed Aug 8, 2017).
150. Paul, P.; Winkler, J. L.; Bartolini, R. M.; Penny, M. E.; Thu Huong, T.; Thi Nga, L.; Kumakech, E.; Mugisha, E.; Jeronimo, J. *Oncologist* **2013,** *18,* 1278–1284. doi:10.1634/theoncologist.2013-0253
151. Sankaranarayanan, R.; Okkuru Esmy, P.; Rajkumar, R.; Muwonge, R.; Swaminathan, R.; Shanthakumari, S.; Fayette, J.-M.; Cherian, J. *Lancet* **2007,** *370,* 398–406. doi:10.1016/S0140-6736(07)61195-7

License and Terms

The definitive version of this article is the electronic one which can be found at: doi:10.3762/bjnano.8.186